National Technical University of Athens
School of Chemical Engineering
Department of Process Analysis
and Plant Design

University of Toulouse
Institut National Polytechnique
de Toulouse (INP Toulouse)

Université Fédérale

Toulouse Midi-Pyrénées

Doctoral Thesis

Multi-scale modelling and experimental analysis of ALD alumina: Interplay of process dynamics, chemistry and interfacial phenomena

by

Georgios P. GAKIS

JURY

Mme Elisabeth BLANQUET, Rapporteur

M. Athanasios DIMOULAS, Rapporteur

M. Emmanuel SCHEID, Examiner

Mme Evangelia PAVLATOU, Examiner

M. Athanasios G. PAPATHANASIOU, Examiner

Mme Asiya TURGAMBAEVA, Examiner

Mme Brigitte CAUSSAT, Thesis Director

M. Andreas G. BOUDOUVIS, Thesis Director

M. Constantin VAHLAS, Invited

M. Hugues VERGNES, Invited

Acknowledgements

First of all, I would like to thank my supervisors, Prof. Andreas Boudouvis from NTUA and Prof. Brigitte Caussat from INPT/LGC, for the opportunity they gave me to carry out this research in a cotutelle framework between two universities, cities and countries. It was a unique experience which was truly enriching, not only scientifically, but more importantly in personal and human aspects, and they are the ones who made all of this possible. I especially thank Prof. Boudouvis for his trust all these years, in both a professional and a personal way, from my undergraduate years up to now. It was a privilege to work with him and his research group, and he mentored me through all these years. I wish to deeply thank Prof. Caussat for always being there when I needed anything despite her busy schedule, for her kindness, and her positive attitude towards my work, even when things were not going as expected. She treated me as a colleague from the first day, without forgetting that I was a PhD student.

I am also thankful to the other members of the "Dream Team": Dr. Constantin Vahlas, Dr. Hugues Vergnes, and Dr. Emmanuel Scheid. I thank Dr. Constantin Vahlas, for his advices, help, and encouragement. I wish to thank him for the way he treated me both professionally and personally over these years. He has helped me take the first steps towards the understanding of material science and characterization techniques, which I

would not have taken without him. I wish to deeply thank Dr. Hugues Vergnes, for his precious time that he dedicated (despite a schedule that is more busy than I had ever imagined) to our meetings and our scientific discussions covering a wide range of topics. I admire his passion, his work and his ethics towards science, as well as his kindness as a person. I am truly indebted to Dr. Emmanuel Scheid, for his fantastic work, his insight on the ALD process, and his willingness to perform new experiments. His expertise on ALD was the spine of this thesis work, and none of it would be possible without his contribution. He is also a very kind and pleasant person who was always there to solve any questions or solve any problems that I faced.

I wish to thank Alessandro Pugliara, Claudie Josse and Teresa Hungria from UMS Castaing for their help with the TEM and STEM/EDX characterizations. I am also thankful to Yann Tison and Herve Martinez from IPREM in Pau, for their contibutions to the XPS characterizations. I thank Sandrine Dourdain from ICSM Montpelier, for her help with the XRR characterizations, as well as David Ruch and Jerome Bour from LIST, for the SIMS characterizations. I deeply thank Fuccio Cristiano from LAAS, for his time and help with the EDX characterizations.

Perhaps the most important thing that I gained during my thesis time that I spent in Toulouse, are the people that I met. For this reason, I thank all of my friends and colleagues in the LGC department and the SURF group in CIRIMAT (I do not name them as there are many). They made all my stays in Toulouse pleasant, leaving only good memories from my thesis years.

I also wish to thank the members of the NTUA group: Giannis Aviziotis, Nikos Chamakos, Giorgos Paschos and Pavlos Gkinis. I especially thank Eleni Koronaki, for

her guidance during all these years, but mainly for being the most pleasant colleague and office mate I could ask for. She always had "my back".

Of course, I would not be able to get by my thesis years without my friends. I do not want to leave anyone out, so I do not name them separately. I am proud to be considered as their friend. Their presence has always encouraged me through not only my thesis years, but throughout my whole life.

However, my most sincere thanks are dedicated to my family: my parents, Giannis and Karin, and my brother, Nikos. They have stood by me all these years, and they have loved and supported me throughout my whole life. They have withstood me and they always encouraged and helped me for all the plans that I had in my life. For this reason, I dedicate this thesis to them.

Contents of the thesis

Abstract

The constant shrinking of microelectronic devices requires the production of conformal and uniform nanometric thin films, with a high chemical purity and abrupt interfaces. In this context, Atomic Layer Deposition (ALD) has emerged as a favorable process to produce such films. Drawing its advantages from the self-limiting nature of the surface reactions involved, ALD can yield thickness control down to the monolayer, producing conformal films of high purity.

Although ALD has many advantages, drawbacks arise when depositing films of some nanometers. In particular, the initial island growth and the formation of an interfacial oxide layer are two of its main limitations, especially for the case of metal oxide ALD on Si. Moreover, the deposition on large area wafers is not always uniform, and depends on the reactor and process design. These drawbacks need to be suppressed in order to establish ALD as the adequate process for the deposition of high-k gate oxides on Si, essential for the production of field effect transistors of the future.

In this thesis, the ALD of Al_2O_3 from TMA and H_2O on Si is thoroughly investigated, in order to tackle the above drawbacks. The investigation consists of a combined multiscale computational and experimental approach. Four different numerical models were developed dealing with different space scales. A complete set of characterization techniques was used, including ellipsometry, XRR, TEM, STEM, EDX, XPS and SIMS. Using this framework, the detailed phenomena involved are illuminated, thus allowing to better understand the process and identify the factors responsible for the drawbacks of ALD.

The competition between surface mechanisms, namely desorption and surface reactions, was found to be the limiting factor for deposition at low temperatures, up to 200°C. The concentration of surface reactive sites was found to limit the deposition at higher temperatures up to 300°C. Although ALD is conceived as a process depending only on surface chemistry, the analysis of the transport phenomena inside the ALD chamber showed that the reactor and process design can affect the reactant and temperature distribution inside the ALD reactor. The multiscale approach and the coupling among the different computational models revealed that the interplay between surface mechanisms and transport phenomena affects the film uniformity. Using this computational approach, it was possible to derive optimal process conditions that ensure maximum film uniformity.

During the first deposition steps, the film deposition was found to be inhibited, leading to an island growth regime. The integrated analysis showed that 25 cycles are needed in order to deposit a continuous Al_2O_3 film. During this regime, interfacial oxidation of the Si substrate led to the formation of a ~2 nm interfacial oxide layer, consisting of SiO_x, AlO_x, and Al-silicates, which degrades the properties and thus the potential applications of the deposited structure.

An *in situ* N_2-NH_3 plasma pretreatment of the HF-cleaned Si substrate was introduced, leading to a formation of a Si_xN_yH layer on the substrate surface. The pretreatment was found to enhance the surface reactivity, as the inhibition period was restricted and linear ALD growth was obtained even after 5 cycles. Furthermore, interfacial Si oxidation was reduced, as the Si_xN_yH layer was found to serve as an effective barrier for O diffusion and Si oxidation.

The work presented in this thesis demonstrates the necessity of such integrated approaches to analyze the detailed phenomena involved in ALD. Such studies help in the thorough understanding of the ALD mechanisms, and consequently in elaborating solutions which restrict the drawbacks arising during the initial deposition steps. This could pave the way for the ALD process to industrially produce uniform and conformal nanometric thin films of high purity and abrupt interfaces, able to answer to the demands of the future electronic industry.

Εκτενής ελληνική περίληψη

Η ερευνητική εργασία που παρουσιάζεται στην παρούσα διατριβή αφορά την ενδελεχή μελέτη των φαινομένων και μηχανισμών που εμπλέκονται κατά τη διάρκεια της Απόθεσης Ατομικού Στρώματος (Atomic Layer Deposition, ALD) οξειδίου του αλουμινίου (Al_2O_3) πάνω σε πυρίτιο (Si). Η ανάλυση πραγματοποιείται με τη χρήση ενός συνδυασμένου υπολογιστικού και πειραματικού πλαισίου. Το πλαίσιο αυτό αποτελείται από φυσικά και χημικά μοντέλα σε πολλαπλές χωρικές κλίμακες, καθιστώντας μια υπολογιστική προσέγγιση πολλαπλών κλιμάκων, ενώ για την πειραματική διερεύνηση χρησιμοποιείται ένας αντιδραστήρας ALD και μια πληθώρα τεχνικών χαρακτηρισμού. Με αυτό το πλαίσιο, οι επιμέρους μηχανισμοί και η επίδρασή τους σε διάφορες πτυχές της διεργασίας ALD και των ιδιοτήτων του υμενίου μελετώνται, οδηγώντας έτσι στην εις βάθος κατανόηση και τον έλεγχο της διεργασίας ALD.

Η συνεχής συρρίκνωση των μικροηλεκτρονικών συσκευών αλλά και γενικότερα η ανάγκη νανομετρικών λεπτών υμενίων σε όλες τις τεχνολογίες-κλειδιά έχει ωθήσει προς την ανάγκη για παραγωγή τέτοιων υμενίων με υψηλό έλεγχο της σύστασης, του πάχους και της ομοιομορφίας τους (George, 2010)(Kingon *et al.,2000*). Στο πλαίσιο αυτό, η ALD έχει αναδειχθεί ως η βέλτιστη διεργασία για την παραγωγή τους. Η ALD είναι κυκλική διεργασία, υποκατηγορία της Χημικής Απόθεσης από Ατμό, που βασίζεται στη διαδοχική έκθεση ενός υποστρώματος σε συνήθως δύο αντιδρώντα Α και Β, με τα οποία αντιδρά μέσω αυτο-περιοριζόμενων αντιδράσεων. Κάθε κύκλος ALD αποτελείται από τέσσερα στάδια (Puurunen *et al.* 2005):

1. Έκθεση του υποστρώματος στο αέριο αντιδρών Α, με το οποίο αντιδρά μέσω αυτοπεριοριζόμενων αντιδράσεων

2. Καθαρισμός του αντιδραστήρα για την αποφυγή συνύπαρξης και αντίδρασης των συστατικών Α και Β στην αέρια φάση

3. Έκθεση του υποστρώματος στο αέριο αντιδρών Β, με το οποίο αντιδρά μέσω αυτοπεριοριζόμενων αντιδράσεων

4. Καθαρισμός του αντιδραστήρα για την αποφυγή συνύπαρξης και αντίδρασης των συστατικών Α και Β στην αέρια φάση

Καθώς οι αντιδράσεις είναι αυτοπεριοριζόμενες, οι επαναλαμβανόμενοι κύκλοι οδηγούν σε μια σταθερή απόθεση ανά κύκλο (Growth per Cycle, GPC), ορίζοντας μια γραμμική σχέση μεταξύ του αποτιθέμενου πάχους και των κύκλων ALD, γνωστή ως γραμμική κατάσταση ALD. Αντλώντας τα πλεονεκτήματά της από την αυτο-περιοριζόμενη φύση των επιφανειακών αντιδράσεων που εμπλέκονται κατά τη διεργασία, η ALD μπορεί θεωρητικά να παράγει υμένια με έλεγχο του πάχους του υμενίου σε κάποια Å. Ο εξαιρετικός έλεγχος πάνω στη σύσταση και την ομοιομορφία του υμενίου κάνουν την ALD ένα σημαντικό εργαλείο για την παραγωγή υμενίων οξειδίων μετάλλου πάνω σε Si (Johnson *et al.*, 2014), που χρησιμοποιούνται ως υμένια υψηλής διηλεκτρικής σταθεράς (high k gate oxides) στη σημερινή τεχνολογία τρανζίστορ μετάλλου-οξειδίου-ημιαγωγού (MOSFETs).

Αν και τα πλεονεκτήματα της ALD είναι υπερέχουν κατά πολύ από αυτά άλλων τεχνικών απόθεσης (Johnson *et al.*, 2014), παρουσιάζονται ορισμένα μειονεκτήματα για την απόθεση λεπτότατων υμενίων μερικών νανομέτρων. Η απόθεση στα αρχικά στάδια της ALD επηρεάζεται από τη φύση του υποστρώματος, που οδηγεί σε πολύπλοκη αρχική μορφή ανάπτυξης όπως ανάπτυξη σε νησίδες (Puurunen *et al.*, 2004), που έτσι απαιτεί έναν ελάχιστο αριθμό των κύκλων ALD για να παραχθεί ένα

συνεχές υμένιο. Εκτός από την μη ιδανική απόθεση κατά τους πρώτους κύκλους ALD, μια διεπιφάνεια σχηματίζεται μεταξύ του αποτιθέμενου υμενίου και του υποστρώματος, η οποία επηρρεάζει τη σύσταση και έτσι τις πιθανές εφαρμογές του αποτιθέμενου υμενίου (Först *et al.*, 2004).

Η ALD σε μεγάλες κλίμακες επίσης παρουσιάζει ακόμη ανωριμότητα για βιομηχανικές εφαρμογές. Για να επιτευχθεί ομοιόμορφη απόθεση σε μεγάλες επιφάνειες, οι συγκεντρώσεις των αντιδρώντων συστατικών πρέπει να είναι ομογενείς κατά μήκος της επιφάνειας όλου του υποστρώματος. Οι παράγοντες αυτοί επηρεάζουν τον απαιτούμενο χρόνο έκθεσης (exposure time) των αντιδρώντων και καθαρισμού του αντιδραστήρα (purge time) σε ALD, καθιστώντας τη διαδικασία δαπανηρή (Muñoz-Rojas *et al.,* 2019), απαιτώντας έτσι βελτιστοποίηση του σχεδιασμού του αντιδραστήρα και της διεργασίας.

Τα παραπάνω απαιτούν σε βάθος κατανόηση των μηχανισμών και των φαινομένων που εμπλέκονται στη διεργασία ALD. Δεδομένου ότι αυτά τα φαινόμενα λαμβάνουν χώρα σε διάφορες χωρικές και χρονικές κλίμακες, η λεπτομερής πειραματική μελέτη της διεργασίας ALD είναι δύσκολη.

Η ALD του Al_2O_3 πάνω σε Si από τρι-μεθυλ-αλουμίνιο (TMA) και νερό (H_2O) επιλέγεται ως η διεργασία προς διερεύνηση, δεδομένου ότι αντιπροσωπεύει μια περίπτωση ALD οξειδίου μετάλλου πάνω σε Si. Αν και είναι μια από τις πιο μελετημένες διεργασίες ALD και θεωρείται μια «ιδεατή διεργασία» (George, 2010), παρουσιάζει τα παραπάνω μειονεκτήματα, και οι μηχανισμοί που εμπλέκονται δεν έχουν ακόμη μελετηθεί και κατανοηθεί λεπτομερώς.

Η ανάλυση της διεργασίας αποτελείται από μια συνδυασμένη υπολογιστική και πειραματική προσέγγιση, με σκοπό να αποκαλύψει τους μηχανισμούς που λαμβάνουν

χώρα στο εσωτερικό του αντιδραστήρα ALD. Αυτή η προσέγγιση επιτρέπει την λεπτομερή κατανόηση των διαφόρων μηχανισμών που συμβάλλουν στην ανάπτυξη των υμενίων ALD, οδηγώντας έτσι στην εύρεση μεθόδων για να ξεπεραστούν τα μειονεκτήματα που προκύπτουν από την αρχική επιφάνεια του υποστρώματος, την διεπιφανειακή οξείδωση του Si και την αλληλεπίδραση των φαινομένων μεταφοράς και επιφανειακών μηχανισμών για απόθεση σε μεγάλες επιφάνειες.

Η απόθεση ALD πραγματοποιήθηκε σε έναν εμπορικό αντιδραστήρα Veeco® Fiji F200 ALD, σε υποστρώματα Si (100) με διάμετρο 200 mm. Τα πειράματα διεξήχθησαν χρησιμοποιώντας μια πληθώρα συνθηκών διεργασίας, για να διερευνηθεί η επίδραση των παραμέτρων λειτουργίας στην εναπόθεση AI_2O_3. Τα αποτιθέμενα υμένια μελετήθηκαν χρησιμοποιώντας ένα πλήρες σύνολο τεχνικών χαρακτηρισμού, συμπεριλαμβανομένων των: Ελλειψομετρία, XRR, TEM, STEM, EDX, XPS και SIMS. Αυτοί οι χαρακτηρισμοί έδωσαν πληροφορίες σχετικά με το πάχος, την μορφολογία, τη δομή, τη χημική φύση και τη σύσταση των υμενίων.

Η υπολογιστική διερεύνηση της διεργασίας πραγματοποιήθηκε χρησιμοποιώντας τέσσερα διαφορετικά υπολογιστικά μοντέλα που μελετούν διαφορετικές χωρικές κλίμακες, καθιστώντας την μια προσέγγιση πολλαπλών κλιμάκων. Δύο μοντέλα υπολογιστικής ρευστομηχανικής (CFD) αναπτύσσονται για τον αντιδραστήρα ALD και το σύστημα τροφοδοσίας αντιδραστηρίων, συνδεδεμένα μεταξύ τους μέσω μιας υπολογιστικής στρατηγικής. Το μοντέλο CFD του αντιδραστήρα συνδέεται ύστερα με ένα μοντέλο επιφανειακής χημείας του υποστρώματος που λαμβάνει υπόψη τη ρόφηση, την εκρόφηση και την επιφανειακή αντίδραση χημικών ειδών στην επιφάνεια. Αυτό επιτρέπει τη διερεύνηση του ανταγωνισμού των διαφόρων επιφανειακών φαινομένων αλλά και της αλληλεπίδρασης μεταξύ των επιφανειακών μηχανισμών και των φαινομένων μεταφοράς, επιτρέποντας

έτσι τη μελέτη των επιδράσεων των παραμέτρων διεργασίας και των φαινομένων στον αντιδραστήρα σε ιδιότητες του υμενίου, όπως η ομοιομορφία.

Το μοντέλο CFD συνδέεται επίσης με ένα στοχαστικό μοντέλο επιφανειακής χημείας kinetic Monte Carlo (kMC), το οποίο επιτρέπει τη διεξοδική μελέτη των διαφορετικών γεγονότων που λαμβάνουν χώρα στην επιφάνεια του υποστρώματος στη νανοκλίμακα. Μικροσκοπικές ιδιότητες της απόθεσης του υμενίου, όπως η εξέλιξη της τραχύτητας, η αποτιθέμενη μάζα και η στοιχειομετρία του υμενίου κατά τη διάρκεια της διεργασίας ALD, μπορούν να υπολογιστούν χρησιμοποιώντας αυτό το μοντέλο.

Τέλος, χρησιμοποιήθηκε γεωμετρικό μοντέλο ανάπτυξης σε νησίδες, ωστε να μελετηθεί η απόθεση κατά τη διάρκεια των αρχικών βημάτων της διεργασίας ALD. Αυτό το μοντέλο τροφοδοτείται από τιμές που προέρχεται από τα συζευγμένα μοντέλα επιφανειακής χημείας της κλίμακας του υποστρώματος και CFD.

Από την ανάλυση της διεργασίας με τη σύζευξη του μοντέλου CFD του αντιδραστήρα και του μοντέλου επιφανειακής χημείας στην κλίμακα του υποστρώματος, προκύπτει η ανάλυση των επιφανειακών μηχανισμών. Το σχήμα χημείας που χρησιμοποιήθηκε παρουσιάζεται στο Σχήμα Π1.
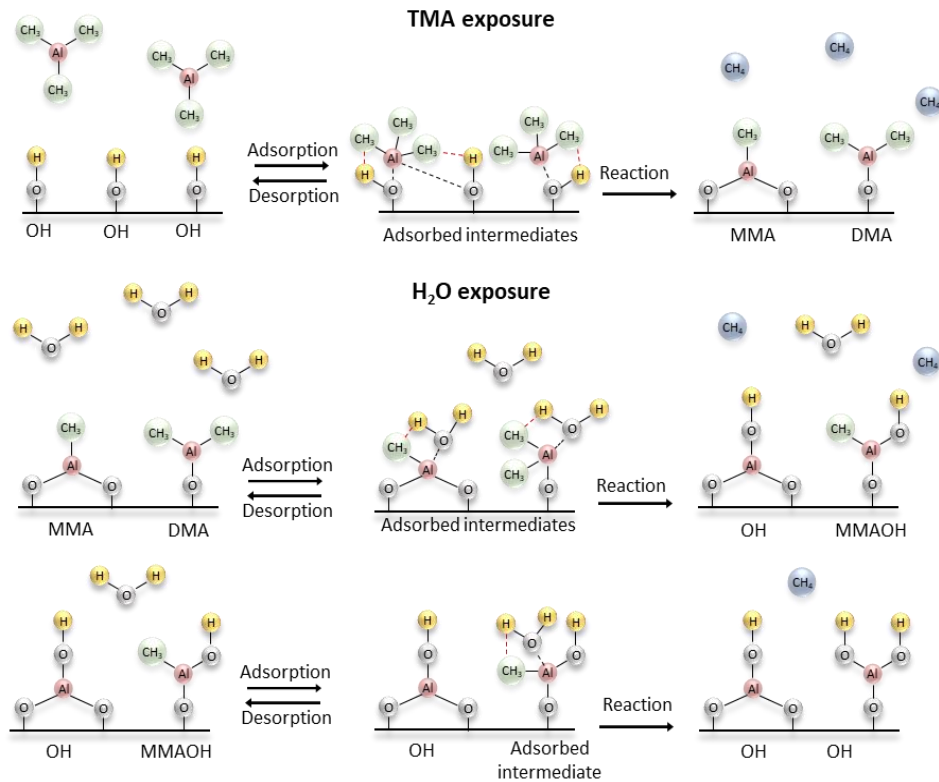
Σχήμα Π1. Σχήμα χημείας που χρησιμοποιήθηκε για την ανάλυση των επιφανειακών μηχανισμών

Το σχήμα χημείας εφαρμόζεται στο μοντέλο επιφανειακής χημείας, χρησιμοποιώντας τις ενέργειες ενεργοποίησης για κάθε μηχανισμό, όπως αυτές παρουσιάζονται στη βιβλιογραφία (Widjaja and Musgrave, 2002).

Τα αποτελέσματα του συζευγμένου μοντέλου CFD και επιφανειακής χημείας στην κλίμακα του υποστρώματος παρουσιάζονται στο Σχήμα Π2. Η υπολογισμένη απόθεση ανά κύκλο ALD (GPC) συναρτήσει της θερμοκρασίας, και η σύγκριση με τις πειραματικές μετρήσεις για δύο διάρκειες παλμών TMA παρουσιάζονται στο Σχήμα Π2α. Η ανάλυση των μηχανισμών παρουσιάζεται στο Σχήμα Π2β, μέσω των υπολογισμένων πιθανοτήτων αντίδρασης των δύο αντιδρώντων, πάνω στα επιφανειακά χημικά στοιχεία.
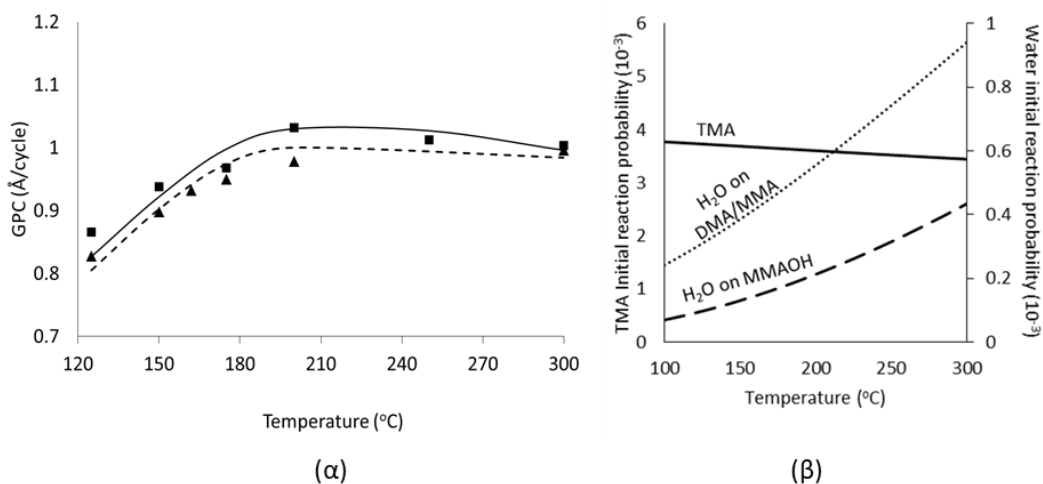
Σχήμα Π2. α) Απόθεση ανά κύκλο ALD συναρτήσει της θερμοκρασίας: 25 ms παλμού ΤΜΑ: πειραματικές μετρήσεις (τρίγωνα) και υπολογισμοί (διακεκομμένη γραμμή). 60 ms παλμού ΤΜΑ: πειραματικές μετρήσεις (τετράγωνα) και υπολογισμοί (συνεχής γραμμή). β) Πιθανότητες αντίδρασης των αντιδρώντων.

Το σχήμα Π2 δείχνει ότι για χαμηλές θερμοκρασίες, η απόθεση είναι περιορισμένη. Αυτό συμβαίνει λόγω του ανταγωνισμού μεταξύ της εκρόφησης και της αντίδρασης των ροφημένων στην επιφάνεια μορίων H_2O. Η εκρόφηση είναι ενισχυμένη σε σχέση με την αντίδραση στις χαμηλές θερμοκρασίες, λόγω της μεγαλύτερης ενέργειας ενεργοποίησης των αντιδράσεων. Αυτό οδηγεί στην χαμηλή πιθανότητα αντιδράσεων (Σχήμα Π2β). Όταν η θερμοκρασία αυξάνεται, ενεργοποιούνται οι αντιδράσεις, οδηγώντας σε μεγαλύτερη πιθανότητα αντίδρασης (Σχήμα Π2β) και μεγαλύτερη απόθεση (Σχήμα Π2α). Για θερμοκρασίες άνω των 200°C, η απόθεση περιορίζεται από την μέγιστη συγκέντρωση των υδροξυλίων (ΟΗ) στην επιφάνεια, η οποία μειώνεται με την αύξηση της θερμοκρασίας. Για το ΤΜΑ, παρατηρείται η αντίστροφη συμπεριφορά. Η πιθανότητα αντίδρασης ου ΤΜΑ είναι υψηλότερη στις χαμηλότερες θερμοκρασίες. Όταν η θερμοκρασία αυξάνεται,

ενεργοποιείται η εκρόφηση του ΤΜΑ από την επιφάνεια, και η πιθανότητα αντίδρασής του ελαττώνεται.

Ο παραπάνω ανταγωνισμός των επιφανειακών φαινομένων φαίνεται στο Σχήμα Π3, όπου παρουσιάζονται τα αποτελέσματα του στοχαστικού μοντέλου kMC. Οι προβλέψεις αφορούν τον αριθμό των γεγονότων που λαμβάνουν χώρα στη διάρκεια ενός κύκλου ALD πάνω σε 10,000 επιφανειακά στοιχεία.

Η λεπτομερής αυτή ανάλυση των επιφανειακών μηχανισμών και του ανταγωνισμού τους δείχνει οτι σε χαμηλές θερμοκρασίες η μεγάλη πλειονότητα των ροφημένων μορίων H_2O εκροφάται προτού αντιδράσει (Σχήμα Π3α). Η αντίθετη συμπεριφορά παρατηρείται για το ΤΜΑ, το οποίο αντιδρά προτού εκροφηθεί με μεγαλύτερη πιθανότητα (Σχήμα Π3β). Αυξάνοντας τη θερμοκρασία, οι αντιδράσεις των μορίων H_2O ενεργοποιούνται (Σχήμα Π3γ), και μικρότερος αριθμός ροφήσεων χρειάζεται ώστε να αντιδράσουν και να κορεστεί η επιφάνεια. Για το ΤΜΑ, η αύξηση της θερμοκρασίας ενεργοποιεί την εκρόφηση (Σχήματα Π3β, Π3δ), και ο απαιτούμενος αριθμός ροφήσεων ώστε να κορεστεί η επιφάνεια αυξάνεται.
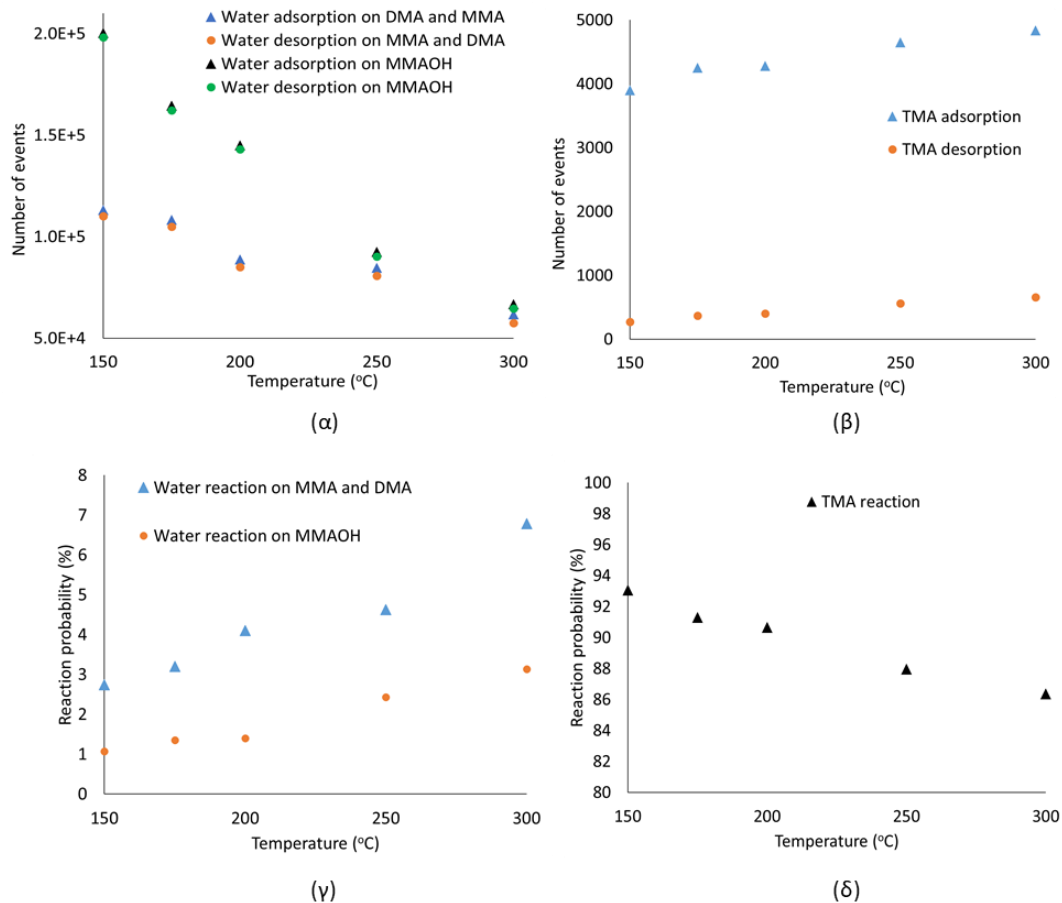
Σχήμα Π3. Προβλέψεις του μοντέλου kMC για τα επιφανειακά γεγονότα α) Ρόφηση και εκρόφηση H_2O, β) Ρόφηση και εκρόφηση TMA, γ) Αντιδράσεις H_2O, δ) Αντιδράσεις TMA

Το συζευγμένο πρότυπο του μοντέλου CFD και επιφανειακής χημείας χρησιμοποιείται επίσης για να μελετηθεί η επίδραση των φαινομένων μεταφοράς μέσα στον κύριο όγκο του αντιδραστήρα στην ομοιομορφία της απόθεσης και συνεπώς στην ομοιομορφία του υμενίου. Στο Σχήμα Π4 παρουσιάζονται στιγμιότυπα των λύσεων του πεδίου ροής σε μορφή των διανυσμάτων ταχύτητας, κατά τη διάρκεια ενός παλμού TMA διάρκειας 25 ms.
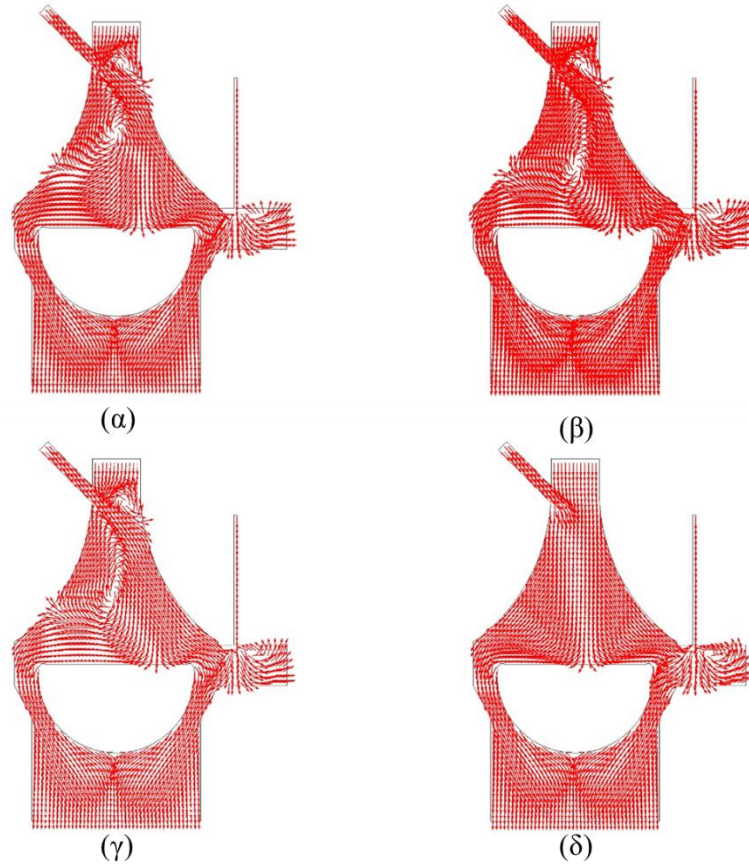
Σχήμα Π4. Προβλέψεις του μοντέλου CFD για το πεδίο ροής στον αντιδραστήρα α) 10 ms, β) 20 ms, γ) 30 ms, δ) 60 ms μετά το ξεκίνημα του παλμού ΤΜΑ.

Τα αποτελέσματα του Σχήματος Π4 δείχνουν ότι το πεδίο ροής δεν είναι ομοιόμορφο κατά τη διάρκεια του παλμού ΤΜΑ. Κατά τα πρώτα ms του παλμού (Σχήματα Π4α-γ), σχηματίζεται μια ανακυκλοφορία στην περιοχή πάνω από την επιφάνεια του υποστρώματος. Αυτό συμβαίνει λόγω της συναγωγής που προκύπτει από τη ροή στην είσοδο. Μετά το τέλος του παλμού (Σχήμα Π4δ), το πεδίο ροής επανέρχεται στην αρχική του κατάσταση, όπου επικρατεί εμβολική ροή.

Αυτή η μη ιδανική συμπεριφορά του πεδίου ροής και ο σχηματισμός της ανακυκλοφορίας οδηγούν σε μη ομοιόμορφη κατανομή του αντιδρώντος ΤΜΑ στον αντιδραστήρα και συνεπώς στην επιφάνεια του υποστρώματος. Αυτό μπορεί να

οδηγήσει σε ανομοιόμορφη απόθεση, εάν η έκθεση του υποστρώματος στο ΤΜΑ δεν είναι αρκετή ώστε οι αντιδράσεις στην επιφάνεια να κορεστούν.

Η επίδραση της ανακυκλοφορίας και της διάρκειας του παλμού ΤΜΑ στην ομοιομορφία του αποτιθέμενου υμενίου στους 300 °C παρουσιάζονται στο Σχήμα Π5, μέσω των προβλέψεων του προτύπου των συζευγμένων μοντέλων CFD και επιφανειακής χημείας (Σχήματα Π5α, Π5γ), αλλά και της σύγκρισής τους με πειραματικές μετρήσεις για το προφίλ της απόθεσης πάνω στην επιφάνεια του υποστρώματος (Σχήματα Π5β, Π5δ).

Όπως φαίνεται στα Σχήματα Π5α και Π5β, η ανακυκλοφορία που αναπτύσσεται κατά τον παλμό ΤΜΑ (Σχήμα Π4α-γ) επηρεάζει την ομοιομορφία της απόθεσης. Το προφίλ της απόθεσης ακολουθεί το πεδίο ροής πάνω στην επιφάνεια του υποστρώματος, δείχνοντας ότι η ανομοιόμορφη κατανομή των συστατικών που προκύπτει από την ανακυκλοφορία όντως επηρρεάζει την ομοιομορφία. Η μέγιστη ανομοιομορφία είναι της τάξης του 2.40%. Όταν η διάρκεια του παλμού ΤΜΑ αυξάνεται στα 60 ms, η ανομοιομορφία ελαττώνεται στο 0.58%, και η κατανομή της απόθεσης παύει να επηρρεάζεται από την ανακυκλοφορία. Αυτό συμβαίνει καθώς η έκθεση του υποστρώματος σε ΤΜΑ είναι πλέον αρκετή ώστε να κορεστούν οι αντιδράσεις σε όλη την επιφάνεια του υποστρώματος. Αυτά τα χαρακτηριστικά δείχνουν ότι τα φαινόμενα μεταφοράς που αναπτύσσονται μέσα στον κύριο όγκο του αντιδραστήρα έχουν σοβαρή επίδραση στην απόθεση του υμενίου. **Αυτό αναιρεί την κυρίαρχη αντίληψη της ALD ως διεργασία η οποία εξαρτάται μόνο από την επιφανειακή χημεία.**
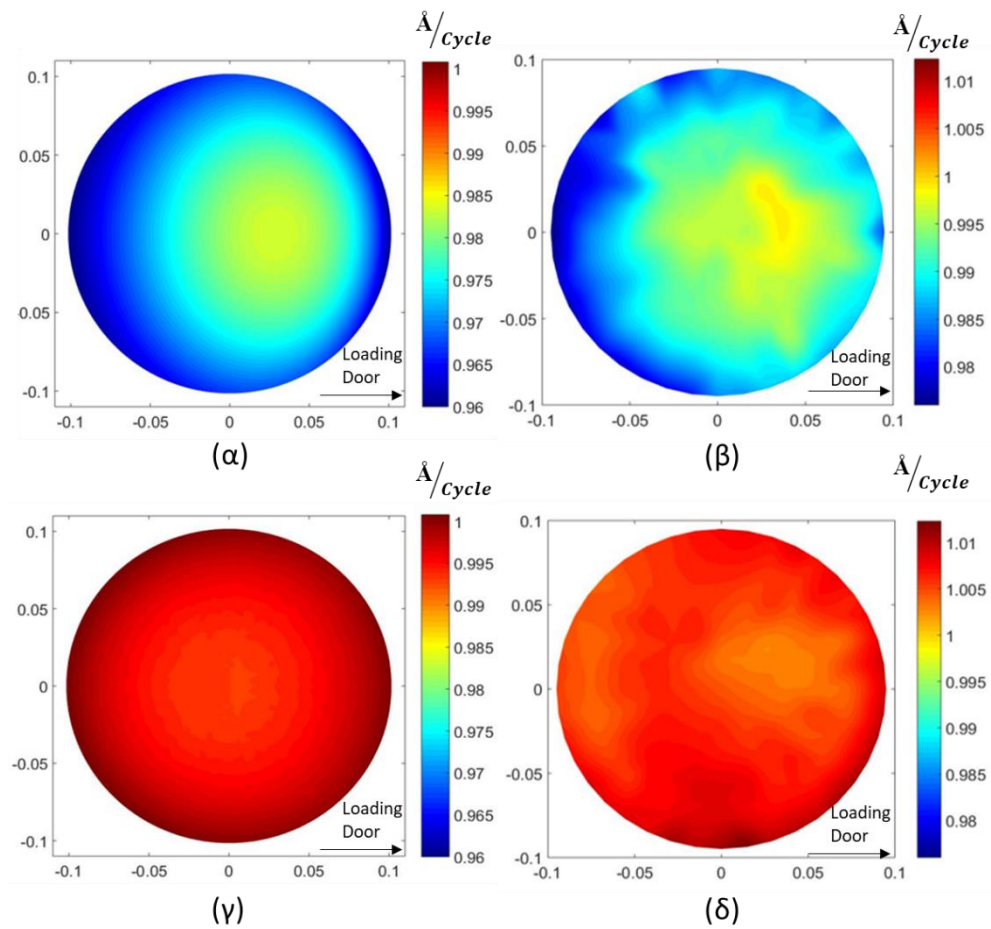
Σχήμα Π5. Προφίλ απόθεσης στην επιφάνεια του υποστρώματος: α) Προβλέψεις μοντέλου, 25 ms παλμού ΤΜΑ β) Πειραματικές μετρήσεις, 25 ms παλμού ΤΜΑ, γ) Προβλέψεις μοντέλου, 60 ms παλμού ΤΜΑ, δ) Πειραματικές μετρήσεις, 60 ms παλμού ΤΜΑ

Οι μηχανισμοί στην επιφάνεια που διέπουν την απόθεση του υμενίου κατά την ιδεατή, γραμμική κατάσταση της ALD όπου το GPC είναι σταθερό, δεν είναι οι ίδιοι

με αυτούς που λαμβάνουν χώρα κατά τους αρχικούς κύκλους. Για τη μελέτη της απόθεσης κατά τους πρώτους κύκλους ALD, χρησιμοποιήθηκε υπολογιστική διερεύνηση με το μοντέλο ανάπτυξης υμενίου σε νησίδες, σε συνδυασμό με πειραματικές μετρήσεις XRR. Μέσα από την διερεύνηση αυτή, είναι δυνατό να ταυτοποιηθούν οι μηχανισμοί που λαμβάνουν χώρα στα αρχικά στάδια της απόθεσης, καθώς και πληροφορίες σχετικά με την αρχική κατάσταση της επιφάνειας.

Το μοντέλο βασίζεται σε γεωμετρικές αρχές και προϋποθέτει την ανάπτυξη του υμενίου σε ημισφαιρικές νησίδες (Nilsen *et al.,* 2007). Η αρχική επιφάνεια, η οποία δεν αντιδρά με τα αντιδρώντα, αποτελείται από επιφανειακά Si-H στοιχεία λόγω του καθαρισμού του υποστρώματος (Si) με HF. Η πυρήνωση και απόθεση ξεκινούν πάνω σε παρασιτικά στοιχεία της επιφάνειας, όπως τα OH, που δεν έχουν απομακρυνθεί ολικά από τον καθαρισμό HF (Puurunen *et al*., 2004). Κατά τους επόμενους κύκλους, η απόθεση γίνεται πάνω και γύρω από το ήδη αποτεθειμένο υλικό, οδηγώντας σε σχηματισμό και ανάπτυξη νησίδων (Puurunen *et al*., 2004) (Puurunen and Vandervorst, 2004).

Τα αποτελέσματα του μοντέλου ανάπτυξης σε νησίδες και της πειραματικής διερεύνησης μέσω μετρήσεων XRR παρουσιάζονται στο Σχήμα Π6, για απόθεση στους 300 °C. Το μοντέλο ανάπτυξης σε νησίδες έχει δύο παραμέτρους. Την απόθεση ανά κύκλο στη γραμμική κατάσταση ALD, η οποία τροφοδοτείται από το πρότυπο συζευγμένων μοντέλων CFD και επιφανειακής χημείας, και την αρχική συγκέντρωση των παρασιτικών στοιχείων πυρήνωσης στην επιφάνεια, τα οποία λαμβάνονται ως ομοιόμορφα κατανεμημένα στην επιφάνεια. Η αρχική ακτίνα των νησίδων είναι μηδενική.
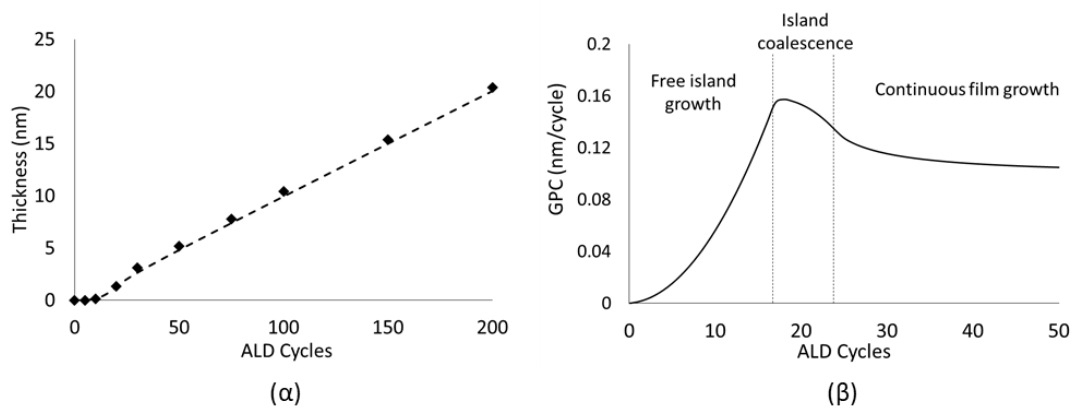
Σχήμα Π6. α) Εξέλιξη του αποτιθέμενου πάχους του υμενίου: πειραματικές μετρήσεις XRR (ρόμβοι) και προβλέψεις μοντέλου ανάπτυξης σε νησίδες (διακεκομμένη γραμμή), β) Εξέλιξη του αποτιθέμενου πάχους ανα κύκλο ALD: προβλέψεις μοντέλου ανάπτυξης σε νησίδες

Η συμφωνία μεταξύ προβλέψεων του μοντέλου και πειραματικών μετρήσεων όπως παρουσιάζεται στο Σχήμα Π6α, δείχνει ότι η ανάπτυξη σε νησίδες εξηγεί την πολύπλοκη συμπεριφορά της εξέλιξης του αποτιθέμενου πάχους του υμενίου. Μέσω της ανάλυσης αυτής, μπορεί να εξαχθεί η τιμή της αρχικής συγκέντρωσης ομάδων πυρήνωσης στην επιφάνεια, που προσδιορίζεται στις 0.08 ομάδες/nm². Η εξέλιξη της ανάπτυξης του υμενίου περνά από τρία στάδια, τα οποία αποτυπώνονται στην εξέλιξη του αποτιθέμενου πάχους ανα κύκλο ALD (GPC), στο Σχήμα Π6β.

Στο πρώτο στάδιο, οι ημισφαιρικές νησίδες αναπτύσσονται, αυξάνοντας την διαθέσιμη προς απόθεση επιφάνεια. Αυτό οδηγεί στην αύξηση του GPC, φτάνοντας μια μέγιστη τιμή, μεγαλύτερη της τιμής του GPC της διεργασίας που προκύπτει στη γραμμική κατάσταση ALD (~0.1 nm/κύκλο, Σχήμα Π2α). Η μέγιστη τιμή λαμβάνεται στο σημείο όπου οι νησίδες εφάπτονται για πρώτη φορά η μία με την άλλη, το οποίο στην συγκεκριμένη περίπτωση συμβαίνει μετά από 18 κύκλους ALD.

Περαιτέρω ανάπτυξη των νησίδων οδηγεί σε συγχώνευση των νησίδων, ελαττώνοντας τη διαθέσιμη προς απόθεση επιφάνεια, και συνεπώς το GPC. Αυτή η συμπεριφορά οριοθετεί το δεύτερο στάδιο της εξέλιξης της ανάπτυξης του υμενίου.

Το στάδιο αυτό περαιώνεται τη στιγμή που οι νησίδες καλύπτουν όλη την επιφάνεια του υποστρώματος, και το υμένιο γίνεται συνεχές. Στη συγκεκριμένη περίπτωση αυτό συμβαίνει μετά από 25 κύκλους ALD. Περαιτέρω ανάπτυξη του υμενίου οδηγεί σε περαιτέρω συνένωση και ελάττωση της διαθέσιμης επιφάνειας, μέχρις ότου η επιφάνεια γίνει λεία και το GPC τείνει στην σταθερή του τιμή, όπου προκύπτει η γραμμική κατάσταση ALD. Η παραπάνω ανάλυση δείχνει ότι χρειάζονται περίπου 25 κύκλοι ALD ώστε να αποτεθεί ένα συνεχές υμένιο, πράγμα που περιορίζει το ελάχιστο πάχος του υμενίου, και συνεπώς τις δυνατές εφαρμογές του σε λεπτότατες νανομετρικές κλίμακες.

Εκτός από τη μη γραμμική και ιδανική ανάπτυξη του υμενίου κατά τους πρώτους κύκλους, διεπιφανειακά φαινόμενα οδηγούν στη δημιουργία ενός διεπιφανειακού στρώματος μη ιδανικής σύστασης. Αυτό το διεπιφανειακό στρώμα αναπτύσσεται μαζί με το υμένιο, όπως φαίνεται από τις αναλύσεις ΤΕΜ και STEM στο Σχήμα Π7, και αποτελείται από SiO_x, AlO_x, και Si_xO_yAl.
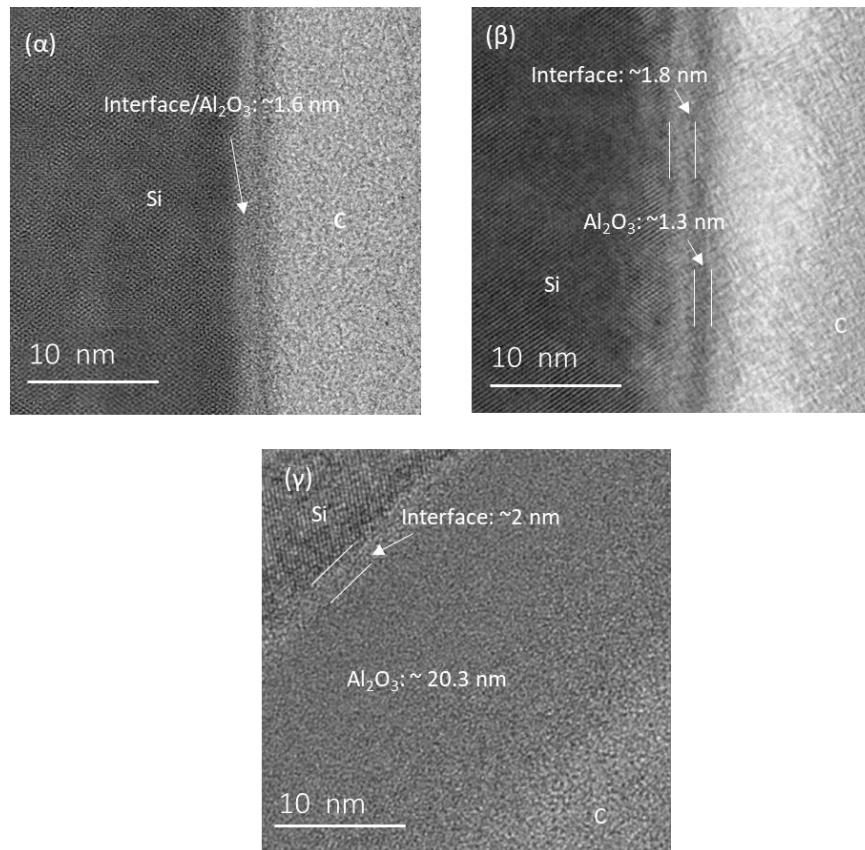
Σχήμα Π7. Αναλύσεις TEM και STEM για υμένια Al_2O_3 πάνω σε Si για α) 5 κύκλους ALD, β) 20 κύκλους ALD, γ) 200 κύκλους ALD

Όπως δείχνει η μικρογραφία Π7, μετά από 5 κύκλους, δεν μπορεί να διαχωριστεί το διεπιφανειακό στρώμα από το υμένιο Al_2O_3. Αυτό συμβαίνει καθώς το υμένιο βρίσκεται ακόμα σε μορφή νησίδων, όπως έδειξε και η ανάλυση του Σχήματος Π6. Αυξάνοντας τους κύκλους ALD, το πάχος του υμενίου αυξάνεται. Ταυτόχρονα αυξάνεται και το πάχος του διεπιφανειακού στρώματος, καθώς αυξάνεται και η διεπιφανειακή οξείδωση του Si. Όταν το υμένιο Al_2O_3 γίνει συνεχές (μετά από 25 κύκλους, σύμφωνα με την ανάλυση του Σχήματος Π6), η περαιτέρω ανάπτυξη του πάχους του καθιστά το υμένιο Al_2O_3 ως προστατευτική επίστρωση ενάντια στη διάχυση O προς την επιφάνεια του υποστρώματος, και συνεπώς προς την οξείδωση και δημιουργία SiO_x. Αυτό φαίνεται από τα Σχήματα Π7β και Π7γ, όπου δεν παρατηρείται περαιτέρω αύξηση του πάχους του διεπιφανειακού στρώματος.

Η ανάλυση της σύστασης του διεπιφανειακού στρώματος γίνεται μέσω αναλύσεων EDX, όπως φαίνεται στο Σχήμα Π8. Μια πολύ μικρή άνοδος στις μετρήσεις Ο ανιχνεύεται στην επιφάνεια Si, για το δείγμα υποστρώματος χωρίς απόθεση (Σχήμα Π8α). Αυτό δείχνει ότι ο καθαρισμός HF του υποστρώματος αφαιρεί την πλειονότητα των επιφανειακών οξειδίων, αφήνοντας την επιφάνεια τερματισμένη με Si-H. Η επιφάνεια Si-H συνεπώς παθητικοποιείται προς οξείδωση. Η μικρή ποσότητα του ανιχνευμένου Ο στην επιφάνεια επομένως αντιστοιχεί σε παρασιτικά στοιχεία, όπως ομάδες Si-OH που δεν έχουν απομακρυνθεί κατάλληλα ή σε SiO_x που σχηματίζεται μετά την έκθεση του δείγματος στον αέρα. Η πυρήνωση ALD κατά τη διάρκεια των πρώτων κύκλων ALD, λαμβάνει χώρα σε τέτοιες ομάδες. Το μοντέλο ανάπτυξης του νησιού, προσαρμοσμένο στις μετρήσεις XRR, υπολογίζει την επιφανειακή συγκέντρωση αυτών των ομάδων, σε 0.08 ομάδες/nm^2 (Σχήμα Π6). Το υμένιο ALD αρχίζει να σχηματίζεται σε αυτά τα ελαττώματα.

Αυτό το αποτέλεσμα παρατηρείται στα προφίλ Al, O, Si σε δείγμα Al_2O_3 5 κυκλων ALD στο Σχήμα Π8β. Σε αυτή την περίπτωση, μεταξύ του υποστρώματος Si και του στρώματος C, παρατηρείται μια καθαρή κορυφή στις μετρήσεις Ο μαζί με μια μικρή κορυφή του Al. Ωστόσο, ακόμη και στο δείγμα 5 κύκλων (Σχήμα Π8β), η κορυφή Ο είναι πιο σημαντική από ότι στο δείγμα υποστρώματος (Σχήμα Π8α). Αυτό αποδίδεται στην οξείδωση του υποστρώματος Si, κάτω από το αποτιθέμενο Al_2O_3. Αυτό το αποτέλεσμα δείχνει ότι η απόθεση Al ενισχύει την οξείδωση του Si ακόμη και σε χαμηλή συγκέντρωση επιφανείας Al. Μέσω των μετρήσεων EDX, εξάγεται το πάχος της διεπιφανειακής περιοχής 1.93 nm, όπου 1.6 nm αντιστοιχούν σε SiO_x, ενώ 0.3 nm αντιστοιχούν σε περιοχή συνύπαρξης Al, O, και Si.
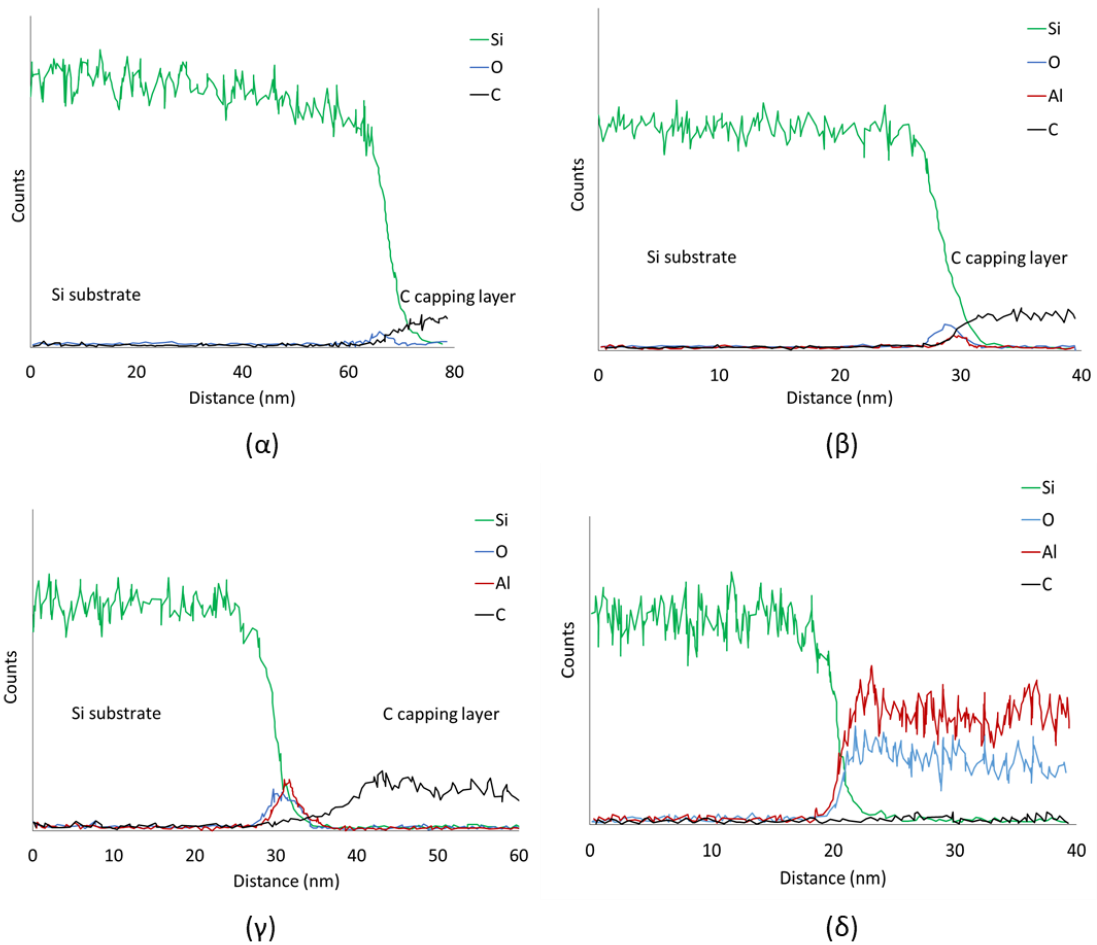
Σχήμα Π8. Μετρήσεις EDX για τα στοιχεία Al, Si, O και C για δείγματα: α)
Υπόστρωμα καθαρισμένο με HF, β) 5 κύκλοι ALD, γ) 20 κύκλοι ALD, δ) 200 κύκλοι
ALD

Το Σχήμα Π8γ δείχνει ένα δείγμα Al_2O_3 που αποτέθηκε με 20 κύκλους ALD.
Οι διαυγείς κορυφές AI και O στο προφίλ οφείλονται στην απόθεση Al_2O_3. Η ανάλυση
της ανάπτυξης σε νησίδες (Σχήμα Π6) δείχνει ότι μετά από 20 κύκλους, η απόθεση του
υμενίου βρίσκεται κοντά στο τέλος της ανάπτυξης σε νησίδες, ωστόσο το υμένιο δεν
είναι ακόμα συνεχές. Χρησιμοποιώντας τις μετρήσεις EDX, συνάγεται μια περιοχή ~
1.5 nm, όπου υπάρχουν μόνο είδη Si και O, συνεπώς ο σχηματισμός στρώματος SiO_x.

Μία περιοχή ~0.7 nm, όπου όλα τα είδη Si, O και Al είναι παρόντα, ανιχνεύεται πριν από το υμένιο Al_2O_3. Το συνολικό πάχος της διεπιφάνειας που περιέχει Si είναι 2.2 nm.

Ο προτεινόμενος μηχανισμός για το σχηματισμό του διεπιφανειακού SiO_x είναι η διάχυση των O στοιχείων μέσα από το αποτεθειμένο Al_2O_3, οδηγώντας σε οξείδωση του Si. Επίσης, η αντίδραση του H_2O με επιφανειακές ομάδες Si κατά την ανάπτυξη σε νησίδες, όπου η επιφάνεια δεν καλύπτεται πλήρως από το υμένιο ALD, καταλυόμενη από την παρουσία Al (Frank *et al.*, 2003)(Lim *et al.*, 2000), είναι επίσης ένας πιθανός μηχανισμός για την ανάπτυξη διεπιφανειακού οξειδίου. Οι OH ομάδες μπορούν να σχηματιστούν κατά την αρχική ανάπτυξη σε νησίδες, και οδηγούν στο σχηματισμό ειδών SiOH (Naumann et al., 2012). Αυτά τα είδη οδηγούν σε περαιτέρω οξείδωση υποστρώματος μετά από περαιτέρω αύξηση των κύκλων ALD. Για να επαληθευθεί αυτή η υπόθεση χρησιμοποιήθηκαν μετρήσεις SIMS κατά μήκος του πάχους ενός υμενίου Al_2O_3, αποτεθειμένο με 200 κύκλους ALD. Τα αποτελέσματα της ανάλυσης SIMS παρουσιάζονται στο Σχήμα Π9.

Η ανάλυση SIMS δείχνει ένα ομοιόμορφο προφίλ συγκέντρωσης για τα είδη Al και O στον πυρήνα του υμενίου, όπου δεν ανιχνεύεται Si. Αυτό επιβεβαιώνει ότι κατά τη διάρκεια της ALD, το υμένιο Al_2O_3 κατατίθεται με σταθερή σύσταση κατά τη διάρκεια κάθε κύκλου.

Όταν η ανάλυση φτάνει στη διεπιφάνεια, οι μετρήσεις AlO και O μειώνονται, μέχρις ότου η ανάλυση φτάσει το υπόστρωμα Si, όπου δεν ανιχνεύονται πλέον τα Al και O. Η συμπεριφορά των μετρήσεων Al είναι διαφορετική. Αρχικά μειώνονται όταν η ανάλυση φτάνει στη διεπιφάνεια, όπως στην περίπτωση των AlO και O. Στη συνέχεια όμως, ο αριθμός Al αυξάνεται παρουσιάζοντας μια μικρή κορυφή στη διεπιφάνεια, πριν μειωθεί στο μηδέν στην περιοχή υποστρώματος Si . Αυτό οδηγεί στη διάκριση δύο

περιοχών στη διασύνδεση: μια περιοχή χαμηλού Al στην κορυφή της διεπιφάνειας, κοντά στο υμένιο Al_2O_3 και μια περιοχή εμπλουτισμένη με Al στη διεπιφάνεια. Η διαφορετική συμπεριφορά των προφίλ βάθους Al και AlO εντός της διεπιφάνειας μαρτυρά ένα πιθανό διαφορετικό χημικό περιβάλλον Al εντός της διεπιφάνειας. Το Al θα μπορούσε να είναι παρόν στη διεπιφάνεια σε κατάσταση εκτός Al_2O_3, όπως τα Si-O-Al.
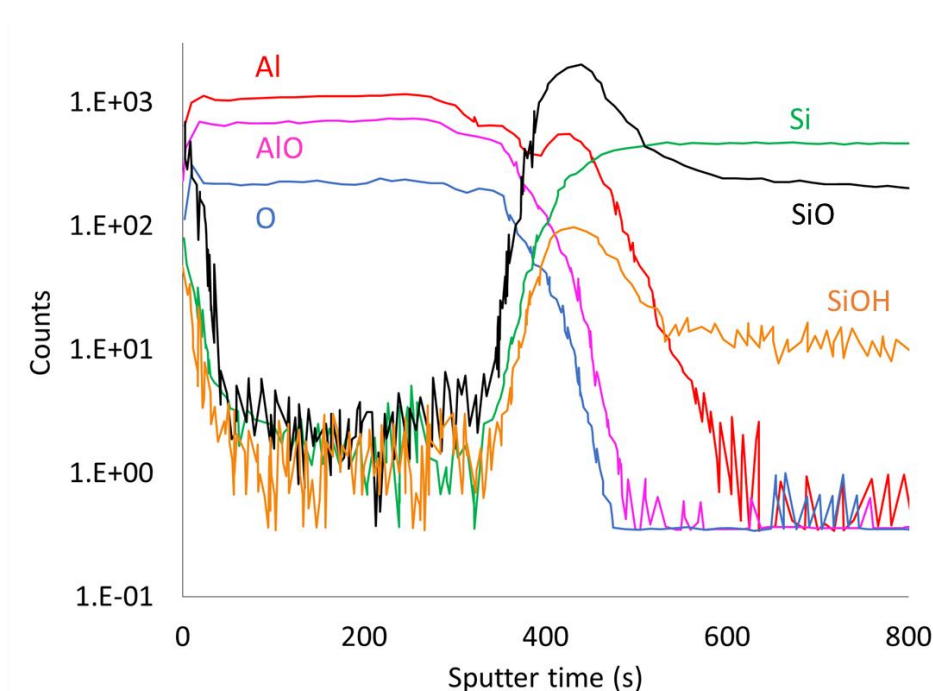
Σχήμα Π9. Μετρήσεις SIMS κατά μήκος του πάχους ενός υμενίου Al_2O_3, αποτεθειμένο χρησιμοποιώντας 200 κύκλους ALD.

Τα SiO και SiOH δείχνουν επίσης μια παρόμοια συμπεριφορά: στη διεπιφάνεια, τα SiO και SiOH αυξάνονται, παρουσιάζοντας μια κορυφή των συγκεντρώσεών τους, πριν μειωθούν καθώς η ανάλυση φτάνει το υπόστρωμα Si. Αυτές οι κορυφές εμφανίζονται στην ίδια θέση με την κορυφή Al, επιβεβαιώνοντας έτσι ότι εντός της διεπιφάνειας υπάρχει ένα διαφορετικό χημικό περιβάλλον Al. Αυτά τα αποτελέσματα

δείχνουν ότι όλα τα είδη Al, O, Si είναι παρόντα εντός της διεπιφάνειας του υμενίου, όπως αποδείχθηκε από τα αποτελέσματα EDX στο Σχήμα Π8.

Τα αποτελέσματα SIMS του Σχήματος Π9 αποκαλύπτουν την παρουσία των ομάδων SiOH στη διεπιφάνεια. Αυτή η παρουσία μπορεί να είναι η πηγή της οξείδωσης του υποστρώματος κατά τη διάρκεια του νησιωτικού καθεστώτος ανάπτυξης (*Naumann et al.*, 2012). Οι ομάδες SiOH σχηματίζονται κατά τη διάρκεια της ανάπτυξης σε νησίδες που λαμβάνει χώρα κατά τους πρώτους κύκλους απόθεσης. Ο μηχανισμός για τον σχηματισμό τους θα μπορούσε να είναι η αντίδραση του είδους Al-OH που δημιουργήθηκε από την χημική επιφάνεια του υμενίου ALD με τα Si της επιφάνειας του υποστρώματος, τα οποία δεν καλύπτονται πλήρως από είδη Al κατά την ανάπτυξη σε νησίδες.

Για να αντιμετωπιστούν τα δύο βασικά μειονεκτήματα της ALD Al_2O_3 πάνω σε Si, δηλαδή η περίοδος πυρήνωσης και ανάπτυξης του υμενίου σε νησίδες καθώς και η δημιουργία του διεπιφανειακού στρώματος λόγω διεπιφανειακής οξείδωσης του Si, εισάγεται η *in situ* έκθεση του καθαρισμένου με HF υποστρώματος Si σε πλάσμα N_2-NH_3 πριν την έναρξη της διαδικασίας ALD. Με αυτήν τη μέθοδο προεργασίας του υποστρώματος, αναπτύσσεται στην επιφάνεια μια λεπτή στρώση Si_xN_yH (PT layer), πάχους 1.8 nm. Η επίδραση της προεργασίας αυτής στην μετέπειτα απόθεση των υμενίων Al_2O_3 μέσω ALD παρουσιάζεται στο Σχήμα Π10, όπου παρουσιάζεται το μετρημένο με STEM αποτιθέμενο πάχος των υμενίων συναρτήσει των κύκλων ALD, για υποστρώματα με την προεργασία με πλάσμα N_2-NH_3 (Δείγματα PT) και χωρίς την προεργασία με N_2-NH_3 πλάσμα (Δείγματα NPT).
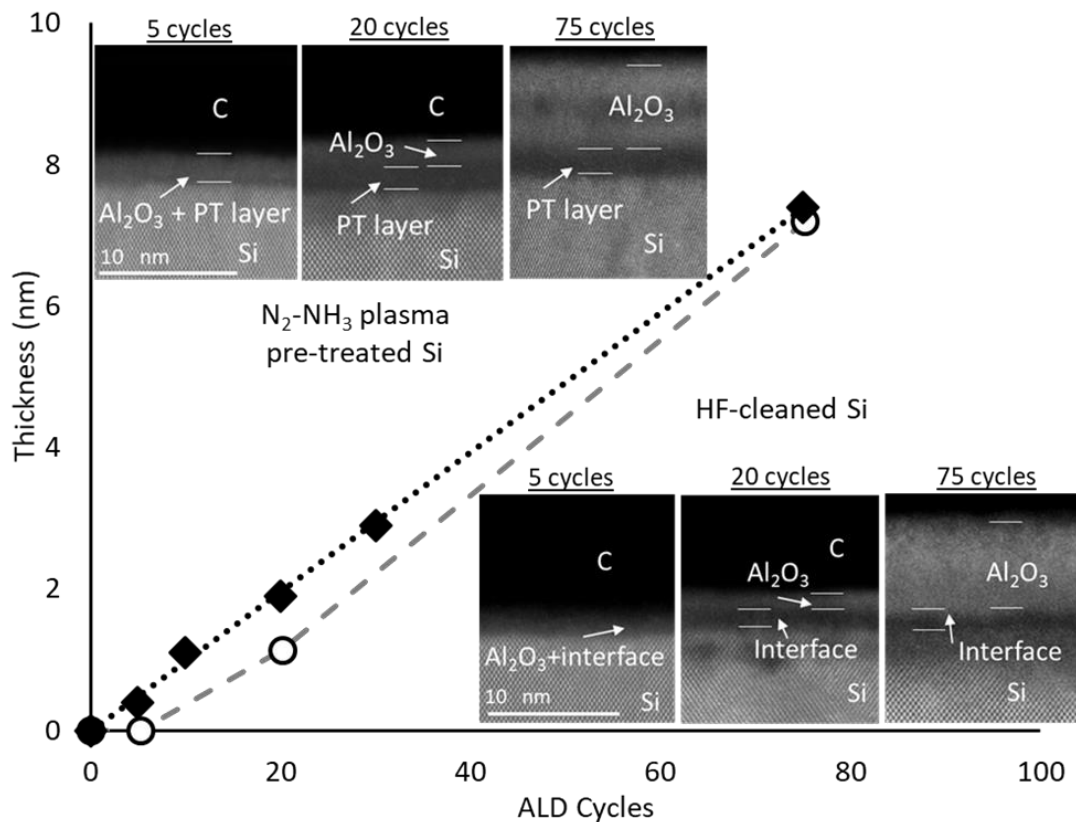
Σχήμα Π10. Μετρήσεις STEM για το αποτιθέμενο πάχος των υμενίων συναρτήσει των κύκλων ALD, για υποστρώματα με την προεργασία με N_2-NH_3 πλάσμα (ρόμβοι), και χωρίς την προεργασία (κύκλοι).

Το Σχήμα Π10 δείχνει ότι όταν η *in situ* προεπεξεργασία πλάσματος N_2-NH_3 πραγματοποιείται πριν από την απόθεση, οι εικόνες STEM δείχνουν ότι ακόμη και μετά από 5 κύκλους ALD, έχει αποτεθεί ένα στρώμα πάχους ~2.2 nm. Το πάχος του Al_2O_3 μπορεί να ληφθεί αφαιρώντας το στρώμα ~1.8 nm που αποτίθεται από την προεργασία, από το ολικό πάχος. Αυτό οδηγεί σε τιμή ~0.4 nm. Μετά από 20 και 75 κύκλους, το συνολικό πάχος Al_2O_3 που αποτέθηκε αυξάνεται σε ~1.9 nm και ~7.3 nm αντίστοιχα. Τα παραπάνω αποτελέσματα δείχνουν αυξημένη απόθεση κατά τους πρώτους κύκλους ALD, σε σύγκριση με τα δείγματα NPT.

Για τα υποστρώματα NPT, δεν υπάρχει παρατηρήσιμο υμένιο μετά από 5 κύκλους, ενώ η μέση GPC είναι μόνο ~0.07 nm / κύκλος μετά από 20 κύκλους και φτάνει ~0.1 nm / κύκλο μετά από 30 κύκλους, όπως φαίνεται από τις μετρήσεις XRR και τα αποτελέσματα του μοντέλου ανάπτυξης σε νησίδες (Σχήμα Π6). Στα υποστρώματα PT, η μέση GPC είναι ~0.1 nm /κύκλο μεταξύ 5 και 75 κύκλων, η οποία είναι η GPC κατά τη διάρκεια της γραμμικής κατάστασης ALD (Σχήματα Π2, Π6). Ως εκ τούτου, η περίοδος πυρήνωσης, που αναφέρθηκε ότι εμφανίστηκε κατά τους πρώτους κύκλους ALD (Σχήμα Π6) αντιμετωπίστηκε με επιτυχία από την προεπεξεργασία πλάσματος N_2-NH_3 του υποστρώματος Si. Αυτό συμβαίνει λόγω των ενισχυμένων αντιδράσεων των αντιδρώντων με τις επιφανειακές ομάδες $SiNH_2$ και $(Si)_2NH$ (Lin and Teplyakov, 2013), οι οποίες δημιουργούνται κατά την προεργασία πλάσματος N_2-NH_3 του υποστρώματος (Δείγματα PT), σε σχέση με τις ομάδες SiH (Δείγματα NPT).

Εκτός από την ενίσχυση της απόθεσης κατά τους πρώτους κύκλους ALD, η προεργασία πλάσματος N_2-NH_3 του υποστρώματος οδηγεί και στον περιορισμό της διεπιφανειακής οξείδωσης του Si υποστρώματος. Αυτό φαίνεται στο Σχήμα Π11, όπου παρουσιάζονται οι αναλύσεις EDX υμενίων Al_2O_3 αποτεθειμένων πάνω σε καθαρισμένο με HF Si (Δείγματα NPT, Σχήματα Π11α-γ) και πάνω σε προεργασμένο με πλάσμα N_2-NH_3 Si (Δείγματα PT, Σχήματα Π11δ-στ).
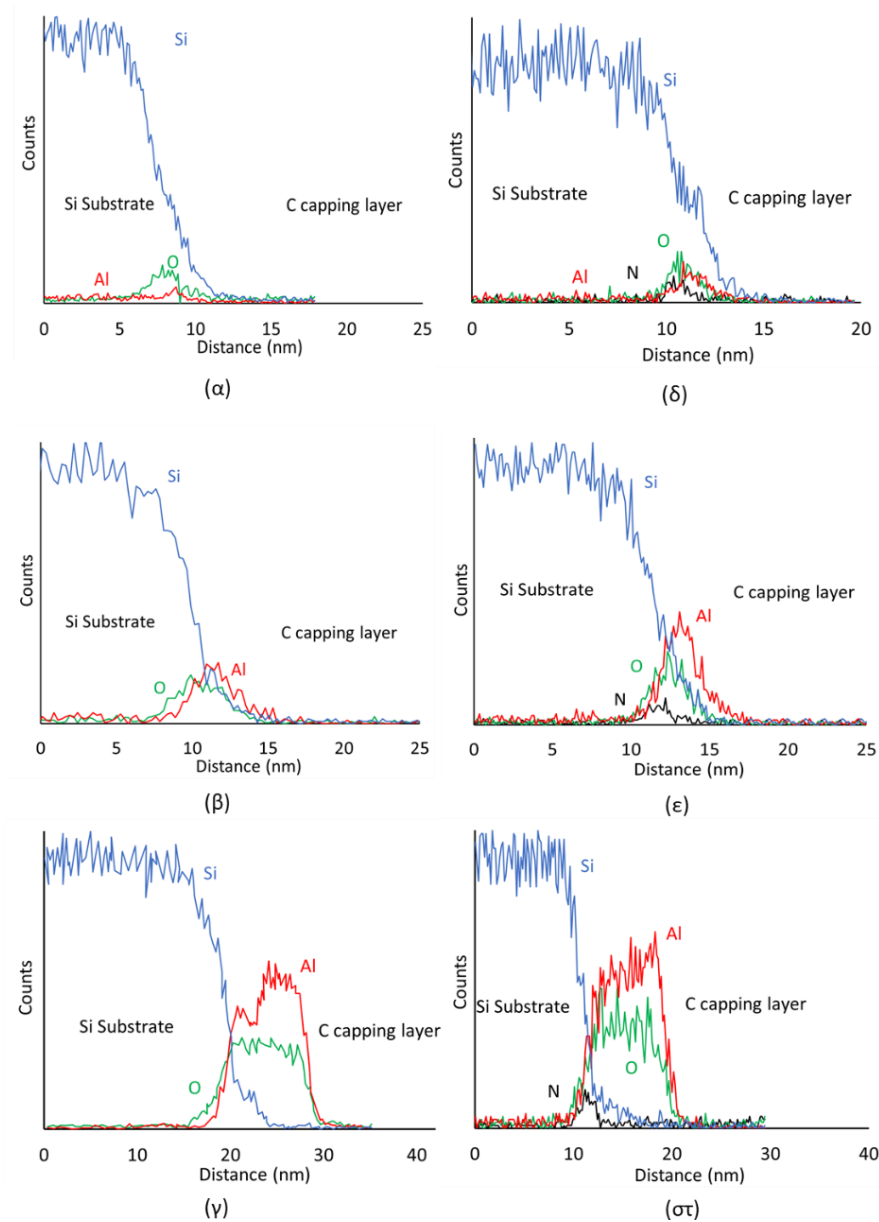
Σχήμα Π11. Αναλύσεις EDX υμενίων Al$_2$O$_3$. Αριστερή στήλη: Δείγματα NPT χρησιμοποιώντας α) 5, β) 20 και γ) 75 κύκλους ALD. Δεξιά στήλη: Δείγματα PT χρησιμοποιώντας δ) 5, ε) 20 και στ) 75 κύκλους ALD.

Μετά από 5 κύκλους ALD στην επιφάνεια του NPT Si (Σχήμα 6.Π11α), μόνο μια πολύ μικρή ποσότητα Al μπορεί να ανιχνευθεί στην επιφάνεια. Μετά από 20 κύκλους (Σχήμα 6.Π11β), εμφανίζεται σαφής αύξηση των μετρήσεων Al στο προφίλ

EDX, δείχνοντας ότι πράγματι αποτίθεται υμένιο στην επιφάνεια, επιβεβαιώνοντας τις προβλέψεις του μοντέλου ανάπτυξης σε νησίδες και τις προηγούμενες αναλύσεις. Το πάχος της οξειδωμένης στρώσης Si είναι ~2.2 nm για το δείγμα των 20 κύκλων όπως αναφέρθηκε και στο Σχήμα Π8. Για το δείγμα που αποτέθηκε χρησιμοποιώντας 75 κύκλους (Σχήμα 6.Π11γ), το οξειδωμένο στρώμα Si έχει πάχος ~2.4 nm (Σχήμα Π8).

Στα δείγματα PT, η σαφής απόθεση Al φαίνεται ήδη μετά από 5 κύκλους ALD (Σχήμα 6.Π11δ) μέσω μιας καθαρής κορυφής των μετρήσεων Al. Το Σχήμα 6.Π11δ δείχνει επίσης σημαντική μείωση της διεπιφανειακής οξείδωσης του υποστρώματος Si. Δεν ανιχνεύεται καμία περιοχή, όπου υπάρχουν μόνο είδη Si και O. Εμφανίζεται ένα στρώμα Si, O και N, με πάχος ~0.9 nm. Στη συνέχεια μετράται περιοχή ~0.8 nm όπου όλα τα στοιχεία Si, O, Al, N είναι παρόντα. Η διάχυση του Al και η απόθεση στο λιγότερο πυκνό στρώμα Si_xN_yH θα μπορούσαν να εξηγήσουν αυτό το αποτέλεσμα. Το συνολικό πάχος του στρώματος που περιέχει N είναι ~1.7 nm, που αντιστοιχεί στο πάχος του στρώματος Si_xN_yH. Αυτόδείχνει ότι ενώ η Si_xN_yH επίστρωση οξειδώνεται, το Si υπόστρωμα κάτω από αυτήν προστατεύεται. Το πάχος της στιβάδας Al_2O_3 είναι ~0.4 nm. Αυτές οι τιμές συμφωνούν με τις μετρήσεις STEM.

Μετά από 20 και 75 κύκλους, παρατηρούνται πιο έντονες κορυφές των μετρήσεων Al στα προφίλ EDX (Σχήματα Π11ε και Π10στ, αντίστοιχα). Η διεπιφανειακή οξείδωση του υποστρώματος Si μειώνεται σε σύγκριση με τα αντίστοιχα μη προεπεξεργασμένα δείγματα (Σχήματα Π11β και Π11γ). Για το δείγμα 20 κύκλων, το πάχος της περιοχής SiONH είναι ~1 nm. Μεταξύ του στρώματος Si-O-N-H και του υμενίου Al_2O_3, υπάρχει μια περιοχή Si, N, AI και O, με πάχος 0.8 nm, οδηγώντας σε μια περιοχή που περιέχει N ολικού πάχους ~1.8 nm. Το αντίστοιχο Si-O-N-H για το δείγμα των 75 κύκλων είναι πάχους ~0.5 nm, ενώ η περιοχή των Si, N, AI και O έχει πάχος ~1 nm, οδηγώντας σε μια περιοχή που περιέχει N συνολικού πάχους ~1.5 nm,

δείχνοντας και πάλι την προστατευτική ιδιότητα της επίστρωσης Si_xN_yH ενάντια στην περαιτέρω οξείδωση του υποστρώματος Si.

Στην περίπτωση των επιφανειών PT, τα αποτελέσματά μας δείχνουν ότι για όλα τα δείγματα, η οξείδωση του υποστρώματος μειώνεται σημαντικά. Αυτή η καταστολή της οξείδωσης του υποστρώματος έχει προηγουμένως αναφερθεί από τους Brewer et al. (Brewer *et al.*, 2004), καθώς επίσης από τους Xu et al. (Xu *et al.,* 2006). Για να καθοριστεί αν η διεπιφάνεια Si_xN_yH των δειγμάτων PT παρουσιάζει καλύτερες διεπιφανειακές ιδιότητες από τη διεπαφή SiO_x των δειγμάτων NPT, πρέπει να εκτελεστούν ηλεκτρικοί χαρακτηρισμοί, οι οποίοι εκφεύγουν των ορίων της παρούσας μελέτης. Πάντως, οι διεπιφάνειες αυτές έχουν δείξει βελτιωμένες ιδιότητες στη βιβλιογραφία (Xu *et al.,* 2006).

Αυτή η μελέτη δείχνει ότι δύο από τα κύρια μειονεκτήματα της ALD του Al_2O_3 από TMA και H_2O πάνω σε Si, δηλαδή η αρχική περίοδος πυρήνωσης, η ανάπτυξη του υμενίου σε νησίδες και η διεπιφανειακή οξείδωση που οδηγεί στην ανάπτυξη του διεπιφανειακού στρώματος SiO_x, μπορούν να κατασταλούν χρησιμοποιώντας μια κατάλληλη προεπεξεργασία επιφάνειας Si. Αυτά τα αποτελέσματα μπορούν να χρησιμεύσουν ως καθοδήγηση για την ανάπτυξη κατάλληλων τεχνικών προεπεξεργασίας επιφανειών για υποστρώματα Si, με στόχο την ενίσχυση της επιφανειακής τους αντιδραστικότητας έναντι των αντιδρώντων ALD και περιορισμό της διεπιφανειακής οξείδωσης του Si.

Αν και η ερευνητική εργασία που παρουσιάζεται σε αυτή τη διατριβή περιορίζεται σε ALD του Al_2O_3 από TMA και H_2O σε Si, αυτή η προσέγγιση μπορεί να χρησιμοποιηθεί για άλλα υλικά, ειδικά για την ALD των οξειδίων μετάλλων στο Si. Αυτό μπορεί να οδηγήσει σε ένα γενικό πλαίσιο για τη διεξοδική μελέτη της ALD

άλλων διηλεκτρικών οξειδίων, όπως τα HfO_2 και ZrO_2. Η έρευνα αυτή θα μπορούσε να ανοίξει το δρόμο για την ALD ώστε να καθιερωθεί ως η κατάλληλη τεχνική για την απόθεση συνεχών και ομοιόμορφων νανομετρικών υμενίων με διεπιφάνειες υψηλής καθαρότητας σύστασης, για τις εφαρμογές των μικροηλεκτρονικών συσκευών του μέλλοντος.

Résumé Français

La miniaturisation continue des dispositifs microélectroniques exige la production des couches nanométriques uniformes et conformes, avec une excellente pureté et des interfaces abruptes. Le procédé de dépôt par couche atomique (ALD) est performant pour produire de tels films. Profitant de la nature auto-limitante des réactions chimiques en jeu, l'ALD peut permettre un contrôle de l'épaisseur à la monocouche près, produisant des films de haute pureté.

Bien que l'ALD présente de nombreux avantages, des inconvénients apparaissent lors du dépôt de films de quelques nanomètres. En particulier, la croissance initiale en ilots et la formation d'une couche d'interface sont deux de ses limitations principales, en particulier pour le dépôt d'oxydes métalliques sur Si. De plus, le dépôt sur des grandes surfaces n'est pas toujours uniforme et dépend du réacteur et des conditions opératoires. Ces inconvénients doivent être supprimés pour déposer des films nanométriques d'oxydes sur Si, essentiels pour produire les transistors à effet de champ du futur.

Dans cette thèse, l'ALD d'Al_2O_3 à partir de TMA et H_2O sur Si est étudiée de façon approfondie, afin de remédier aux inconvénients pré-cités. L'étude consiste en une approche combinée, expérimentale et numérique multi-échelles. Quatre modèles numériques différents ont été développés pour traiter différentes échelles d'espace. Un ensemble complet de techniques de caractérisation a été utilisé, incluant ellipsométrie, XRR, TEM, STEM, EDX, XPS et SIMS. Dans ce cadre, les phénomènes en jeu sont analysés en détails, ce qui permet de mieux comprendre les mécanismes à l'origine de ces inconvénients.

La compétition entre la désorption et les réactions de surface s'est avérée être le facteur limitant pour le dépôt à basse température, jusqu'à 200°C. La concentration des sites réactifs en surface limite le dépôt à des températures supérieures, jusqu'à 300°C. Bien que l'ALD soit reconnue comme dépendant uniquement de la chimie de surface, l'analyse des phénomènes de transport à l'intérieur du réacteur a montré que la conception du réacteur et le choix des conditions opératoires peuvent affecter la distribution des réactifs et la température à l'intérieur du réacteur ALD. Le couplage entre les différents modèles numériques aux différentes échelles ont révélé que l'interaction entre les phénomènes de transport et les mécanismes de surface influençait l'uniformité du dépôt. Ces travaux ont permis de trouver des conditions optimales pour l'uniformité des films.

Au cours des premières étapes, le dépôt est inhibé, ce qui conduit à un régime de croissance en ilots. L'analyse expérimentale a montré que 25 cycles d'ALD sont nécessaires pour déposer un film continu d'Al_2O_3. De plus, l'oxydation du Si conduit à la formation d'une couche d'oxyde interfacial d'environ 2 nm, composée de SiO_x, AlO_x et Si_xO_yAl, qui altère les propriétés et donc les applications potentielles de la structure déposée.

Un prétraitement *in situ* par plasma N_2-NH_3 du substrat a été introduit, conduisant à la formation d'une couche de Si_xN_yH sur la surface du substrat. Le prétraitement a augmenté la réactivité de surface et réduit la période d'inhibition. Une croissance linéaire a été obtenue seulement après 5 cycles. En outre, l'oxydation interfaciale du Si a été réduite, car la couche de Si_xN_yH s'est avérée servir de barrière efficace contre la diffusion de l'O et l'oxydation du Si.

Le travail présenté dans cette thèse montre la nécessité de telles approches intégrées pour analyser les phénomènes impliqués dans l'ALD. De telles études permettent une compréhension approfondie des mécanismes, afin de proposer des solutions réduisant les inconvénients des premières étapes de dépôt. Elles contribuent à ouvrir la voie pour que le procédé ALD produise industriellement des couches minces nanométriques uniformes et conformes de grande pureté avec des interfaces abruptes, capables de répondre aux exigences de l'industrie électronique du futur.

Chapter 1: Atomic Layer Deposition: Principles, concept and challenges

The thesis is focused on the ALD of alumina from TMA and H_2O, for potential application as a gate oxide in a Metal-Oxide-Semiconductor Field Effect Transistors (MOSFET) structure. With the miniaturization of the microelectronic devices (Kingon *et al., 2000)* and hence of the MOSFETs, the required thickness of the gate oxide on the semiconductor (Si) is reduced down to some nanometers. Besides all the advantages that ALD presents, the deposition of metal oxide layers on Si with a thickness of some nanometers is problematic, since the initial deposition occurs under the form of discontinuous islands, while a non-abrupt and an interface with Si is formed with Si that damages the dielectric properties of the deposited structure (Schilirò et al., 2015, Först et al., 2004).

The TMA+H_2O process is considered as a "model system" for ALD (George, 2010), and is the most widely studied one (Puurunen, 2005). Although this system is considered as ideal once the ALD regime is attained, the surface mechanisms and their competition are not yet well understood. Furthermore, the deposition on large area wafers introduces difficulties for the deposition uniformity, related to reactor and process design parameters. The Si surface also affects the deposition during the first stages. The initial deposition is inhibited on Si (Puurunen *et al.*, 2004), while the interface formed between the Si substrate and Al_2O_3 damages the dielectric properties of the film.

This chapter consists in a bibliographic survey of the ALD process. The basic principles of ALD in general, its advantages and drawbacks, as well as the challenges

in the field of ALD are presented. The particular case of alumina ALD from TMA and water on silicon (Si) is presented, and the relevant literature is analyzed. Finally, the necessity of computational modelling of ALD processes is discussed. The relevant literature works and the challenges remaining to be answered are presented and analyzed.

1.1. The Atomic Layer Deposition process

1.1.1 Basic principles

ALD, introduced as Atomic Layer Epitaxy (Suntola and Antson, 1977) or Molecular Layering (Aleskovskii and Koltsov, 1965), is a sub-category of CVD techniques. Instead of exposing the surface to be covered to a permanent gas mixture of reactants, as in traditional CVD, ALD is based on the sequential use of self-terminating gas–solid reactions (Puurunen, 2005), which are called half-reactions of the process. The ALD process consists of repetitive sequences of half-reactions, called ALD cycles, which lead to the deposition of the desired film Most ALD processes are based on binary reaction sequences, where the two surface reactions are self-limiting (George, 2010).. A typical ALD cycle consists of the following characteristic four steps, and is schematically presented in Figure 1.1 (Puurunen *et al.* 2005):

1. A self-terminating reaction of the first reactant (Reactant A)

2. A purge or evacuation to remove the non-reacted reactants and the gaseous reaction by-products.

3. A self-terminating reaction of the second reactant (Reactant B)

4. A purge or evacuation to remove the non-reacted reactants and the gaseous reaction by-products.
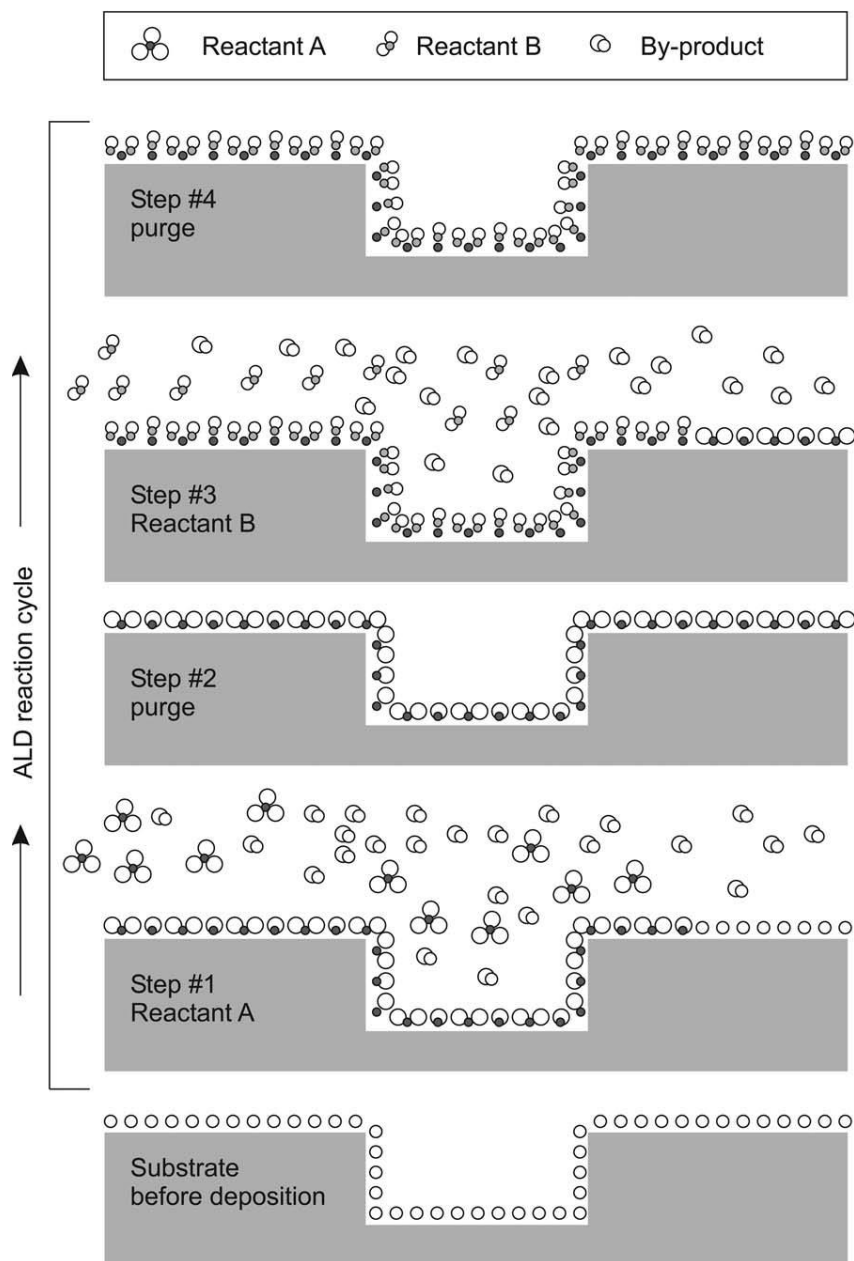
Figure 1.1. Schematic representation of an ideal ALD cycle (Puurunen, 2005)

The above four steps, when performed sequentially, constitute an ALD cycle. During the first and third step, the reactants are injected in the reactor chamber, and are

referred to as pulse or exposure steps, each corresponding to a half-reaction step. These exposure steps are often in the order of tens of miliseconds, for the ALD processes under high vacuum. However, exposure steps of some seconds can be used for high pressure ALD processes, or for deposition on large area wafers or trenched surfaces. Each cycle consists of two half reactions, leading to the formation of a monolayer of the deposited material. During a reactant exposure, the gas phase precursor must react with the surface species, through reactive sites on the substrate surface. The process continues until all reactive sites are covered. However, the reaction must not produce surface sites where chemisorption of the same gas phase reactant can occur. In this way, multi-layer deposition is averted

During the second and fourth step, the reactor chamber is purged with inert gas to remove gas-phase byproducts and unreacted precursors, and are called purging steps. These steps ensure a layer by layer deposition. The purging steps can last for tens of seconds, especially for low temperature processes, where the desorption of adsorbed reactants from the reactor walls is slower. If the second reactant is injected in the reactor while the first one is not completely purged, gas phase reactions may take place and lead to the deposition of more than a monolayer per ALD cycle. Hence, the self-terminating nature of the reactions is ensured by an effective purging step.

The advantages of ALD are derived from the self-saturating nature of the gas-surface reactions. The conformality of ALD-deposited films is often the critical factor in choosing ALD over competing deposition techniques such as CVD or sputtering (Johnson *et al.*, 2014). Although ALD has a lower throughput and is less cost effective than CVD, its monolayer thickness control, higher conformality and its ability to deposit pinhole-free quality films has made ALD the favorable technique for the production of nanometric films, especially for microelectronic applications.

Conformality of the deposition in high aspect ratio structured materials is made possible by the self-limiting characteristics of ALD, which restrict the reactions at the surface to no more than a monolayer. CVD may suffer from less perfect film thickness control, uniformity and conformality due to faster surface reactions, (Johnson *et al.*, 2014).

A second advantage of ALD is the thickness control of the deposited thin films. Each reaction cycle adds a given amount of material to the surface, referred as the growth per cycle (GPC). Ideally the GPC is the same for all cycles, hence leading to a linear relation between the deposited film thickness and the number of ALD cycles, as shown in Figure 1.2. Hence, to deposit a thin film, ALD cycles are repeated until the desired thickness is reached (Puurunen, 2005). The GPC for many ALD films has been summarized in previous reviews (George, 2010) (Puurunen, 2005) and is typically some Å/cycle, depending on the process.
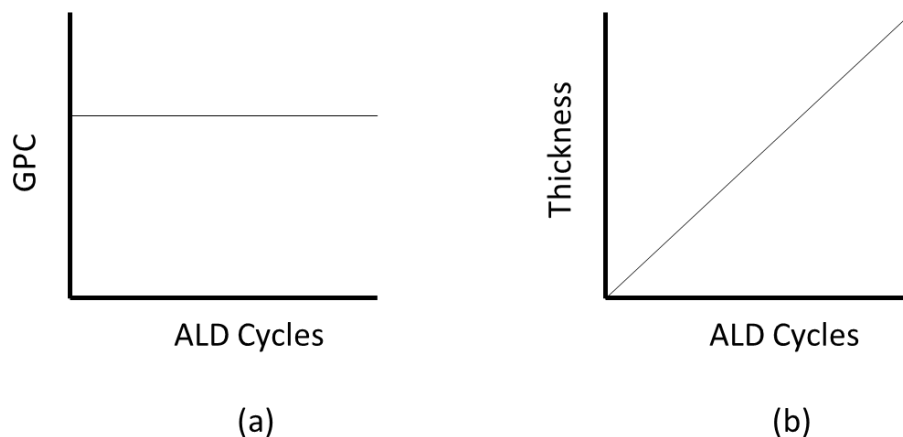
Figure 1.2. a) GPC and b) Thickness evolution as a function of ALD cycles for an ideal ALD process

General requirements of reactants used in ALD are that they must be volatile (either at room or elevated temperatures), and thermodynamically stable at the ALD processing temperatures. Furthermore, the gas–solid reactions of the reactants with the surface have to fulfill the criterion of self-termination and irreversibility (Puurunen,

2005). A wide number of materials have been deposited by ALD, using different reactant systems. A detailed overview on the classes of materials that have been deposited can be found on the reviews of S.M. George (George, 2010) and R.L. Puurunen (Puurunen, 2005).

Due to the advantages described above, ALD is able to produce high quality thin films with a unique thickness control and a high composition purity. Its ability to deposit conformal films on large area substrates (Fryauf *et al.,* 2018), powders and nanoparticles (Adhikari *et al.,* 2018), as well as on surfaces with high aspect ratio features (Ritala *et al.,* 1999) makes it an adequate technique to produce thin films for a wide variety of applications such as microelectronics, , nanophotonics (Ponraj *et al., 2013*), photovoltaics, fuel cells, batteries and OLEDs (Johnson *et al., 2014*)(Muñoz-Rojas *et al.,* 2019).

1.1.2 ALD process windows

Although ALD has considerable advantages drawn by the self-limiting nature of its reactions, the process conditions must be such as to allow this self-limiting aspect to take place. Hence, a certain range of operating conditions, referred to as operating "windows", must be defined in order to obtain the ideal ALD growth behavior.

1.1.2.1. ALD Temperature

The ALD temperature window, often referred to as the "ALD window", is considered to be the most important process window of ALD. The "ALD window" is the temperature range where the deposition rate is nearly unaffected by the temperature (George, 2010), and usually serves as an indicator for the activation of certain surface mechanisms. A representation of the ALD GPC behavior within the ALD window is

shown in Figure 1.3. At lower temperatures, the reactants could condense or the surface reactions may not be activated, thus leading to non-ideal deposition. At higher temperature, the reactant species could decompose and allow additional reactant adsorption, leading to multi-layer deposition during the ALD cycle, corresponding to CVD deposition. The surface species needed for ALD could also desorb from the surface at higher temperatures and be unavailable for additional surface reactions. Also, desorption of adsorbed species could be activated, prohibiting the full coverage of the surface.
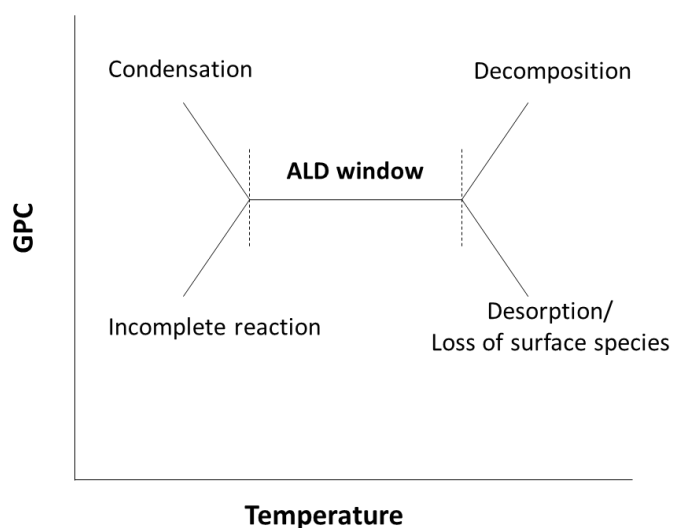
Figure 1.3. Schematic representation of the growth behavior within the ALD temperature window

A temperature window has been determined for the various ALD systems used for the deposition of different material films. The apparent GPC, which seems steady within the temperature range however, does not mean that the chemistry is unaffected by temperature. Different simultaneous and even competing mechanisms take place during ALD, which are progressively activated by the increase of temperature. For a

thorough and detailed understanding of the surface chemistry, all of these mechanisms owe to be studied. Due to the short time and space scales, this investigation is experimentally challenging, making theoretical and computational studies an indispensable tool in the research field of ALD.

1.1.2.2. Exposure time

The first step of the ALD surface mechanisms is the adsorption of the precursor molecule on the surface. Depending on the energy barrier needed, adsorption can be divided into physisorption (physical adsorption) and chemisorption (chemical adsorption). As physisorption is always reversible, whereas chemisorption can be either reversible or irreversible, the requirement of irreversibility restricts the type of adsorption to irreversible chemisorption, for ALD applications (Puurunen, 2005).

The surface saturation can be caused by two factors: steric hindrance of the ligands or the number of reactive surface sites (Puurunen, 2005). In any case, the reactant pulse duration must be long enough in order to achieve saturation of the surface. Shorter pulse times lead to smaller GPC, but also to non-fully covered layers, and the layer by layer deposition is not achieved. If the pulse times are longer than needed to achieve saturation, then the reactant consumption is uselessly increased. The three different behaviors of the GPC as a function of the exposure time are shown in Figure 1.4.
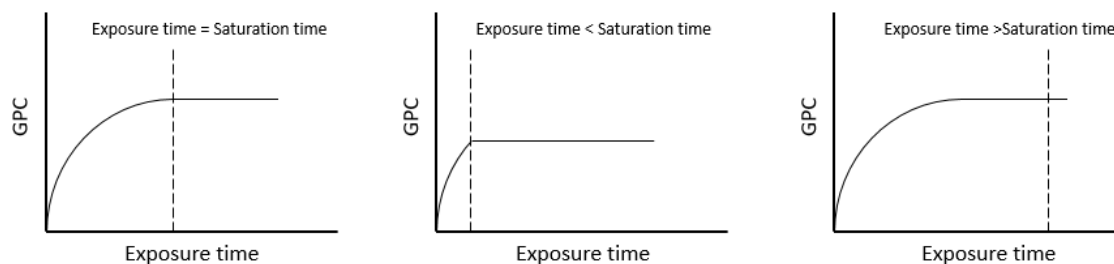
Figure 1.4 GPC as a function of reactant exposure time

The exposure times required for saturation in ALD are usually short, for the deposition on planar, low surface area substrates. The fast kinetics of the surface reactions lead to the duration reactant pulses in ALD being less than one second long (Elam *et al.*, 2002). However, for conformal deposition on high aspect ratio structures or on particles, the exposure times are longer, as the reactants need to diffuse and deposit on the surface features (Van Bui *et al.*, 2017).

1.1.2.3. Purge time

The purge time is a central parameter in ALD. It must ensure the removal of all the reactants of the previous exposure steps, as well as the byproducts of the surface reactions. If the purge step is not efficiently performed, the subsequent reactant exposure step would lead to the simultaneous presence of both reactants in the gas phase, leading to CVD reactions. The self-limiting, layer by layer nature of the film deposition is hence dependent on the efficiency of the purge step.

The purging step is performed by a flow of inert gas through the reactor. The duration of this step is critical for its efficiency. When the purge time is sufficient for the removal of all the residual gas phase species, further increase of the purging time does not affect the deposition. However, as the purge time is usually the slowest step of the ALD process, a longer purge than required increases the processing time, and

44

thus reduce the process throughput over time. The purging time effect on the GPC is shown schematically in Figure 1.5.
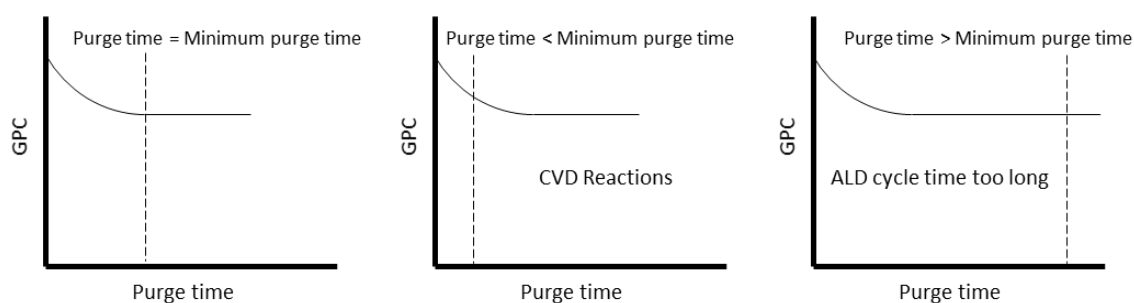
Figure 1.5. Effect of purging time on the GPC

1.2.2.4. Process pressure

Pressure is a factor usually undermined in ALD processes (Van Bui *et al.,* 2017). Nonetheless, the reactant partial pressures and the total pressure effects have to be studied in order to get a detailed insight of the ALD process. The partial pressure generally plays a major role on the equilibrium coverage of reversible adsorption processes. However, for the irreversible chemisorption processes on which ALD is based (Puurunen et al.), even low partial pressure of reactants can lead to full coverage of the surface, given enough exposure time. Furthermore, low pressure facilitates species diffusion, thus leading to more uniform concentrations within the reactor. Nevertheless, an adequate choice of reactant partial pressures may lead to shorter reactant pulses, thus optimizing the process.

The choice of the total pressure in ALD processes is usually based on process scale-up aspects rather than on surface chemistry (Van Bui *et al.,* 2017). Most conventional ALD reactors operate under reduced pressure because this facilitates the purge step (Van Bui *et al.,* 2017). Operating in high pressure increases the minimum

purging step duration, and thus the processing time. However, operating at higher and even atmospheric pressures can yield significant advantages, such as lower equipment cost and complexity, as well as a wider range of precursor partial pressures to be used, which can be suitable for the deposition on high-surface-area surfaces (Van Bui *et al.,* 2017).

1.1.3 Effect of the substrate nature

Although the film GPC during ALD is considered constant, with a monolayer being deposited in each cycle, the actual deposition is more complex. The substrate nature has a significant impact on both the initial ALD nucleation and growth and on the composition of the deposited film, leading to the formation of interfaces between the substrate and the deposited material.

1.1.3.1. Effect on the initial deposition steps

The ALD deposition modifies the chemical nature of the surface. The first ALD cycle occurs on the surface sites of the original substrate species, while during the following cycles deposition takes place on a surface with both the original substrate sites and the ALD-formed sites (Puurunen, 2005). Once the ALD film covers the whole surface, subsequent deposition occurs only on the ALD sites where ideal ALD behavior is obtained. Hence, the deposition depends on the nature and the number of surface sites. The initial deposition steps can be classified in four categories (Puurunen, 2005), which are schematically represented in Figure 1.6:

- Linear growth: The GPC is constant, and the film thickness is linear as a function of the number of cycles, from the first cycle onwards. This happens when the reactivity and number of surface reactive sites are the same on the initial substrate surface and the already grown ALD material. Such behavior has previously been observed for CrO_x ALD on γ-Al_2O_3 (Kytökivi *et al.*, 1996, Hakuli *et al.,* 2000), HfO_2 ALD on chemical Si oxide (Green *et al.,* 2002) and plasma enhanced AlN ALD on Si (Van Bui *et al.,* 2015).

- Substrate enhanced growth: In this growth mode, the GPC is higher in the first ALD cycles, and then decreases to a constant value, as the process attains linear growth. This can be due to a higher reactivity or number of reactive sites on the substrate than on the ALD grown film. Such growth has been reported for the ALD of HfO_2 on Ge (Delabie *et al.*, 2005), and Ti ALD on various metal surfaces (Kim and Rossnagel, 2002).

- Substrate inhibited growth, Type 1: This growth mode presents a lower GPC during the first ALD cycles, which increases until linear growth is obtained. This behavior is due to the lower reactivity or number of sites on the substrate than on the ALD film. HfO_2 ALD on H-terminated Si has shown such behavior (Green *et al.,* 2002).

- Substrate inhibited growth, Type 2: This growth mode also begins with a reduced growth during the first ALD cycles, but then exhibits a maximum, before slightly decreasing to the steady GPC. This behavior is assigned to island growth (Volmer–Weber growth) of the ALD film. In this regime, the new material preferentially deposits on and around already deposited material, thus forming islands. The islands then coalesce, forming a continuous film. Such behavior has been observed for the ALD of Al_2O_3 and ZrO_2 on H-terminated Si (Puurunen *et al.,* 2004).
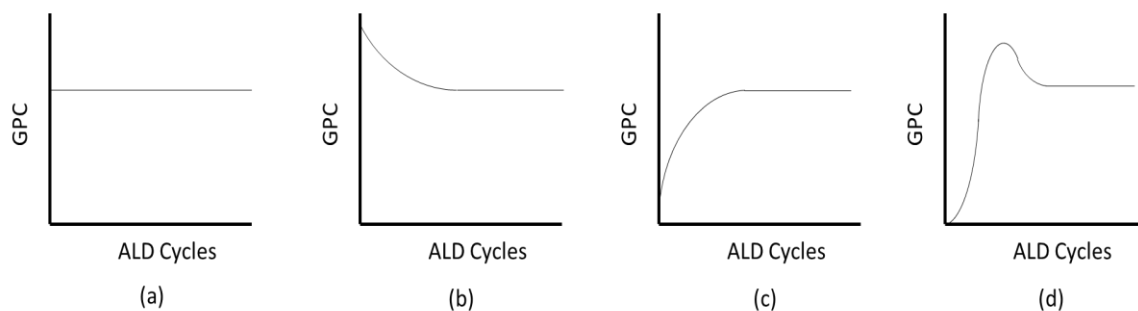
Figure 1.6. Initial deposition steps regimes: a) Linear growth, b) Substrate enhanced growth, c) Substrate inhibited growth type 1, d) Substrate inhibited growth type 2.

The substrate inhibited initial growth regime presents major drawbacks. Besides the implications it has on the film thickness control, a substrate-inhibited growth imposes a minimum number of ALD cycles that need to be used to obtain a continuous material layer, due to the initial induction period. Hence, the minimum continuous film thickness is limited. If this period is long enough, this minimum thickness may be too high for certain applications of the film, especially in nanoelectronics. Furthermore, if the initial regime is the island growth regime, the films roughness is higher and more ALD cycles may be needed in order for the film to smoothen. All these aspects make the detailed investigation of the ALD mechanisms during the first cycles a necessity.

1.1.3.2. Film/substrate interface

The ideal perception of ALD envisages the material film depositing on the substrate surface, without any physicochemical interaction between them. The actual deposited film however, is affected by the substrate. A non-abrupt interface may be formed between the ALD film and the substrate, as reported in published works (Figure 1.7).

The composition and density of this interface may affect the properties of the deposited structure, thus harming its potential applications. This is the case for the ALD of *high k* metal oxides on Si substrates (Först *et al.,* 2004). The deposited gate oxides form a non-abrupt interface with Si. If the deposited *high k* oxide has a thickness of just some nm, which is the case in today's MOSFETs, this interface may be comparable in thickness with the ALD film, thus damaging the dielectric properties of the resulting structure. This is a decisive factor for the selection of materials to replace SiO_2 as a dielectric.
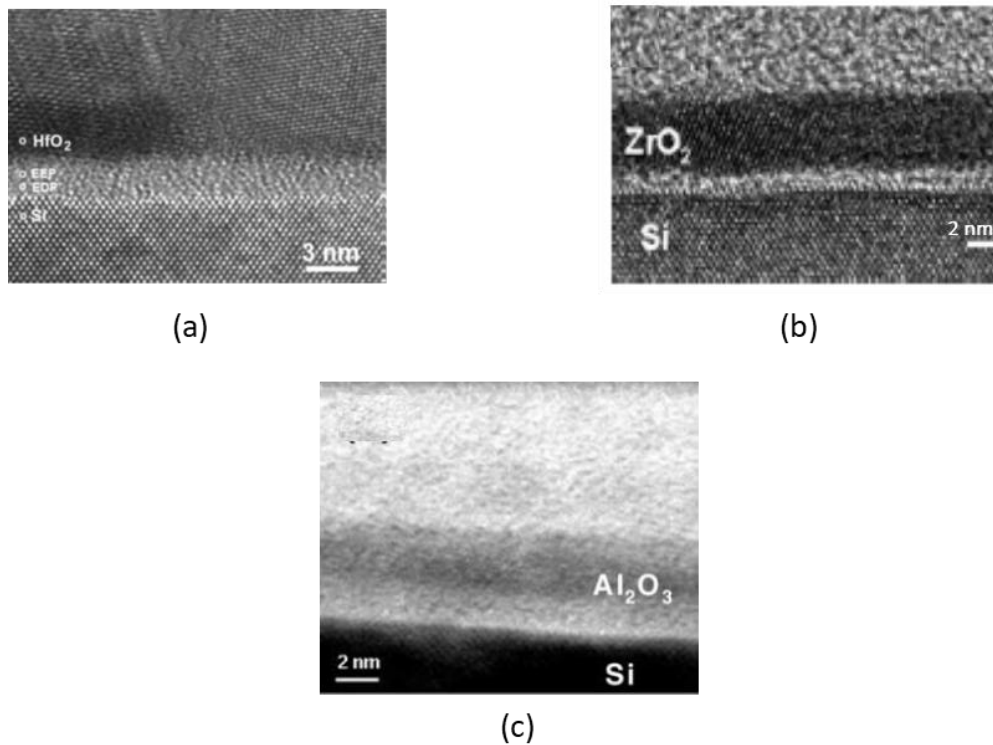
Figure 1.7 TEM images of deposited films and their interfaces: a) HfO_2 on Si (Lu *et al.,* 2005), b) ZrO_2 on Si (Lee *et al.*, 2009), c) Al_2O_3 on Si (Chang *et al.*, 2004).

1.1.4 ALD at the reactor scale

ALD is a process widely conceived to depend only on surface chemistry. Although this may be the case for the deposition on small planar surfaces, the deposition on one or multiple large area wafers presents more complex behavior. Within an ALD reactor, transport phenomena dictate the flow of reactants through the chamber. These phenomena in turn are highly affected by the reactor design and process setup.

For the deposition of uniform films on a large area wafer or on a series of multiple wafers in a reactor, the reactant fluxes on the whole surface to be coated must be uniform, or at least attain a minimum value which ensures full coverage of the surface reactive sites. Furthermore, the temperature distribution must be homogeneous along the wafer surface, as it severely affects surface kinetics. If these conditions are not ensured, non-uniform films are deposited. The process parameters (Li *et al.,* 2007), the reactor design and the wafer position (Pan *et al.,* 2015) can thus affect the uniformity of the deposited films (Henn-Lecordier, *et al.,* 2011, Salami *et al.*, 2017).

Besides the desired uniformity of the films, the ALD process is affected by the reactor setup in terms of cost. Longer exposures are required for the deposition on large area substrates or multi-wafer reactors (Pan *et al.,* 2015, Muñoz-Rojas *et al.,* 2019). The required purge time is also increased (Muñoz-Rojas *et al.,* 2019). Reactants adsorb on the larger walls of the reactors, and need time to desorb and be purged from the chamber during the purge time.

All the above aspects reveal the necessity to study the ALD process not only in terms of surface chemistry, but also in terms of interplay of the surface mechanisms with the transport phenomena taking place inside the reactor. The reactor design and process setup, as well as the reactant flows must be thoroughly studied and understood.

This is necessary in order to optimize the ALD process both in terms of quality of the deposited film, but also in terms of throughput and cost, for its industrial application.

1.2. ALD of Al$_2$O$_3$

1.2.1. Overview

Al$_2$O$_3$ is a widely used thin film material. Depending on its crystallization phase, it can serve as a protective diffusion (Bae *et al.,* 2013) or thermal barrier (Wang *et al.*, 2016) and as a catalyst (Marturano *et al.*, 1997). Its stability, favorable thermal conductivity, hardness, and low refractive index make it a technologically promising material in optics, machinery, batteries, and microelectronic applications (Houska *et al.*, 2012, Shi *et al.*, 2018). Furthermore, Al$_2$O$_3$ is a favorable candidate to replace SiO$_2$ as a high-k layer. Its higher dielectric constant and similar band gap make it an appropriate dielectric material for microelectronic applications (Renault et al., 2002). All the above have made Al$_2$O$_3$ one of the most studied materials in the field of ALD.

Over the last decades, numerous works have investigated the ALD of Al$_2$O$_3$ (Fan and Toyoda, 1993). Early works presented investigations on the self-limiting nature of the deposition process (George *et al.* 1996), characterizations of the deposited material (Ritala *et al*., 1996), and the identification of the surface reactions (Dillon *et al.*, 1995). Due to requirements for the deposition of thinner gate oxides films and the interest for a replacement for SiO$_2$ as a *high k* oxide layer, the deposition of Al$_2$O$_3$ films by ALD was a subject of many works (Elam et al., 2002, Juppo *et al.,* 2000). The surface chemistry (Wind et al, 2010), the initial steps of deposition (Puurunen *et al.*,

2004) and the deposited film composition and dielectric properties have been the subject of such works (Renault *et al.*, 2002)(Park *et al.*, 2001).

Al$_2$O$_3$ has been deposited using a variety of different reactant systems. The most common metal precursor is Al(CH$_3$)$_3$ (Tri-methyl Aluminum, TMA) (Puurunen, 2005). AlCl$_3$ has also been used as the metal precursor (Ritala *et al.*, 1996). Less cited precursors include tris(diethylamino) aluminum (Katamreddy et al., 2006) and Aluminum Triisopropoxide (Tai *et al.* 2019), among others. For the oxygen reactant, the most common is H$_2$O (Puurunen, 2005). Other oxidants have been used, namely D$_2$O, O$_2$, O$_2$ plasma and O$_3$ (Frank *et al.*, 2003)(Ha *et al.*, 2005). In this thesis, the study is focused on the ALD of Al$_2$O$_3$ using TMA and H$_2$O as metal precursor and oxygen source, respectively.

1.2.2. Al$_2$O$_3$ ALD from TMA and H$_2$O

1.2.2.1. *General description*

The ALD of Al$_2$O$_3$ using TMA and H$_2$O has been considered as a "model" process for thermal ALD (George, 2010). Both reactants are volatile and thermally stable over a range of temperatures (<300°C), thus fulfilling the criteria as an ALD reactant (Puurunen, 2005). The reactions are self-terminating, while the by-product (CH$_4$) is inert. The surface chemistry of TMA+H$_2$O and the ALD process have been widely studied, both experimentally (Ott *et al.,* 1997)(Vandalon and Kessels, 2016) (Vandalon and Kessels, 2017), as well as with the usage of Density Functional Theory (DFT) calculations (Widjaja and Musgrave, 2002)(Halls and Raghavachari, 2004).

The high reactivity of the reactants and the self-terminating nature of the surface reactions lead to the deposition of conformal films of high compositional purity, with a high control over the deposited thickness.

Figure 1.8 summarizes some characteristic literature results for this system. The self-terminating nature of the surface reactions (Figure 1.8a) is shown by the GPC behavior as a function of the reactant exposure, where the GPC reaches a maximum and remains unaffected with further increase of the exposure time. This leads to a linear thickness evolution as a function of the number of cycles once the ALD regime is attained (Figure 1.8b). The growth behavior within the ALD temperature window (Figure 1.8c) is shown by the GPC evolution as a function of the process temperature. The GPC is initially low and increases with the temperature, where it remains almost unchanged for a range of temperature values. Further temperature increase after a certain point leads to a decrease of the GPC, due to the decrease of the number of reactive surface sites (OH) and the activation of the reactant desorption from the surface. The high conformality and step coverage of the deposition on surface features is displayed in Figure 1.8d, validating the choice of ALD as the appropriate technique for conformal deposition in trenched surfaces.

The wide variety of published works and data on this system makes it a good choice to be used as a landmark for the study of fundamental or non-understood aspects of *high-k* metal oxide ALD on Si.
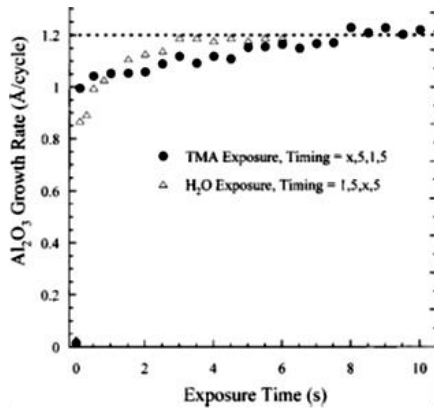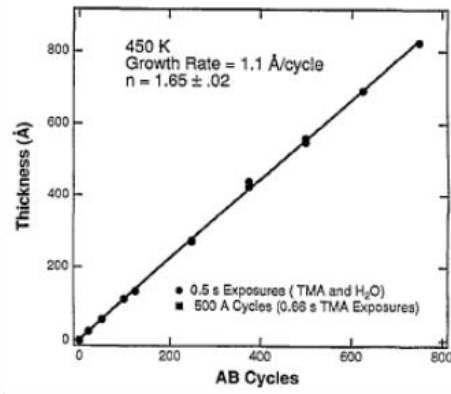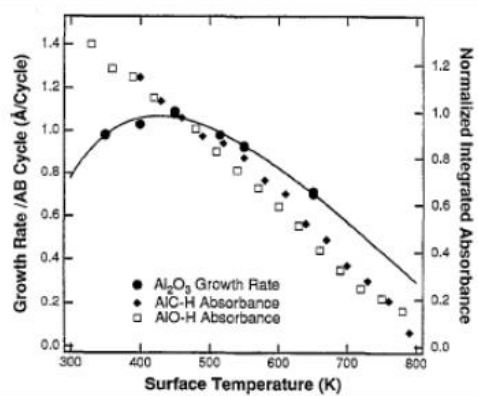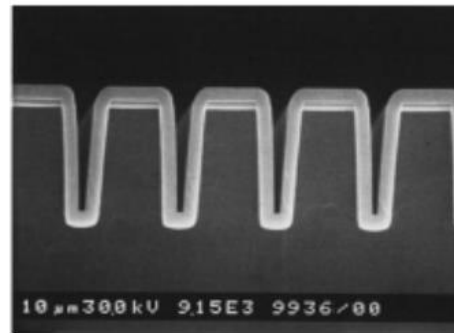
Figure 1.8. Representative literature results for the ALD of Al_2O_3 using TMA and H_2O. a) GPC vs reactant exposure time (Elam *et al.*, 2002), b) Thickness vs number of cycles (Ott *et al.*, 1997), c) GPC vs temperature (Ott *et al.*, 1997), d) Conformal Al_2O_3 ALD films on trenched surface (Ritala *et al.,* 1999)

1.2.2.2.   *Surface chemistry*

The surface mechanisms involved during the TMA + H_2O ALD have been identified and widely reported in the literature. In this section, the surface chemistry is summarized. It is important to note that this section deals with the surface chemistry during the "ideal ALD regime", where the GPC is constant and linear thickness as a function of the number of ALD cycles is obtained. During this regime, the deposition occurs on already deposited Al_2O_3.

The overall reaction is:

$$2Al(CH_3)_3 + 3H_2O \rightarrow Al_2O_3 + 6CH_4 \hspace{4cm} (R1.1)$$

The reactions involved for each exposure step are detailed below.

TMA exposure:

The Al_2O_3 surface is covered with OH groups, which are the reactive surface sites for the TMA reactant. During the TMA exposure, TMA chemisorbs on surface OH groups as follows:

$$Al(CH_3)_{3(g)} + n \, OH_{(s)} \rightarrow Al(CH_3)_{3-n(s)} + n \, CH_{4(g)} \hspace{2cm} (R1.2)$$

The above chemisorption mechanism leads to a surface covered by $Al(CH_3)_x$ species. The reaction is considered irreversible, as CH_4 desorbs from the surface.

H$_2$O exposure:

During the water pulse, the methyl-terminated surface generated by the previous TMA step of the cycle, is exposed to H_2O vapor. The H_2O molecules adsorb on the DMA species:

$$Al(CH_3)_{x(s)} + x \, H_2O_{(g)} \rightarrow Al(OH)_x + x \, CH_{4(g)} \hspace{2.5cm} (R1.3)$$
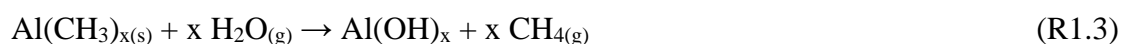
After the H_2O exposure, the surface is thus terminated by surface OH groups. Hence, the subsequent TMA exposure takes place on a surface of the same chemical nature as in the previous cycle, as the starting surface is regenerated.

However, the above representation of the surface chemistry overview is rather simplistic, as more phenomena actually contribute to the deposition. The detailed surface mechanisms along with the surface reactions, are presented in detail in Chapter 3.

The surface chemistry of TMA+H_2O ALD is summarized and schematically represented in Figure 1.9.
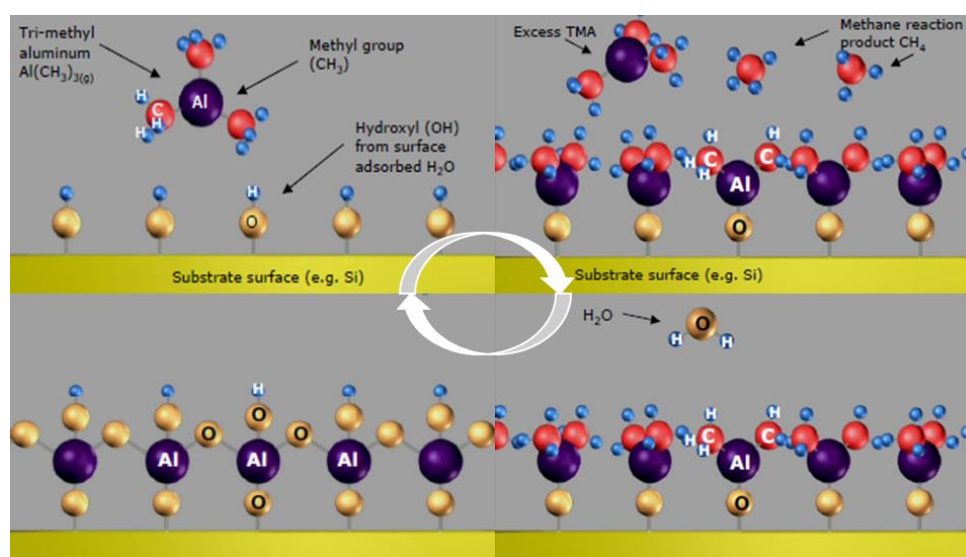
Figure 1.9. Schematic representation of the detailed surface chemistry of Al_2O_3 ALD from TMA and H_2O (Fiji F200 installation and use manual, 2009).

1.2.2.3. *Reaction self-termination*

As previously discussed, the self-limiting nature of the reactions has previously been demonstrated. The factors that cause this saturation are an important aspect of the ALD chemistry, as they ensure the high control over the deposited material during each ALD cycle.

During the TMA exposure, two decisive factors can lead to saturation: the steric hindrance of ligands and the concentration of surface reactive sites. The CH_3 ligands of

TMA can occupy area for deposition, thus limiting the deposition of further TMA molecules to a maximum (Puurunen, 2005). Furthermore, as TMA chemisorbs on OH sites, the surface concentration of those OH sites limits the amount of Al that can be deposited on the surface. The surface OH concentration during the ALD process, in turn, depends on the process temperature. It has been shown that a linear decrease of the OH reactive sites occurs with the increase of temperature (Haukka and Root, 1994). The decrease of the GPC at higher temperatures in the ALD of Al_2O_3 from TMA and H_2O has been attributed to this behavior of the OH groups (Puurunen, 2005).

For the H_2O exposure, the molecules chemisorb on the surface $Al(CH_3)_x$ species and react producing CH_4, leaving the surface terminated by $Al(OH)_x$. The factor causing saturation for the H_2O exposure is the number of surface CH_3 species. Once all the methyl groups are replaced by OH groups and CH_4 is desorbed, further reactions of H_2O do not take place. However, further adsorbed H_2O may be adsorbed on the alumina surface. This excess H_2O must be desorbed and removed during the purging time, in order to ensure the layer by layer deposition in ALD. Such parasitic reactions with adsorbed water that has not been totally removed during the purge have previously been reported to lead to non- uniform films (Henn-Lecordier *et al.*, 2011).

1.2.2.4.   *Challenges*

Although the TMA/H_2O ALD process has been the subject of numerous works in the past decades, there are some aspects of the surface chemistry which are not well understood. The "ALD temperature window" for the TMA/H_2O can have a complex behavior, as shown in Figure 1.8c. Using pre-determined reactant exposures, the deposition is limited at lower temperatures. An increase of the process temperature leads to GPC increase where it remains more or less stable before decreasing at higher

temperatures. The identification of the exact reaction mechanisms that lead to this behavior and their quantification is still an open question. Recently, the works of Vandalon and Kessels, dealing with these aspects, re-opened the discussion for the surface mechanisms of TMA/H_2O ALD. Using a broadband sum-frequency generation (BB-SFG) study, they showed that the deposition is limited at low temperatures due to the low reactivity of H_2O towards certain persistent CH_3 surface species (Vandalon and Kessels, 2016) (Vandalon and Kessels, 2017). Their results are presented in Figure 1.10.

Figure 1.10a shows that the TMA initial reaction probability is independent of temperature. This means that negligible or no thermal activation is involved in the surface kinetics during the TMA exposure. This is not the case for the H_2O reactions, as shown in Figure 1.10b. The initial reaction probability increases with temperature, which shows that in low temperatures the reactions with certain CH_3 groups are not activated. With the increase of temperature, the reactions are activated and H_2O reacts with the surface CH_3 coverage. This is also shown in Figure 1.10c, where the fraction of the CH_3 surface groups remaining unremoved after the H_2O exposure is plotted as a function of temperature. Results show that although 60% of the surface CH_3 groups is unremoved at 100ºC, the totality of CH_3 groups is removed at 300ºC, thus validating the thermal activation of the H_2O reactions shown in Figure 1.10b. Although this analysis provides information regarding the presence of some persistent CH_3 groups on the surface at low temperatures, the identification and quantification of those CH_3 groups need to be studied more thoroughly.
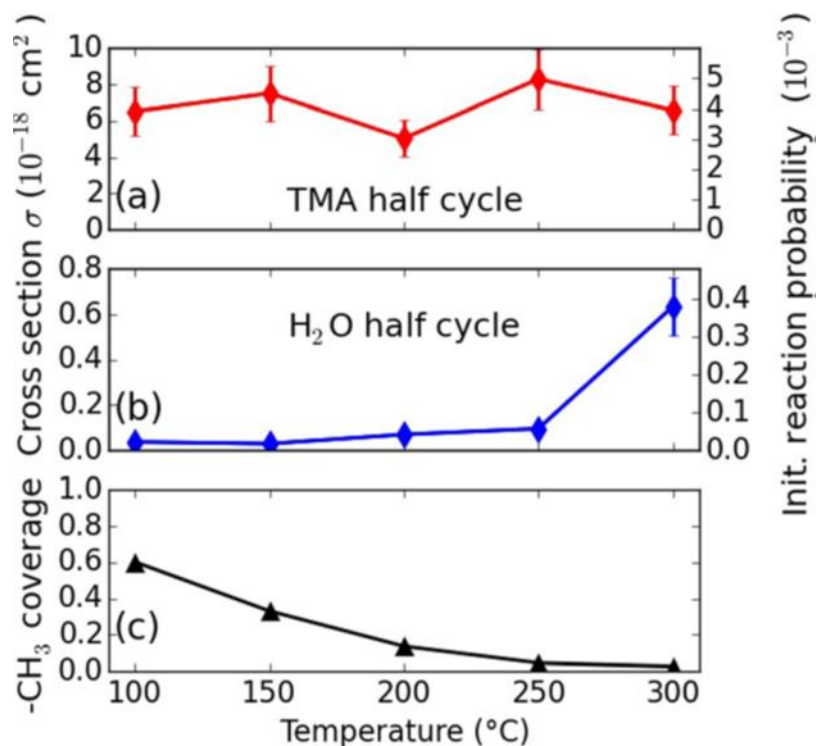
Figure 1.10. Results from the BB-SFG study of Vandalon and Kessels. Temperature dependence of the reaction cross section (left hand axis) and the initial reaction probability (right hand axis) for the a) TMA and b) H2O half-cycle. Panel (c) shows the fraction of –CH$_3$ groups persisting after the H$_2$O exposure as a function of temperature (Vandalon and Kessels, 2016).

The surface kinetics during TMA/H$_2$O ALD are also yet to be thoroughly discussed. This is of major importance as the time scales of the surface mechanisms dictate the required exposure times. The scaling-up of this process for large area wafer or multi-wafer reactors, as well as for the coating of particles in fixed or fluidized bed reactors is dependent on those times. Hence, the understanding of those kinetics are crucial for the industrial applications of TMA/H$_2$O ALD in large scale.

Finally, as presented in section 1.2.2.2, the surface mechanisms (adsorption, desorption and surface reactions) involved are not simple. Once the reactants are adsorbed on the surface, they can either desorb or react with the surface reactive species.

These are two competing mechanisms that take place simultaneously. The understanding and quantification of these mechanisms, the identification of the prevailing ones, and the effect that process parameters can have on this competition of surface phenomena will ensure a higher control over the surface chemistry. This fine tuning of the surface chemistry may help solve the non-ideal aspects of the ALD growth.

1.2.3. TMA/H$_2$O ALD on Si

As discussed in section 1.2.3, the substrate nature has an impact on the ALD chemistry, in particular for the ALD of Al$_2$O$_3$ from TMA and H$_2$O. The deposition has been studied on various types of substrates, including semiconductors, metals, as well as polymers (Delabie *et al.*, 2012)(Gong *et al.*, 2011) (Foroughi-Abari and Cadien, 2012).

1.2.3.1. *Initial growth*

The ALD of Al$_2$O$_3$ from TMA and H$_2$O on Si is substrate inhibited. The classical Si substrate pre-treatment is made in a liquid HF bath in order to remove the native oxide, leaving the surface terminated by Si-H species. This surface termination is unreactive towards both reactants. Frank et al. have confirmed this low reactivity using in situ infared (IR) spectroscopy (Frank *et al*., 2003). It has also been confirmed by computational studies using DFT (Halls and Raghavachari, 2003) (Lin and Teplyakov, 2013). The reactions on the H-Si surface were found to have a very high energy barrier, thus explaining the non-reactivity of the surface.

The ALD nucleation hence initiates on surface defects, such as unremoved O bridges or OH species from the HF pre-treatment (Frank *et al.*, 2003). The activation energies for TMA deposition on Si-OH groups have been studied by DFT and are found to be much lower than on the Si-H surface (Lin and Teplyakov, 2013), comparable with the activation energies on already deposited Al-OH (Widjaja and Musgrave, 2002).

Once TMA deposition occurs on these defects, subsequent reactions of H_2O are facilitated. During the next cycles, the reactivity on already deposited Al_2O_3 is significantly more favorable than on H-Si. This leads to preferential deposition on and around already deposited material, leading to island-like growth (Volmer–Weber growth). This growth mode has been studied both experimentally (Puurunen *et al.*,2004) (Mack *et al.*, 2006), as well as with the use of computational models (Puurunen and Vandervorst, 2004) (Nilsen *et al.,* 2007). The island-like, substrate inhibited growth mode on H-Si has been reported for the ALD of other oxides as well, showing that it is a more generalized drawback of ALD, not only for the deposition of Al_2O_3. Characteristic results from published works are presented in Figure 1.11.
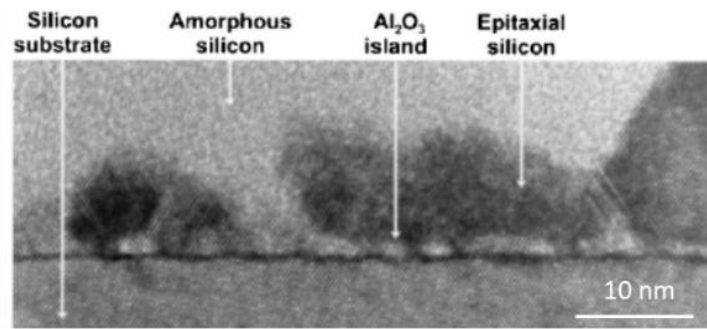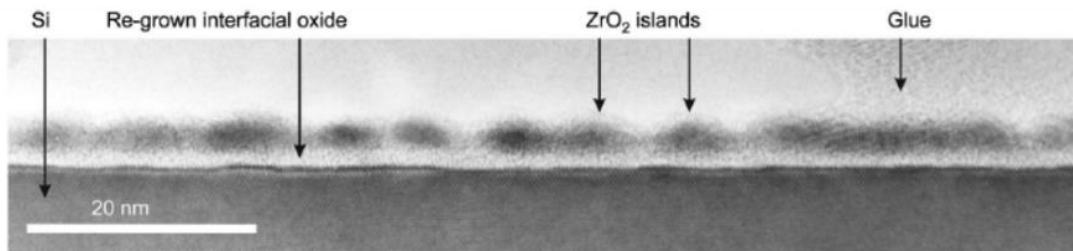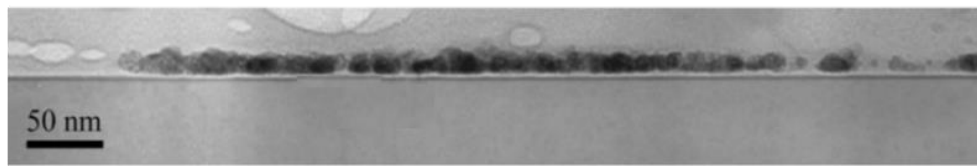
Figure 1.11. Island growth during the ALD of oxides on Si: a) Al_2O_3, 15 cycles (Puurunen *et al*.,2004), b) ZrO_2, 60 cycles (Puurunen *et al*.,2004), c) RuO_2, 700 cycles (Salaün *et al.,* 2011)

1.2.3.2. Al_2O_3 interface with Si

Besides its effect on the initial deposition steps, the Si substrate also affects the composition of the deposited film. Notably, a non-abrupt interfacial layer is formed between the deposited Al_2O_3 film and the Si substrate. Although this interfacial layer has been the topic of research works over the past years, its exact composition and its formation mechanisms have yet to be defined concretely.

The choice of the oxidizing reactant has an impact on the formation of this layer. Ha et al. (Ha *et al.*, 2005) have shown that the thickness of this interfacial layer is lower when H_2O is used as the oxidant source, than when using O_2 plasma or O_3. Nonetheless, the interfacial layer is formed even when H_2O is used as a reactant (Renault *et al.*, 2002) (Naumann *et al.*, 2012). Its thickness is 1-2 nm (Werner *et al.,* 2011)(Kaur *et al.*, 2017). Post deposition thermal annealing has also shown to increase the interfacial oxidation, showing a temperature dependence for the mechanisms involved (Chang *et al.*, 2004). Finally, an increase of the oxidizing reactant flows and exposure time enhances the interfacial layer formation (Kuse *et al*., 2003). Characteristic TEM images of the interfacial layer from published research works are presented in Figure 1.12.

(a)   (b)

(c)
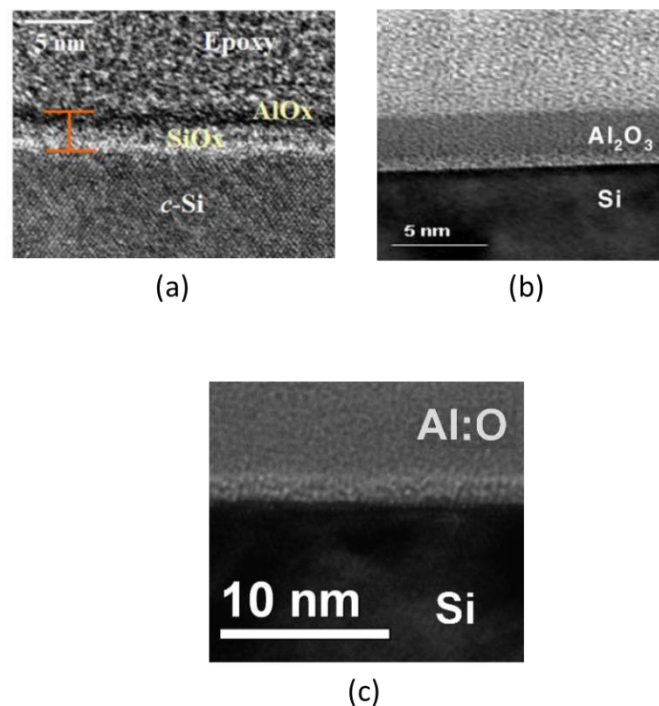
Figure 1.12. Characteristic TEM images of the interfacial layer grown from Al_2O_3 ALD on Si: a) Kaur et al. (Kaur *et al.*, 2017), b) Chang et al. (Chang *et al.,* 2004), c) Werner et al. (Werner *et al.*, 2011).

The Al_2O_3/Si interfacial layer consists mainly of oxidized Si, in various oxidation states (Renault *et al.,*2002). Al-silicates, hydrogen and carbon have also been reported to be present within the layer (Renault *et al.,*2002)(Gosset *et al.,* 2002)(Schilirò *et al.,* 2015).

One of the interfacial layer formation mechanisms has been suggested to be the Si oxidation by H_2O during the initial island growth regime, where the surface is not totally covered by the ALD film (Naumann *et al.*, 2012). Although the initial Si surface is non-reactive towards H_2O, the presence of Al catalyzes the Si oxidation (Frank *et al.*, 2003) (Lim *et al.*, 2000). Once the ALD film is continuous, interdiffusion and reaction of species occurs, thus leading to further formation of the interfacial layer (Naumann et al., 2012)(Schilirò *et al.,* 2015). Furthermore, non-removed H_2O impurities during the purging time can lead to non- ideal reactions that can contribute to the formation of the interfacial layer (Halls *et al.*, 2003).

1.2.3.3. *Challenges*

The initial growth inhibition and the interfacial layer formation during the ALD of Al_2O_3 on Si are two significant drawbacks for the deposition and applications of ultra-thin films by ALD. Even for the "ideal process" of TMA/H_2O ALD, an induction period corresponding to island growth, and a non-abrupt interface is obtained on Si. Puurunen et al. have shown that a continuous ALD film is obtained after 20-30 ALD cycles (Puurunen *et al.*, 2004). This would imply that the number of cycles used for Al_2O_3 film deposition is restricted to a minimum for the production of continuous films. Furthermore, due to the island growth mode, the film has a certain roughness, and a higher number of ALD cycles is needed in order to obtain smoother films, with the island coalescence (Nilsen *et al.*, 2007). The above aspects of the initial growth make

the deposition of nanometric films with a thickness less than 2 nm a challenge which needs to be overcome for the effective use of such films for microelectronic applications.

The interfacial phenomena taking place lead to the formation of a layer with a lower dielectric constant, as well as non-ideal leakage current, interface trap density, minority carrier lifetime and lower thermal stability (Groner *et al.,* 2002) (Kaur *et al.,* 2017) (Chang *et al.*, 2004). This shows that the formed interfacial layer has a damaging effect for the applications of ALD Al_2O_3 films of a very low thickness, such as high-k oxides for MOSFETs. Hence, both the initial growth induction period, as well as the formation of the interfacial layer must be restricted for the deposition of functional ALD films with a thickness of some nanometers.

One of the ways to restrict these two phenomena during the ALD of Al_2O_3 on Si, is the Si surface pre-treatment prior to deposition. Such pretreatments can effectively change the reactivity of the initial surface, thus enhancing the initial nucleation and growth. This initial enhancement can also lead to the restriction of interfacial phenomena and Si oxidation, as no more island growth takes place.

Previous studies have developed such pre-treatments for the Si surface prior to the ALD of Al_2O_3. Si-OH surface termination has been realized by exposing the H-terminated Si to $Cl_{2(g)}$ (Damlencourt *et al.*,2003)(Lee *et al.*, 2004), or by dipping in a H_2O_2:HCl solution (Kaur *et al.,* 2017). This surface termination was used to increase the reactivity of the substrate, thus leading to the suppression of the initial induction period observed on Si-H (Kaur *et al.,* 2017)(Damlencourt *et al.*,2003)(Lee *et al.*, 2004). A long exposure of the Si surface to TMA (3600 s) prior to ALD has been reported to lead to an enhanced nucleation and growth during the first cycles, as well as to a

suppression of the interfacial Si oxidation (Frank *et al.,* 2003)(Xu *et al.,* 2006). The chemisorption of TMA over the whole surface during the initial long exposure leads to the formation of a monolayer. During subsequent deposition, no island growth takes place, and hence the Si oxidation is limited. However, this pre-treatment exhibits experimental and technical difficulties as it involves the exposure of TMA inside the chamber with no pumping for a long period of time (3600 s). No oxygen leak must take place during this time period, which is very challenging.

The substrate pre-treatment by NH_3 or NH_3 plasma has shown comparable effects on the reduction of the induction period and the interfacial layer formation (Brewer *et al.*, 2004)(Lu *et al.*, 2007). Brewer et al. have used a thermal N_2-NH_3 pre-treatment prior to deposition and have shown an increase in the deposition during the initial steps using infared spectroscopy (Brewer *et al.*, 2004). Lu et al. have performed an *ex situ* NH_3 plasma pre-treatment, which exhibited an increased ALD deposition during the initial steps (Lu *et al.*, 2007). Xu et al. have compared Al_2O_3 films deposited by ALD on Si surfaces pre-treated *ex situ* by NH_3 plasma and long TMA exposures prior to deposition, in terms of thermal and electrical properties (Xu *et al.*, 2006). Although both pre-treatments resulted to enhanced initial growth and restricted interfacial layer formation, the films on NH_3 plasma pre-treated Si exhibited better thermal stability and lower leakage current.

1.3. Computational modelling of ALD processes

1.3.1. Modelling as a powerful tool for ALD

As discussed in the previous sections, complex physical and chemical phenomena take place during the ALD process that dictate the film GPC and composition. Hence, a thorough understanding of these phenomena is required, so as to be able to fine tune the ALD process, in order to deposit uniform, conformal films with high composition purity and thickness control, with abrupt interfaces.

Although experimental measurements can reveal the fundamental reactions taking place, the detailed information on surface chemistry mechanisms and their interplay with other phenomena is very difficult to extract. Furthermore, the different time scales for the phenomena involved within a reactor are also a limiting factor for experimental studies. The transport phenomena inside an ALD reactor, such as diffusion and convection of reactants can be in the range of seconds or minutes, while the surface reaction in typical ALD processes are in the order of some milliseconds.

There are also different space scales involved in ALD. The reactant gas flows take place inside an ALD reactor, with dimensions ranging from cm to m. In the same time, the reactant diffusion and deposition occurs on surface features, such as trenches, which range from nm to μm. The nano-morphology of the film may be in the same scale. Finally, the reactions take place between gas phase and surface sites, hence in the atomic scale. This is another factor that limits the experimental analysis when studying the different mechanisms during ALD.

In this context, physical based mathematical modelling has emerged as a powerful tool for the thorough study and understanding of the ALD process. These models can study the different mechanisms and their effects on the film deposition.

Using such a computational framework, it is possible to identify reaction mechanisms, test the validity of certain chemical reaction schemes, as well as determine optimal process windows. Computational models can be developed for the different spatial scales of interest of the ALD process. These models may also be coupled through the exchange of computational information, thus leading to multiscale computational frameworks. Such approaches can link film properties at the nanoscale, such as film roughness or step coverage, with controllable process conditions at the reactor scale, such as temperature or gas flows.

1.3.2. Modelling at micro, nano, and atomic scales

As the ALD process is conceived as a process based on surface chemistry, the nature of the surface mechanisms and reactions taking place during the deposition process is one of the most important aspects of ALD. The detailed identification of the individual chemical mechanisms is performed with computational models using DFT calculations results. Numerous works have investigated the ALD reactions for various reactant systems (Lin and Teplyakov, 2013)(Widjaja and Musgrave, 2002)(Elliott and Greer, 2004)(Halls and Raghavachari, 2004). Using such models, it is possible to identify different mechanisms and reaction paths that are thermodynamically favorable. Furthermore, activation energies using transition state theory can be obtained for the different reactions, which reveal the kinetically favored reactions.

The activation energies obtained from DFT calculations can then be used to investigate the reaction kinetics. They can be studied using surface kinetic models, which can include a large number of reactions. From these models, computational

predictions of the GPC can be obtained (Travis and Adomaitis, 2013,2014). The limiting mechanisms under different conditions can be identified and the competition between surface phenomena may also be studied (Remmers *et al.*, 2015)(Adomaitis, 2015).

Using a validated mechanism, the evolution of the film nucleation and growth can be studied using stochastic approaches. Kinetic Monte Carlo (kMC) models for the film thickness evolution and morphology on a surface lattice have been used for the ALD of Al_2O_3 from TMA and H_2O (Mazaleyrat *et al.*, 2005) and for the ALD of HfO_2 (Shirazi and Elliott, 2014) (Dkhissi *et al.*, 2009). These models can analyze the effects of multiple detailed events on the film nucleation and growth at the atomic scale. Such models can also provide information about the nano-morphology of the film, such as surface roughness (Dkhissi *et al.*, 2009)(Neizvestny *et al.*, 2006). Using a combined experimental and computational approach with such kinetic models, it is possible to derive and validate chemistry schemes, as well as examine new reaction mechanisms and pathways, in connection with experimental measurements.

To study the growth during the ALD process, R.L. Puurunen developed a random deposition model (Puurunen, 2004). The model is phenomenological, and does not take into account surface reactions. The coverage during each cycle is predefined and used as a model parameter. Using this model, the evolution of the deposition with the ALD cycles, and the number of deposited monolayers can be monitored. Using such models, film properties at the nanoscale, such as the evolution of surface roughness, can be predicted

The initial island growth regime, occurring during the first ALD cycles, as discussed in section 1.3.3.1 of the present chapter, can also be studied using

phenomenological models (Puurunen and Vandervorst, 2004) or models based on geometrical principles (Nilsen *et al.*,2007), for a variety of deposited materials, including Al_2O_3 and ZrO_2. Although these models do not involve chemical reactions, several aspects of the nucleation and growth mechanisms can be revealed. The initial growth regime, the island coalescence, surface roughness, surface concentration of nucleation sites, as well as the number of cycles needed to produce a continuous film can be obtained using such models (Puurunen and Vandervorst, 2004)(Puurunen *et al.*, 2004)(Nilsen *et al.*,2007).

To study the step coverage and conformality of deposition, gas diffusion-reaction and ballistic models have been developed for the ALD of HfO_2 and Al_2O_3 (Adomaitis, 2011)(Gobbert *et al.*, 2002). With such computational approaches, the effect of certain process parameters on the film deposition within surface features, such as trenches, can be investigated in detail (Kim *et al.*, 2007). This allows the fine tuning of the deposition in such features, by altering controllable process parameters in the reactor.

In this thesis, the surface mechanisms and the competition between them is studied in detail using a stochastic kMC model, presented in Chapter 3. Its results are presented and validated in Chapter 5. The initial growth regime is studied using a geometrical island growth model, presented in Chapter 3. Its results are presented, validated and analyzed in Chapter 6.

1.3.3. Modelling at the reactor scale

The modelling of ALD reactors is based on the mechanics of continuum approach. The transport phenomena are described by a set of partial differential

equations (PDEs). This set of PDEs consists of conservation equations for mass, momentum, energy and chemical species. This set of equations can incorporate expressions for reactions, either in the bulk of the reactor or on a surface. These equations are discretized into a computational domain, and are solved numerically.

The reactor scale models can provide valuable information, about the gas flow, pressure and temperature fields within the reactor, as well as the reactant distribution (Deng *et al.,* 2016) (Pan *et al.*, 2015)(Peltonen *et al.,* 2018). When coupled with surface reactions, such computational approaches can reveal the link between process parameters, transport phenomena, reaction mechanisms and film properties, such as film uniformities (Xie et al., 2015)(Pan *et al.,* 2015). Furthermore, with the use of such models, it is possible to identify optimal process windows, as well as modification of the equipment design, in order to optimize film quality and reactant consumption (Shaeri *et al.,*2015)(Pan *et al.,* 2016)(Xie *et al.*, 2016). Reactor scale models have previously been used for the study of CVD reactors (Gakis *et al.*, 2015) (Koronaki *et al.*, 2016) (Gkinis *et al.*, 2017).

Although such models have been used in previous research works for ALD reactors, the actual process dynamics have not been represented in detail. The precise simulation of the vacuum pump behavior and the reactant pulses is usually incomplete (Pan *et al.*, 2015)(Shaeri *et al.*, 2015), while viscosity and diffusion coeffecients of gases are assumed constant (Xie *et al.*, 2015). Furthermore, the surface mechanisms only incorporate surface reaction of gas phase species with surface sites, through one phenomenological reaction (Xie *et al.,* 2015) (Pan *et al.*, 2015). In this thesis, the process dynamics are studied in detail, while the surface phenomena such as adsorption, desorption and reaction are all taken into account for the computational investigation (Chapter 3).

1.3.4. Multiscale modelling of ALD processes

As the mechanisms involved range over various length scales, ALD is by nature a multiscale process. Hence, besides separated models dealing with only one length scale, multiscale models can also be used for the study of the ALD process. Within a multiscale approach, each model deals with a separate scale. The models are coupled through the exchange of computational information, where a result from one model is fed as input to the other. Such models have included the coupling of DFT calculations with kMC models to study the film nucleation and growth for the growth of HfO_2 on SiO_2 (Dkhissi *et al.*, 2009), or the coupling of a kMC model to a diffusion model inside surface features for the ALD of Al_2O_3 (Adomaitis, 2010). Such multiscale approaches are more common for the study of CVD processes, where the coupling of various length scales has been the topic of research studies (Cavallotti *et al.,* 2005) (Cheimarios *et al.,* 2011) (Crose *et al.,* 2015) (Aviziotis *et al.,* 2016)

Summary –Conclusions

ALD is recognized as a deposition technique able to produce thin films with a high control over the deposited layer thickness, conformality and uniformity. The aim of the thesis is the study and thorough understanding of the non-ideal aspects of ALD deposition mechanisms. Although ALD is considered as an ideal process, dependent only on surface chemistry, many complex phenomena are involved during the film deposition, in particular during the first steps. The limiting mechanisms that dictate the

nucleation and growth must be identified, as well as their interplay with transport phenomena inside an ALD reactor, in order to obtain uniform, conformal films of high compositional purity.

Furthermore, the substrate has an effect on the ALD film nucleation and growth. During the initial stages of deposition, the chemical nature of the substrate can either enhance or inhibit the deposit, which makes the deposition of nanometric thin continuous films challenging. Moreover, the substrate affects the composition of the film. All these aspects of deposition must be investigated in depth, in order to suggest ways to overcome such drawbacks.

The process of choice is Al_2O_3 ALD from TMA and H_2O on Si. This ALD system represents high k metal oxide ALD on Si, which is the thinner layer in the constantly shrinking MOSFETs of today's microelectronic devices. The high thickness control needed for these dielectric layers make ALD the adequate choice to produce such layers. The choice of this system is based on the fact that it has been the topic of numerous published works. Although this ALD system is considered ideal, it nonetheless exhibits the drawbacks associated with ALD chemistry and the substrate nature. The study of this "ideal" system can lead to an integrated understanding of these non-ideal ALD and establish guidelines to study ALD processes in a more general frame.

The analysis in this thesis is performed using a combined experimental and computational approach. The multiscale computational framework consists of a reactor scale model, which investigates the transport phenomena inside the ALD reactor, coupled with a surface chemistry model. This model is coupled to a nanoscale kMC

model, for the detailed study of surface chemistry. Finally, the nucleation and growth evolution during the first cycles is studied using a model based on geometric principles.

Chapter 2: Experimental materials and methods

In this chapter, the experimental setup used for the ALD of Al_2O_3 films from TMA and H_2O is presented. The ALD reactor, the reactant feeding system, as well as the heating and vacuum systems of the ALD setup are introduced and explained in detail. The substrate cleaning and pretreatment procedures and the process conditions used for the deposition of the Al_2O_3 films are detailed. Finally, the basic principles of different techniques, along with the conditions used for the characterizations of the ALD films are presented and described in the final section of the chapter.

2.1. The ALD setup

The ALD deposition experiments were performed by E. Scheid in a commercial Veeco® Fiji F200 ALD setup, situated in LAAS, Toulouse, France. This reactor can coat wafers with a diameter up to 200 mm. It can be used either for thermal or for plasma–enhanced ALD. The setup is schematically presented in Figure 2.1 (Fiji F200 Installation & use manual), while its different parts are presented in the next subsections.
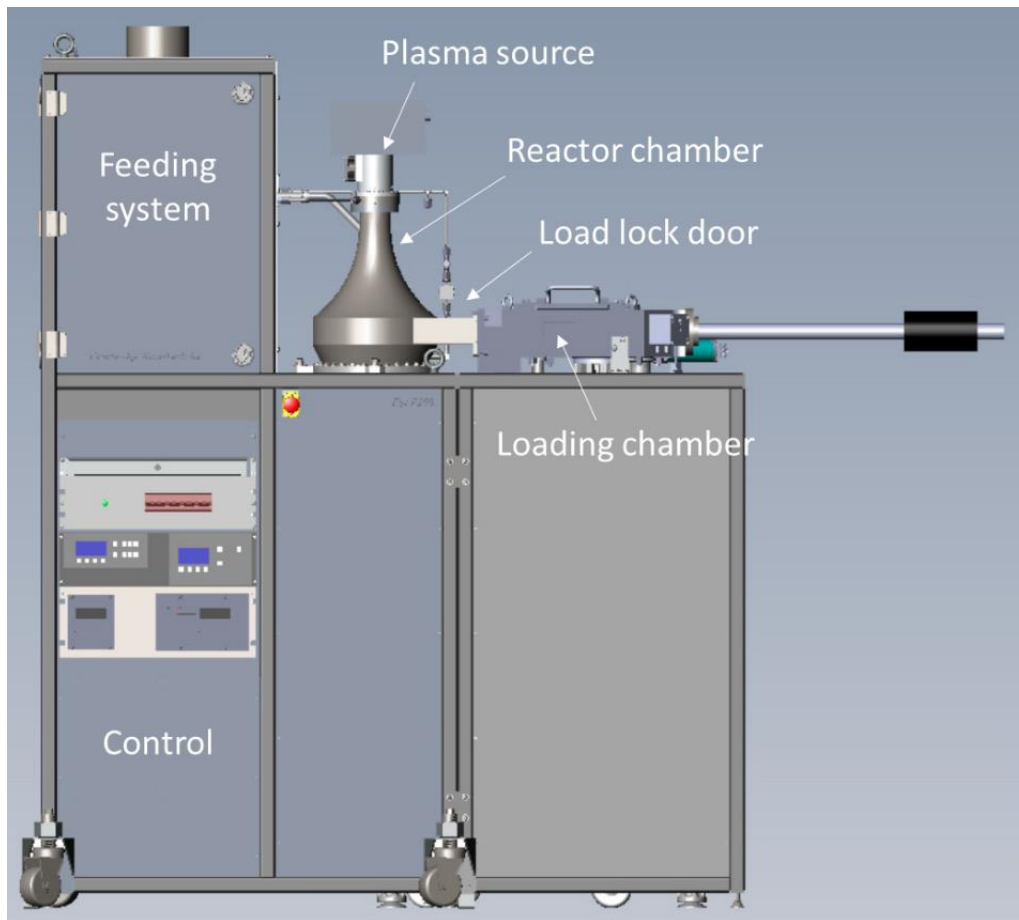
Figure 2.1. Schematic representation of the Veeco® Fiji F200 ALD setup (Fiji F200

Installation & use manual)

2.1.1. Reactor main chamber

The reactor main chamber consists of the reactor walls, three inlets, an outlet, a

loading door, and a wafer holder. The reactor photograph and schematics are shown in

Figures 2.2a (Fiji F200 Installation & use manual) and 2.2b, respectively.
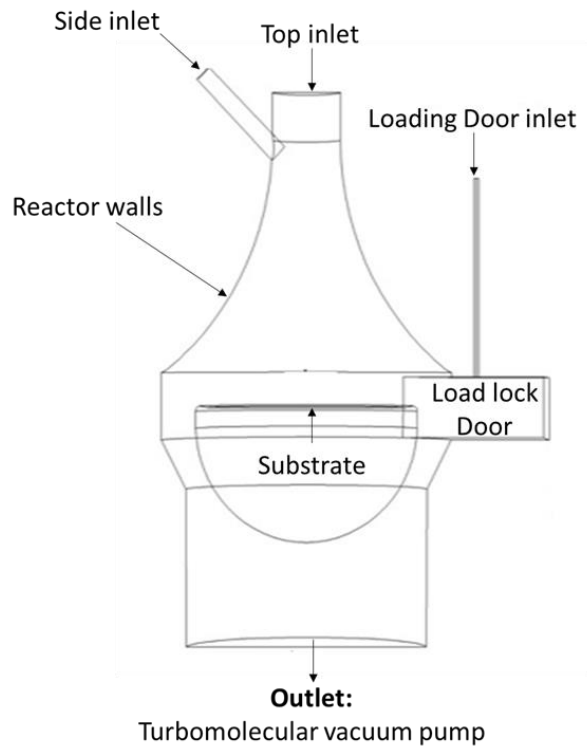
Figure 2.2. a) Photograph (Fiji F200 Installation & use manual), b) Schematic

representation of the reactor main chamber

The reactor main walls are made of stainless steel and are covered by a thermally

isolated heating jacket that allows the heating of the walls. The load lock door walls are

not covered by the jacket. During deposition, the load lock door connection to the

loading chamber is kept closed. The substrate holder is situated in the center of the

reactor and is heated by a heating chuck. The wafer is placed on top of the holder. The

wafer diameter can be up to 200 mm.

The reactor has three inlets, hereafter called top inlet, side inlet and loading door

inlet, as shown in Figure 2.2b. All three inlets serve a different purpose. The top inlet

is the main purging gas (Ar) inlet. For PE-ALD, this inlet is also used as the plasma

reactant inlet. The side inlet is connected to the reactant feeding system. From this inlet, the reactants enter the main reactor chamber, during the reactant exposure steps of the process. Inert Ar gas is also used as a carrier gas for the reactants. The loading door inlet is a purging gas inlet. Ar enters the reactor in the load lock region, so as to avoid deposition within the load lock area and its walls. The Ar gas flows are all regulated using mass flow controllers (MFCs), while the outlet of the main chamber is connected to an Edwards® STPH301 turbomolecular vacuum pump.

2.1.2. Reactant feeding system

The reactant feeding system is connected to the reactor main chamber through the side inlet. The feeding system consists of the reactant bottles, the ALD valves and a tube circuit that leads to the reactor side inlet. A photograph (Fiji F200 Installation & use manual) and the schematic representation of the reactant feeding system are shown in Figure 2.3a and 2.3b, respectively.

During the ALD process, Ar flows continuously through the feeding system and enters the reactor main chamber through the side inlet. During the purging steps, Ar serves as a purging gas. During the reactant exposure steps, the ALD valves open and the respective reactant is injected into the reactor main chamber. During these exposure steps, the Ar flow serves as a carrier gas flow. Although the Ar flow is regulated by a mass flow controller (MFC), the reactant flows are not. The reactant flow is dictated by the pressure difference between the reactor chamber and the reactant bottles, as well as the opening time of the ALD valves, which is regulated by an external control unit.
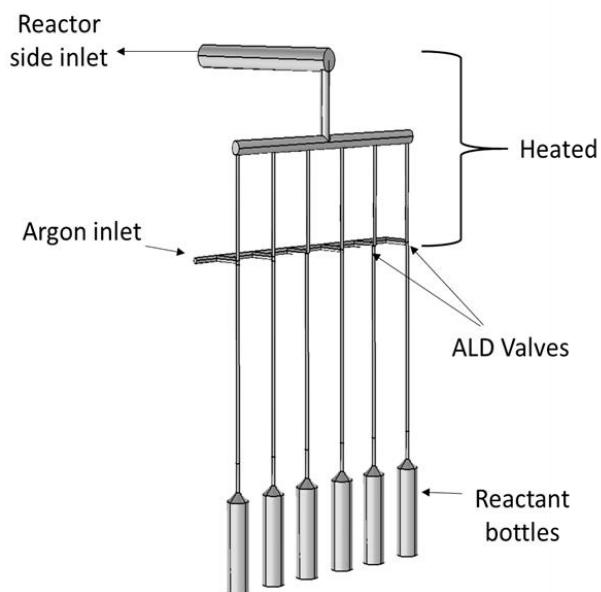
Figure 2.3. a) Photograph (Fiji F200 Installation & use manual) and b) schematic representation of the reactant feeding system

The reactants are stored inside stainless steel Swagelok® SS-4CS-TW-50 sample cylindrical bottles. The bottles are half-full of liquid reactants. So, they contain both liquid and vapor phases of the reactant at its vapor pressure. The bottles may be heated, in order to achieve higher vapor pressure of less volatile reactants. In the present case, the TMA and H_2O bottles are not heated during the ALD process. Once the ALD valves are open, the reactants are guided towards the reactor chamber through a tube circuit. This tube circuit is heated, as shown in Figure 2.3b.

2.1.3. Reactor heating system

The temperature inside the reactor main chamber and the reactant feeding system is regulated using thermocouples connected to PID controllers. The tube circuit in the reactant feeding system (Figure 2.3b) is heated using a heating jacket, to 150°C. The Ar flow entering the feeding system is not heated, and its temperature is 20°C. Although the reactant bottles are not heated, heat conduction from the tube circuit heating jacket leads to a measured reactant bottle temperature of 28°C.

In the reactor main chamber, the side inlet is heated to 150°C. The reactor walls are heated by an electrical heating jacket, to the desired temperature. The top inlet and loading door inlet Ar flows enter the reactor chamber at 20°C. The load lock walls are not heated, and are exposed to the atmospheric air. Finally, the substrate is heated by a heating chuck, to the desired temperature. It is important to note that although for the reactor walls sensors are placed in various positions on the walls, for the substrate the thermocouple is placed at the center of the chuck. For all process recipes used, the reactor walls were kept at the same temperature as the substrate, except from the recipe at the maximum temperature of 300°C, where the reactor walls were kept at 270°C. This is to prohibit gas phase decomposition of TMA (Puurunen *et al.,* 2005).

2.1.3. Vacuum system

The reactor outlet is connected to an Edwards® STPH301 turbo-molecular vacuum pump. For turbo-molecular pumps, the volumetric pumping speed stays constant, for a wide range of pressures at the pump inlet. The pumping speed and base pressure are regulated with an automatic pressure controller (APC) unit. The APC unit consists of a heated throttling and sealing butterfly valve, installed upstream of the turbo

pump. The ALD base pressure is regulated in advance using a Baratron® capacitance manometer and a butterfly valve at the reactor outlet. Once the base pressure is set by adjusting the opening of the butterfly valve, the valve opening remains fixed during the whole process. During deposition, the outlet pressure is monitored by an Edwards APGX-H Pirani gauge. Indeed, the capacitance manometer isolation valve is automatically closed during an ALD recipe, to prevent deposition on the measuring device. Hence, the only data provided during deposition is the pressure variation at the reactor outlet measured by the Pirani gauge. This Pirani gauge is a gas dependent gauge, which indirectly measures the pressure through the gas thermal conductivity. In the present case, the Pirani gauge is calibrated for N_2. Hence, the pressure reading is dependent on the gas mixture composition. The base pressure for all the process recipes used in this thesis was 0.072 Torr, as measured by the Baratron® capacitance manometer.

2.2. The experimental procedure

2.2.1. Substrate cleaning and pretreatment

For all ALD experiments, Si(100) wafers were used as substrates. For the investigation of thickness uniformity over large area substrates, Si wafers of 200 mm diameter were used. For the investigations during the initial ALD cycles, 100 mm Si wafers were used. The Si(100) wafers were cleaned by deionized (DI) water rinsing, followed by dipping in a 5% HF solution for 1 min, in order to remove the native oxide on the Si surface, and a final DI water rinsing. After the pretreatment, the wafer was dried with N_2 and immediately loaded into the chamber via the loading chamber, which

was pumped out to its base pressure (10^{-4} – 10^{-5} Torr) during 10 min, then to the base pressure of the ALD process (0.072 Torr) with Ar nominal flows during 5 min.

For the Si samples pre-treated by N_2-NH_3 plasma, the previous steps are followed by an *in situ* exposure to a N_2-NH_3 gas mixture without plasma (100 sccm N_2, 20 sccm NH_3), at 0.08 Torr, during 5 min. Then the plasma was activated for 1 min. Inductively coupled N_2-NH_3 plasma with a power of 300 W was used for the pretreatment. The samples were heated to 300°C during the pretreatment. Through the precursor line, 10 sccm of Ar were also fed during the pretreatment, in order to avoid retro-diffusion towards the ALD valves. After the pretreatment, the N_2-NH_3 plasma mixture feed was stopped, and the system was pumped to the base pressure of the ALD process (0.072 Torr) during 5 min, prior to starting the ALD process.

2.2.2. Atomic Layer Deposition

For the ALD of Al_2O_3 on the Si(100) wafers, TMA and H_2O vapor were used as metal precursor and oxidant source, respectively. Once the Si surface pre-treatment is complete, as described in the previous section, the isolation valve of the capacitance manometer is closed and the process is initiated.

Deposition takes place under process conditions that are implemented according to predefined recipes. In all experiments, the top inlet, loading door and side inlet Ar flows were set to 100 sccm, 50 sccm and 30 sccm, respectively. The Ar flows are controlled by MFCs, with standard conditions of T=24°C and P=1 bar. Using these Ar flows, the ALD base pressure (pressure during the purging steps) is set at 0.072 Torr, by correctly adjusting the heated throttling and sealing butterfly valve of the APC unit.

The top and loading door gas temperatures were set at 20°C, while the heating of the feeding line is at 150°C. The substrate and reactor wall temperatures varied within 125-300ºC

The reactant pulses are regulated only by the ALD valve opening time. For the study of the ALD dependence on process conditions, the TMA valve opening was varied between 0.025 s and 0.06 s, while the H_2O valve opening between 0.06 s and 0.1 s. The purge time was varied from 5 s to 60 s, depending on the process temperature. The experiments performed and the respective process conditions for this study are summarized in Table 2.1.

Experiment #	$T_{substrate}$ (ºC)	T_{walls} (ºC)	TMA pulse time (s)	H_2O Pulse time (s)	TMA Purge time (s)	H_2O Purge time (s)	No. of cycles
1	125	125	0.025	0.100	30	30	500
2	125	125	0.060	0.100	30	30	500
3	150	150	0.025	0.100	20	20	500
4	150	150	0.060	0.100	20	20	500
5	162	162	0.025	0.100	20	20	500
6	175	175	0.025	0.100	15	15	500
7	175	175	0.060	0.100	15	15	500
8	200	200	0.025	0.100	10	10	500
9	200	200	0.060	0.100	10	10	500
10	250	250	0.060	0.100	8	8	500
11	300	270	0.025	0.100	5	5	550

12	300	270	0.060	0.100	5	5	550
13	300	270	0.025	0.100	2	3	550
14	150	150	0.025	0.100	10	10	500
15	150	150	0.060	0.100	5	5	500
16	300	270	0.025	0.060	5	5	550

Table 2.1. Thermal and cycle conditions used for the study of the ALD process

parameters

For the investigation of the initial Al_2O_3 ALD nucleation and growth and the interfacial layer formation on both HF and N_2-NH_3 plasma pretreated Si, a series of ALD films using 0, 5, 10, 20, 30, 50, 75, 100, 150, 200, 500, and 550 cycles were deposited. For this series, the TMA and H_2O valve opening times were kept at 0.025 s and 0.1 s, respectively, while the process temperature was kept at $300^{o}C$, and the purging times after each reactant exposure were set to 5 s.

2.3. Deposited film characterizations

In order to study the thickness, morphology and composition of the Al_2O_3 films, the deposits were analyzed using a wide range of characterization techniques. Such characterizations yield to experimental measurements that can reveal valuable information about the ALD film formation during the linear ALD regime, the initial nucleation and growth of the film on the Si surface, as well as the composition of the

deposited Al_2O_3 and its interface with Si. The techniques used for this investigation are presented in this section.

2.3.1. Ellipsometry

Ellipsometry is based on the measurement of the change in the polarization state of a beam of light upon reflection from the sample of interest (Tutas *et al.,* 1964). The exact nature of the polarization change is determined by the sample's properties. The polarization change is quantified by the amplitude ratio, Ψ, and the phase difference, Δ (Whiteside *et al.*, 2016). As the signal depends on the thickness as well as the optical properties of the sample material, ellipsometry can be used for their determination (Tutas *et al.,* 1964), (Arwin and Aspnes*,* 1984).

The thickness of the deposited films was measured via ellipsometry with a Horiba UVISEL Variable Angle Spectroscopic Ellipsometer, located in LAAS, Toulouse. The wavelength interval ranged between 265 and 650 nm, with a step of 20 nm, using an incidence angle of 70° and 76°. This technique was used for thickness measurements on relatively thick samples (50-60 nm) to minimize the measurement error due to any uncertainty on the thickness and composition of the interface between the silicon substrate and the pure Al_2O_3 deposited film.

2.3.2. Transmission electron microscopy

Transition electron microscopy (TEM) is used for a detailed investigation of the film thickness, structure and morphology. During TEM, a beam of electrons is

transmitted through an ultra-thin sample and interacts with it. This interaction causes the creation of an image of the electrons transmitted through the sample. The image is then visualized through an imaging device (Petford-Long and Chiaramonti, 2008). Besides the film thickness and morphology, the structure of a specific material by the analysis of the image can be obtained.

In scanning TEM (STEM), an electron beam focused to a small surface area is scanned in parallel across the sample surface. The detector collects the signal arising from the interaction of the electrons with the sample material (Petford-Long and Chiaramonti, 2008). Further, dark field STEM allows the observation of STEM images with higher resolution and compositional information.

The samples were characterized into the UMS Castaing (Toulouse) by Transmission Electron Microscopy (TEM) using a 200 kV JEOL Cold FEG probe-corrected ARM200F microscope for either High Resolution (HREM) or Scanning TEM (STEM) analysis. STEM images were recorded in both Bright Field (BF) and High Angle Annular Dark Field (HAADF) conditions.

The TEM cross section lamellas were prepared into the UMS Castaing (Toulouse) by Focused Ion Beam (FIB) in a FEI Helios Nanolab 600i dual beam SEM/FIB. For the STEM analysis, the Al_2O_3 film was capped with a 200 nm carbon layer using an electron beam, followed by a 3 μm Pt layer deposited with an ion beam.

2.3.3. X-ray photoelectron spectroscopy

X-ray photoelectron spectroscopy (XPS) uses a monochromatic beam of X-rays with sufficiently high energy to ionize the atoms of the material to be analyzed. An electron from the atoms is thus omitted and its kinetic energy is detected and measured (Kazmerski, 1988). This implies that the latter photoelectron reaches vacuum, and therefore that the surface is at a distance shorter than the photoelectron inelastic mean free path. Thus, detected photoelectrons only originate from some nm below the surface of the sample. The kinetic energy of the omitted photoelectron is dependent on its chemical environment, thus indicative of the chemical nature of the characterized sample. Hence, XPS measurements can allow the qualitative and semi-quantitative determination of the chemical nature and composition of the sample.

X-ray photoelectron spectroscopy (XPS) was performed in a Thermo ESCALAB 250 Xi XPS and a Thermo Scientific K-Alpha system, located at IPREM laboratory, Pau, France, in order to study the chemical nature of the film bulk and interface. XPS was performed using a Al Kα source (1486.7 eV) with a 20 eV pass energy,, while the XPS binding energy scale was calibrated by the adventitious C 1s peak at 285.0 eV. To study the chemical composition along the depth of the film, Ar^+ ions were used to etch the surface along its depth. Ar^+ ions of 200eV were used, with an etching cycle of 20 s before each measurement. Curve fitting has been performed using CasaXPS ©; for 1s core peaks (O 1s, C1s), a single peak has been used for each chemical environment while doublets have been used for 2p core peaks (Si 2p, Al 2p), accounting for spin-orbit coupling.

2.3.4. Energy dispersive X-ray spectroscopy

In energy dispersive X-ray spectroscopy (EDX), a high-energy electrons or protons is focused into the sample being studied. The atoms in the sample contain electrons in discrete energy levels or electron shells. The excitation of the sample atoms lead to the emission of an electron in an inner shell, creating an electron vacancy (Whiteside *et al.*, 2016).. An electron from a higher energy outer shell may fill the vacancy, and the difference in energy between the electron shells may be released in the form of X-rays (Whiteside *et al.*, 2016).. The number and energy of the X-rays emitted from a specimen can be measured by an energy-dispersive spectrometer. As the energies of the X-rays are characteristic of the difference in energy between the two shells and of the atomic structure of the emitting element, EDX allows the elemental composition of the specimen to be measured (Whiteside *et al.*, 2016).. EDX is mainly used for qualitative analysis.

EDX characterizations were performed with the TEM analysis using a 200 kV JEOL JEM-ARM200F Cold FEG microscope, coupled to an Energy-dispersive X-ray spectroscope (EDX), which was used for the chemical characterization of the films. The microscope is located at UMS Raimond Castaing Microcharacterization center (Toulouse).

2.3.5. X-ray reflectivity

In X-ray reflectivity (XRR), a beam of X-rays is reflected from the sample surface under an incident angle. The intensity of X-rays reflected in the specular direction is then measured (Whiteside *et al.*, 2016). The monitoring of the reflected X-

rays with the incident angle can be analyzed, to derive the electron density, thickness and surface roughness of the layers on the sample.

For the investigation of the initial deposition evolution, XRR measurements which were performed in ICSM, CEA Marcoule, France. Measurements were carried out using a Bruker D8 diffractometer with Cu Kα1 (λ = 0.154056 nm) radiation. All measurements were carried out in $\theta-\theta$ geometry for which the sample was kept fixed during the measurements. Experimental curves were fitted using the reflex software based on the Parratt algorithm (Vignaud and Gibaud, 2019), to obtain the thickness and the electron density profile of the prepared layer.

2.3.6. Secondary ion mass spectrometry

Secondary ion mass spectrometry (SIMS) is used to analyze in detail the elemental composition along the sample depth. In SIMS, a focused high energy primary ion beam is used to sputter the sample surface (Wen *et al.,* 2011). This leads to the emission of secondary ions from the surface of the sample, which are subsequently detected by a mass spectrometer. This yields the different chemical species present into the sample material, along its depth (Wen *et al.,* 2011). Although SIMS is a qualitative technique, it is also high sensitivity. Used with Time-of-Flight Mass Spectrometry (ToF-SIMS), it is a very powerful tool for the analysis of the composition of thin films.

In order to analyze the film composition as a function of the film depth, dynamic SIMS analysis was performed using a ToF SIMS V (IonToF) in LIST, Luxembourg. For the depth profile measurement, a 25 keV pulsed Bi^{3+} cluster ion source delivering 0.31 pA target current was used for the analysis, while a 3 keV Cs^+ source was operated

for the sputtering with 20 nA target current. The sputtered crater size was 250 μm × 250 μm and only a 100 μm × 100 μm area in the middle was analyzed. To limit the charging effect, an electron flood gun was used. The data were recorded in positive mode and ions combined with a Cs atom were followed for the depth profile.

Summary-Conclusions

For the deposition of the ALD Al_2O_3 films, a commercial Veeco® Fiji F200 ALD reactor was used. This reactor can coat wafers with a diameter up to 200 mm, thus allowing the study of the deposition on large area wafers.

TMA and H_2O were used as reactants, stored in precursor bottles, while Si(100) wafers were used as substrates. Two series of substrate pretreatments were studied: a classical HF cleaning and a HF cleaning followed by an *in situ* N_2-NH_3 plasma pre-treatment. In order to analyze the effect of the key process parameters on the deposition mechanisms and film characteristics, a wide range of substrate temperatures, reactant pulse durations and purge times were studied.

The deposited films were characterized by a complete set of technics. Ellipsometry was used to measure the film thickness during the linear ALD regime, for the relatively thick samples. XRR was able to monitor the film thickness during the initial steps. TEM and STEM were used to thorough investigate the thickness, morphology and structure of the deposited layers. Finally, XPS, SIMS and EDX measurements allowed the investigation of the chemical nature and composition of the ALD films and their interface with the Si substrate.

Chapter 3: ALD process modelling: Computational methods and strategies

Four different models have been developed during this thesis.

A Computational Fluid Dynamics (CFD) model allows to study the transport phenomena inside the ALD reactor. This CFD model is then coupled to a wafer scale detailed surface reaction model, to study the reaction kinetics and their interplay with transport phenomena. The wafer scale model investigates the chemistry only during the linear, layer by layer ALD regime. These two models are coupled by the interchange of computational information, from and towards both models, and are solved simultaneously.

An island growth (IG) model based on geometric principles has been developed to study the nucleation, growth and morphology evolution of the films during the initial ALD cycles. This model is fed by the growth per cycle (GPC) of the linear ALD regime, computed by the coupled CFD and wafer scale surface chemistry model. Hence, the computational information is only fed from the CFD and wafer scale models towards the IG model, and not vice versa.

Finally, a stochastic lattice kinetic Monte Carlo (kMC) nanoscale model has been developed for more detailed investigation of the surface chemistry and the deposit evolution. This model is fed by the reactant fluxes and temperature from the coupled CFD and wafer scale models, and not vice versa.

The interaction between the different models is schematically represented in Figure 3.1. The computational formulation of the above models, as well as the

computational strategies used to simulate the ALD process, are presented in the following sections.

Reactor scale model

Feeding system CFD model:

Reactor CFD model:

2D surface chemistry model:
Wafer surface chemistry

Investigation of surface mechanisms
Interplay between surface mechanisms and transport phenomena

GPC at the steady regime

Reactant fluxes

Geometrical model:
Island growth

Stochastic kMC model:
Nanoscale chemistry

Initial growth regime

Detailed surface mechanisms
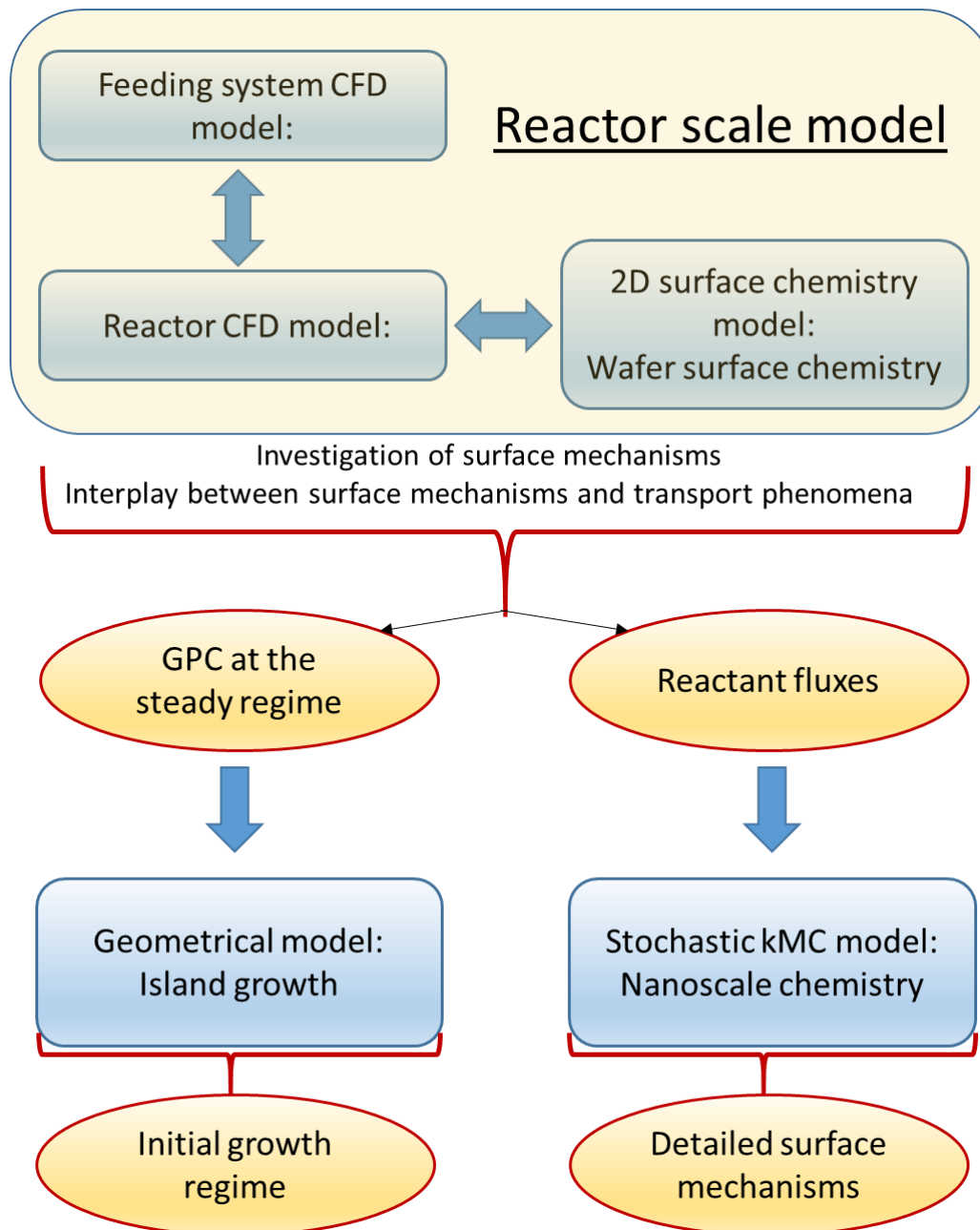
Figure 3.1. Representation of the different models and their interaction.

3.1. Reactor scale CFD model

3.1.1. Computational domains

As previously described, the reactor scale model aims at the investigation of the transport phenomena inside the ALD reactor and the reactor dynamics. The CFD model developed for the ALD reactor should be realistic and experimentally validated, in order to advance with the investigation of the surface reactions and the deposition process. Hence, the model must be fed with realistic data concerning the deposition process.

The most significant difficulty in simulating the ALD system described in Chapter 2, is the lack of measurements and information regarding the ALD reactant flows, during the reactant exposure steps. The only measurements available during the deposition process are the pressure measurements from the Pirani gauge at the reactor outlet. These measurements must serve for the validation of the reactor CFD model, thus they cannot be used for the reactant flows estimation.

For this reason, a second CFD model is developed, for the feeding system of the ALD reactor. Using this model, an estimation of the reactant flows can be computed, which will be used as an inlet condition in the reactor model. Hence, following this computational strategy, two three dimensional computational domains were generated in Comsol Multiphysics®, for the reactor and feeding system of the reactor, presented in Figure 3.2.
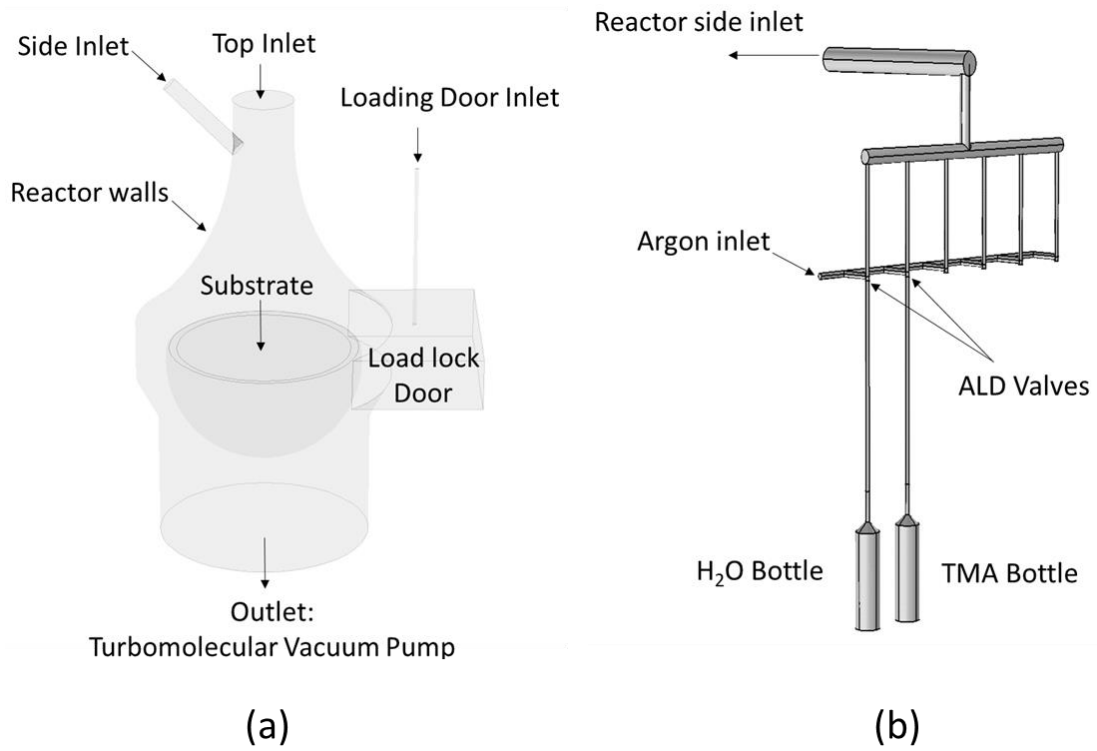
Figure 3.2. Computational domains for a) the ALD reactor b) the reactant feeding system

3.1.2. Governing equations and model assumptions

The gas mixture flowing inside the ALD reactor is modelled using the continuum medium hypothesis. This hypothesis can be validated by computing the Knudsen number, defined as:

$$Kn = \frac{\lambda}{L} \tag{3.1.1}$$

where λ is the mean free path of a gas particle and L is the characteristic length. The continuum medium hypothesis is valid when Kn<0.1. The gas mixture in the low

pressure of the ALD process is also assumed to behave as an ideal gas. Hence, the mean free path can be calculated using the kinetic theory of gases:

$$\lambda = \frac{k_B T}{\sqrt{2}\pi d^2 P} \tag{3.1.2}$$

where k_B is the Boltzmann constant, T is the temperature, d is the particle diameter, and P is the pressure. The maximum Knudsen number was 0.00642, calculated during the Ar purge step, when the total pressure is minimum, taking the outlet diameter as a characteristic length. As this maximum Kn number was below 0.1, the continuum medium assumption is validated.

The gas mixture flow inside the ALD reactor is also assumed laminar. This assumption is validated by calculating the Reynolds number:

$$Re = \frac{\rho u L}{\mu} \tag{3.1.3}$$

Where ρ is the density, u is the velocity and μ is the dynamic viscosity of the gas mixture, where L is a characteristic length. The maximum Reynolds number was calculated at 300ºC. During the purging times, the Reynolds number was equal to 2.05, while the maximum value during the reactant pulses was of 129.15 for the TMA pulse and 37.08 for the H_2O pulse, at the side inlet. The characteristic length used was the side inlet diameter, as this was the region where the maximum gas velocity was found. The low values of the Reynolds number validate the laminar flow assumption.

Finally, the gas mixture is also considered as a Newtonian fluid.

Using the above assumptions, the governing equations that describe the transport phenomena inside the ALD reactor include the conservation of mass,

momentum, and energy, coupled with the conservation of chemical species, as detailed below (Xie *et al.*, 2015):

Conservation of mass

$$\frac{\partial \rho}{\partial t} = \nabla \cdot (\rho \boldsymbol{u}) = 0 \tag{3.1.4}$$

where ρ is the mass density of the gas mixture and $\boldsymbol{u}$ the velocity

Conservation of momentum

$$\frac{\partial (\rho \boldsymbol{u})}{\partial t} + \nabla \cdot (\rho \boldsymbol{u} \boldsymbol{u}) = -\nabla P + \nabla \cdot \left[\mu (\nabla \boldsymbol{u} + \nabla \boldsymbol{u}^T) - \mu \frac{2}{3} (\nabla \cdot \boldsymbol{u}) \mathbf{I} \right] + \rho \boldsymbol{g} \tag{3.1.5}$$

where P is the pressure, μ the viscosity, $\mathbf{I}$ the unit tensor and $\boldsymbol{g}$ the gravity acceleration

Conservation of energy

$$C_p \frac{\partial (\rho T)}{\partial t} + C_p \nabla \cdot (\rho \boldsymbol{u} T) = \nabla \cdot (k \nabla T)$$

$$\tag{3.1.6}$$

where C_p is the specific heat of the gas mixture, T the temperature and k the thermal conductivity.

Conservation of chemical species

$$\frac{\partial (\rho \omega_i)}{\partial t} + \nabla \cdot (\rho \boldsymbol{u} \omega_i) = -\nabla \cdot \boldsymbol{j}_i \tag{3.1.7}$$

where ω_i is the mass fraction of the i species in the gas phase.

The diffusion flux is calculated:

$$j_i = -\rho \omega_i \sum_{k=1}^{n-1} D_{ik} \left[\nabla x_k + (x_k - \omega_k) \frac{\nabla P}{P} \right] - D_{T,i} \frac{\nabla T}{T}$$

(3.1.8)

where D_{ik} is the Maxwell Stefan Diffusion coefficient, and x_k is the mole fraction. Equation 3.1.8 is an expression of Fick's law, including the Soret effect, for constant mixture composition. The thermal diffusion coefficients are calculated using the following equation:

$$D_{T,i} = -2.59 \cdot 10^{-7} T^{0.659} \left[\frac{M_i^{0.511} x_i}{\sum_{i=1}^{n} M_i^{0.511} x_i} - \omega_i \right] \cdot \left[\frac{\sum_{i=1}^{n} M_i^{0.511} x_i}{\sum_{i=1}^{n} M_i^{0.489} x_i} \right]$$

(3.1.9)

where M_i is the molar mass of species i. The set of equations is then completed with the ideal gas law,

$$P_i = c_i RT$$
(3.1.10)

where c_i is the species concentration, and R the ideal gas constant.

The thermal conductivity, dynamic viscosity, and diffusion coefficients for the chemical species are calculated using the kinetic gas theory (COMSOL Multiphysics Reference Manual). The Lennard-Jones parameters for the species are obtained from the CHEMKIN-PRO database (CHEMKIN-PRO, 2013):

Dynamic viscosity:

$$\mu_i = 2.669 \cdot 10^{-6} \frac{\sqrt{TM_i \cdot 10^{-3}}}{\sigma_i \Omega_D}$$
(3.1.11)

Where μ_i is the dynamic viscosity for species i, σ_i is the Lennard Jones characteristic diameter, while Ω_D is the collision integral for viscosity is a function of the dimensionless temperature $k_B T / \varepsilon_i$ $\quad \Omega_D = f\left(\frac{Tk_B}{\varepsilon_i}\right)$, where ε_i / k_B is the Lennard Jones energy potential.

Diffusion coefficient:

The binary diffusion coefficient can be given by the following expression:

$$D_{i,j} = 2.695 \cdot 10^{-3} \frac{\sqrt{T^3(M_i+M_j)/(2\cdot10^{-3}M_iM_j)}}{\rho\sigma_i\sigma_j} \cdot f\left(\frac{\varepsilon_k}{k_B}\right) \quad\quad (3.1.12)$$

$$\varepsilon_k = \sqrt{\frac{\varepsilon_i\varepsilon_j}{k_B^2}} \quad\quad (3.1.13)$$

Where ρ is the density, T is the temperature, M_i is the molar mass of the species, σ_i is the characteristic diameter, and ε_i/k_B is the Lennard Jones energy potential. The function f expresses the diffusion collision integral (Aviziotis, 2016).

Thermal conductivity:

 The thermal conductivity of the gas is calculated by the following equations, derived from the kinetic theory of gases.

$$k_i = 2.669 \cdot 10^{-6} \frac{\sqrt{TM_i\cdot10^{-3}}}{\sigma_i^2} \cdot \frac{1.15C_{p,i}+0.88R}{M_i\Omega_D} \quad\quad (3.1.14)$$

Where $C_{p,I}$ is the specific heat capacity of species i.

Specific heat capacity:

The heat capacity for each species is given as a polynomial function of temperature, following the NASA format (McBride *et al.*, 1993):

$$\frac{C_P}{R} = a_1 + a_2 T + a_3 T^2 + a_4 T^3 + a_5 T^4 \tag{3.1.15}$$

3.1.3. Discretization and solution of the equations

3.1.3.1. Computational mesh

The above conservation equations constitute a set of partial differential equations (PDEs). These PDEs are solved over the computational domain, using the finite elements method (FEM). In this method, the computational domains are discretized into small three dimensional cells, called elements. The set of elements that are used for the computational domain is called the computational mesh.

Meshing is an important step of the computational process since it is connected with the reliability of the simulations. The mesh density and quality influences the convergence of the solution procedure, the accuracy of the obtained solution and the associated computational effort (Aviziotis, 2016). The density of the mesh should be sufficiently high for obtaining solutions with high enough accuracy. However, mesh refinement should be done with care, since unnecessarily too fine discretization could be harmful, in terms of required computer memory and time. To establish solution reliability requires its mesh independence verification. This is performed by systematically monitoring the dependence of the values of chosen variables on mesh density.

Based on the shape of the cells, meshes can be distinguished into: a) structured meshes, comprised by rectangular/quadrilateral (2D) or hexahedral elements (3D), following a uniform pattern, b) unstructured meshes composed by triangular (2D) or pyramidal (3D) elements that are not following any pattern and they are randomly arranged in space. Although for other computational methods, such as the finite volume method, a structured mesh is preferred, the finite element method can accommodate both types of meshes.

The computational meshes developed using Comsol Multiphysics ® for the ALD reactor and the reactant feeding system, are shown in Figure 3.3a and 3.3b, respectively. The computational mesh consists of 149,226 tetrahedral elements for the ALD reactor, while 35,246 tetrahedral elements are used for the feeding system.

(a)   (b)
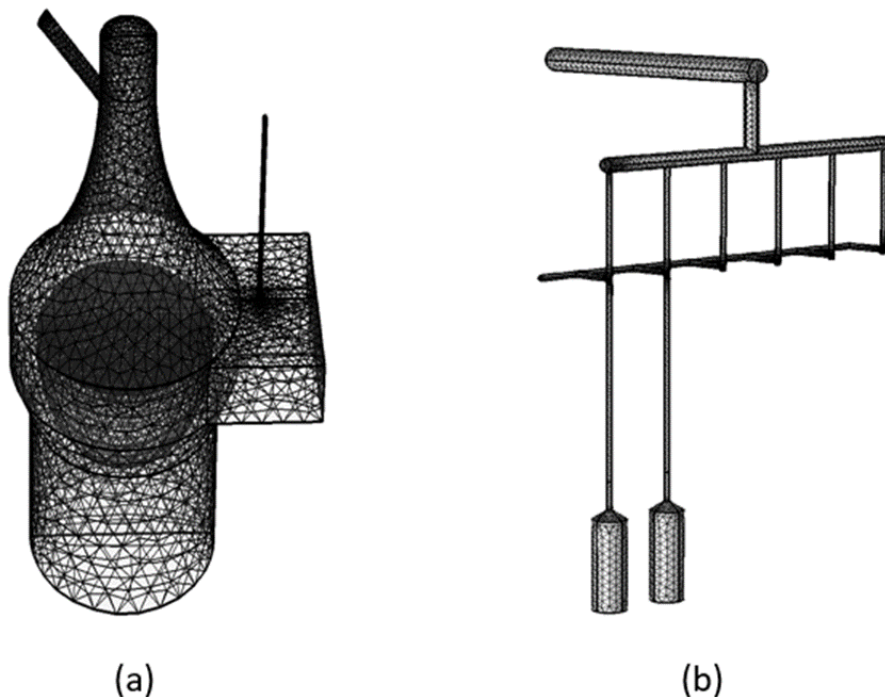
Figure 3.3. Computational mesh for a) the ALD reactor and b) the reactant feeding system

3.1.3.2. Solution of the equations

The set of PDEs is solved along the computational mesh using Comsol Multiphysics®, which uses the FEM method. The set of PDEs (A(u)), along with the boundary conditions (B(u)), constitute boundary value problem, of the form:

$$A(u) \equiv \mathbf{L} \, u = f, \text{ in domain } \Omega \tag{3.1.16}$$

$$B(u) \equiv \mathbf{M} \, u = g, \text{ in } \partial\Omega \tag{3.1.17}$$

Where, $\mathbf{L}$ and $\mathbf{M}$ are differential operators in domain Ω and boundary $\partial\Omega$, respectively, while u is the unknown function. In FEM, the solution for u is in an approximate form $\tilde{u}$:

$$u \approx \tilde{u} = \sum_{j=1}^{N} u_j \varphi^j$$

(3.1.18)

where u_j are the nodal unknowns at each node j of the elements, while φ^j are the basis functions, which are known functions, usually first, second, or higher order polynomials. The solution approximation is realized with the method of weighted residuals. Hence, the residual R_i is defined as:

$$R_i \equiv \int_{\Omega} (\mathbf{L}u - f) w_i \, dV \tag{3.1.19}$$

Where w_i is a weight function. The FEM uses Garlekin's method of weighted residuals, where the weight function is equal to the basis function. As eq. 3.1.19 needs to approach zero, and by substituting eq. 3.1.18:

$$R_i = \int_\Omega \varphi^i (\boldsymbol{L}\left(\sum_{j=1}^{N} u_j \varphi^j\right) - f) dV = 0 \tag{3.1.20}$$

The only unknown in equation 3.1.20 are the nodal unknowns u_j. From this point, the order of the derivative can be reduced in eq. 3.1.20, using integration by parts, divergence theorem, or other methods, followed by the implementation of the boundary conditions. Dirichlet boundary conditions are imposed directly, while Neumann and Robin boundary conditions are imposed at the boundary term after integration by parts.

For example, if L is linear then equation 3.1.20 can be written as:

$$\sum_{j=1}^{N} u_j \varphi^j \int_\Omega \varphi^i L\left(\varphi^j\right) dV = \int_\Omega f\varphi^i dV \tag{3.1.21}$$

Which leads to a linear system of the form:

$$\sum_{j=1}^{N} u_j a_{ij} = b_i \tag{3.1.22}$$

Which can be solved numerically, after the boundary conditions have been implemented.

For the implementation in Comsol Multiphysics®, first order polynomial basis functions are used for the pressure, while second order polynomials are used for the velocity, temperature and chemical species basis functions. The PARDISO solver is used to solve the system of equations.

3.1.4. Boundary conditions and computational strategy

An appropriate set of boundary conditions must be imposed on the PDEs to represent the physical process conditions. Furthermore, the coupling between the reactor and reactant feeding system models must be appropriate in order to effectively simulate the reactant exposure and purging steps.

3.1.4.1. Boundary conditions for the purging step

During the purging steps, where only Ar continuously flows through the reactor, a no slip boundary condition is imposed on the walls of both the reactor and the feeding system CFD models. The ALD valves in the feeding system of the reactor are modelled as an impermeable interface, with no slip conditions, when they are closed. The inlets of the reactor are set to the respective Ar flows (Top inlet: 100 sccm, Side inlet: 30 sccm, Loading door inlet: 50 sccm), using a mass flow boundary condition. The same boundary condition is used for the inlet Ar flow for the feeding system (30 sccm). The heated reactor and feeding system walls are set to their respective temperature, as discussed in Chapter 2. The heating chuck is modelled by imposing a uniform heat flux on the substrate surface, so that the temperature at its center is the desired one. The loading door walls are not heated. The inlet temperature of Ar was set to 20 ºC for the top and loading door inlet, and to 150ºC for the side inlet. A zero species flux is imposed on the reactor walls. Danckwerts conditions were fixed at the exit of the reactor for the gas temperature and species concentrations.

3.1.4.2. Vacuum pump simulation

One more boundary condition for pressure is needed for the model. As the only data available during deposition was the outlet pressure variation, this data was used for validation. Hence, the turbo-molecular pump connected to the reactor outlet was simulated. One of the

technical aspects of the turbo-molecular pump is that it retains a steady volumetric flow rate for a wide range of pressures. This aspect was used for the pump simulation, using the following computational strategy. First, a simulation was performed by imposing an outlet pressure condition, equal to the base pressure of the ALD process, as measured by the capacitance manometer (0.072 Torr). Once a solution is obtained, the computed volumetric flow rate at the outlet represents the volumetric flow rate of the pump. This volumetric flow rate was then imposed as an outlet boundary condition, and the results of the previous simulation of the ALD reactor purging step is used as an initial condition for subsequent simulations.

3.1.4.3. Reactant exposure steps: Coupling of the two models.

The reactant flows are computed by the feeding system model. The computational strategy for the coupling of the reactor and feeding system models is presented in this section.

After the purge time has been simulated, as described in the previous section, the solution about the velocity, pressure and temperature distribution inside the reactor is computed. As the side inlet is connected to the feeding system, the computed side inlet pressure of the reactor is imposed as an outlet pressure condition for the feeding system model.

The feeding system was first simulated with the two valves of the reactants vessels closed. This was done by using the 30 sccm of Ar, serving as a carrier gas, as an inlet boundary condition. An impermeable interface is used to account for the closed ALD valves. The feeding system outlet, connected to the side inlet of the reactor, was set to the pressure computed for the side inlet in the previous step (constant flow of Ar inside the reactor). The gas volume in each vessel above the liquid reactants is assumed

to be half that of the bottle, at a pressure equal to the vapor pressure of the respective reactant 1,940 Pa (14.55 Torr) for TMA and 3,820 Pa (28.65 Torr) for H_2O (NIST Chemistry WebBook, 2005).

The solution for the steady Ar flow in the feeding system is then used as an initial condition to simulate the reactant exposure steps. This is done by removing the impermeable interface corresponding to each reactant exposure and simulating the process for the valve opening times. After the simulation of the valve opening time, the impermeable interface is set again and the process is simulated until no more reactant is present in the feeding system. This leads to the calculation of the reactant flows at the feeding system outlet, during the ALD exposure steps. The computed flows are then implemented as a transient inlet condition to the side inlet of the reactor model. As previously presented, a steady volumetric flow rate is set at the reactor outlet and coincides with that of the steady Ar flow in the reactor. Using the computed pulses as inlet conditions and the computed constant outlet flow rate as an outlet condition, the ALD exposure steps inside the reactor chamber are simulated, and the computed outlet pressure can be monitored and compared to the experimental measurements. The computational strategy is schematically represented in Figure 3.4.
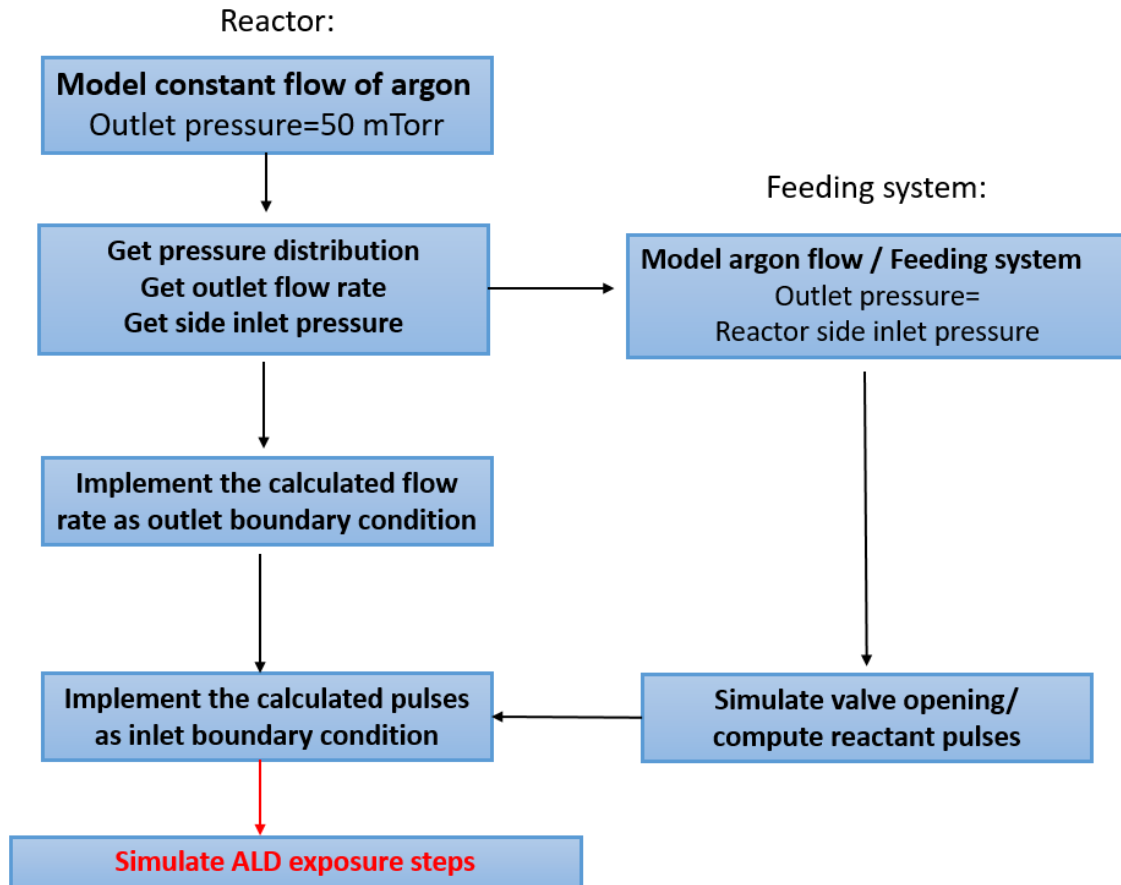
Figure 3.4. Representation of the computational strategy used to couple the reactant and feeding system models

3.1.4.4. Pirani gauge simulation

As discussed in Chapter 2, the outlet pressure is the only measurement during deposition. It is measured by the Pirani gauge, a gas dependent gauge that measures the pressure of a gas through its thermal conductivity. In this case, the Pirani gauge used is calibrated for nitrogen (N_2). Typically, the pressure reading by a Pirani gauge must be multiplied by a correction factor, different for each gas, in order to calibrate the measurements to the real pressure value. In our case, these correction factors are

unknown. As mentioned in Chapter 2, the capacitance manometer isolation valve is automatically closed during an ALD process, to prevent deposition on the measuring device. Hence, the only data provided during deposition is the pressure variation at the reactor outlet measured by the Pirani. So, in order to compare the computed pressure values from the CFD model, P_{calc}, with the Pirani measurements, P_{exp}, we convert the former following Eq. 3.1.23, which accounts for the dependence, assumed linear, of the pressure reading on the ratio of the thermal conductivities of the gas mixture and nitrogen. This conversion is hence based on the principles of the Pirani gauge (indirect measurement of pressure via the gas thermal conductivity), with the assumption that the pressure measurement is linearly dependent on the thermal conductivity of the gas. The converted value, denoted by P_{conv} is used for the comparison with the experimental measurements (P_{exp}). Although this assumption is not could not be tested for H_2O or TMA, experiments showed that it is validated for the pure Ar flow (Chapter 4).

$$P_{conv} = P_{calc} \cdot \frac{k_{mixture}}{k_{N2}}$$

(3.1.23)

where $k_{mixture}$ is the thermal conductivity of the gas mixture, k_{N2} is the thermal conductivity of N_2, P_{calc} is the calculated pressure from the CFD model, and P_{conv} is the converted pressure value by equation 3.1.23. The thermal conductivity of pure nitrogen is calculated at the outlet temperature, using the kinetic gas theory.

3.2. ALD surface reactions: Wafer scale model

3.2.1. Surface chemistry

The surface mechanisms taking place during the TMA + H_2O ALD have been identified and widely reported in the literature. In this section, the surface chemistry is summarized. It is important to note that this section deals with the surface chemistry during the "ideal ALD regime", where the GPC is constant and linear growth as a function of the number of ALD cycles is obtained. During this regime, the deposition occurs on already deposited Al_2O_3 sites.

The overall reaction is:

$$2Al(CH_3)_3 + 3H_2O \rightarrow Al_2O_3 + 6CH_4 \tag{R1}$$

The detailed steps of the TMA/H_2O ALD for each exposure step are the following.

TMA exposure:

The Al_2O_3 surface is covered with OH groups, which are the reactive surface sites for the TMA reactants. The first mechanism taking place during the TMA exposure is the reversible adsorption of TMA on a surface hydroxyl group (Widjaja and Musgrave, 2002):

$$Al(CH_3)_{3(g)} + OH_{(s)} \leftrightarrow H\text{-}O\text{-}Al(CH_3)_{3(ads)} \tag{R2}$$

hereafter named $TMA_{(ads)(s)}$. This TMA molecule, after it adsorbs on the OH site, can either desorb or proceed in a reaction where a CH_3 ligand of TMA reacts with the hydrogen atom of the hydroxyl group, forming CH_4 that is desorbed as a gaseous byproduct (Widjaja and Musgrave, 2002):

$TMA_{(ads)(s)} \rightarrow O\text{-}Al(CH_3)_{2(s)} + CH_{4(g)}$ (R3)

where the $O\text{-}Al(CH_3)_{2(s)}$ surface species is hereafter referred to as dimethyl aluminum or $DMA_{(s)}$.

Studies using density functional theory calculations have shown that a DMA molecule can undergo a second reaction with a neighboring OH site on the surface, releasing CH_4 as a gaseous byproduct and forming an aluminum bridge between the neighboring O sites (Elliot and Greer, 2004)(Delabie *et al.,* 2012):

$DMA_{(s)} + OH_{(s)} \rightarrow (O)_2\text{-}Al(CH_3)_{(s)} + CH_{4(g)}$ (R4)
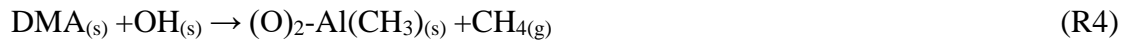
with the new surface species hereafter referred to as monomethyl aluminum, or MMA. Further dissociation of MMA to surface Al with the elimination of methyl groups can be excluded, as it has been found to be endothermic and with a high-energy barrier (Delabie *et al.,* 2012).

H_2O exposure

During the water pulse, the methyl-terminated surface generated by the previous TMA step of the cycle, is exposed to H_2O vapor. The H_2O molecules adsorb on the DMA species (Widjaja and Musgrave, 2002):

$DMA_{(s)} + H_2O_{(g)} \leftrightarrow DMA\text{-}OH_{2 \text{ (ads)}}$
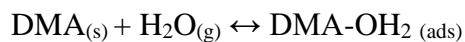
(R5)

onwards called $DMAH_2O_{(s)}$

The adsorbed H_2O molecule can then either desorb or react with one of the methyl groups, leaving a OH group at its place, and releasing $CH_{4(g)}$ as a byproduct (Widjaja and Musgrave, 2002):

$$DMAH_2O_{(s)} \rightarrow O\text{-}Al(CH_3)\text{-}OH_{(s)} + CH_{4(g)} \tag{R6}$$

with the $O\text{-}Al(CH_3)\text{-}OH_{(s)}$ species hereafter named $MMAOH_{(s)}$.

A second H_2O molecule then adsorbs on the MMAOH species:

$$MMAOH_{(s)} + H2O_{(g)} \leftrightarrow H_2O_{(ads)}\text{-}MMAOH \tag{R7}$$

onwards called $MMA(OH)H_2O_{(s)}$, which can then either desorb or react with the methyl group on the surface, releasing CH_4, leaving the surface OH-terminated (Widjaja and Musgrave, 2002):

$$MMA(OH)H_2O_{(s)} \rightarrow O\text{-}Al(OH)_{2(s)} + CH_{4(g)} \tag{R8}$$
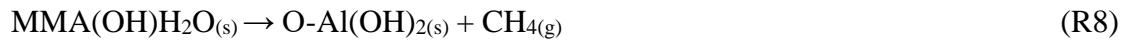
Finally, water can adsorb on MMA species on the surface:

$$MMA_{(s)} + H_2O_{(g)} \leftrightarrow MMA\text{-}H_2O_{(ads)} \tag{R9}$$

onwards called $MMAH_2O_{(s)}$, which can either desorb or react with the methyl group on the surface, releasing $CH_{4(g)}$ and leaving the surface OH-terminated:

$$MMAH_2O_{(s)} \rightarrow (O)_2\text{-}Al\text{-}OH_{(s)} + CH_{4(g)} \tag{R10}$$

3.2.2. Implementation of the surface chemistry

Let us recall that our model represents the ALD regime, where the growth per cycle (GPC) is constant as a function of the number of cycles. Therefore, after each ALD cycle, the surface must be regenerated so as to maintain a constant number of OH groups on the surface from one cycle to another, while depositing stoichiometric alumina. As previously described, the initial reaction of a TMA molecule with a hydroxyl group on the surface may be followed by a further reaction with a neighbouring hydroxyl. Taking into account the mechanisms in the previous section,

the surface after the TMA pulse must contain equal proportions of MMA and DMA species. This ensures the stoichiometric overall reaction, where two TMA molecules react with three H_2O molecules, producing Al_2O_3. Therefore, we implement this condition to our mechanism, leading to the following overall reactions at each reactant exposure.

For the TMA exposure:

$2\ TMA_{(g)} + 3\ OH_{(s)} \leftrightarrow 2\ TMA(ads)_{(s)} \rightarrow DMA_{(s)} + MMA_{(s)} + 3\ CH_{4(g)}$

(R11)

For the H_2O exposure:

$H_2O_{(g)} + MMA_{(s)} \leftrightarrow MMAH_2O_{(s)} \rightarrow Al\text{-}(OH)_{(s)} + CH_{4(g)}$

(R12)

$H_2O_{(g)} + DMA_{(s)} \leftrightarrow DMAH_2O_{(s)} \rightarrow MMAOH + CH_{4(g)}$

(R13)

$H_2O_{(g)} + MMAOH_{(s)} \leftrightarrow MMA(OH)H_2O_{(s)} \rightarrow Al\text{-}(OH)_2 + CH_{4(g}$

(R14)
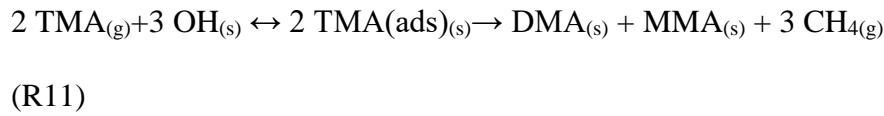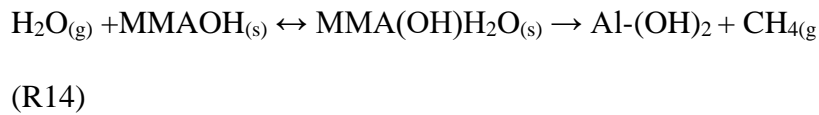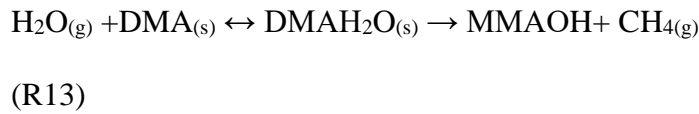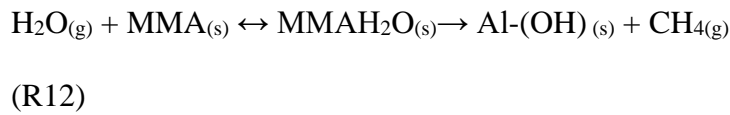
The model takes into account gas molecule adsorption (reactions R2, R5, R7, R9), desorption of adsorbed molecules (reverse reactions R2, R5, R7, R9) and forward surface reactions of the adsorbed molecules. The adsorption rate of each adsorption step for species i ($R_{ads,I}$) is given by the following equation, in $mol \cdot m^{-2} \cdot s^{-1}$:

$$R_{ads,i} = s_i \cdot Flux_i$$

(3.2.1)

where Flux$_i$ is the molar flux of gaseous species i, and s is the sticking coefficient.

The molar flux is calculated by the Hertz-Knudsen equation:

$$Flux_i = \frac{P_i}{\sqrt{2\pi M_i RT}}$$ (3.2.2)

where P$_i$ is the species i partial pressure, M$_i$ is its molecular mass, R is the ideal gas constant, and T is the temperature. The sticking coefficient depends on the surface coverage of surface sites which are available for the species i to deposit on. The surface coverage of each surface species k is denoted as θ, and the sum of all coverages of the surface sites, n in number, must be equal to unity.

$$s_i = s_{0,i} \cdot \theta_{av} \cdot e^{\frac{-E_{ads}}{k_b T}}$$ (3.2.3)

$$\sum_{k=1}^{n} \theta_k = 1$$ (3.2.4)

In equation (3.2.3), E$_{ads}$ is the activation energy for adsorption, k$_b$ is the Boltzmann constant, T is the temperature, s$_{0,i}$ is the initial sticking probability of species i, when the whole surface is available for deposition, and no energy barrier needs to be overcome i.e. θ$_{av}$=1. The s$_{0,i}$ value is treated as a model parameter. The surface coverage of each species is given by:

$$\theta_k = \sigma_k \frac{C_k}{C_{tot}}$$

(3.2.5)

where σ$_k$ is the site occupancy number, C$_k$ and C$_{tot}$ are the surface concentration of species k and the total concentration of surface sites, respectively, both in mol·m^{-2}. The site occupancy number describes how many surface sites are occupied by each surface species. In our case, C$_{tot}$ is the maximum number of OH groups that can be present on the surface, which depends on the surface temperature.

The reversible step of adsorption, i.e. the desorption of the adsorbed surface species k on the surface is modelled as a first order surface reaction:

$$R_{des,k} = k_{des,k} \cdot C_k$$

(3.2.6)

where R_{des} is the desorption rate of adsorbed surface species k, in mol·m^{-2}·s^{-1}., and $k_{des,k}$ is the desorption rate coefficient in s^{-1}., that is calculated using an Arrhenius expression:

$$k_{des,k} = A_{des,k} \cdot e^{\frac{-E_{des,k}}{k_b T}} \qquad (3.2.7)$$

where $A_{des,k}$ is the pre-exponential frequency factor, E_{des} is the activation energy for the desorption of a molecule, and k_b is the Boltzmann constant.

The surface reactions are treated the same way as desorption:

$$R_{r,k} = k_{r,k} \cdot C_k$$

(3.2.8)

$$k_{r,k} = A_{r,k} \cdot e^{\frac{-E_{r,k}}{k_b T}} \qquad (3.2.9)$$

By developing the mechanism described above using the described phenomena, we have 8 surface species, namely $OH_{(s)}$, $TMA(ads)_{(s)}$, $DMA_{(s)}$, $MMA_{(s)}$, $DMAH_2O_{(s)}$, $MMAOH_{(s)}$, $MMA(OH)H_2O_{(s)}$, $MMAH_2O_{(s)}$.

The implemented surface chemistry of TMA+H$_2$O ALD is summarized and schematically represented in Figure 3.5 below.
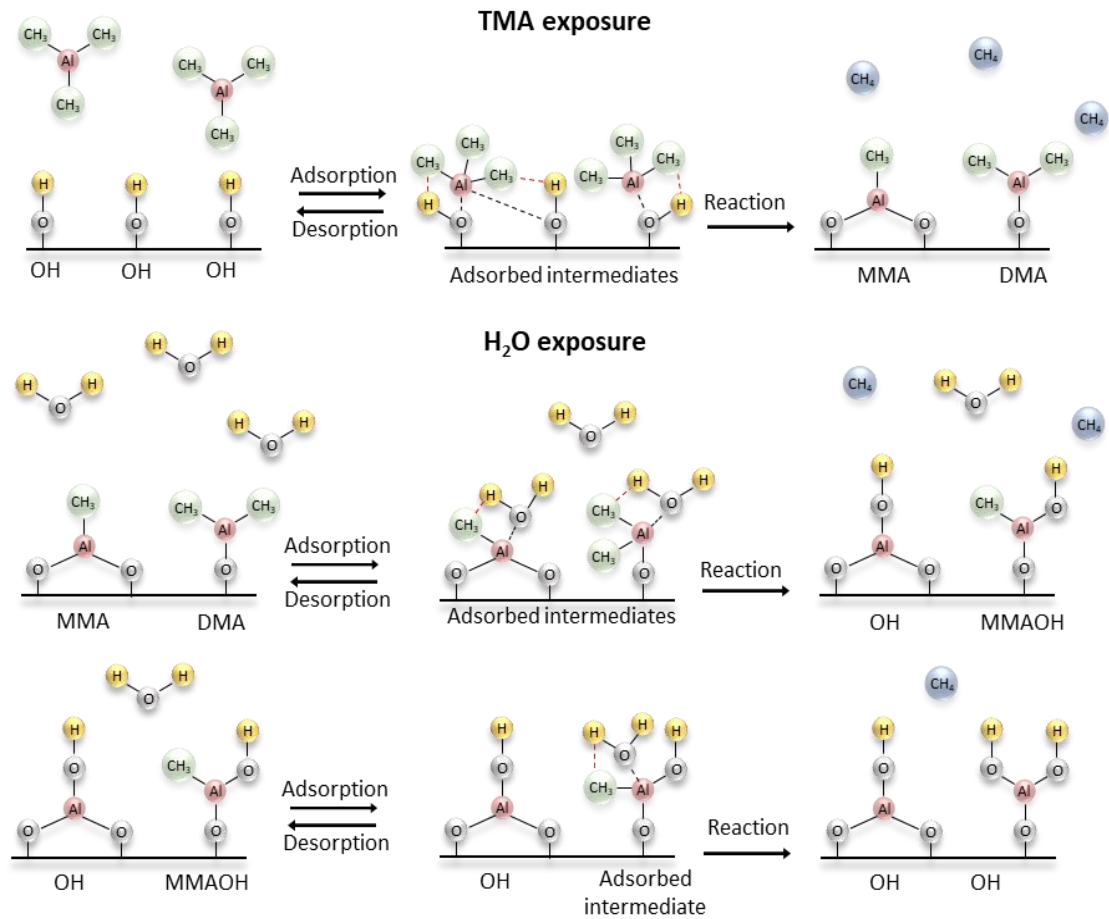
Figure 3.5. Schematic representation of the detailed surface chemistry of Al_2O_3 ALD

from TMA and H_2O

3.2.3. Surface chemistry model formulation

TMA pulse:

As presented in Figure 3.5, two TMA molecules react with 3 hydroxyl groups. In our model, each TMA molecule will adsorb on 1.5 OH groups. The site occupancy number of the $TMA_{(ads)}$ species will then be 1.5. When each adsorbed TMA molecule reacts, half a DMA and half a MMA species will be produced. The DMA and MMA species have a site occupancy number of 1 and 2, respectively. The surface species conservation equations are then:

$$\frac{\partial C_{OH}}{\partial t} = -1.5 \cdot (R_{ads,TMA} - R_{des,TMA(ads)}) \tag{3.2.10}$$

$$\frac{\partial C_{TMA(ads)}}{\partial t} = R_{ads,TMA} - R_{des,TMA(ads)} - R_{r,TMA(ads)} \tag{3.2.11}$$

$$\frac{\partial C_{DMA}}{\partial t} = 0.5 \cdot R_{r,TMA(ads)}$$

(3.2.12)

$$\frac{\partial C_{MMA}}{\partial t} = 0.5 \cdot R_{r,TMA(ads)} \tag{3.2.13}$$

H₂O Pulse:

As presented in Figure 3.5, the H_2O molecules adsorb on the methyl terminated surface. All species have a site occupancy number equal to 1, with the exception of adsorbed water on MMA (MMAH₂O), for which $\sigma_k=2$. The surface species conservation equations are then:

$$\frac{\partial C_{DMA}}{\partial t} = -(R_{ads,DMAH_2O} - R_{des,DMAH_2O}) \tag{3.2.14}$$

$$\frac{\partial C_{DMAH_2O}}{\partial t} = R_{ads,DMAH_2O} - R_{des,DMAH_2O} - R_{r,DMAH_2O} \tag{3.2.15}$$

$$\frac{\partial C_{MMAOH}}{\partial t} = R_{r,DMAH_2O} - (R_{ads,MMA(OH)H_2O} - R_{des,MMA(OH)H_2O})$$

(3.2.16)

$$\frac{\partial C_{MMA}}{\partial t} = -(R_{ads,MMAH_2O} - R_{des,MMAH_2O}) \tag{3.2.17}$$

$$\frac{\partial C_{MMA(OH)H_2O}}{\partial t} = R_{ads,MMA(OH)H_2O} - R_{des,MMA(OH)H_2O} - R_{r,MMA(OH)H_2O}$$

(3.2.18)

$$\frac{\partial C_{MMAH_2O}}{\partial t} = R_{ads,MMAH_2O} - R_{des,MMAH_2O} - R_{r,MMAH_2O}$$

(3.2.19)

$$\frac{\partial C_{OH}}{\partial t} = R_{r,MMAH_2O} + R_{r,DMAH_2O} + R_{r,MMA(OH)H_2O} \qquad (3.2.20)$$

As the product of the ALD process is the alumina thin film, species in the solid bulk of the film must be produced during the ALD cycle. The alumina solid bulk species is produced by the reaction of the adsorbed TMA on the surface, while the oxygen solid bulk species is produced by the reaction of adsorbed water on DMA, MMAOH and MMA.

$$\frac{\partial C_{O_{bulk}}}{\partial t} = R_{r,MMAH_2O} + R_{r,DMAH_2O} + R_{r,MMA(OH)H_2O}$$

(3.2.21)

$$\frac{\partial C_{Al_{bulk}}}{\partial t} = R_{r,TMA(ads)} \qquad (3.2.22)$$

The two bulk species react with each other to give an Al_2O_3 molecule:

$2\ Al_{bulk} + 3\ O_{bulk} \rightarrow Al_2O_3$ \hfill (R15)

The above set of equations is solved using Comsol Multiphysics®, which uses the FEM, using second order polynomial basis functions. The equations are solved in a coupled scheme with the CFD reactor model, as presented in section 3.2.5.

3.2.4. Computational parameters

For the surface chemistry model, values regarding the activation energies, reaction enthalpies, sticking coefficients, initial maximum concentration of surface

sites and pre-exponential factors must be set. The activation energies and reaction enthalpies are taken from literature (Widjaja and Musgrave, 2002), where are reported the computed energy barriers needed for the adsorbed TMA molecule to react according to (R3). These energy barriers are used as activation energies for the TMA surface reactions. In these studies, the adsorption step of the gaseous TMA molecule on an OH site is exothermic. This binding energy of the TMA is used in our study as the activation energy for desorption. The same is done for the water activation energies for surface reaction and desorption on DMA and MMAOH sites. We assume that the energies for the H_2O reaction and desorption on the MMA species are equal to those on DMA, calculated by Widjaja and Musgrave (Widjaja and Musgrave, 2002).

The initial surface is assumed to be covered by OH sites, i.e. $C_{init, OH} = C_{tot}$. The value of C_{tot} hence indicates the maximum number of OH groups that can be present on the surface. As the deposition of Al_2O_3 is dependent on the surface OH (Haukka and Root, 1994) site concentration, this maximum concentration must be carefully chosen. The maximum OH concentration depends on the temperature, as the OH groups are thermally unstable. Two neighbouring OH sites can react with each other, in order to form an oxygen bridge and desorb one molecule of H_2O (Puurunen, 2005)(Zhuravlev, 2000). In our study, the maximum OH concentration is implemented as a function of the surface temperature, based on data on silica surface reported by Haukka and Root (Haukka and Root, 1994). This data shows an almost linear relation between the OH concentration and the silica surface temperature, for the range of 200-560°C. This behaviour has also been reported in Dillon et al. on porous alumina (Dillon *et al.*, 1995). We assume that the same relation is also valid at lower temperatures down to 125°C, and we implement this linear relation to calculate the maximum OH concentration for each process temperature.

The pre-exponential factors were assumed to be equal to:

$$A = \frac{k_b T}{h_{pl}}$$

(3.2.24)

for all surface reactions and desorption, where k_b is the Boltzmann constant, T is the temperature, and h_{pl} is the Planck constant. With the above model assumptions and parameters, only the initial sticking coefficients need to be determined.

In our study, the sticking coefficient of H_2O was assumed to be equal on all three available sites (DMA, MMA, MMAOH). Hence the surface chemistry model has two fitting parameters ($s_{0,TMA}$, $s_{0,H2O}$).

The parameters used for our chemistry model are summarized in Table 3.1.

Parameter	Value
Adsorption activation energy	TMA: 0 eV, H_2O: 0 eV (Widjaja and Musgrave, 2002).
Desorption activation energy	TMA: 0.61 eV, H_2O on DMA and MMA: 0.57 eV, H_2O on MMAOH: 0.74 eV (Widjaja and Musgrave, 2002).
Reaction activation energy	TMA: 0.52 eV, H_2O on DMA and MMA: 0.7 eV, H_2O on MMAOH: 0.91 eV (Widjaja and Musgrave, 2002).
Reaction Enthalpy	TMA: 1.09 eV, H_2O on DMA and MMA: 0.91 eV, H_2O on MMAOH: 0.56 eV (Widjaja and Musgrave, 2002).
Maximum OH concentration	y = -2,1661E-08 ·T + 1,68935E-05 , in mol/m^2, T in K (Haukka and Root, 1994)
Sticking coefficient	$s_{0,TMA}$=0.004 (Fitted), $s_{0,H2O}$=0.014 (Fitted)

Table 3.1. Computational parameters for the surface chemistry model.

3.2.5. Coupling of the CFD and surface chemistry models

The coupling of the CFD model with the surface chemistry one is realized through the boundary conditions implemented on the substrate surface, for the species transport and heat transport equations. On the substrate surface, a species flux is implemented as a boundary condition for TMA, H_2O, and CH_4 species.

$$J_{TMA} = -(R_{ads,TMA} - R_{des,TMA(ads)}) \cdot M_{TMA} \tag{3.2.25}$$

$$J_{H_2O} = -\left(R_{ads,DMAH_2O} + R_{ads,MMA(OH)H_2O} + R_{ads,MMAH_2O} - R_{des,DMAH_2O} - R_{des,MMA(OH)H_2O} - R_{des,MMAH_2O}\right) \cdot M_{H_2O}$$
$$\tag{3.2.26}$$

$$J_{CH_4} = \left(1.5 \cdot R_{r,TMA(ads)} + R_{r,MMAH_2O} + R_{r,DMAH_2O} + R_{r,MMA(OH)H_2O}\right) \cdot M_{CH_4}$$
$$\tag{3.2.27}$$

where J (in kg/m^{2}s) is the species mass flux, with the positive sign denoting that the species is generated at the surface.

A heat flux is also generated on the substrate surface, corresponding to the enthalpies of the surface reactions:

$$Q = \sum_{m=1}^{r} R_m \cdot \Delta H_m, \tag{3.2.28}$$

where r is the total number of reactions, and ΔH is the reaction enthalpy.

3.3. Island growth model

The computational model for island growth is inspired from the works of Nilsen et al. and is based on geometric principles. The islands are assumed to be hemispherical due to the amorphous nature of the films, and grow on discrete nucleation sites (Nilsen *et al*, 2007). The nucleation sites are uniformly distributed, assumed to form a square surface lattice. Due to the uniform distribution, the analysis is simplified to only one of the squares of the lattice, by imposing periodic boundary conditions. Finally, the radius, r, of the islands after each ALD cycle is assumed to increase by a given amount, Δr.

The size of the squares from which the surface lattice is composed can be deduced from the nucleation density, N_d, which is the surface concentration of nucleation sites. If A is the area of the squares and b is their side length, then:

$$A = b^2 = \frac{1}{N_d}$$

(3.3.1)

$$b = \sqrt{\frac{1}{N_d}}$$

(3.3.2)

The thickness is computed as a mean thickness of the island over the whole square area A:

$$Thickness = \frac{Volume}{Area} = \frac{Volume}{A}$$

(3.3.3)

The island growth is divided into three regimes as illustrated in Figure 3.6. The first regime is the free island growth regime, where the islands grow in hemispheres

within the square lattice. The starting point for the second regime, island coalescence, is the moment when the island coalescence starts. The third regime, continuous film growth, starts when the whole surface is covered by the deposited film, hence when the film is continuous on the whole surface lattice. As the islands continue to grow and coalesce, this regime leads the ALD process to its steady state, where linear growth is obtained as a function of the ALD cycles.

The three regimes are taken into account in the geometric model. The critical island radius value for the transition from the first regime to the second is:

$$r_{c\ 1\to2} = \frac{b}{2}\ ,$$

(3.3.4)

While the critical value for the transition for the second regime to the third is:

$$r_{c\ 2\to3} = \frac{\sqrt{2}\cdot b}{2}$$

(3.3.5)

Hence, the volume of the islands, is computed as follows:

If r_n is the island radius at the nth cycle:

for $r_n \leq r_{c\ 1\to2}$

the island volume is equal to the volume of the hemisphere:

$$Volume = \frac{2\pi r_n^3}{3}$$

(3.3.6)

For $r_{c\ 1\to2} \leq r_n \leq r_{c\ 2\to3}$

the island volume is equal to the volume of the hemisphere, minus four times the equivalent volume of half of a top spherical cap.

$$Volume_{hemisphere} = \frac{2\pi r_n^3}{3} \qquad\qquad (3.3.7)$$

$$Volume_{cap} = \frac{\int_{\frac{b}{2}}^{rn} \pi \sqrt{r_n^2 - z^2}^{2} \, dz}{2} \qquad\qquad (3.3.8)$$

$$Volume = Volume_{hemisphere} - 4 \cdot Volume_{cap} \qquad\qquad (3.3.9)$$

For $r_n \geq r_{c\,2 \to 3}$

the film is continuous, and the island occupies the whole square. The volume of the island is:

$$Volume = \int_{-\frac{b}{2}}^{\frac{b}{2}} \int_{-\frac{b}{2}}^{\frac{b}{2}} \int_0^{\sqrt{r_n^2 - x^2 - y^2}} dz\,dx\,dy$$

(3.3.10)

Using the above model, the GPC evolution can be computed as a function of the number of ALD cycles, as follows:

$$GPC_n = Thickness_n - Thickness_{n-1} \qquad\qquad (3.3.11)$$

The island radius at the nth cycle is given by:

$$r_n = r_{n-1} + \Delta r, \qquad\qquad (3.3.12)$$

Where Δr is the radius increase during each ALD cycle. Its value is equal to the GPC at the steady ALD regime, where the thickness is a linear function of the ALD cycles. This value is easily accessible by experimental measurements, once the ALD regime is

reached. The initial island radius prior to ALD deposition, r_0, is a model parameter. Although it is usually taken as zero, it is nonetheless included for the generality of the model. Surface functionalization can lead to the presence of nucleation sites with a radius of some number of Å.
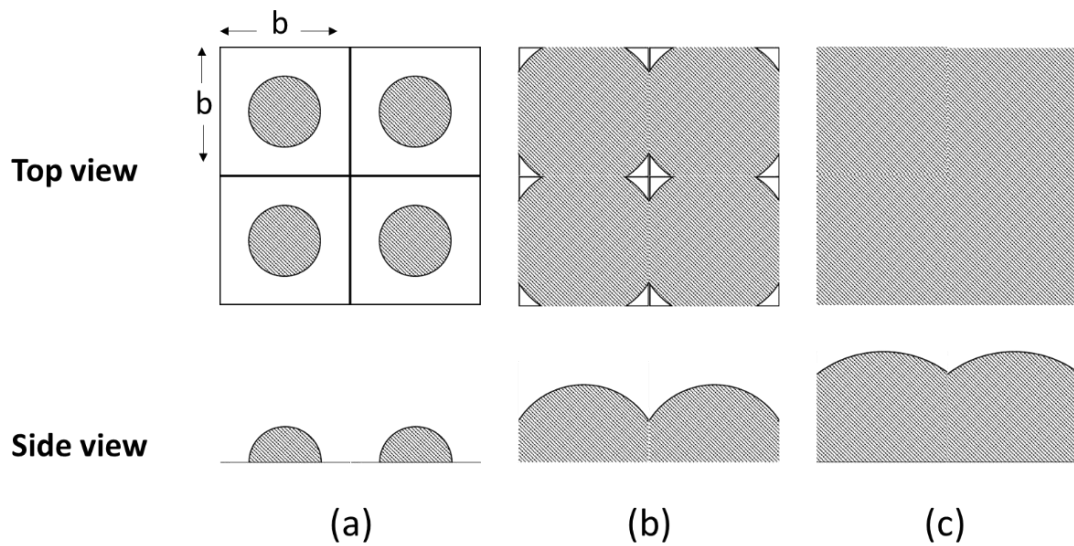
Figure 3.6. Top and side view of the different regimes: a) free island growth b) island coalescence c) continuous film growth

The model has two fitting parameters, which are the nucleation density, N_d and the initial radius of the islands, r_0. The value of r_0 represents the apparent radius of a surface nucleation site. As nucleation sites are usually surface defect sites, r_0 varies from zero to some number of Å. Once this value is set, by tuning the values of N_d, an estimation of the surface concentration of nucleation sites can be derived, by fitting the model results to experimental data.

The above set of equations is solved using Matlab®, and the resulting thickness is obtained.

3.4. Nano-scale chemistry model

The nano-scale model is stochastic, and is based on the kinetic Monte Carlo (kMC) algorithm, that has previously been used for multi-scale computational approaches on CVD processes (Cavallotti *et al.,* 2005)(Crose *et al.,* 2015)(Aviziotis *et al.,*2016). In this thesis, a lattice kMC approach is used, studying the evolution of a surface. The film deposition is modelled as a Markov process of events (Battaile and Srolovitz, 2002). The surface state evolves through known transition rates, which express an event. In a Markov process, the probability of an event under which a system can transition through different states is dependent only on the state of the system, and not on the previous events that have occurred. After each event, the surface has a new state, with new event probabilities.

The two main ingredients of a kMC algorithm are hence the identification of the possible surface events and the determination of the rates at which these events can occur. Time steps are inserted as the time period between two sequential events, and are computed by the total rate of all events. In this thesis, the events taking place are adsorption, desorption, and surface reactions. The computational lattice, the considered events, the kMC algorithm and the coupling to the reactor model are presented in the following sections.

3.4.1. Computational lattice

The computational lattice used is a one-dimensional solid-on-solid surface lattice, similar to the one used by Crose *et al.,* for the CVD of Si (Crose *et al.,* 2015). The number of sites N is hence the size of the surface lattice, which is a 1xN size matrix. As an approach to the surface chemistry, the model is coarse grained. Coarse grained models use pack of atoms as surface sites, instead of modelling the actual atomic structure of the surface (in this case Si(100)). Hence, each site in the surface lattice represents an adsorption site. In this thesis, two different coarse graining and surface chemistry schemes have been used for the nano-scale model.

The first coarse graining scheme, hereafter called coarse graining scheme A, is a simplified chemistry scheme. As presented in Section 3.2 of the present chapter, TMA can adsorb and react with either one or two surface OH groups, forming DMA and MMA species, respectively. Subsequently, two H_2O molecules adsorb and react with the two DMA species, while one H_2O molecule is needed for the hydroxylation of MMA. In order to satisfy reaction R1 and produce stoichiometric Al_2O_3, the DMA and MMA molecules need to be produced in equal proportions. Hence, 2 TMA species need 3 OH species (1:1.5 TMA:OH ratio) to form one DMA and one MMA species.. With the use of this hypothesis, the coarse graining scheme A assumes that the surface lattice sites represent 1.5 OH groups, where one TMA is going to deposit. In turn the product of the surface reaction is a pseudo-DMA group, which can then be hydroxylated by two H_2O speciess. Specifically, the pseudo-DMA group forms a pseudo-MMAOH group after the reaction with the first H_2O group, while a reaction with a second H_2O molecule reproduces the starting surface. As the maximum surface concentration of OH groups is known as a function of temperature (Haukka and Root, 1994), the surface lattice sites can be defined to represent a surface:

$$A_{site} = \frac{1.5}{C_{max,OH}} \qquad\qquad\qquad (3.4.1)$$

where $C_{max, OH}$ is the maximum surface concentration of OH groups, in OH/ nm^2.

Using this coarse graining scheme, the GPC, as well as the roughness evolution, can be estimated. Although this approach needs many improvements, it can make quantitative predictions that can be compared to experimental measurements.

The second coarse graining scheme, hereafter called coarse graining scheme B, is a more detailed chemistry scheme. In this scheme, the dissociation of TMA to DMA or MMA is only dictated by the neighboring OH groups, while the proportion of DMA and MMA species is not imposed, but is rather obtained as a result. Using this model, the stoichiometry of the deposited films can be computed, as well as the proportion between surface species. In this scheme, the surface sites represent the surface occupied by an OH group:

$$A_{site} = \frac{1}{C_{max,OH}} \qquad\qquad\qquad (3.4.2)$$

where $C_{max, OH}$ is the maximum surface concentration of OH groups (Haukka and Root, 1994), in OH/ nm^2.

Although this definition is logical, the problems arise for the comparison of the computed GPC with experimental measurements, due to the fact that the chemistry is dependent on the surface topography, as the deposition of MMA is dependent on the existence or not of neighboring OH groups on the surface, during the TMA exposure. The number of OH groups created during the subsequent H$_2$O exposure is in turn dependent on the number of DMA and MMA surface sites deposited. If the surface is initially assumed to be completely covered with OH groups, the evolution of the film growth will affect the topography of sites, and hence the surface chemistry, until the

topography stabilizes, after a certain amount of simulated cycles. All the above will be discussed in the next sections.

3.4.2. The kMC algorithm

As previously discussed, the surface events simulated by the kMC algorithm are modelled as Markov processes, using the rate of each event as a transition probability per unit time. Three events are taken into account: adsorption, desorption and surface reaction, as presented in section 3.2.

The adsorption rate on an adsorption site is computed as:

$$R_{ads} = s \quad \cdot Flux \quad \cdot A_{site} \tag{3.4.3}$$

Where the species flux is taken from the reactor scale model, and is calculated by equation 3.2.1. The sticking coefficient value is fitted. The reaction and desorption rates for an adsorbed species on the surface are computed as first order Arrhenius expressions:

$$R_r = \frac{k_b T}{h} \cdot e^{\frac{-E_r}{k_b T}} \tag{3.4.4}$$

$$R_{des} = \frac{k_b T}{h} \cdot e^{\frac{-E_{des}}{k_b T}} \tag{3.4.5}$$

Where k_b is the Boltzmann constant, h is the Planck constant, while E_r and E_{des} are the reaction and desorption activation energies respectively. These activation energies are taken from Widjaja and Musgrave, as in the surface chemistry model (Widjaja and Musgrave, 2002). The total rate of events, for each separate reactant exposure is calculated as:

$$R_{tot} = \sum_{i=1}^{k} R_i N_i \qquad (3.4.6)$$

Where k is the total number of events, R_i is the rate of event i, and N_i is the number of surface sites where event i can take place. The probability of each event is then calculated as:

$$p_i = \frac{R_i N_i}{R_{tot}} \qquad (3.4.7)$$

While the sum of all probabilities is equal to unity.

$$\sum_{i=1}^{k} p_i = 1 \qquad (3.4.8)$$

The kMC algorithm proceeds as follows. Initially, the surface is assumed to be flat and fully covered by OH adsorption sites. The transition probabilities are calculated *a priori* and every kMC trial leads to the realization of an event. This realization is done through the generation of random numbers. A random number λ_1 in the interval (0,1] is generated. The event n for which $\sum_{i=1}^{n-1} p_i < \lambda_1 \leq \sum_{i=1}^{n} p_i$ is the event selected. A second number λ_2 is selected in the interval (0,N_n], where N_n is the number of sites where event n can occur. From this procedure, the surface site on which the event will take place is selected. The event is implemented on the selected site, and the surface is updated. The new total reaction rate and the respective probabilities computed, and the time is renewed using a mean time step:

$$\Delta t = \frac{1}{R_{tot}} \qquad (3.4.9)$$

The process is then repeated, until the simulation time is equal to the duration of the reactant exposure time.

The detailed procedure for each coarse graining scheme, as presented in section 3.4.1, is described below.

Coarse graining scheme A

As described in the previous section, in this scheme the free surface sites represent 1.5 OH groups. During the TMA exposure, TMA adsorbs on the free surface site. From then on, it can either desorb or proceed with a forward reaction, leading to the formation of (pseudo) DMA species, which occupies one surface site. In the same time, a bulk Al atom is assumed to be deposited. During the subsequent H_2O exposure, the H_2O are assumed to adsorb on DMA, from where they can either desorb or proceed with the surface reaction, producing MMAOH. A second H_2O follows the same procedure, leading to the formation of a free surface site representing 1.5 OH, thus regenerating the surface. The thickness h at each is calculated assuming Al_2O_3 stoichiometry, as follows:

$$h = \frac{n_{Al} \cdot M_{Al2O3}}{N \cdot A_{site} \cdot N_{av} \cdot \rho},$$

(3.4.10)

Where n_{Al} is the total number of bulk aluminum deposited, N is the total number of the lattice sites, A_{site} is the surface represented by each surface lattice, N_{av} is the Avogadro number, M_{Al2O3} is the molecular weight of Al_2O_3, and ρ is the density of Al_2O_3, taken at 3500 kg/m^3 (Ott *et al.*, 1997).

A local thickness h_i on a lattice site i can be computed as follows:

$$h_i = \frac{n_{Al,i} \cdot M_{Al2O3}}{A_{site} \cdot N_{av} \cdot \rho},$$

(3.4.11)

Where $n_{Al,I}$ is the number of bulk aluminum deposited at each surface site. In this way, the root mean squared (RMS) roughness can be calculated:

$$RMS = \sqrt{\frac{1}{N} \cdot \sum_{i=1}^{N}(h_i - h_{mean})^2},$$

(3.4.12)

Where h_{mean} is the mean thickness on the surface.

Coarse graining scheme B

As previously described, in this scheme the free surface sites represent an OH group. The surface is initially assumed to be fully covered by OH sites. During the TMA exposure, TMA adsorbs on a free surface site. If a neighboring surface site is occupied by a surface OH site, then the TMA molecule is considered to occupy this site two. Hence an adsorbed TMA molecule can occupy two neighboring sites. If both of the neighbouring sites are covered by OH, then one of those sites is randomly selected. From then on, the adsorbed TMA can either desorb or proceed with a forward reaction. This reaction leads to the formation of DMA species (if TMA is adsorbed on one OH group), or MMA species (if TMA is adsorbed on two surface sites), which occupy one and two surface sites, respectively. In the same time, a bulk Al atom is assumed to be deposited.

During the subsequent H_2O exposure, the H_2O are assumed to adsorb on DMA, and MMA from where they can either desorb or proceed with the surface reaction. The H_2O reaction with DMA produces a surface OH group and a surface MMAOH group. A second H_2O can adsorb on MMAOH, following the same procedure, resulting to the formation of a second OH surface group. The reaction of H_2O with MMA leads to the formation of a surface OH group. For each H_2O reaction, a bulk O atom is assumed to be deposited. The bulk species are assumed to form Al_2O_3, with the following reaction:

$2\ Al_{(b)} + 3\ O_{(b)} \rightarrow Al_2O_{3(b)}$
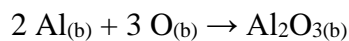
The thickness h at each is calculated assuming Al_2O_3 stoichiometry, as follows:

$$h = \frac{n_{Al2O3} \cdot M_{Al2O3}}{N \cdot A_{site} \cdot N_{av} \cdot \rho},$$

(3.4.13)

3.4.3. Coupling to the reactor scale model

Apart from setting the temperature value, the nano-scale kMC model is coupled with the reactor scale model through the reactant flux, used for the calculation of the adsorption rate, as shown in equation 3.4.3. However, as the adsorption rate is also used to calculate the time step, the kMC algorithm is highly dependent on the species flux taken from the reactor model.

In the actual case, the substrate surface is exposed to reactant pulses. This means that at the beginning of the respective reactant exposure step, the reactant flux will be very low, to a value approaching zero. This is also the case at the end of the reactant exposure. As adsorption is the only possible event when the kMC algorithm is initiated (surface fully covered by OH groups), the time step is inversely proportional to the adsorption rate (eq. 3.4.9), and hence the reactant flux. Hence, if the reactant flux is low, the time step will be very high and will overcome the total exposure time.

For this reason, the reactant flux is averaged over the reactant exposure duration. The time integral of the reactant flux is calculated, yielding the total reactant exposure time of the substrate. This value is then divided by the exposure time, yielding an average reactant flux over the exposure time. This process is schematically represented in Figure 3.7.
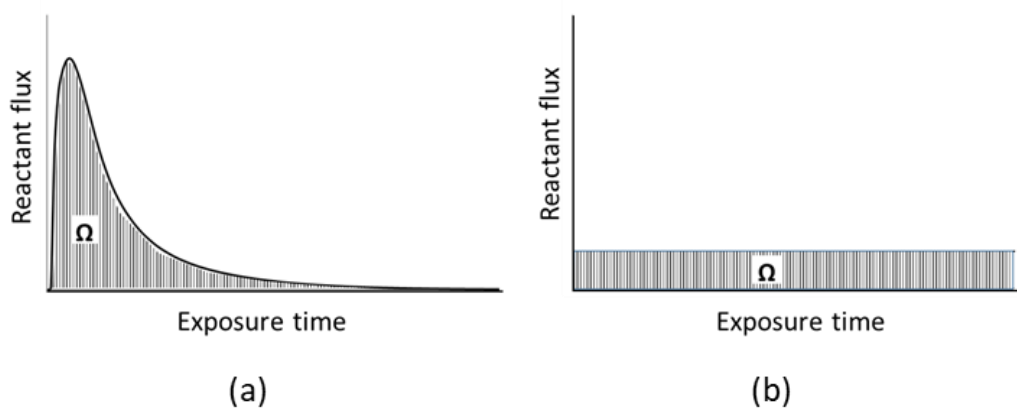
Figure 3.7. Reactant flux: a) as computed from the reactor scale model, b) as implemented in the nano-scale kMC model. The area Ω is the total substrate exposure to the reactant, equal for both cases.

3.4.4. Computational aspects of the simulations

In this section, the computational aspects of the nano-scale model are presented, for the two coarse graining schemes.

Coarse graining scheme A

In this scheme, each OH group on the surface represents 1.5 OH surface species, as described in section 3.4.2. In order to monitor the solutions of the kMC algorithm for the coarse graining scheme A, the number of OH groups on the surface at the end of each ALD cycle, are plotted as a function of the ALD cycles, in Figure 3.8. For the results in Figure 3.8, the total number of surface sites was set to 100, and the simulation is for an ALD temperature of 200°C (simulated experiment 8, in Table 2.1).

Figure 3.8. OH groups on the surface after each ALD cycle using a lattice size of 100 surface sites: kMC model predictions.

Figure 3.8 shows that after the first ALD cycle, the OH groups after each cycle stay more or less the same, as expected during the linear ALD regime. The surface is regenerated after each ALD cycle. However, due to the stochastic nature of the model, the OH groups as a function of cycles have a discrepancy around the predicted average value. This discrepancy is 3.9%. This discrepancy is dependent on the lattice size, i.e. the total number of surface sites. The number of OH groups after the end of each cycle, using different lattice dimensions, are plotted in Figure 3.9a. The respective average discrepancy around the mean value as a function of the lattice size is plotted in Figure 3.9b.
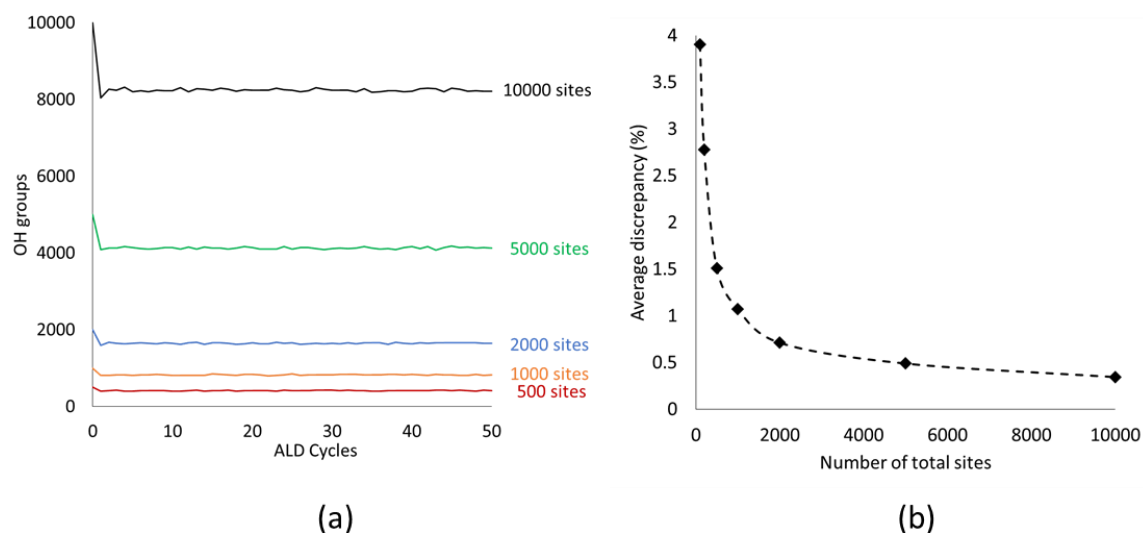
Figure 3.9. a) Number of OH groups on the surface after each ALD cycle, using different lattice dimensions, b) Average discrepancy of the computed OH groups around the mean value as a function of the lattice dimension.

Results of Figure 3.9 show that, by increasing the lattice dimension, i.e. the total number of surface sites, the averaged discrepancy is decreased. For this reason, for subsequent simulations, a lattice of 10,000 sites is selected, which lead to an average discrepancy of <0.5% (Figure 3.9b).

Coarse graining scheme B

In this scheme, each surface site represents one OH species. For the coarse graining scheme B, a lattice size of 10,000 sites is selected, as for the coarse graining scheme A. In order to investigate the behavior of this model, it is first ran assuming full reaction activation: no species are left unreacted on the surface and full surface coverage is obtained. The evolution of the number of OH species on the surface after each ALD cycle is shown in Figure 3.10.
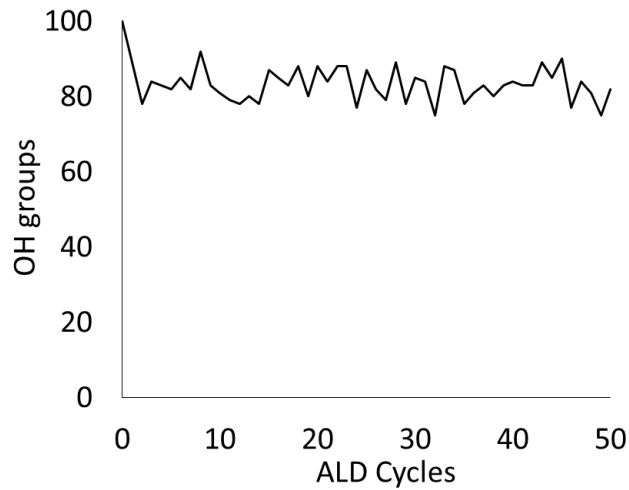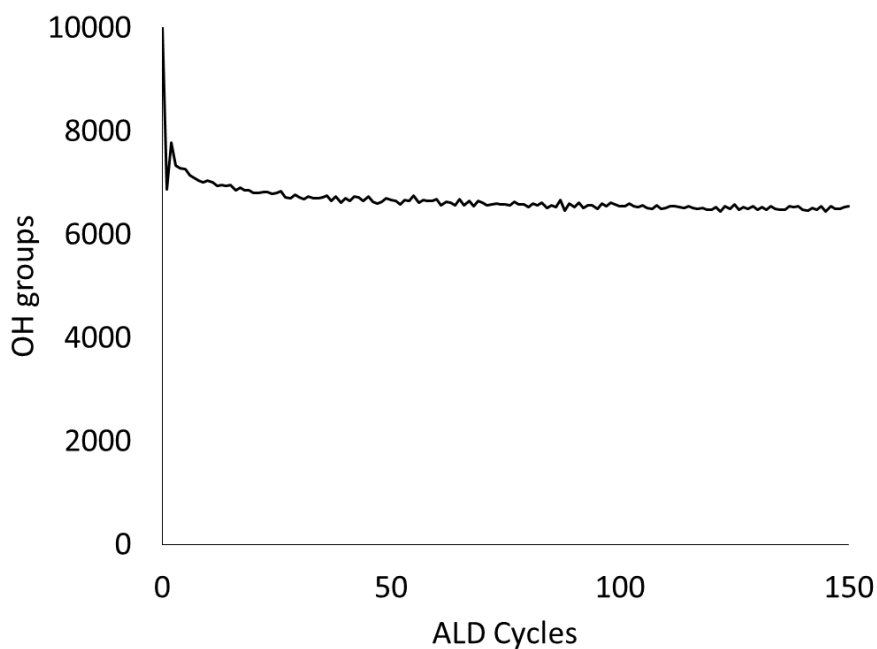
Figure 3.10. Number of OH groups on the surface after each ALD cycle, using a

lattice size of 10,000 surface sites: kMC model predictions.

Figure 3.10 shows that, even though full surface coverage is assumed during

each reactant exposure, the number of OH groups on the surface reach a value where

they are regenerated after each cycle, which is lower than the initial number of OH

groups (10,000 surface groups). This value is close to 65% (~6500) of the initial value.

This happens due to the chemistry scheme and the initial condition assumed for the

surface lattice. The surface is assumed to be fully covered by OH, where TMA can

adsorb on two neighboring OH groups. Hence, during the first cycle, more MMA

species will be deposited after the TMA exposure, which occupy two surface sites and

yield one OH group, after the reaction with H_2O. In the second cycle, due to the surface

topography of OH groups, more DMA species will be deposited. This evolution of the

surface species leads to a surface topography of OH groups, where MMA and DMA

species are deposited in equal proportions, thus regenerating the same number of OH

groups after each cycle. The evolution of the surface MMA and DMA species deposited after the TMA exposure of each ALD cycle, is shown in Figure 3.11.

Figure 3.11 shows that the evolution of the surface topography leads to the deposition of MMA and DMA species in equal proportions (with a discrepancy associated with the stochastic nature of the kMC method), and the state of the surface is regenerated after each ALD cycle, once a number of ALD cycles (~50 cycles in the case of results of Figure 3.10) is simulated, as shown in Figure 3.10.
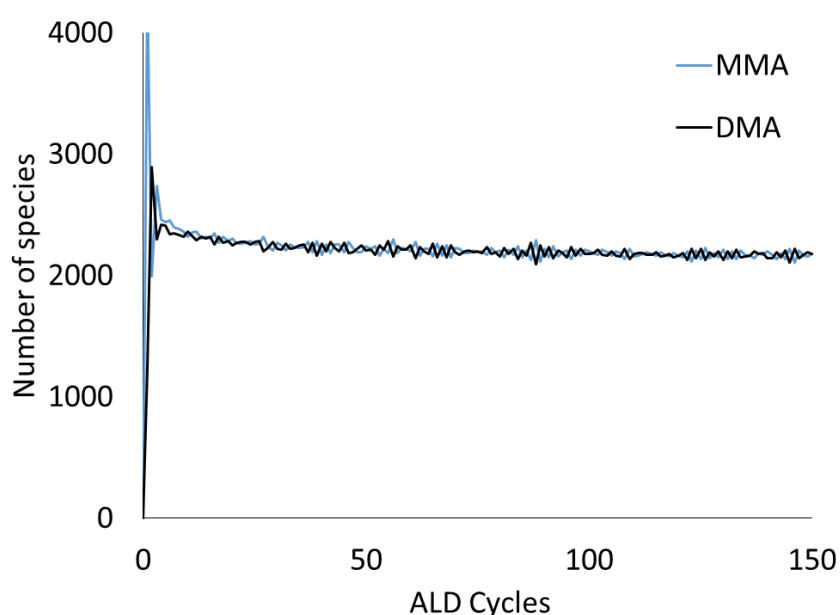
Figure 3.11. Evolution of the surface MMA and DMA species number after the TMA exposure, as a function of the ALD cycles: kMC model predictions.

In order to compare the results predicted by the kMC model with the coarse graining scheme B, the above model behavior must be taken into account for the definition of the surface lattice. With the assumption of full coverage of species, the results of Figure 3.10 show the maximum number of OH species on the lattice surface that can be predicted by the coarse graining scheme B. This number, as seen by Figure 3.10, is ~ 65% of the initial value. Hence, in order to compare the predictions of the

kMC model with the coarse graining scheme B to the experimental measurements, the surface of each surface site of the lattice must be corrected:

$$A_{site} = \frac{0.65}{c_{max,OH}},$$

(3.4.14)

Where $c_{max,OH}$ is the maximum OH concentration on the surface, taken from Haukka and Root (Haukka and Root, 1994).

Summary – Conclusions

In this chapter, the different computational models developed for the simulation of the ALD process are presented. The computational strategies and the coupling between the different models are discussed.

For the investigation of the transport phenomena inside the ALD system and the study of the process dynamics, two coupled three dimensional CFD models are used, for the reactant feeding system and the reactor chamber, respectively. The governing equations include the conservation of mass, momentum, energy and chemical species. These equations constitute a set of partial differential equation, which are discretized and solved using the finite elements method.

A wafer scale surface chemistry model is used to simulate the reactions on the wafer surface. This model is coupled to the reactor CFD model through the interchange of computational information between the two models, by setting appropriate boundary conditions on the wafer surface. This coupling between the two models allows to investigate the effect of process conditions on the chemical reactions, the film deposition rate, as well as on film properties, such as the deposited film uniformity.

In order to study the deposition evolution during the initial ALD cycles, an island growth model, based on geometric principles, is developed. This model does not take surface chemistry mechanisms into account. It is fed by the combined reactor CFD and wafer scale surface chemistry model, and is used to study the island formation, growth and coalescence, until the formation of a continuous film.

The surface chemistry at the nanoscale is studied using a stochastic lattice-kMC nano-scale chemistry model, dealing with the detailed aspects of chemistry. This model is fed by the reactor CFD model. Two coarse graining schemes for the surface lattice and the chemistry mechanisms are used, in order to reduce computational effort. This model is used to investigate the surface mechanisms in more detail, as well as to extract predictions for the film properties at the nano-scale, such as surface roughness.

Chapter 4: ALD reactor dynamics

In this chapter, the dynamics of the reactor are investigated, without the contributions of surface reactions. As described in Chapter 3, significant difficulties arise for the modelling of the ALD system. The computational strategy introduced in Chapter 3 for the ALD system simulation has to be validated. The validation of the turbo-molecular vacuum pump, as well as the fluid flow and temperature field inside the ALD reactor during the Ar flow are presented in section 4.1 and 4.2, respectively. The results of the feeding system simulations are presented in section 4.3. The coupling of the reactor and feeding system models, as well as the distribution of reactants during the exposure steps, are shown in section 4.4. Finally, the purging steps of the ALD process are presented in section 4.5. The results presented in this chapter have been the subject of a scientific journal article, published in Chemical Engineering Research and Design (Gakis *et al.*, 2018).

4.1. Vacuum system

4.1.1. Pirani gauge

As a first step, the reactor's outlet pressure was monitored via the Pirani gauge during various ALD cycles, as deposition took place. A typical resulting pressure evolution with time is shown in Figure 4.1, for process conditions of experiment 16 of Table 2.1. The pressure peaks correspond to the TMA and H_2O reactant pulses. As shown by Figure 4.1, the base pressure of the process ie. the system pressure during the purge step of the ALD cycle, is set at 0.05 Torr, measured via the Pirani gauge. This same pressure measured by the capacitance manometer was 0.072 Torr. As presented in Chapter 3, the starting point for the calculations is the base pressure of the ALD

process, measured via the Pirani gauge, which is a gas dependent gauge that measures the pressure of a gas through its thermal conductivity. In order to compare the CFD model predictions with the experimental measurements, the reading of the Pirani gauge is simulated using equation 3.1.23.
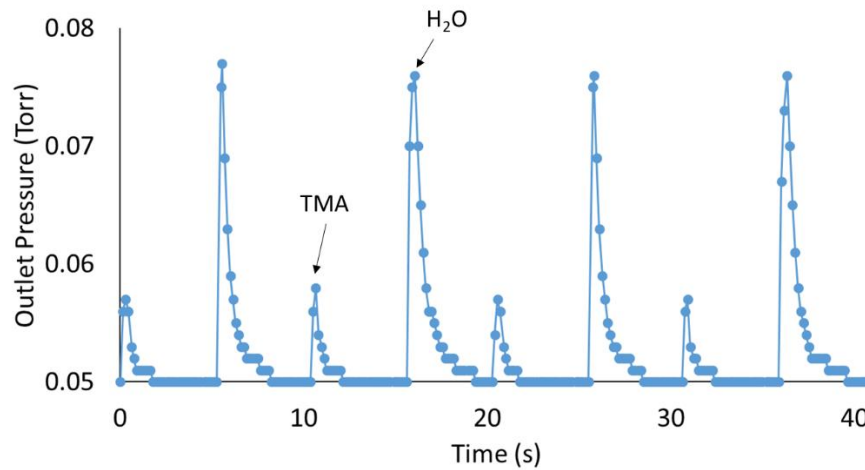
Figure 4.1. Outlet pressure evolution with time during the ALD process for experiment 16

To validate this approach for the Ar flow, the reactor outlet pressure was measured, for a varying Ar inlet, using a constant butterfly valve opening at the outlet (different valve opening than for ALD deposition). Both the Pirani gauge and the capacitance manometer were active during these measurements, and the relation between their readings is linear as shown in Figure 4.2. The capacitance manometer shows the true pressure inside the chamber, while the Pirani gauge reading needs to be multiplied by a correction factor, equal to the slope of the line that connects the measured points. The slope of the line is equal to 1.4203, a value very close to the ratio of the thermal conductivities of nitrogen and Ar (1.4401), as computed using the kinetic gas theory at the outlet temperature, ie. 270°C.
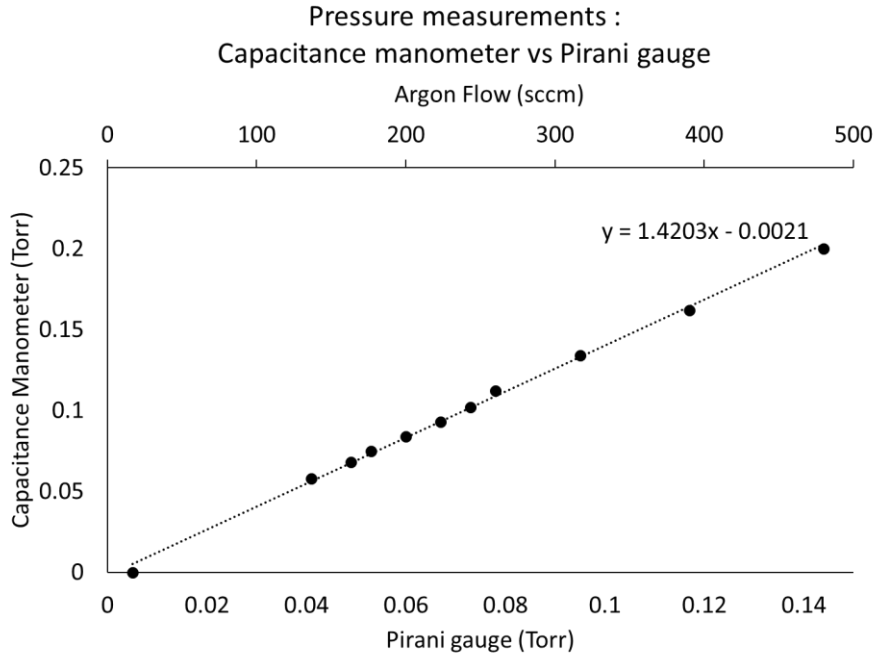
Figure 4.2. Comparison between experimental pressure readings by the capacitance manometer and the Pirani gauge

The above analysis in Figure 4.2 shows that indeed the relation between the Pirani and capacitance manometer experimental measurements is linear. Furthermore, this linear relation is close to the one obtained using equation 3.1.23, which assumes a linear relation between the Pirani gauge reading and ratio of the thermal conductivites of the gas mixture and nitrogen.. Although the above assumption is not yet validated for H_2O or TMA (isolation valve could not be open during deposition), experimental measurements of Figure 4.2 show that it can be used for the Ar flow. However, we use the same assumption for the reactants, as it is the only way to compare the outlet measurements with the model predictions.

4.1.2. Vacuum pump

As presented in Chapter 3, the turbo-molecular vacuum pump connected to the outlet of the ALD reactor has a steady volumetric flow rate for a wide range of working pressures. This technical aspect of the pump is used for the computational strategy of the present study, as presented in Chapter 3.

In order to validate the above strategy, the following procedure was followed. The substrate temperature was set to 300°C, the walls temperature to 270°C, the Ar flow rates were set to the flows of the ALD process (180 sccm total), and by regulating the butterfly valve, the base pressure was set to 0.05 Torr, as measured by the Pirani gauge (0.072 Torr measured by the capacitance manometer). Then, the Ar flows were altered, in order to monitor the outlet pressure evolution as a function of the total inlet Ar flow.

In the CFD model, the Ar inlet flows were set as during the ALD process, and the outlet pressure was set to 0.072 Torr. Once the solution was obtained, the computed volumetric flow rate at the reactor outlet was $Q_{out} = 57.1255 \frac{L}{s}$. This volumetric flow rate was set as an outlet boundary condition instead of the initial outlet pressure. The Ar flows were changed the same as experimental ones. The obtained outlet pressure from the computed solution was then converted using equation 3.1.23. The comparison between the model predictions and the experimental measurements is shown in Figure 4.3.
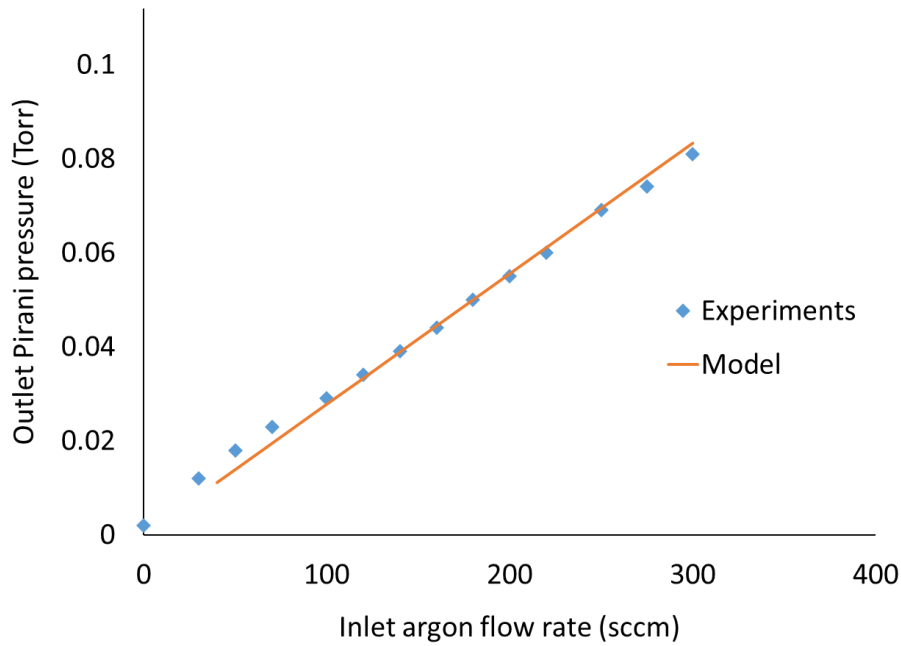
Figure 4.3. Outlet pressure vs Inlet Ar flow rate: Model predictions and experimental

measurements

The good agreement between measurements and model predictions with the conversion of equation 3.1.23 validates the treatment of the vacuum pump operation by the model. The resulting linear relation between the inlet Ar flow and the outlet pressure is as expected, considering that the volumetric flow rate of the pump remains constant within the typical operating pressure range. From the results of Figure 4.3, the gauge pressure conversion in equation 3.1.23 is also validated for the case of pure Ar flow. Once the computational approach for the simulation of the vacuum system has been validated, the analysis of the Ar flow inside the ALD reactor chamber can be performed. The results of this analysis are presented in the next section.

4.2. Continuous Ar flow

4.2.1. Flow field

The continuous Ar flow inside the reactor was first simulated. The inlet Ar flows were set (100 sccm Top inlet, 30 sccm Side inlet, 50 sccm Loading door inlet), along with the process temperatures and the outlet pressure was set to 0.072 Torr, as described in the previous section. The resulting flow field for the temperatures of experiment 16 of Table 2.1 is presented in Figure 4.4. The arrows length is uniform, showing the direction of the flow.

Figure 4.4. Calculated flow field for the continuous Ar flow for experiment 16

Figure 4.4 shows that a plug flow develops inside the reactor chamber and close to the substrate. No recirculation takes place, and the gas flows uniformly around the substrate. An interesting result is the effect of the Ar flow entering from the loading door inlet. As Figure 4.4 shows, the loading door flow is suppressed by the top inlet Ar

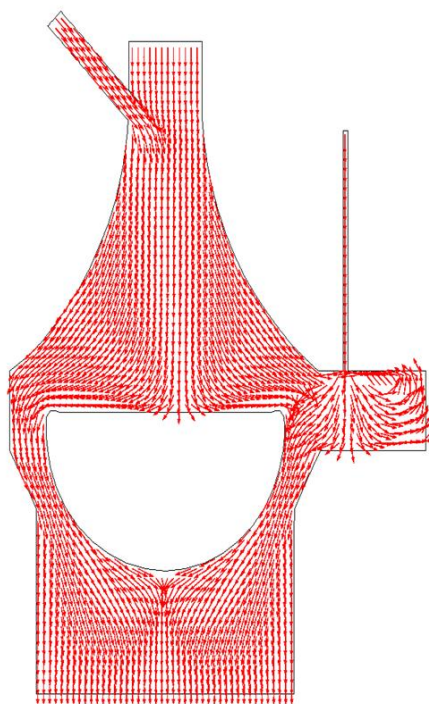flow, near the right edge of the substrate surface. If the top inlet flow rate of Ar is not high enough, the loading door Ar flow will affect the flow and hence the species distribution on the substrate surface, that could lead to non-uniform deposition.

To study this effect, the top inlet flow was varied, while keeping the side and loading door inlets constant. For this analysis, the computed volumetric flow of $Q_{out} = 57.1255 \frac{L}{s}$ was implemented as an outlet condition, as described in the computational strategy in Chapter 3, and the previous solutions were used as an initial solution for subsequent computations. The results of this analysis are shown in Figure 4.5 which highlights the region of interest.

It appears that the relation between the top and loading door inlet flows plays a major role on the purging homogeneity inside the reactor. If the top Ar inlet flow is not high enough, the purging Ar flow coming from the loading door inlet affects the region above the substrate surface. Increasing the top inlet flow leads to the suppression of this effect, and leads to uniform purging of the region above the substrate surface.

If the inlet flows are not optimized, the side of the substrate exposed to the loading door flow will be purged more efficiently than the rest of the substrate surface. This non-uniform purge of the substrate surface can lead to non-uniform reactant distribution, and hence non-uniform deposition. The flows used during the ALD experiments (100 sccm Top Ar flow) are optimized in order to ensure the purging uniformity.
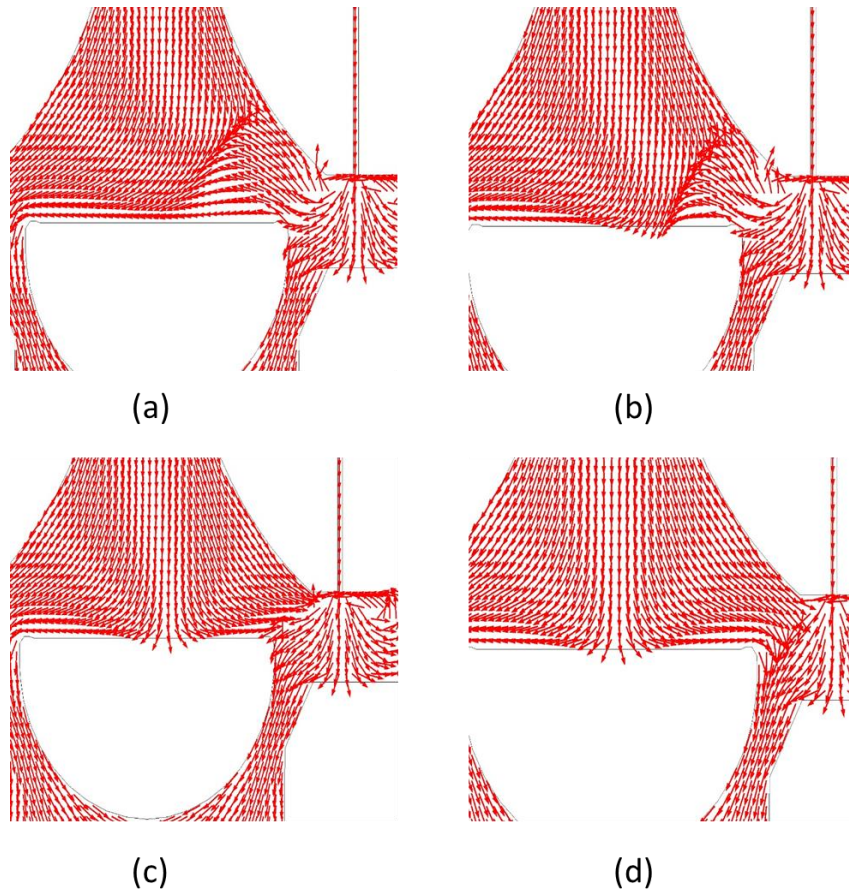
Figure 4.5. Flow field results for a varying top inlet Ar flow: a) 10 sccm, b) 30 sccm, c) 70 sccm, d) 200 sccm.

4.2.2. Temperature field

The calculated temperature field in the reactor chamber and the temperature profile on the substrate are shown in Figure 4.6, for the process recipe of experiment 16.
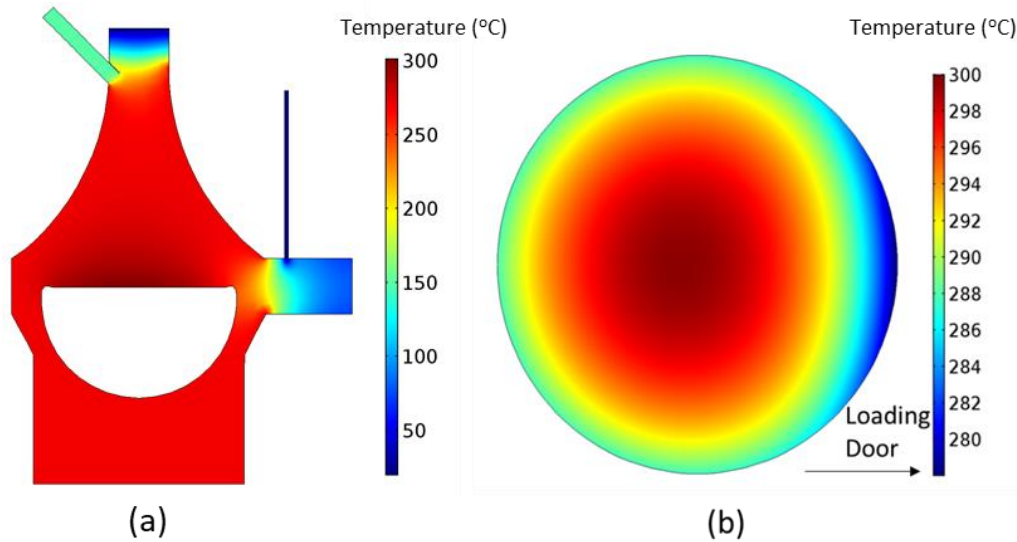
Figure 4.6. a) Temperature field inside the reactor chamber, b) Temperature profile on the substrate surface for the substrate center at 300°C.

Figure 4.6a shows that the gas is quite isothermal into the reactor with a temperature close to that of the walls (270°C), except near the inlet zones where it is colder and near the substrate where it is hotter (300°C). The substrate is not isothermal (Figure 4.6b), due to the cooling provided by the gas coming from the vicinity of the reactor walls. The average temperature on the substrate perimeter is equal to 289°C. Results also show the effect of the loading door purge. The Ar flow entering the reactor chamber at 20°C lowers the temperature in the area close the loading door (Figure 6a) and at the nearby substrate side (at 278°C). The temperature difference between the substrate center and the loading door side reaches 22°C.

The temperature profile on the substrate for the process recipes at lower temperatures, namely at 150°C and 200°C, are shown in Figure 4.7. For these process recipes, the substrate walls temperature is equal to the substrate center temperature.
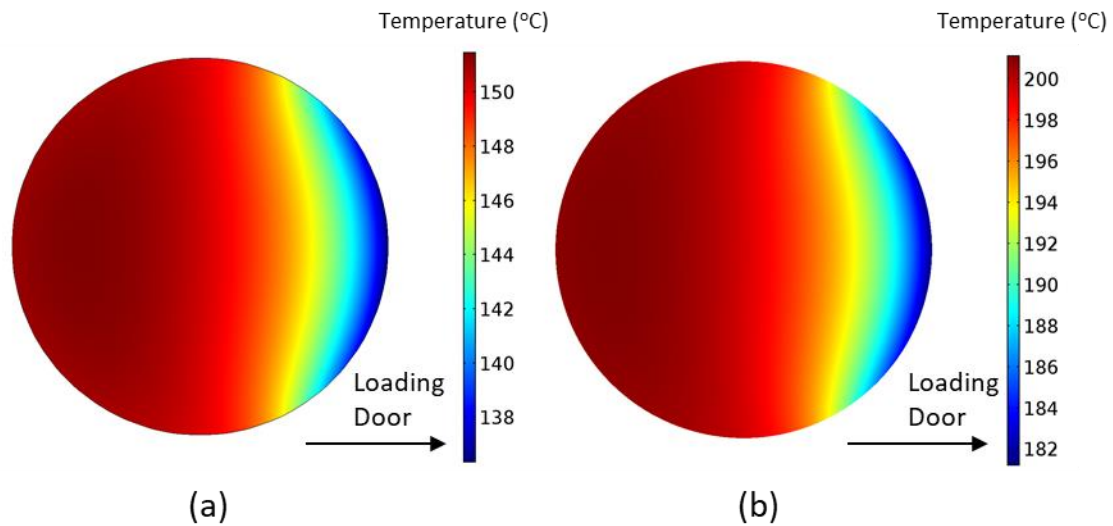
Figure 4.7. Calculated temperature profiles on the substrate for the process

recipe at: a) 150°C, b) 200°C

The results of Figure 4.7 show a gradual temperature decrease, moving from the substrate left part towards the loading door of the reactor. This temperature difference can impact the deposition process in various ways. For example, it may affect the adsorption of the species on the substrate. Lower temperature favors adsorption of reactants on the loading door side of the substrate. Reaction will also be slower on the colder side of the substrate. Moreover, the minimum purging times required to effectively purge the reactor depend on the temperature. Lowering the temperature reduces the H_2O desorption rate from the surfaces of the reactor and thus purging should last longer (Groner *et al.,* 2004). If the purging time is not long enough, the subsequent TMA pulse will lead to non-ideal, CVD-like reactions on the loading door side of the substrate, as TMA will react with adsorbed H_2O molecules on the substrate surface. An experimental study has shown the effect of an excess H_2O pulse on the thickness uniformity in a cross-flow reactor, with increased purging times needed to desorb the remaining adsorbed H_2O (Henn-Lecordier *et al.*, 2011). This situation is enhanced at low process temperature, where the surface reactions are slower and highly dependent

on the surface temperature. The surface temperature gradient can also affect the number of hydroxyl active sites present on the substrate (Puurunen, 2005)(Haukka and Root, 1994). Ultimately, it may lead non-uniform film thickness, as it will be presented and further discussed in Chapter 5.

4.3. Reactant feeding system

In this section, the results on the feeding system simulations are presented for the simulation of experiment 16 of Table 2.1. The reactant feeding system is simulated using the computational strategy described in Chapter 3. As described in section 3.1.4, the pure Ar flow simulation in the ALD reactor is followed by the simulation of the feeding system. It uses the pressure computed at the reactor's side inlet as an outlet pressure condition. This pressure, computed to be 0.142 Torr, is set as the outlet pressure, and the Ar flow is simulated inside the feeding system, with both of the ALD valves closed. In Figure 4.8, the pressure and TMA mole fraction distributions inside the feeding system, with the valves closed, are presented.

(a)   (b)
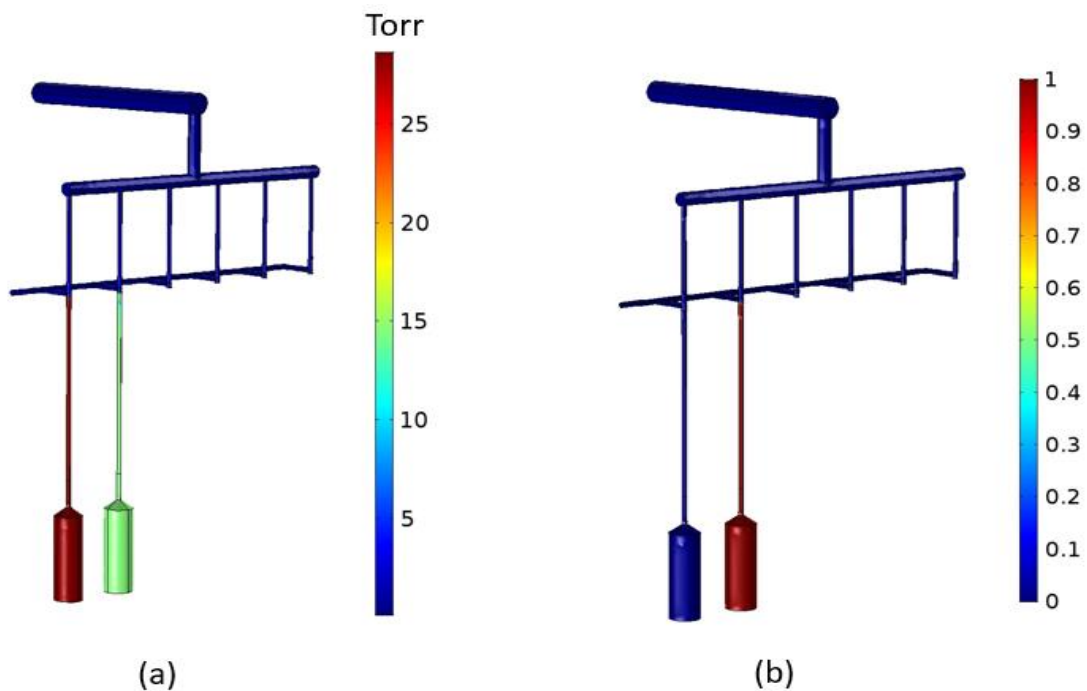
Figure 4.8. Feeding system simulation results for the pure Ar flow, with the ALD valves closed: a) Pressure distribution, b) TMA mole fraction distribution (experiment 16)

Figure 4.8a shows a high pressure difference between the reactant bottle (reactant vapor pressure, TMA: 14.55 Torr, H_2O: 28.65 Torr) and the reactant feeding system. Upon the ALD valve opening, the reactant is pulsed inside the reactor with a high velocity flow, driven by this pressure difference.

Once the result is obtained for the flow inside the feeding system with the valves closed, it is used as an initial condition for the pulsing steps simulations. The impermeable interface that approximates the ALD valve for each reactant is removed for each pulsing step respectively. When the valve closes, the impermeable interface is re-set, until all remaining reactant species are removed from the feeding system. The total flow rate and the average mole fraction are obtained at the feeding system outlet. As the outlet of the feeding system is connected to the side inlet of the ALD reactor, these values will serve as time-dependent inlet conditions for the reactor side inlet, thus simulating the ALD reactant exposure steps. The flow rates calculated by the feeding system will be used as an inlet condition for the Navier-Stokes and continuity equations in the reactor model, whereas the mole fractions will be used as an input to the chemical species conservation equation.

Figure 4.9 presents the calculated TMA and H_2O pulses as a function of time, in terms of flow rate (4.9a) and averaged molar fraction (4.9b) at the feeding system outlet. The molar fraction was found to be homogeneous along the feeding system outlet.
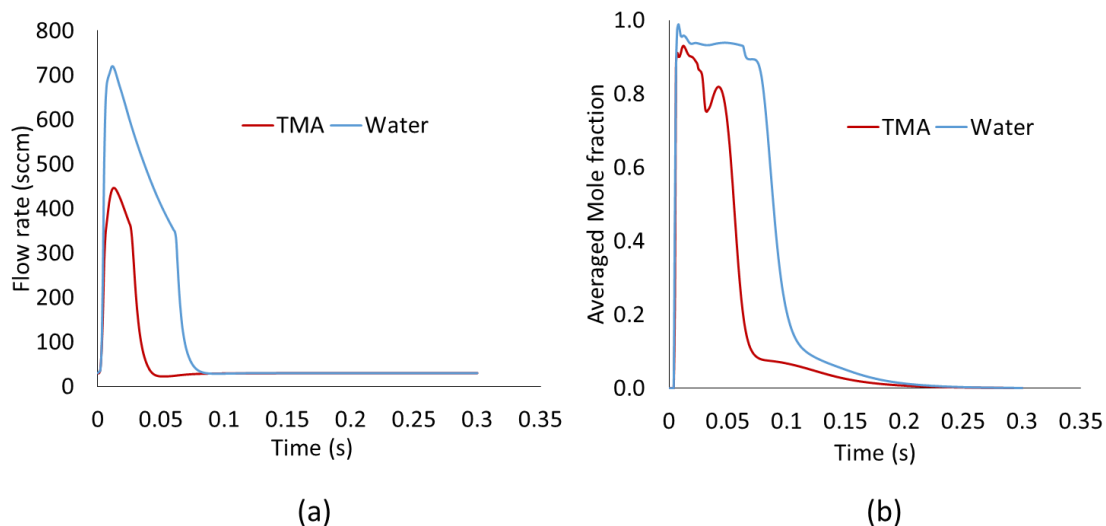
Figure 4.9. Feeding system model results for the TMA and H_2O reactant pulses: a) Flow rate, b) Molar Fraction averaged at the feeding system outlet (experiment 16 TMA pulse = 25 ms; H_2O pulse = 60 ms)

Results of Figure 4.9a show a higher flow rate for H_2O than for TMA for the whole duration of the pulse, leading to an overall higher quantity of delivered H_2O. This is attributed to the higher vapor pressure of H_2O inside the reactant bottles and to the longer opening time of the ALD valve above the H_2O bottle (60 ms and 25 ms for H_2O and TMA, respectively). It is noted that the initial and final values of the outlet flow rate of the feeding system after the reactant pulses are 30 sccm, equal to the Ar carrier gas flow.

As shown in Figure 4.9b, the reactant molar fraction is substantial during both pulses, whereas Ar represents less than 10% of the gas mixture. Notably, it is predicted that although the H_2O valve opening time is longer and the quantity of H_2O entering the feeding system is higher, the TMA molecules evacuate the feeding system slower, i.e the feeding system takes more time to purge. This is attributed to the slower diffusion rate in Ar of TMA compared to H_2O, since the molecules of the former are bigger and

154

heavier than the latter. However, the feeding system is purged from both reactants in 0.3 seconds for the conditions studied. The total calculated weights entering the reactor per cycle are 0.63 mg for TMA and 0.408 mg for H_2O.

4.4. Reactant exposure steps

After the calculations of the reactant pulses from the reactant feeding system, the reactant flows and the respective mass fraction evolution during the pulses are implemented in the reactor model as a transient inlet boundary condition on the reactor side inlet. The reactant exposures are simulated using time dependent computations, and the results are presented in the following sections, always for experiment 16.

4.4.1. Outlet pressure variation

In order to validate the coupling of the two models and the overall computational strategy, the model predictions for the outlet pressure are compared to experimental measurements. The predicted outlet pressure with the Pirani conversion (P_{conv}) variation during three ALD cycles is shown in Figure 4.10 and is compared with the experimental measurements.
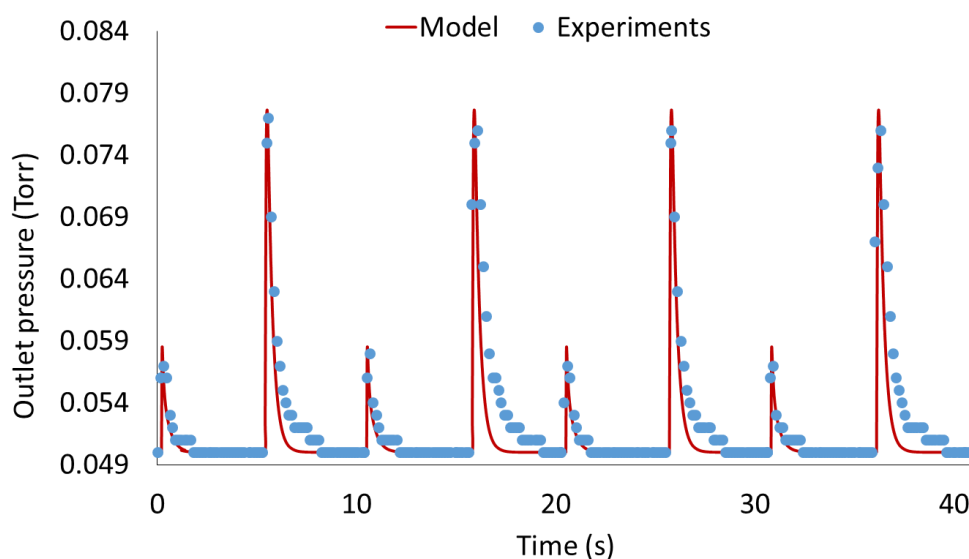
Figure 4.10. Outlet pressure variation vs time: Model predictions vs Pirani gauge measurements.

As shown in Figure 4.10, the model predictions for the pressure variation at the reactor outlet are in good agreement with measurements. In particular, the outlet peak heights are captured and thus the dynamic response to the reactant pulses. This validates the coupling of the two CFD models, as well as the computational approach for the simulation of the vacuum pump and the Pirani gauge.

Regarding the peak widths, it is noticed that the predictions slightly underestimate the time needed to restore the system to its base pressure for the H_2O pulse. As the pressure reading given by the Pirani gauge is gas dependent, it will vary with the gas composition. Let us recall that the pressure reading is performed via the measurement of the gas thermal conductivity, which is inversely proportional to the molecular mass of the gas. As the gauge is calibrated for nitrogen, a gas with a higher molecular mass than N_2 (28 g/mol) will lead to a lower pressure reading, while a gas with a lower molecular mass will have the opposite effect.

During the H_2O exposure, the surface kinetics plays a role on the pressure reading. H_2O molecules, despite chemisorbing on the substrate surface, can also adsorb on the reactor walls. Due to their polar nature, they stick strongly on the reactor walls, and take time to desorb. Therefore, the time needed for their desorption is significant and the corresponding purging time will be higher than for TMA. The presence of colder zones, such as the loading door of the reactor, makes the removal of the adsorbed molecules more difficult. This is evident from the measured pressure peaks for the H_2O exposure. The pressure at the outlet takes more time to restore to its initial value. Thus, the larger width of the H_2O measured pressure peak at the reactor outlet is attributed to the adsorption/desorption of H_2O molecules on the reactor walls, which are not considered in the present model.

The above analysis validates the approach for the study of the reactor dynamics during the reactant exposures. The flow field and the reactant distribution in the ALD reactor chamber during the reactant exposure steps are presented and discussed in the following section.

4.4.2. TMA exposure

As shown in Figure 4.9a, the TMA pulse entering the reactor reaches a peak above 400 sccm. Due to the high molecular mass of TMA, a high momentum pulse will enter the reactor chamber through the side inlet, leading to a disturbance of the flow field. As the flow rate entering the reactor is time dependent, the resulting flow field inside the reactor main volume will be affected during the exposure steps of the process. Snapshots of the flow field at different time instants during the TMA exposure are shown in Figure 4.11.

(a)

(b)

(c)

(d)
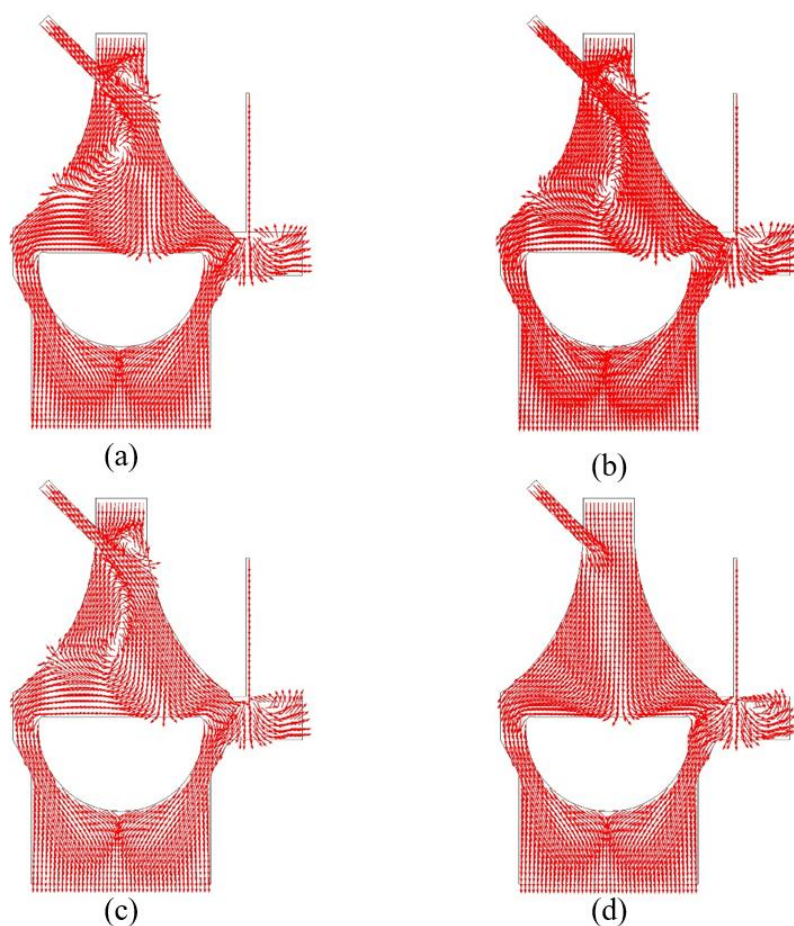
Figure 4.11. Snapshots of the flow field developed during the TMA exposure, inside the reactor chamber: a) 10 ms, b) 20 ms, c) 30 ms, d) 60 ms, after the start of the TMA exposure.

Results show a recirculation inside the reactor, during the first ms of the TMA exposure step. Notably, one recirculation area is located in the gas phase above the substrate, while a second one near the reactor top inlet. After 60 ms, the TMA pulse stops (Figure 10d), and the recirculation disappears. The predicted flow field and, in particular, the recirculation above the substrate, can have a significant effect on the gaseous species distribution inside the reactor chamber and then on the substrate.

In Figure 4.12, snapshots of the TMA concentration profiles on the substrate surface are plotted. The scale for each snapshot is different for the sake of clarity.
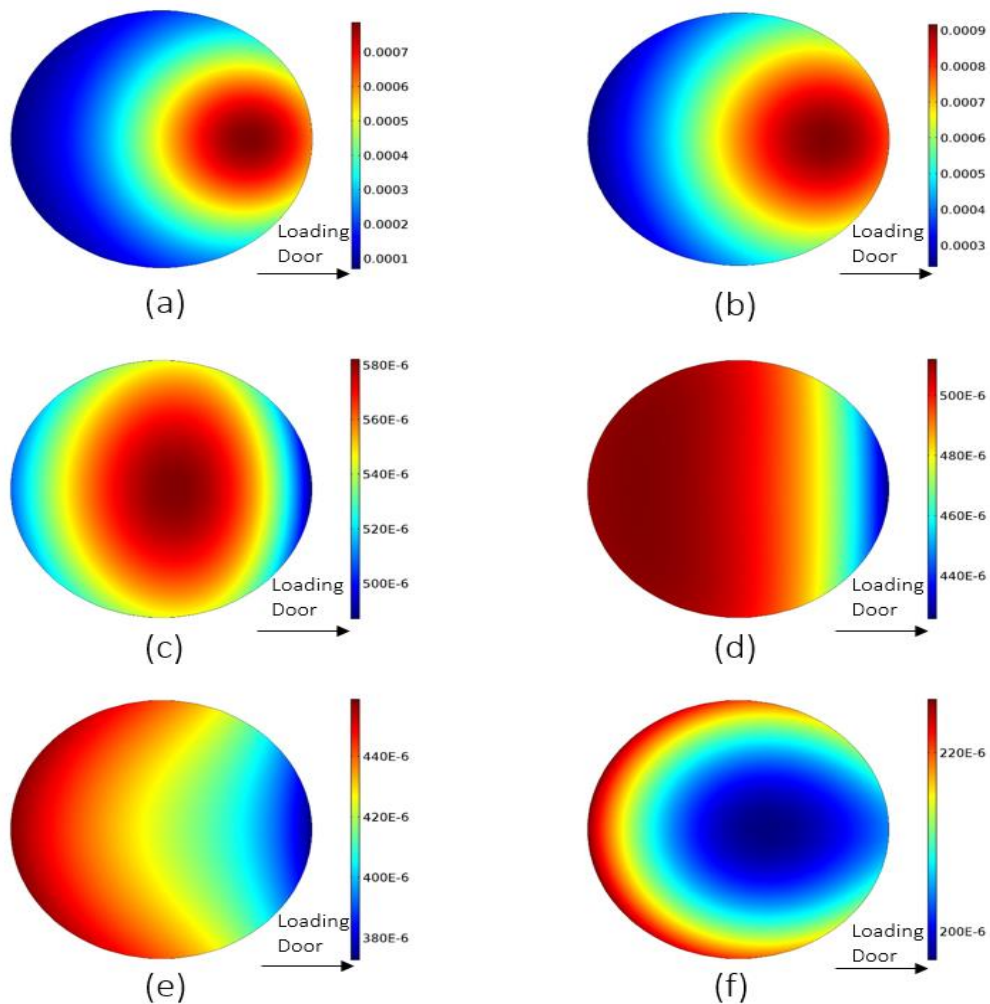
Figure 4.12. Snapshots of TMA concentration profiles on the substrate surface, scales in $\frac{mol}{m^3}$: a) 20 ms, b) 30 ms, c) 60 ms, d) 80 ms, e) 100 ms, f) 200 ms, after the start of the TMA pulse.

A non-uniform TMA concentration profile appears on the substrate, during the TMA exposure. The TMA concentration profile on the substrate evolves along with the gas flow field inside the reactor chamber. While a recirculation exists in the gas phase (0-40 ms, snapshots a to c, Figure 4.11), the TMA concentration reaches a maximum between the substrate center and the loading door side of the substrate, as shown in Figures 4.12a and 4.12b. Notably, 20 ms after the start of the TMA pulse, the maximum concentration computed near the substrate exceeds $7 \cdot 10^{-4} \frac{mol}{m^3}$, while the minimum value is seven times smaller, i.e $1 \cdot 10^{-4} \frac{mol}{m^3}$ (Fig. 4.12a), leading to a concentration difference of 93%. The maximum and minimum values are $9 \cdot 10^{-4}$ and $3 \cdot 10^{-4} \frac{mol}{m^3}$ respectively, after 30 ms. As the side inlet flow rate establishes to its initial value of 30 sccm, the maximum moves to the center of the substrate, as shown in Figure 4.12c. At that point, the concentrations are lower by two orders of magnitude, compared to the previous time snapshots. The maximum value is $5.8 \cdot 10^{-6} \frac{mol}{m^3}$ and the minimum is below $5 \cdot 10^{-6} \frac{mol}{m^3}$ – a difference of 16.3%. It is noted that while the side inlet flow rate is higher, the loading door purging flow effect is suppressed, as shown in Figures 4.11a-c. However, once the flow rate establishes to its initial value, the loading door purge starts gaining influence on the species distribution on the substrate surface, as seen in Figure 4.12c.

For the time period between 60 ms to 200 ms after the start of the TMA pulse, snapshots 4.12d to 4.12f show that while the flow field is established, the gas mixture entering the reactor through the side inlet still contains TMA flowing inside the reactor chamber. During this period, the loading door purge affects the concentration of TMA above the substrate surface. As shown in Figures 4.12d and 4.12e, the loading door Ar flow purges the side of the substrate exposed to it. The loading door side of the substrate is exposed to a lower TMA concentration during the whole TMA exposure step after 60 ms from the start of the TMA pulse. The concentrations remain in the same order of magnitude as in Figure 4.12c. The maximum concentration difference is 15.3% for Figure 4.12d and 15.6% for Figure 4.12e.

After 200 ms, the side inlet flow consists of Ar only. During the remaining purging time, the reactor chamber is purged from the already present TMA molecules. The flow field is established and the resulting concentration profile on the substrate is shown in Figure 4.12f. This species distribution profile remains constant during the remaining purging time of the process.

As Figure 4.12 shows, the TMA concentrations on the substrate during the first ms of the TMA exposure (Figures 4.12a, 4.12b) are significantly higher than the concentrations at the next time snapshots (Figures 4.12c-4.12f). In order to analyze the exposure of the substrate to TMA molecules, we have calculated the species flux on the substrate surface, using the Hertz-Knudsen equation, in terms of $\frac{mol}{m^2 \cdot s}$:

$$Flux_i = \frac{P_i}{\sqrt{2\pi M_i RT}}$$

(4.1)

The above species flux is integrated over the whole TMA exposure and purging time of the ALD cycle. The resulting exposure of the substrate to TMA molecules is plotted in Figure 4.13.
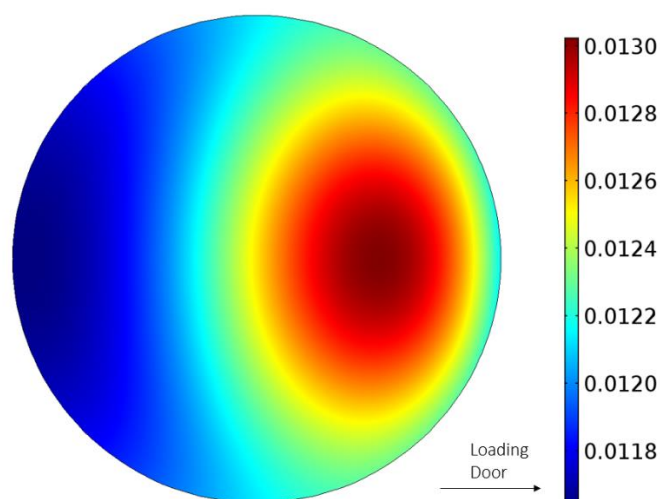
Figure 4.13. Integral over time of the TMA flux on the substrate surface, scale in $\frac{mol}{m^2}$, during the whole TMA exposure and purging time.

The TMA flux integral over time is not uniform; it has a maximum between the substrate center and the loading door side. This corresponds to the concentration profiles on the substrate during the TMA pulse, when the recirculation in the gas phase exists, as shown in Figures 4.12a and 4.12b. This means that the majority of the substrate exposure to TMA occurs during the first ms of the TMA pulse. The computed maximum exposure difference on the substrate surface during the TMA exposure is 10.7%. The predicted exposure difference across the substrate surface can lead to deposited film non-uniformity, especially if the rate limiting step of the process is mass transfer toward the substrate, i.e at high temperatures. However, if the species flux is higher than the flux required to cover all available reactive sites, the substrate surface

will be saturated and the deposited film will be uniform. The effect of the reactant pulses

on the resulting film uniformity is presented and discussed in Chapter 5.

4.4.3. H_2O exposure

Snapshots of the gas flow field inside the reactor during the H_2O exposure are

shown in Figure 4.14.
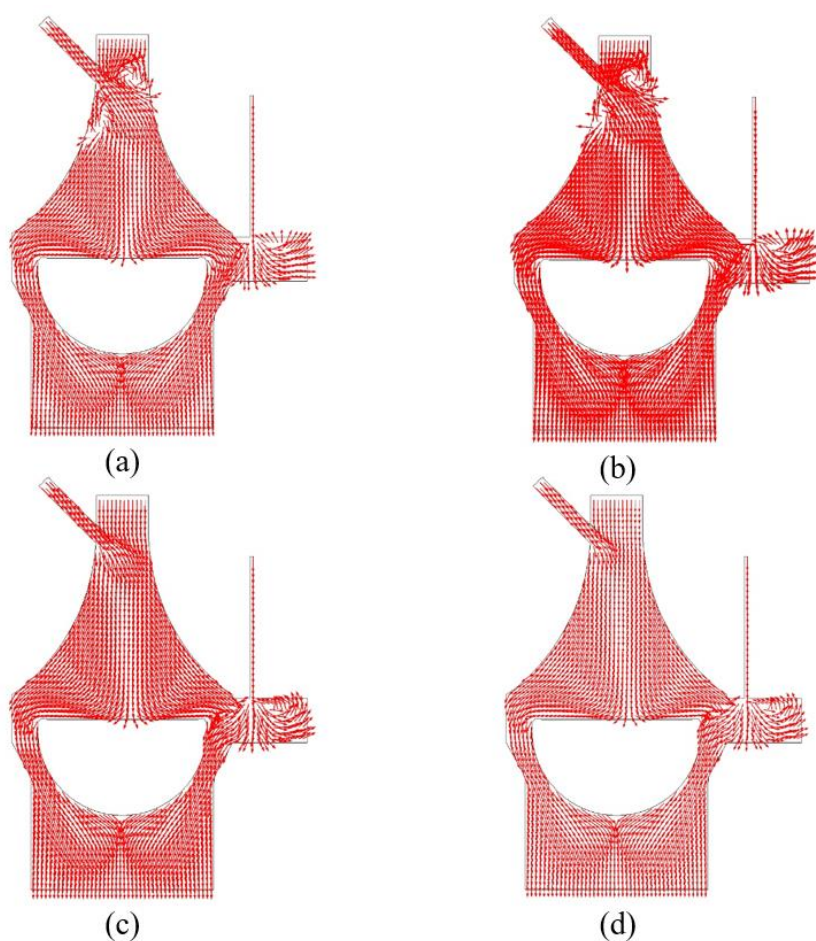
Figure 4.14. Snapshots of the flow field inside the reactor chamber: a) 10 ms, b) 20

ms, c) 60 ms, d) 200 ms after the start of the H_2O pulse.

During the H_2O pulse, as a high flow rate enters the reactor chamber, a

recirculation is again predicted near the reactor inlet. Another recirculation is located

below the side inlet tube connection to the main volume of the reactor (Figures 4.14a,b).

The recirculation is less significant for H_2O than for TMA, and no recirculation appears above the substrate, contrary to the TMA pulse, despite the fact that the flow rate entering the reactor is higher than during the TMA pulse (Figure 4.9a). This is due to the fact that although the molar flow rate is smaller, the mass flow rate is higher, as TMA is four times heavier than H_2O. Hence, the TMA pulse has a higher momentum than the H_2O pulse, thus leading to the recirculation. After 60 ms (Figure 4.14c), the recirculation disappears, while a high flow rate is still entering the reactor. The side inlet flow rate returns to its initial value (Figure 4.9a) after 120 ms, and the flow field inside the chamber establishes to its initial condition.

The effect of the flow on the species distribution on the substrate is shown in Figure 4.15, where snapshots of the H_2O concentration profile are presented. The scale for each snapshot is different, to highlight the concentration profile.

During the first ms of the H_2O pulse, the high flow rate coming from the side inlet of the reactor suppresses the loading door purging flow, thus leading to a concentration profile with a maximum at the substrate center (Figure 4.15a). At this snapshot, the maximum concentration is $4.7 \cdot 10^{-4} \frac{mol}{m^3}$ and the minimum $3.03 \cdot 10^{-4} \frac{mol}{m^3}$, leading to a maximum concentration difference of 35.5%, As the flow rate from the side inlet decreases, the loading door purge influences the species distribution, thus leading to a constantly lower H_2O concentration on the loading door side of the substrate, which is exposed to the purging gas. This gradual effect is shown in Figure 4.15b-e. Figures 4.15b and c correspond to results obtained for a high side inlet flow rate due to the H_2O pulse. However, the momentum of this flow is not high enough to suppress the loading door Ar flow effect. The maximum concentration differences at these snapshots are 26.6% and 17.65% for Figures 4.15b and 4.15c, respectively.

Figures 4.15 d and e correspond to results obtained while the side inlet flow rate has established to its initial value, however the gas entering the side inlet still has an amount of water. The maximum concentration difference is 8.7% and 4.5%, respectively; the concentration minimum is located at the loading door side of the substrate. The H_2O concentration profile on the substrate during the purging step of the reactor is shown in Figure 4.15f; the remaining water is removed from the chamber.
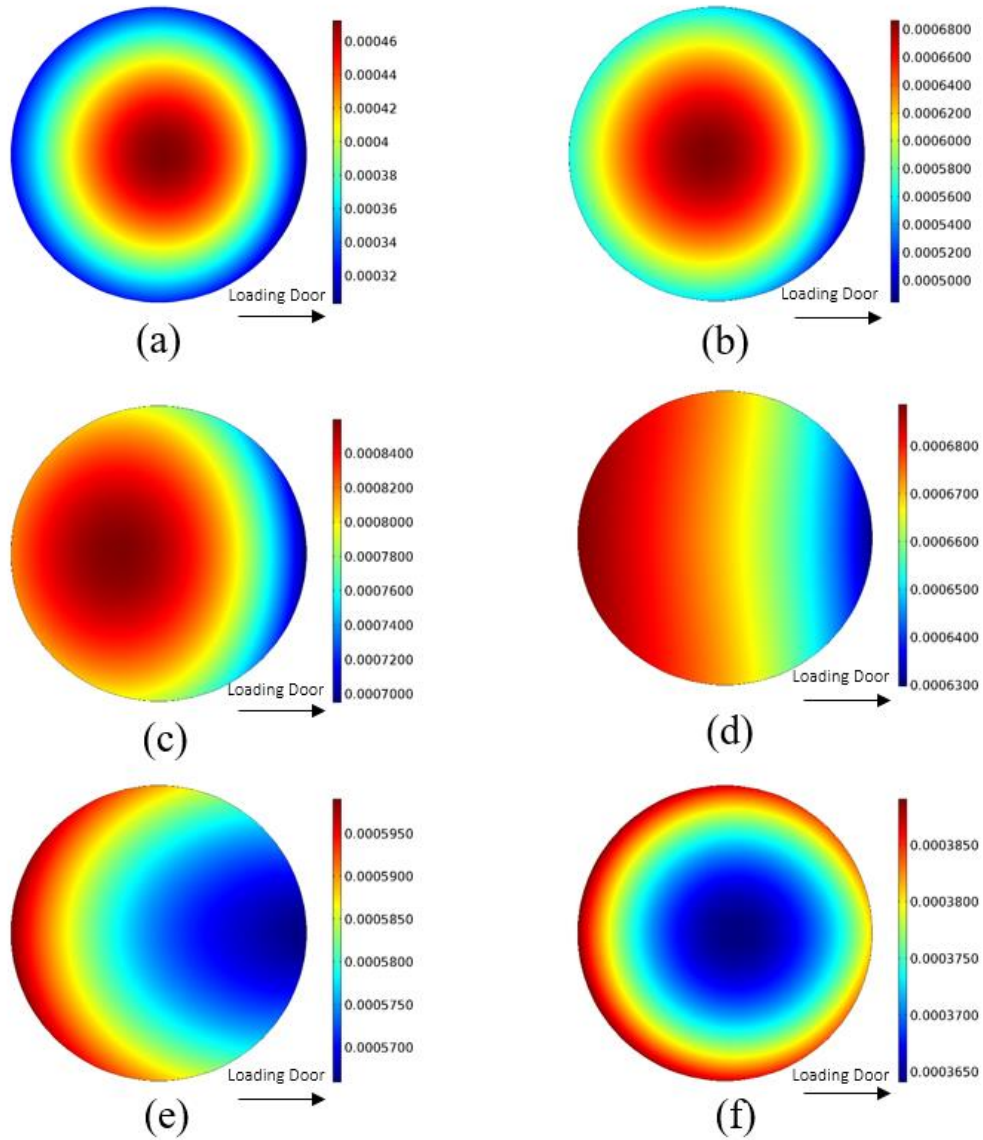
Figure 4.15. Snapshots of the H_2O concentration profile near the substrate surface,

scales in $\dfrac{mol}{m^3}$: a) 20 ms, b) 30 ms, c) 60 ms, d) 100 ms, e) 120 ms, f) 200 ms after

the start of the H_2O pulse.

From the predictions in Figure 4.15 it is concluded that during the first ms of

the H_2O pulse, the values of the H_2O concentrations on the substrate surface are of the

same order of magnitude, unlike the TMA pulse, where it took 30 ms for an almost full

substrate surface exposure to TMA. It is also noted that the overall H_2O concentrations

are higher than in the TMA case. As done before, equation 4.1 is integrated over the

166

whole duration of the H_2O exposure and purge, to yield the total exposure presented in Figure 4.16.
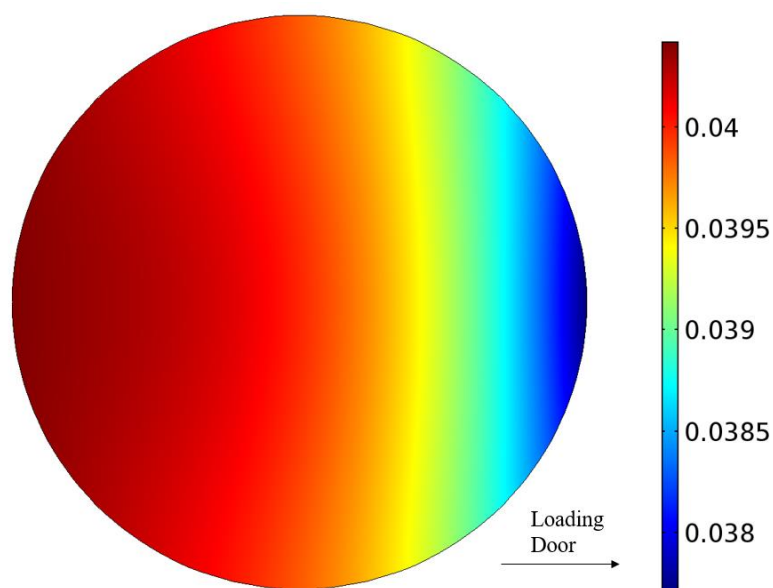
Figure 4.16. Integral over time of the H_2O flux on the substrate surface, during the whole H_2O exposure and purge time, scale in $\dfrac{mol}{m^2}$.

The computed time integral of the species flux shows a non-uniform exposure of the substrate surface to H_2O. A lower exposure is observed on the loading door side of the substrate, while a maximum is calculated on the opposite side. It is shown than in the H_2O exposure, the profile of the substrate exposure to the reactant is different than in the case of the TMA exposure. For the TMA exposure, the profile is dictated by the recirculation taking place in the reactor main volume, while for the H_2O exposure it is dictated by the effect of the loading door inlet flow. The maximum total exposure difference is 6.7%. This value is lower than the corresponding value for the TMA exposure. The above result shows a significant effect of the loading door purge on the gaseous H_2O species distribution near the substrate. Under ALD conditions, if the H_2O exposure is not high enough to saturate the surface, a non-uniform film will be

deposited, with a lower film thickness on the loading door side. With the mechanism presented in Chapter 3, two TMA molecules would need three H_2O molecules to fully remove the methyl ligands. This means that the ratio between the H_2O and TMA exposure should be at least 1.5. The ratio between the H_2O and TMA exposures exceeds this value. However, this is only a first approach, since the kinetics of the reactants chemisorption are not yet considered. The actual reaction kinetics and their interplay with the transport phenomena described above, are presented and discussed in Chapter 5.

4.5 ALD purging steps

The whole ALD exposures and purging steps were simulated for one complete cycle of experiment 16. As Ar flows constantly into the chamber, the substrate is exposed to reactant molecules even during the purging steps. In order to study the purging efficiency of the reactor, the maximum reactant mole fraction inside the whole chamber was traced during the ALD pulses and purging steps of the ALD cycle, as detailed in Figure 4.17, for both reactants.
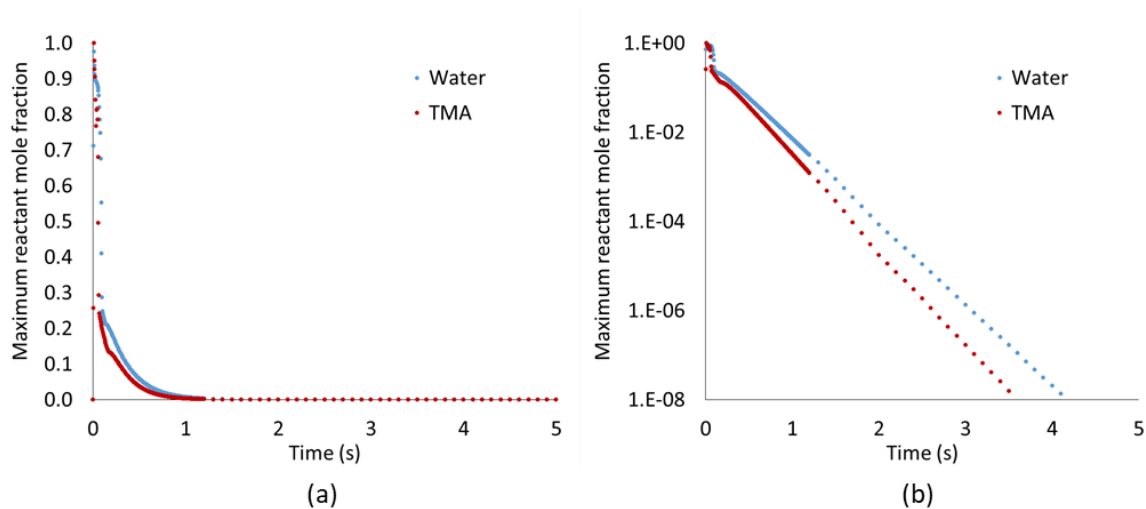
Figure 4.17. Time evolution of the maximum reactant mole fraction inside the reactor chamber: a) Linear mole fraction scale, b) logarithmic mole fraction scale.

As expected, this maximum mole fraction during the first stages of the exposure time is close to 1, as the computed reactant pulses have a high reactant composition (Figure 4.9b). After the reactant pulses, the maximum mole fraction quickly drops, as the reactor purging step begins.

In order to calculate a minimum purging time, we assumed that when the maximum reactant mole fraction inside the ALD reactor drops below a threshold, here taken arbitrarily to 10^{-6}, the reactor is purged. The obtained results are 2.7 s for TMA and 3.1 s for H_2O. Let us recall that these results are obtained by simulating only the transport of chemical species inside the reactor. In order to get a more reliable value for the purging time, chemical reaction kinetics and adsorption/desorption of species on the reactor walls must be taken into account. Enough time must be given to the reactions to saturate the surface, while the by-products must desorb and diffuse away from the substrate surface, and be removed from the ALD chamber via convection and diffusion. The species also adsorb on the reactor walls and the time needed for their desorption contributes to the total purging time. Especially for the H_2O molecules, the slow

169

desorption from the reactor walls can significantly affect the purging time, especially under low temperature conditions, such as on the loading door walls. Hence, the present model results can provide valuable information regarding the purging efficiency of the reactor in terms of gas species transport inside the chamber. However, an efficient minimum purge time will only be predicted when the above described physicochemical phenomena will be incorporated in the model. The effect of the purge time on the film growth per cycle and uniformity is experimentally and theoretically studied in Chapter 5.

Summary- Conclusions

In this chapter, the dynamics of the ALD system are studied. The computational strategy used to simulate the vacuum system is validated by comparing model predictions to experimental measurements. Both the turbo-molecular pump and the Pirani gauge pressure conversion were validated, which allowed to proceed with the study of the transport phenomena inside the reactor.

The complex geometry of the main chamber, as well as the gas inlets were found to affect the gas flow field inside the reactor. The top inlet Ar flow needs to be high enough to suppress the flow coming from the loading door inlet. If the top inlet Ar flow is not high enough, a non-homogeneous purge of the region above the substrate can take place, which could lead to non-uniform deposition. Furthermore, the non-heated loading door walls lead to a non-uniform temperature field inside the reactor and affect the temperature distribution on the substrate surface. The substrate region close to the loading door is found to have a lower temperature than the rest of the substrate, for all

process recipes. This temperature distribution inside the reactor can affect the film uniformity, as it impacts both the ALD reaction kinetics, as well as the desorption of adsorbed molecules on the reactor walls during the purging steps of the process.

The reactant pulses were calculated from the reactant feeding system, using the computational strategy described in Chapter 3. The flow rate and composition during the reactant pulses is calculated at the feeding system outlet and implemented on the reactor side inlet as a transient inlet boundary condition. The resulting model predictions for the converted Pirani pressure were compared to the experimental Pirani gauge pressure measurements. The good agreement between the measurements and model predictions allows the analysis of the transport phenomena during the reactant exposure steps.

The substrate exposure to each reactant is monitored by a time integral of the reactant flux on the substrate surface. A recirculation was found to take place during the TMA exposure, which leads to non-uniform species distribution on the substrate surface. For the H_2O exposure, a non-uniform distribution occurs, driven mainly by the loading door purge. These different phenomena leading to non-uniform reactant distribution can have an impact on the film uniformity, if the reactant exposure is not enough to saturate the surface during each reactant exposure. However, in this Chapter, no chemical reactions are taken into account. The impact of the flow field on the chemical mechanisms and the film uniformity is further discussed in Chapter 5.

Finally, the purging efficiency of the reactor was investigated. The minimum purging time was found to be 2.7 s for TMA and 3.1 s for H_2O. However, this analysis does not take into account the adsorption and desorption of reactants on the reactor walls, which can have a serious impact on the minimum purge time duration.

Specifically, the colder loading door region could be a source of inefficient purge, as the reactant desorption is slower, due to the low temperature of the loading door walls. This impact is shown in Chapter 5.

The above analysis shows that contrary to the perception of ALD being dependent solely on surface reactions, the transport phenomena inside the ALD reactor can have an influence on the deposited film. The reactor design and the process setup can lead to non-ideal reactant flow on the substrate, as well as a non-uniform temperature field inside the ALD reactor. This can affect the uniformity of the deposited film, as well as the minimum time needed to effectively purge the ALD chamber. The effects of these aspects of ALD on the deposited film uniformity are presented and discussed in Chapter 5.

Chapter 5: Surface reactions and their interplay with transport phenomena

In this chapter, the detailed surface mechanisms involved during the ALD of Al_2O_3 from TMA and H_2O, as well as their interplay with the transport phenomena taking place inside the ALD reactor main volume are discussed. The impact of the surface mechanisms and the competition between them on the ALD film formation is presented in section 5.1. The limiting surface mechanisms over the whole range of the ALD window are identified, and the deposition behavior is explained. In section 5.2, the detailed aspects of the surface chemistry and their effect on certain film properties are presented and discussed. Finally, in sections 5.3 and 5.4, the effect of the process conditions and the transport phenomena on the deposited film uniformity are thoroughly discussed, thus providing the framework for the optimization of the process. The results of this chapter have been the subject of a scientific journal article, published in Chemical Engineering Science (Gakis *et al.*, 2019).

5.1. Surface reactions at the wafer scale

5.1.1. Effect of temperature on the film growth per cycle

In order to analyze the kinetics of the surface reactions, a study of the film deposition rate as a function of temperature is performed, both computationally and experimentally, for two different TMA pulse durations. As we assume an ideal ALD regime, the thickness of the deposited film is divided by the respective number of ALD cycles used, in order to determine the growth per cycle (GPC). As the fully

hydroxylated surface is used as an initial surface condition, the GPC obtained by the chemistry model is not constant from the first cycle onwards. A certain number of cycles needs to be simulated first, so that the kinetics implemented in the model lead to a constant GPC as it will be detailed in section 5.1.3.

The thickness of the layer was calculated using the following equation:

$$h = M_{Al_2O_3} \frac{C_{Al_2O_3}}{\rho_{Al_2O_3}} \tag{5.1}$$

where $M_{Al_2O_3}$ is the molecular mass of alumina, $C_{Al_2O_3}$ is the surface concentration (in mol/m^2) of the produced alumina film, and ρ_{Al2O3} is the density of alumina, taken at 3500 kg/m^3 (Ott *et al.*, 1997).

The comparison of the experimental (experiments 1-12 in Table 2.1) and calculated GPC at the center of the substrate (Simulated experiments 1-12), as a function of temperature and the TMA pulse duration, is presented in Figure 5.1.
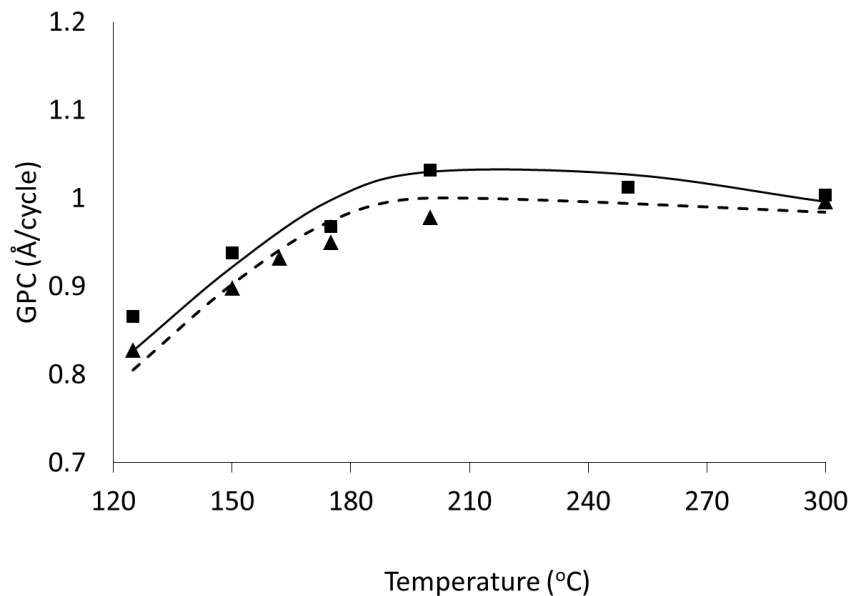
Figure 5.1. GPC as a function of temperature. 25 ms TMA pulse: Triangles (experiments), dashed line (model). 60 ms TMA pulse: Squares (experiments), bold line (model).

The model accurately predicts the experimental GPC for this range of operating conditions. Therefore, the model will be used for the analysis of the surface chemistry mechanism.

When using a 25 ms TMA pulse, for the range of 125-300°C, the measured GPC increases with temperature from $0.83\frac{\text{Å}}{Cycle}$ at 125°C (experiment 1) to $1\frac{\text{Å}}{Cycle}$ at 300°C (experiment 11). This can be explained by the thermal activation of surface reactions, which under low temperatures is too low. When a 60 ms TMA pulse is used, an overall increase of the GPC is both measured and computed in comparison with 25 ms. This implies that the TMA pulse of 25 ms was not long enough to cover the whole surface.

For the experiments with 60 ms TMA pulse, the GPC increases with temperature in the range 125-200°C, as in the case of the 25 ms TMA pulse, this time reaching $1.03\frac{\text{Å}}{Cycle}$. Further temperature increase leads to a slight GPC decrease, with the value of the GPC at 300°C being $1\frac{\text{Å}}{Cycle}$. This behavior has been reported in other works (Ott *et al.*, 1997) (Vandalon and Kessels, 2016)(Xie *et al.*, 2015) (Pan *et al.*, 2015). It is usually ascribed to the activation of the TMA desorption at high temperature, or the decrease of the surface concentration of OH sites, with temperature increase.

In our experiments, the GPC value at 300°C (experiments 11 and 12) changes slightly with the increase of the TMA pulse; at 300°C the OH surface sites were almost

totally covered even with the 25 ms TMA pulse. This shows that the linear decrease of the surface concentration of OH sites with temperature (Haukka and Root, 1994) increase is the limiting factor for the film deposition at 300°C.

The surface chemistry model takes into account species adsorption, desorption, and surface reaction, as well as the surface OH concentration as a function of the process temperature, which is original regarding the state of the art. The experimental behavior reveals a complex mechanism and the surface chemistry model with all the considered phenomena seems capable to catch this complexity, thus validating our analysis in the considered parametric window.

5.1.2. Reaction mechanisms

Before discussing the results of the surface chemistry model, the activation energies associated with each mechanism can give useful insight. Results from Widjaja and Musgrave (Widjaja and Musgrave, 2002), summarized in Table 3.1, show that the adsorption step has no activation energy barrier for TMA nor H_2O. Hence, as we assume a steady initial sticking coefficient s_0 for each species as a function of temperature, the adsorption step, at each time, will depend on the species flux on the surface and the state of the surface. The adsorbed reactant molecule can then either react on the surface, with an irreversible reaction, or desorb. These are two competing mechanisms, taking place at the same time on the surface, and their relative rates will show whether the reaction or the desorption is more favorable.

Again, results from Widjaja and Musgrave (Widjaja and Musgrave, 2002) presented in Table 3.1, show that for the adsorbed TMA molecule, the activation energy

for desorption is higher than the energy barrier to reach its transition state, from which the irreversible reaction step is exothermic. Therefore, the adsorbed TMA molecule is more likely to react on the surface, producing DMA and subsequently MMA species, than desorbing back to the gas phase. The opposite is shown for H_2O. The adsorbed H_2O molecule desorption has a lower energy barrier than the irreversible surface reaction, meaning that the adsorbed H_2O molecule is more likely to desorb than react on the surface.

To study these behaviors as a function of temperature, we introduce a reaction probability approach. Specifically, we study the reaction probability, p_k, of an already adsorbed molecule k, given as the ratio of the forward surface reaction rate R_r to the sum of the rates of the possible events, i.e. reaction and desorption rates.

$$p_k = \frac{R_r}{R_r + R_{des}} \tag{5.2}$$

Here k denotes that the adsorbed molecules are surface species. If we multiply this value with the initial sticking coefficient $s_{0,i}$ for each gas species, we obtain the total initial probability p_i of a gas molecule i to adsorb and react on the surface, fully covered by available adsorption sites.

$$p_{init,i} = s_{0,i} \cdot p_k$$

(5.3)

Here, i denotes gas phase species. The temperature influence on the initial reaction probability of the two reactants is shown in Figure 5.2.
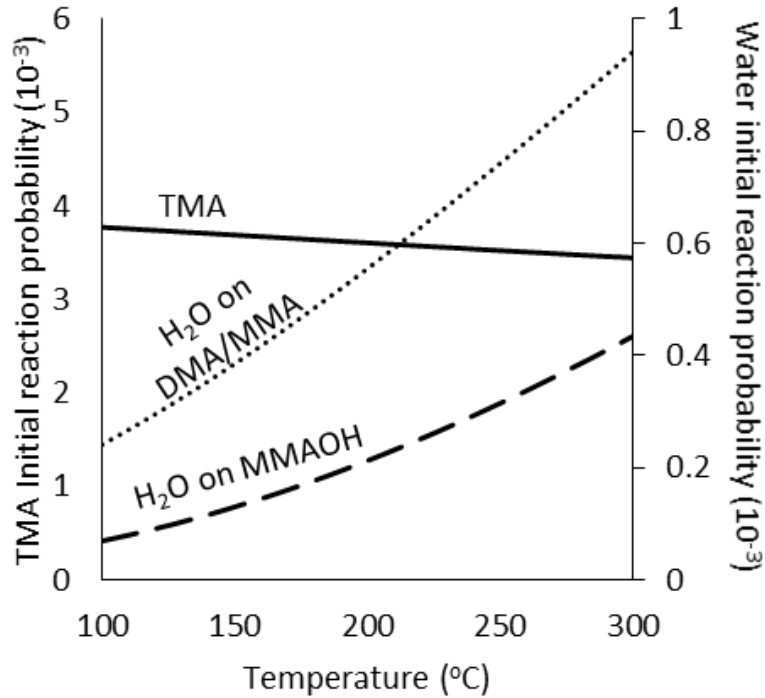
Figure 5.2. Model predictions for the temperature influence on the gas species initial reaction probabilities $p_{init,i}$: TMA (continuous line, left hand axis), H_2O on DMA/MMA species (dotted line, right hand axis) and H_2O on MMAOH species (dashed line, right hand axis).

At 100°C, the reaction probability of a TMA molecule is $p_{init,TMA} = 3.77 \cdot 10^{-3}$, a low value due to the low sticking probability ($s_{0,TMA} = 0.004$). Once the TMA molecule is adsorbed, it has a $p_{TMA} = 94\%$ probability of reacting (Equation 5.2). As the temperature increases, the TMA desorption is activated, and the reaction probability slightly decreases. At 300 °C, the reaction probability of the adsorbed TMA is $p_{TMA} = 86\%$, while the overall initial probability is $p_{init,\ TMA} = 3.44 \cdot 10^{-3}$. It is seen that the reaction probability of the already adsorbed TMA on the surface is high for all temperatures. Hence, the TMA step is limited by the adsorption process, and the low sticking probability of the molecule. To obtain a maximum coverage of the surface after the TMA pulse, the pulse duration must be adjusted, so that the TMA chemisorbs on

179

the whole substrate surface. The temperature has a small effect on the reaction probability of TMA. The results for the TMA initial reaction probability are in good agreement with those experimentally found by Vandalon and Kessels (Vandalon and Kessels, 2016), presented in Figure 1.10 of Chapter 1, and confirm the small effect of temperature on the TMA half step discussed in this work.

Figure 5.2 also shows the reaction probabilities of the H_2O molecules on the adsorbed DMA, MMA and MMAOH species. It is shown that for 100ºC, the reaction probability of H_2O is $2.4 \cdot 10^{-4}$ on DMA and MMA, while a lower value of $0.7 \cdot 10^{-4}$ is computed on MMAOH. These low probabilities are due to the higher activation energy for the surface reaction than for desorption. In addition to the higher activation energies of the H_2O reactions, deposition at low process temperatures is also impacted by the lower energy barrier for desorption of the H_2O molecule, leading to incomplete H_2O reactions.

As temperature increases, both surface reaction and desorption are activated, with the latter at a smaller rate. The resulting reaction probability increases, reaching $9.3 \cdot 10^{-4}$ on DMA and MMA, and $4.3 \cdot 10^{-4}$ on MMAOH at 300ºC. Based on these values, our model shows that the limiting mechanism would be the removal of the methyl group present on the MMAOH species. This could possibly be related to the conclusions of Vandalon and Kessels (Vandalon and Kessels, 2016) (Vandalon and Kessels, 2017), namely that isolated CH_3 groups are persistent and harder to remove during the H_2O exposure, as detailed in Chapter 1, and presented in Figure 1.10.

The probability of already adsorbed H_2O molecules to react are computed to be $p_{H_2O} = 1.72\%$ on DMA and MMA, and $p_{H_2O} = 0.5\%$ on MMAOH at 100 ºC. With the increase of temperature, these values reach $p_{H_2O} = 6.7\%$ on DMA and MMA and p_{H_2O}

=3.1% on MMAOH at 300°C. The sticking probability for the H_2O molecules (s_{0,H_2O}=0.014) is higher than the TMA sticking probability ($s_{0,TMA}$=0.004) thus showing that the adsorption step is faster for H_2O. However, the competition with desorption is very significant in the H_2O case, leading to less than 7% of adsorbed H_2O molecules to react on DMA, MMA and MMAOH species, even at 300°C. These values are significantly lower than for the TMA molecules, explaining the longer exposure times needed for the H_2O step, and the effect of temperature on the activation H_2O reactions (Vandalon and Kessels, 2016) (Vandalon and Kessels, 2017).

The values predicted for the initial reaction probabilities of H_2O on MMAOH are close to the ones in literature taking into account the uncertainty of the measurements and calculations for the reactant flux reported by Vandalon and Kessels (Vandalon and Kessels, 2016).

It can then be deduced from these results that the GPC increase with temperature in the region 125-300°C is attributed to the H_2O half reactions, and their competition with desorption. An increase of temperature favors the H_2O reactions with the methyl groups on the surface, hence leading to a higher GPC. The decrease of the GPC at higher temperatures can be attributed to two factors. Both the TMA desorption is favored and the maximum OH groups concentration on the surface decreases with temperature. However, as Figure 5.2 shows, the relative decrease of the TMA probability with temperature is not very significant. The decrease of the GPC is thus attributed to the maximum number of OH groups. This will be further discussed in the next section.

5.1.3. Surface coverage dynamics

Figure 5.3 presents the evolution of the surface coverage of all stable (OH, DMA, MMA and MMAOH) species, as a function of the number of cycles at 150°C and 25 ms of TMA pulse (simulated experiment 3 of Table 2.1), at the center of the wafer for the five first simulated cycles. For the sake of clarity, the purge time is omitted. The exposure step of each reactant is shown as a half-cycle, and each half-cycle duration corresponds to 1.2 s. This duration has been chosen as after 1.2 s, the reactant flux on the substrate surface, predicted by the CFD model, is not significant enough to affect the adsorption-reaction process.

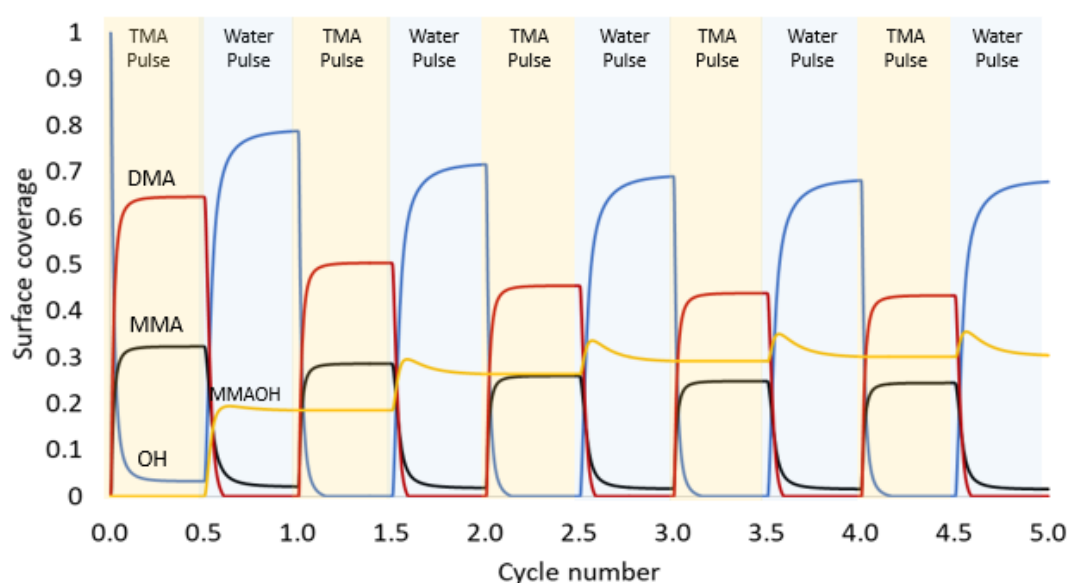Figure 5.3. Model predictions of the surface coverage evolution of the four stable surface species during the 5 first simulated cycles in simulated experiment 3.

Results show that, starting from a fully hydroxylated surface, the surface coverage of all four surface species reaches a steady regime after a certain number of cycles. In this regime, the surface state at the end of each cycle is the same as at its start,

and the GPC is constant. Characterizations (Chapter 6) showed no carbon contamination. In the simulation, all methyl intermediate species formed during the cycle, in particular MMAOH, are eliminated during the next cycle and immediately re-formed in the same proportions on the new reactive surface, so as to have no buried carbon.

In Figure 5.3, the OH surface species start from a surface coverage of 1 in the first cycle, while in the steady regime (cycles 4 and 5) the surface coverage of OH groups at the start and end of the ALD cycle is 0.685. The same trend is observed for the coverage of the DMA and MMA species, at the end of the TMA pulse. The MMAOH groups are the most difficult to remove. Hence, during the 3 first cycles of deposition, the MMAOH coverage of the surface increases after each cycle. Once the steady regime is established (4th and 5th cycles), the MMAOH serves as an intermediate species, generated from the hydroxylation of a DMA and removed by the second hydroxylation of its last methyl group. This explains why the MMAOH coverage on the surface at the start and end of each cycle in the steady regime remains constant, as for all the other species.

The above observations confirm that the major mechanisms limiting the ALD film formation at low temperature such as $150^{o}C$ are the H_2O reactions. However, as shown experimentally and predicted by the model, an increase of the TMA pulse duration increases the GPC (Figure 5.3). Indeed, both the TMA and H_2O pulses inhibit the deposition, when using a 25 ms TMA pulse. However, the H_2O step is the thermally activated mechanism, as discussed in the previous section. The H_2O reaction with MMAOH is the main mechanism limiting the deposition at low temperatures. This is why the increase of the TMA pulse duration leads only to a marginal increase of the GPC. This is consistent with results of Vandalon and Kessels (Vandalon and Kessels,

2016), who showed that at low temperature, the alumina thermal ALD process is limited by the H_2O step, which is unable to remove persistent methyl groups on the surface.

When the steady regime is reached, all surface species concentrations present the same evolution; they are generated and eliminated, and their coverage at the start of each cycle is the same. This regime is dependent on the surface reactions, their kinetics and the reactant fluxes. Hence, the initial assumption of the hydroxyl group concentration does not affect the GPC results of the model, once the steady regime is achieved. This however, is valid only if the surface kinetics and the reactant fluxes result in a deposit that leads to non-full coverage of the surface sites. If the surface kinetics and reactant fluxes allow the deposition process to cover the maximum OH group concentration, the deposition is limited by the maximum OH group concentration value. It will be shown below (Figure 5.4) that this is the case at 300°C, where at steady state, the initial OH coverage is close to unity.

In order to analyze the effect of temperature on the surface kinetics, the surface coverage evolution of the four stable species (OH, DMA, MMA, MMAOH) is presented in Figure 5.4 as a function of the ALD cycle for three different temperatures. The surface coverages shown are the ones obtained at the center of the wafer once the steady regime has been reached, using a 25 ms TMA pulse. The purge times are not shown. As in Figure 5.3, each reactant exposure is equivalent to a half cycle, which equals 1.2 s, for all temperatures, for comparison.
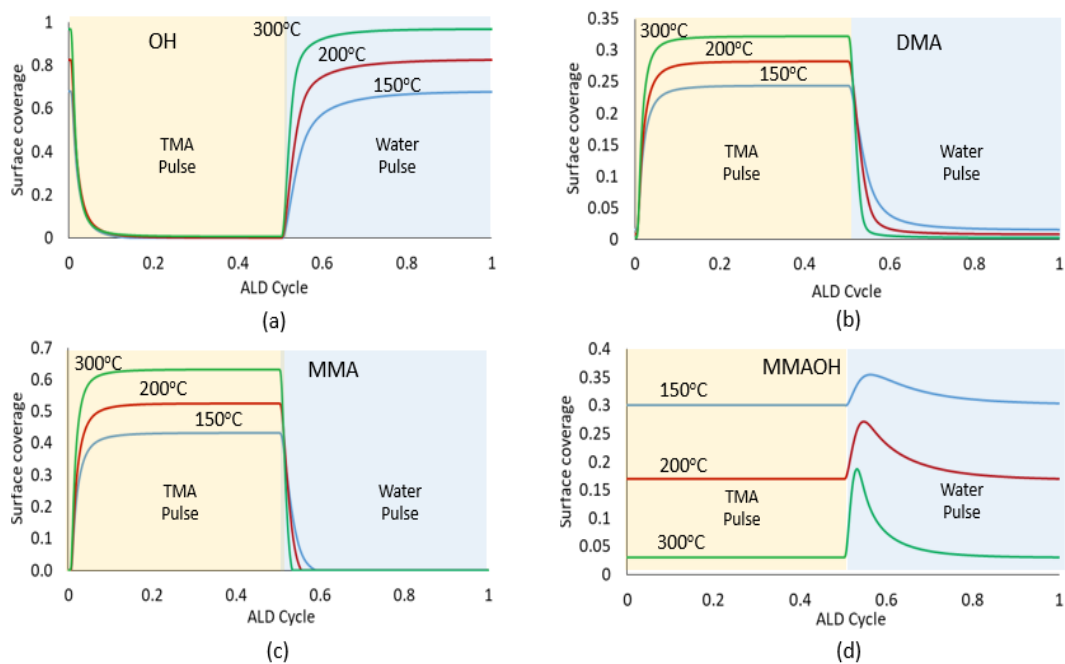
Figure 5.4. Model predictions of the surface coverage evolution of the four stable surface species during an ALD cycle, for three different temperatures: a) OH species coverage, b) DMA species coverage, c) MMA species coverage, d) MMAOH species coverage.

The initial coverage of the OH species during an ALD cycle in the steady state regime increases with temperature, namely 68.5%, 82.6% and 96.8% at 150°C, 200°C and 300°C, respectively. It is worth recalling that, for the steady state regime, the species distribution on the surface is regenerated at the end of each cycle. The DMA, MMA, MMAOH species present at the start of each cycle in Figure 5.4, are the sum of the species that could not be removed during the TMA and H_2O pulses of the previous non-steady regime simulated cycles.

During the TMA pulse, TMA molecules adsorb on the OH surface groups, and react according to reactions (R3) and (R4). So, the OH surface coverage decreases asymptotically, reaching zero. The DMA and MMA species are created, hence leading to the increase of their surface coverage. No significant effect of temperature can be

185

observed on the kinetics of these reactions. This is consistent with results from Vandalon and Kessels (Vandalon and Kessels, 2016) (Vandalon and Kessels, 2017), as detailed in Chapter 1, who showed that the temperature does not have a significant effect on the evolution of the surface methyl group coverage, during the TMA pulse.

The results are different for the H_2O exposure. During the H_2O pulse, water molecules adsorb on DMA and MMA molecules. The H_2O reaction leads to the formation of MMAOH species, on which a second H_2O molecule can adsorb and react. The product of all these surface reactions is the elimination of methyl groups and the formation of OH groups. So, during the H_2O pulse, the OH surface coverage increases and saturates to the initial value of the OH coverage at the start of the ALD cycle. The opposite behavior is observed for the DMA and MMA species, whose surface coverage decreases until they reach their initial value, at the start of the ALD cycle. The MMAOH surface coverage has the behavior of an intermediate species; it is created during the first instants of the H_2O exposure, as a product of the reaction between DMA and adsorbed H_2O species, and then is eliminated, by its reaction with another H_2O molecule. Indeed, its surface coverage first increases, reaching a maximum, and then decreases back to its initial value at the start of the ALD cycle.

The effect of temperature on the evolution of the surface coverage during the H_2O pulse is straightforward. At low temperature, the DMA and MMA group elimination, and then the OH group regeneration are slower. When the temperature is increased, the reactions are faster, explaining that the OH, DMA, MMA groups are regenerated or eliminated faster. The faster reactions of H_2O and DMA species at high temperature lead to a rapid formation of MMAOH, which reaches its maximum surface coverage faster than in the lower temperature regime (<200°C). Then the subsequent

reaction of MMAOH with H_2O is also favored at higher temperature, leading to the formation of OH groups.

Figure 5.4 also shows the mechanisms responsible for the decrease of the GPC at 300°C. In the steady state regime of the ALD cycle at 300°C, the initial and final OH surface coverage is 96.9%, which is higher than in the case of 200°C (82.6%). However, as shown in Figure 5.1, the GPC decreases from 200°C to 300°C, for the 60 ms TMA pulse. The decrease of GPC at higher temperature is attributed either to the activation of TMA desorption and/or to the decrease of the stable OH groups. Results of Figure 5.4 show that the TMA pulse is able to remove almost all the surface OH groups, even for the 25 ms step. Consequently, the major factor limiting the GPC at 300°C is the maximum number of OH groups that can be present on the surface. This is also validated by the fact that when the TMA pulse time is increased to 60 ms, the increase of thickness at 300°C is minimal.

5.2. Nano-scale model predictions

The nano-scale kMC model is used to extract predictions regarding the detailed surface chemistry, as well as some microscopic film properties, such as surface roughness. In particular, the coarse graining scheme As detailed in Chapter 3 is a simplified chemistry scheme used for the surface roughness predictions and the initial film nucleation and growth (Chapter 6), while the coarse graining scheme B corresponds to a detailed surface chemistry scheme.

Coarse graining scheme A

The resulting GPC as a function of temperature, as computed by the kMC model using the coarse graining scheme A, is shown in Figure 5.5. The sticking coefficients used for the model were the same as in section 5.1, i.e. $s_{0,TMA}=0.004$ and $s_{0,H2O}=0.014$.

Figure 5.5. GPC as a function of temperature: 25 ms TMA pulse (blue) and 60 ms TMA pulse (orange). Lines: kMC model results (Coarse graining scheme A), Circles: Experimental measurements.

Figure 5.5 shows that the kMC model can predict the GPC behavior with temperature, even for the simplified coarse graining scheme A, for temperatures above 150°C. For lower temperatures, the model predicts a lower GPC, due to the fact that it does not take into account the MMA species deposition. However, the thermal activation of the reactions at low temperatures and the GPC decrease at higher temperatures due to the OH concentration decrease can be predicted by this coarse graining scheme.

The coarse graining scheme A was also used to calculate the surface roughness evolution as a function of the number of cycles. The results are presented in Figure 5.6a, for three different process temperatures. As a qualitative comparison, the results of Puurunen (Puurunen, 2004) are plotted in Figure 5.6b. They are derived from a random deposition model, where a defined fraction of the surface is assumed to be covered during each ALD cycle, as discussed in section 1.3.2 of Chapter 1.
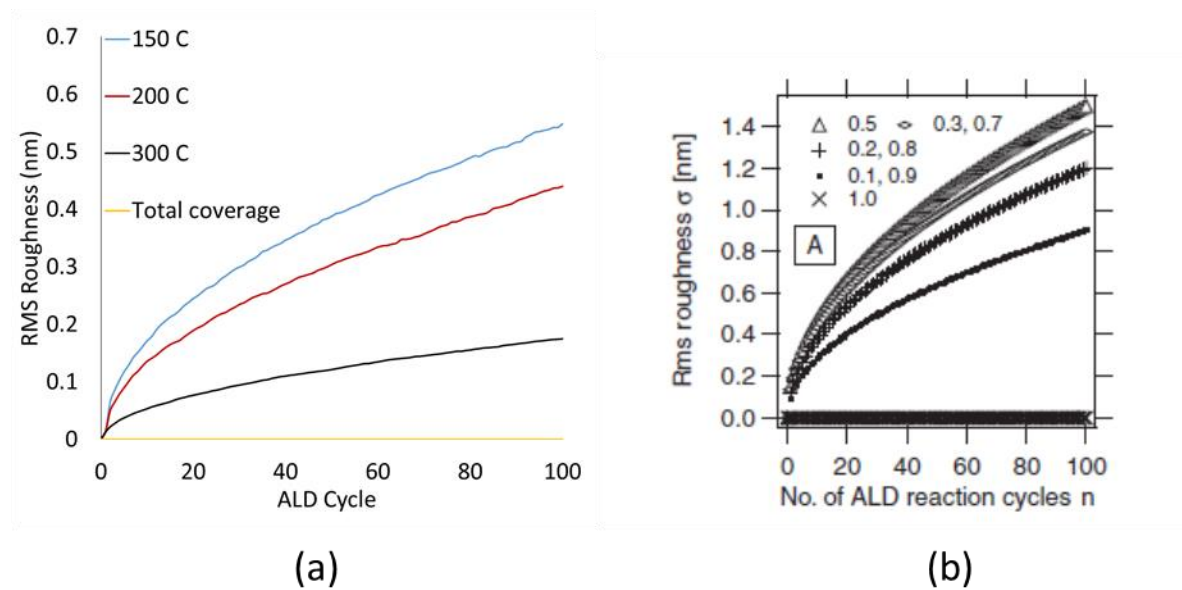
Figure 5.6. Roughness as a function of ALD cycles. a) kMC model predictions, for three different process temperatures, and assumed total coverage during each exposure step. b) Predictions of the random deposition model of Puurunen, for various predefined surface coverages after each ALD cycle (Puurunen, 2004)

Figure 5.6 shows the qualitative agreement for the predictions of the kMC model and the random deposition model of Puurunen. As the temperature is increased, the fraction of the surface covered after each ALD cycle is higher, resulting to more conformal deposition with a smaller roughness. If total coverage is achieved, the

roughness of the film is zero, as all the surface is covered after each exposure and a material monolayer is deposited on the whole surface after each ALD cycle. It is here reminded that this coarse graining scheme assumes a lattice consisting of adsorption sites, and does not take into account the substrate or the deposited material structure. Figure 5.6a shows that after 100 cycles, the roughness is below 1 nm, for all deposition temperatures. The low surface roughness of the deposited Al_2O_3 films was also confirmed by TEM and XRR measurements, presented in Chapter 6.

Coarse graining scheme B

With this coarse graining scheme, the deposition mechanisms were studied in detail. The computed GPC predictions of the kMC model as a function of temperature are presented in Figure 5.7, together with the experimental results. A good agreement is observed.
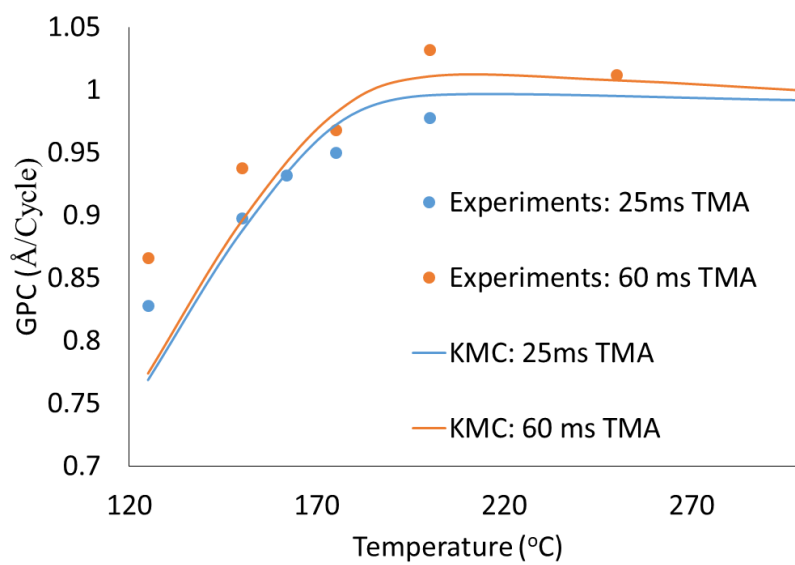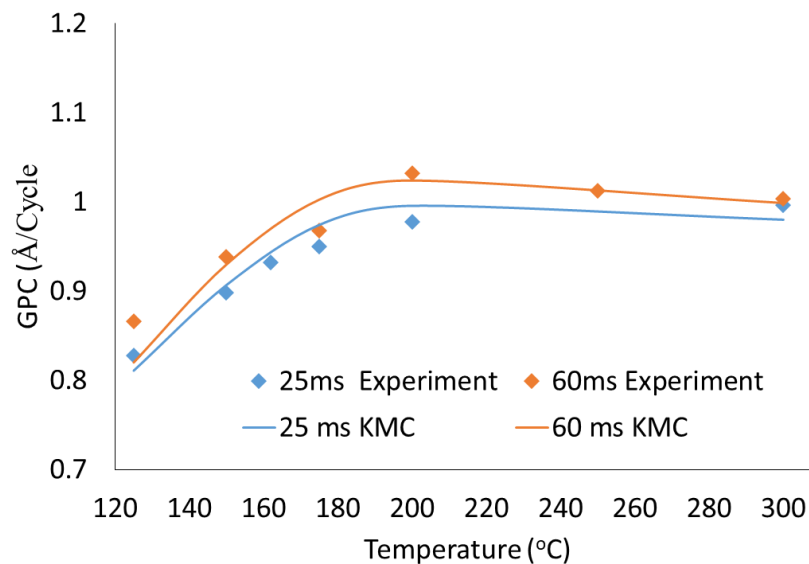
Figure 5.7. GPC as a function of temperature: 25 ms TMA pulse (blue) and 60 ms TMA pulse (orange). Lines: kMC model results (Coarse graining scheme B), Circles: Experimental measurements.

Figure 5.7 shows that the kMC model can predict the GPC behavior with temperature, for the detailed chemistry scheme. The model is more accurate for lower temperatures than in the simplified chemistry scheme. The thermal activation of the reactions at low temperatures and the GPC decrease at higher temperatures due to the OH concentration decrease can be predicted by the detailed chemistry scheme.

The computed number of surface events for a 10,000 sites lattice as a function of the surface temperature is presented in Figure 5.8a, for the H_2O exposure, and Figure 5.8b, for the TMA exposure. Results of Figure 5.8 are obtained once the surface has attained the topography where the number of OH groups is regenerated after each cycle, and the linear ALD regime is obtained (Chapter 3). The number of adsorption and desorption events are presented, in order to highlight the competition between the surface phenomena. The respective behavior of the reaction probabilities, computed as the percentage of reaction events over adsorption events, are presented in Figure 5.8c and 5.8d, for the H_2O and TMA exposure, respectively.
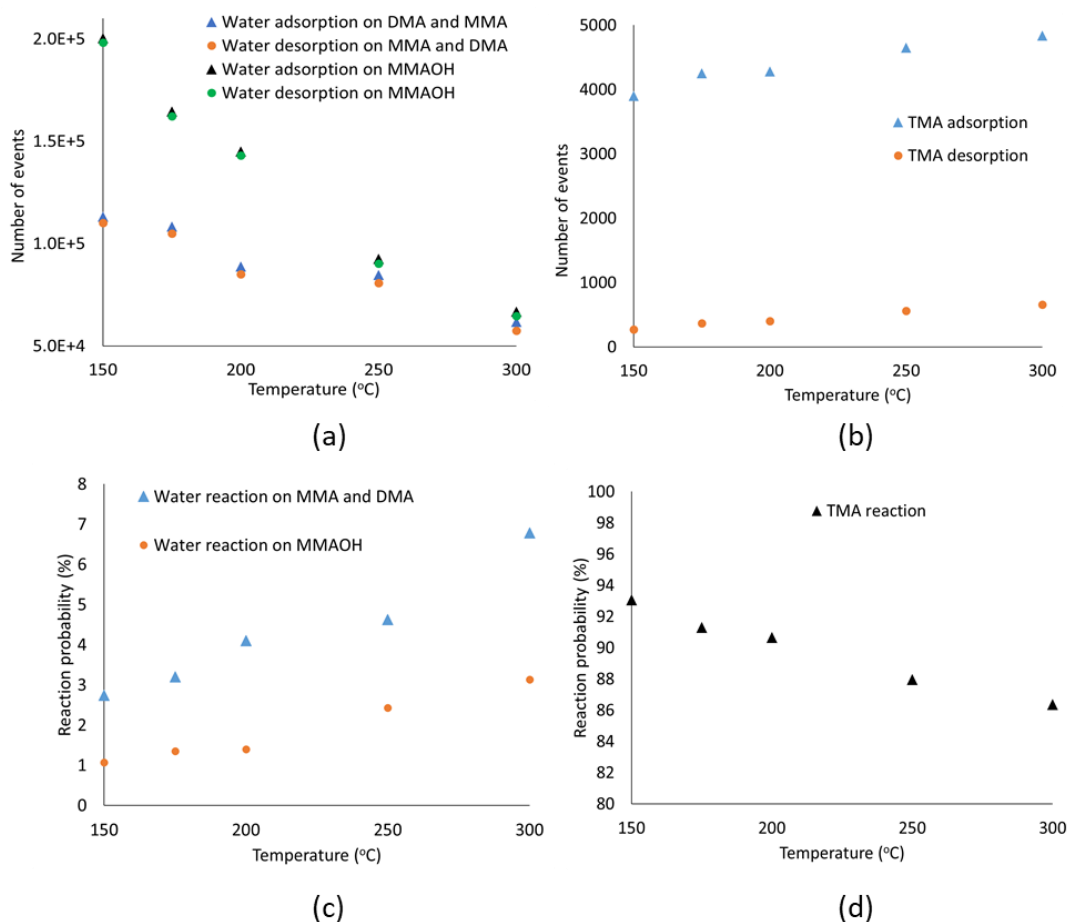
Figure 5.8. Top row: Number of surface adsorption and desorption events as a function of temperature for: a) H$_2$O exposure, b) TMA exposure. Bottom row: Reaction probabilities for: c) H$_2$O exposure, d) TMA exposure.

Figure 5.8a shows that by increasing the temperature, the number of H$_2$O desorption events is decreased, as the reaction probability is increased, as shown in section 5.1.2 of the present chapter, and Figure 5.8c. The number of adsorption events during the exposure is also decreasing with the temperature increase, as fewer adsorption events are needed to lead to the surface reactions. Once the surface reactions take place, the number of available sites for adsorption decreases, thus leading to a lower adsorption probability. The effect of temperature is observed for H$_2$O adsorption and desorption on all surface species. However, it is more evident in the case of H$_2$O

on MMAOH species, as the temperature increase has a higher thermal activation of the surface reaction, due to its higher activation energy, as shown in section 5.1.2 of the present Chapter and Figure 5.8c.

Figure 5.8b shows the number of TMA adsorption and desorption events on OH groups. An opposite behavior is observed than for H_2O. As the temperature increases, the TMA desorption is activated, and the number of TMA desorption events increases. This also increases the number of TMA adsorptions. More adsorption events are needed for surface reactions to take place and reduce the number of available adsorption sites. The reaction probability is decreased with the increase of temperature, due to the activation of desorption, as shown in section 5.1.2 of the present Chapter and Figure 5.8d.

The deposited mass during the ALD cycle at 300°C, for simulated experiment 11 (Table 2.1) once the surface topography has reached a point where it is regenerated after each cycle (Chapter 3, Section 3.4.4), is presented in Figure 5.9a. Quartz crystal microbalance (QCM) measurements by Elam et al. (Elam *et al.*, 2002) are presented for qualitative comparison in Figure 5.9b.

(a)   (b)
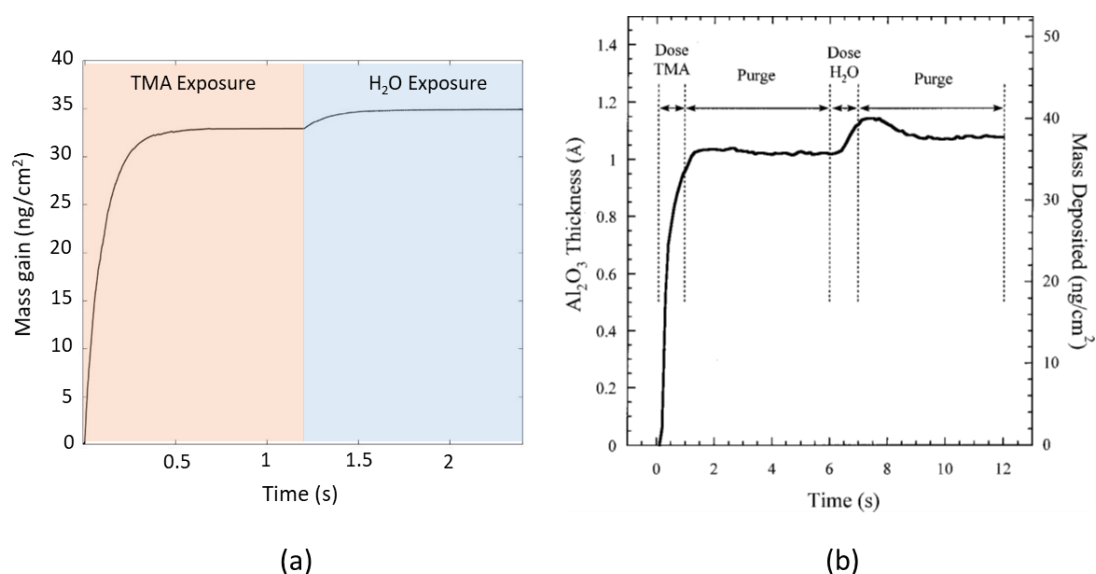
Figure 5.9. Mass gain evolution during an ALD cycle: a) kMC model predictions, for

simulated experiment 11, b) QCM measurements from Elam et al. (Elam *et al.*, 2002)

.

Figure 5.9 shows that the model can predict the behavior of the mass uptake

during the ALD cycle. Although the results of Elam et al. are for a process at 177°C,

the mass uptake after one cycle is comparable to the kMC model predictions (35-40

ng/cm^2). This is due to the fact that the reactant exposure times are significantly higher

(1 s) in the work of Elam et al.

The majority of the mass gain is realized during the TMA exposure (~31

ng/cm^2). This happens as TMA is deposited (M_{TMA}= 0.072 kg/mol) and one or two CH_4

species (M_{CH4}= 0.016 kg/mol) are desorbed, depending on the production of DMA or

MMA species, respectively. As seen in Chapter 3, MMA and DMA must be produced

in equal proportions for the surface OH groups are regenerated. Hence, two TMA

species lead to the deposition of one DMA and one MMA surface species, and

desorption of three CH_4 species.

During the H_2O exposure, a H_2O species (M_{H2O}=0.018 kg/mol) reacts with one

surface CH_3 species, leading to desorption of one CH_4 species (M_{CH4}= 0.016 kg/mol).

Hence, the mass uptake is considerably lower compared to the TMA exposure. In the

results of Elam et al., the mass uptake initially rises during the H_2O exposure, followed

by a slight decrease to a constant value. This can be assigned to H_2O physisorption on

the already deposited Al_2O_3 surface, which is finally desorbed during the purging time.

The kMC model does not take into account this physisorption and desorption, and hence

cannot predict this behavior.

The kMC model predictions for the number of bulk species deposited after the end of each ALD cycle is presented in Figure 5.10a. The O/Al atomic ratio of bulk species as a function of temperature after 100 cycles is presented in Figure 5.10b.
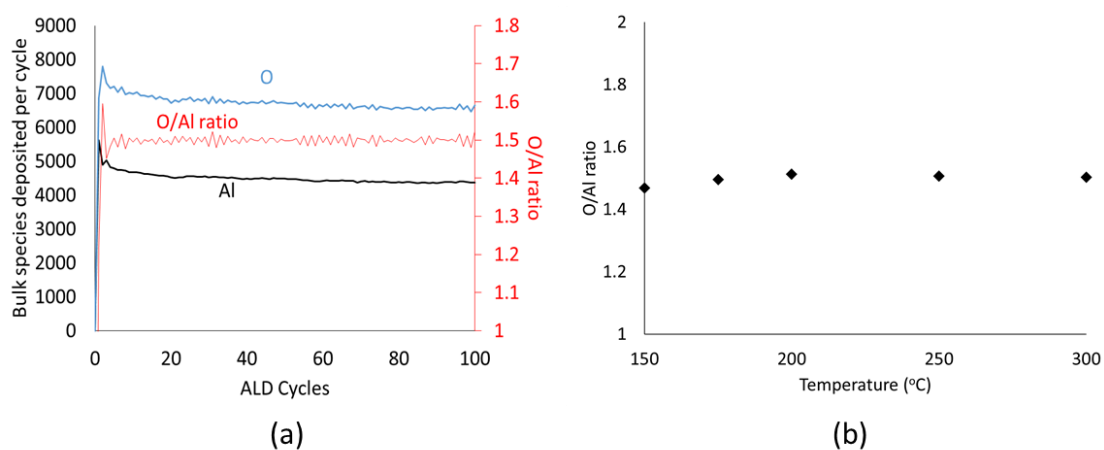
Figure 5.10. a) Evolution of the deposited bulk species number after the end of each ALD cycle, b) O/Al atomic ratio of bulk species as a function of temperature.

Figure 5.10a shows that after some ALD cycles (~50 cycles), the surface attains a state where the distribution of surface species is such that the surface can regenerate itself after each ALD cycle, as discussed in Chapter 3. Once this surface species distribution is reached, the deposited O and Al species are the same for each ALD cycle, and their ratio follows the Al_2O_3 stoichiometry (1.5 O/Al ratio). Hence, with the stochastic kMC model, the stoichiometry can be predicted by the model, without being assumed as for the wafer scale surface chemistry model.

Figure 5.10b shows that a stoichiometry close to Al_2O_3 is obtained for all process temperatures, for the linear ALD regime. Once the surface has attained the state and surface distribution of surface species where the number of OH groups can be regenerated during each cycle, the stoichiometry of the deposited bulk species is close to the Al_2O_3 stoichiometry, regardless of the temperature. This stoichiometry is

achieved due to the balance between DMA and MMA species deposited in equal proportions, as presented in Figure 3.10. Hence, the deposition in equal proportions of DMA and MMA species, is a valid assumption for the wafer scale surface chemistry model.

5.3. GPC profile on the substrate

Once validated, it is of main interest to couple the surface kinetic model with the reactor scale CFD one. In Chapter 4, it was shown that during the TMA pulse, a recirculation takes place inside the reactor chamber, which results in a non-uniform species distribution on the substrate surface. Figures 4.11 and 4.12 showed that the recirculation existing in the gas phase above the substrate affects the species distribution on the substrate, leading to a higher TMA concentration on the area between the substrate center and the side of the substrate near the loading door. The recirculation is due to the high convective flow that enters the reactor chamber during the first ms of the TMA pulse.

Figure 5.11 shows two alumina thickness profiles obtained in conditions corresponding to experiment 11 of Table 2.1 (Chapter 2), performed at 300°C. The profile in 5.11a is computed and was obtained by the coupled reactor CFD and surface reaction model at the wafer scale.. The profile 5.11b is experimental and was obtained though ellipsometry measurements on various points, covering the whole surface of the 200 mm wafer. For better visualizing the experimental measurements, the experimental points are interpolated, and a color map figure was developed in MATLAB®. The two

color maps of Figure 5.11 have a different color scale, in order to better show the thickness profile shape.
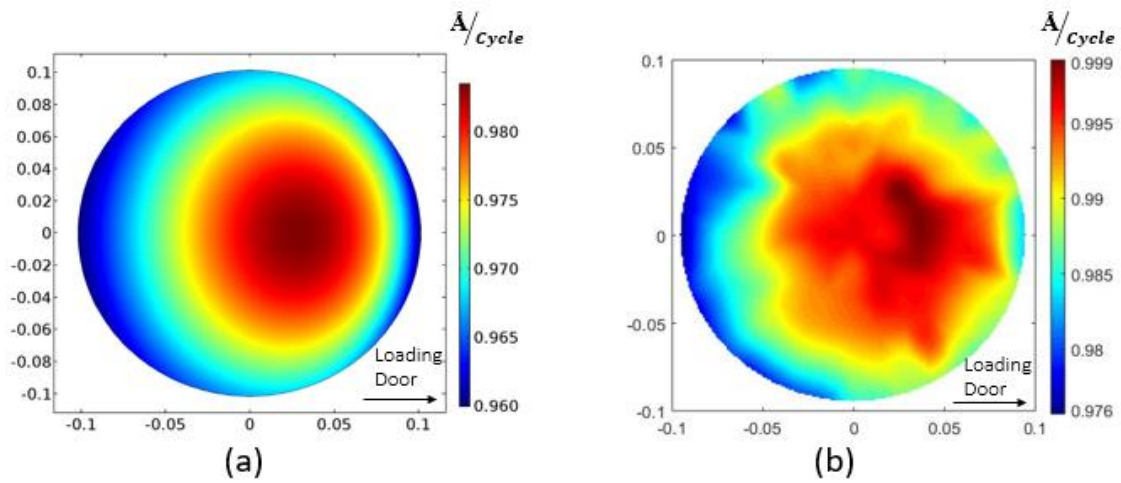
Figure 5.11. Profile of the GPC on the substrate surface corresponding to the experiment 11 (Table 2.1), performed at 300°C. a: Model predictions, b: Experimental measurements.

Comparison of the two maps reveals a qualitative agreement between model predictions and experimental GPC mapping. The higher GPC is obtained between the center of the wafer and the loading door side of the substrate. This GPC profile corresponds to the TMA species distribution profile on the surface, during the TMA pulse, as was shown in Figure 4.12. We can conclude that the recirculation taking place in the gas phase is dictating the species deposition profile on the substrate surface.

In most cases, ALD is considered as an ideal process, dependent only on surface kinetics. However, results of Figure 5.11, alongside with the results of Figure 4.11 and 4.12 infirm this statement and reveal that the flow field has a direct influence on the GPC profile.

Figure 5.12 presents the experimentally determined and computed evolution of the GPC along the surface of the substrate. The results correspond to two process

conditions, namely to experiments 11 and 12 (Table 2.1), characterized by two different TMA pulse durations, 25 ms (experiment 11) and 60 ms (experiment 12). Two different color scales are used: one for the simulation results and one for the experimental measurements.
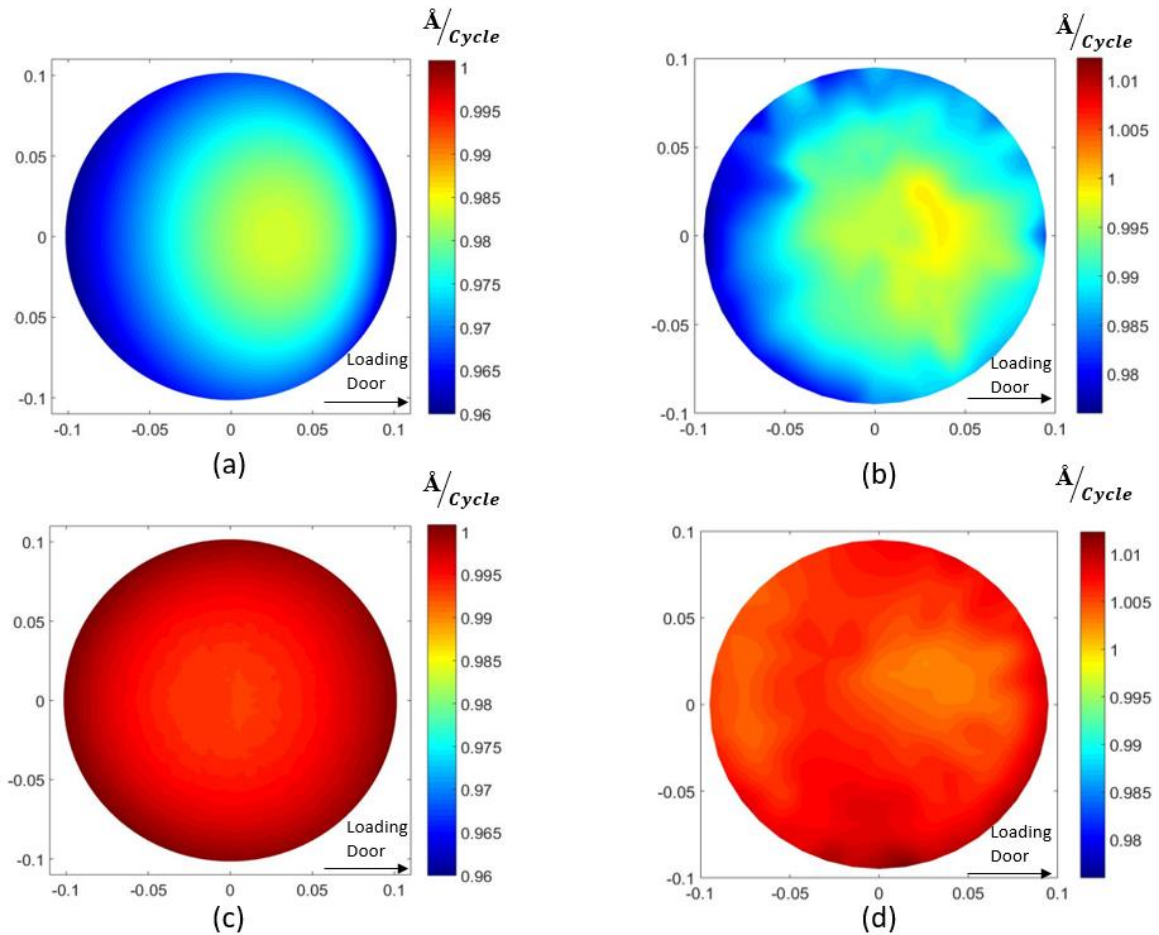
Figure 5.12. GPC profile on the substrate surface. a) Simulated Experiment 11, b) Experiment 11, c) Simulated Experiment 12, d) Experiment 12 (Table 2.1).

The measured GPC profile for experiment 11 corresponds to the gas phase TMA species distribution on the substrate, as presented in Figure 4.12. When the TMA pulse is increased (experiment 12), a more uniform GPC profile is obtained. The model predictions are in good agreement the experimental measurements.

We set the maximum non-uniformity, as the difference between the maximum and the minimum GPC obtained along the substrate, divided by the minimum GPC value:

$$Non - uniformity\% = \frac{max - min}{min} \cdot 100 \tag{5.4}$$

The experimentally determined maximum non-uniformity is 2.40% when using a 25 ms pulse (experiment 11), and decreases to 0.58% for the 60 ms TMA pulse (experiment 12). The equivalent values for the model are 2.45% for the 25 ms (simulation 11) and 0.83% for the 60 ms (simulation 12) TMA pulse. The GPC profile on the surface is also different for the 60 ms TMA pulse. From the above, it can be concluded that during experiment 11, the TMA pulse duration was not long enough to allow the adsorption of TMA on all the OH groups. Hence, the recirculation in the gas phase, which dictates the species distribution on the substrate surface, also dictates the thickness profile of the deposited film. In the case of experiment 12, the pulse duration is long enough to cover all the OH groups. Hence, the recirculation in the gas phase no longer dictates the thickness profile on the substrate. From the above we can conclude that, in contrast to the preconceived idea that ALD depends only on surface kinetics, the uniformity of the deposited film can also depend on the process conditions and reactor geometry.

5.4. Effect of purge time decrease

In Chapter 4, it was shown that a low temperature zone was present in the loading door region of the reactor, due to the non-heating of the loading door walls

(Figure 4.6a). This low temperature zone can seriously affect the purging efficiency, especially for the H_2O exposure. H_2O molecules are more difficult to desorb from cold surfaces. H_2O molecules will adsorb on the colder loading door walls and will take time to desorb. Hence, this increases the minimum purge time required to remove the reactant species present in the gas phase that could lead to CVD reactions during the next reactant exposure. The CFD model does not take into account CVD reactions and adsorption/desorption on the reactor walls. Hence the purging time effect was studied only by experiments.

In order to see the effect of this low temperature zone on the purging efficiency, a series of experiments using a reduced purge recipe (experiments 13-15 of Table 2.1) were performed. Thickness of the deposited film was measured along the diameter of the substrate, in order to see the effect of the colder loading door zone on the film uniformity.

The GPC along the substrate diameter is plotted for all four recipes in Figure 5.13.
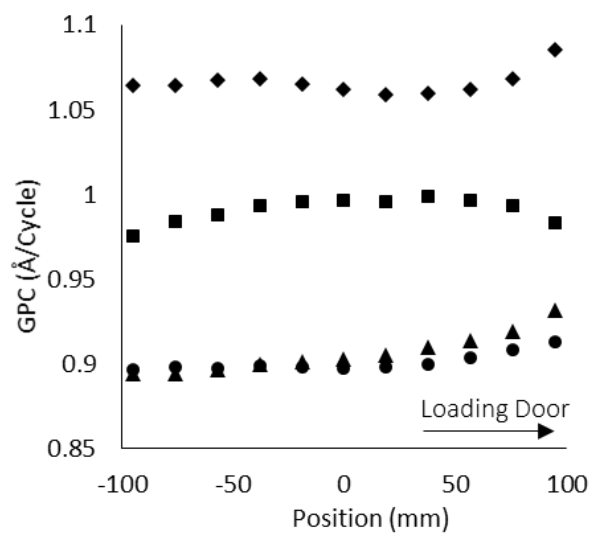
Figure 5.13. Effect of the purge time decrease (25 ms TMA pulse). Rhombus: 300°C reduced purge (experiment 13), Squares: 300°C 5 s purge (experiment 11), Circles: 150°C 20 s purge (experiment 3), Triangles: 150°C 10 s purge (experiment 14).

Reducing the purge time in the 300°C process leads to a significant increase in the GPC all over the substrate surface (experiment 13). This result can be attributed to the occurrence of CVD reactions, due to the co-existence of both TMA and H_2O in the gas phase. The GPC profile in the standard purge regime (experiment 11) was found to be dictated by the recirculation in the gas phase during the TMA pulse, as discussed in section 5.3. It differs from that of the reduced purge regime (experiment 13). Indeed, in experiment 13, a higher GPC is found at the side of the substrate exposed to the loading door. This is attributed to the fact that in the low-temperature loading door zone, there is a higher concentration of unremoved species, probably H_2O molecules due to their slow desorption (Chen *et al.*, 1994) from the loading door walls.

At 150°C, as the temperature is lower, the purge time needs to be increased because the desorption and diffusion processes are slower. When using a standard purge (20 s, experiment 3 in Table 2.1), the loading door side has a higher GPC than the rest of the substrate. This is caused by the lower temperature close to the loading door for the 150°C process. The desorption of H_2O molecules being even slower, the 20 s standard purge is not long enough. This effect is also present when the purge time is reduced to 10 s (experiment 14). In this case, the purge time reduction has no effect on the whole side of the substrate that is situated on the opposite side from the loading door. However, on the loading door side of the substrate, the thickness is increased. The closer we get to the loading door, the higher the GPC increase due to purge time reduction. This is expected since the low temperature in the loading door region favors CVD reactions due to unremoved reactants. The maximum non-uniformity was 1.8%

for the 20 s purge (experiment 3), while this value increased to 4.2% for the 10 s purge (experiment 14). This effect was more evident when the purge time decreased at 150°C to a highly reduced 5 s purge (experiment 15). The effect of the lower temperature of the loading door zone on the uniformity is shown in Figure 5.14, where the GPC profile along the substrate diameter is plotted, for experiments 4 and 15.
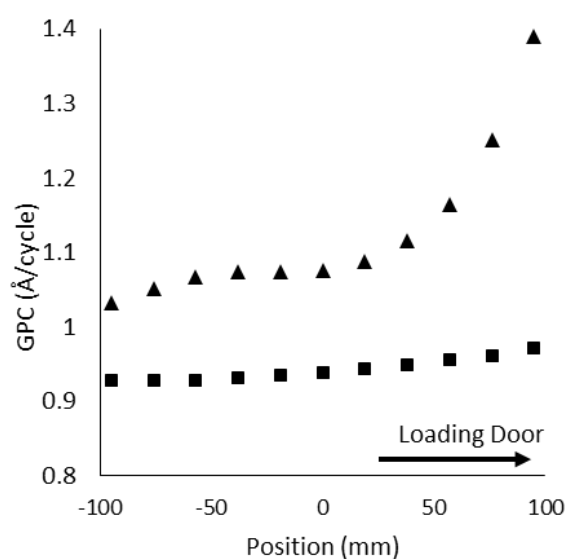
Figure 5.14. Effect of the purge time decrease (150°C, 60 ms TMA pulse). Squares: 20 s purge (experiment 4), Triangles: 5 s purge (experiment 15).

The effect of the lower temperature zone in the loading door is clear. For the experiment 4, the GPC is still higher in the loading door side of the substrate, showing that the 20 s purge time is not long enough. The maximum non-uniformity is 4.6%, which is higher than for the 25 ms TMA pulse (experiment 3). When the purge is reduced to 5 s (experiment 15), the whole substrate has a higher GPC, proving that CVD reactions take place all over the substrate due to the co-existence of reactants in the gas phase. However, the GPC near the loading door is highly increased, leading to a significant increase of non-uniformity (maximum value of 34.5%).

The above results show that a better design of the reactor with a heated loading door would allow the reduction of the purge time, ensuring high uniformity, while with the present design even the 20 s purge is not long enough to remove the influence of the loading door. This shows that although ALD is perceived as a process dependent only on surface chemistry, the transport phenomena inside the reactor, affected by the process design and the reactor geometry can have a major impact on the film deposition. These results reveal the importance of such studies for the efficient design of the ALD reactor geometry and optimization of the process conditions, in order to deposit ALD films of high purity and uniformity.

Summary – Conclusions

In this Chapter, the surface mechanisms involved in the ALD of Al_2O_3 are thoroughly investigated, with the use of computational models. The model predictions are compared with experimental measurements and literature results, in order to validate the approach.

As revealed by a reaction probability analysis, the competition of surface reactions with desorption is found to be the main factor that limits the deposition at low temperature. The TMA exposure is limited by the adsorption process, and the competition with desorption is not significant. However, the H_2O exposure is limited by the competition between desorption and surface reaction of H_2O with MMAOH species at low temperatures. The adsorbed H_2O molecules on the MMAOH species are more likely to desorb than react, thus leading to non-full coverage. These results are in good agreement with the experimental results of Vandalon and Kessels (Vandalon and

Kessels, 2016)(Vandalon and Kessels, 2017), who showed that the H_2O step cannot remove the totality of the surface CH_3 groups, during the H_2O pulse.

Our work also demonstrates that the decrease of the GPC at higher (300°C) temperature, previously presented in the literature (Ott *et al.*, 1997)(Vandalon and Kessels, 2016)(Pan *et al.,* 2015) (Xie *et al.,* 2015) is mainly due to the decrease of the number of stable surface OH groups present on the surface, which decreases with temperature (Haukka and Root, 1994), and secondarily to the activation of the TMA desorption. It is shown that temperature increase does not significantly impact the TMA kinetics on the surface. However, in the case of H_2O, the time needed for reaching surface saturation was found to decrease with increasing temperature. These results are also in agreement with those of Vandalon and Kessels (Vandalon and Kessels, 2016)(Vandalon and Kessels, 2017).

The stochastic kMC surface chemistry model provided estimations for properties in the nano-scale, with the detailed chemistry mechanisms. The evolution of surface roughness as a function of the ALD cycles was computed and compared to models for random deposition previously presented in literature. The deposited mass evolution with time during a single ALD cycle was also predicted by the model, yielding a qualitative agreement with QCM measurements presented in literature, for the same ALD process. Finally, the deposited bulk species after each cycle were computed by the model. The deposited species could be used to compute the stoichiometry of the deposited film, yielding Al_2O_3 stoichiometry. This analysis shows that such models can be used to extract information about the detailed surface mechanisms and some microscopic properties of the film.

The effect of the transport phenomena prevailing in the reactor chamber on film deposition was investigated, both computationally and experimentally. Results show a direct link between phenomena taking place in the gas phase, such as the gas recirculation and low temperature zones presented in Chapter 4, and the resulting film uniformity, and thus nuance the established vision of ALD as being solely controlled by surface kinetics. They confirm the necessity to integrate CFD and surface kinetics coupled modeling analyses to the ALD process design and development, as the interplay between surface mechanisms and transport phenomena is dictating key aspects of deposition.

Chapter 6: Initial deposition steps of Al_2O_3 films on HF cleaned and in situ plasma pretreated Si

In this Chapter, a complete set of characterization techniques are used to characterize the initial deposition steps, the composition and the chemical nature of the deposited Al_2O_3 films and their interface with HF- cleaned Si.

The island growth model is validated by comparing its predictions to literature data in section 6.1. In section 6.2, the film growth regime during the initial deposition steps is studied with the use of XRR measurements and the geometric island growth model. The film morphology, as well as the interfacial oxide layer thickness and its evolution with the number of ALD cycles is investigated in section 6.3. The chemical nature and composition of the interfacial oxide layer, as well as its formation mechanisms, are presented and discussed in section 6.4.

Furthermore, the effect of an *in situ* plasma N_2-NH_3 pre-treatment of the HF-cleaned Si substrate on the initial deposition steps and the Si substrate oxidation is studied and discussed in section 6.5. The results of this chapter have been the subject of two scientific journal articles, published in Applied Surface Science (Gakis *et al.*, 2019) and Journal of Applied Physics (Gakis *et al.*, 2019).

6.1. Island growth model validation

The analysis of the initial deposition steps during the ALD of Al_2O_3 from TMA and H_2O is realized using a combined experimental and computational approach. The experimental investigation consists of XRR and TEM/STEM characterizations, supported by results from the coupled CFD - wafer scale surface reaction models, combined with the geometric island growth model presented in Chapter 3. In order to test the validity of the island growth model, its results are compared to literature data.

The island growth model does not consider chemical mechanisms, and is dependent only on the geometric characteristics of the island growth. Hence, it is independent to the deposited material, as long as the deposition takes place in island-like mode and the material is amorphous (Nilsen *et al.*, 2007). To demonstrate the validity of the model, its results are compared with literature experimental data, for the ALD of Al_2O_3 on Si-H (Besling *et al.*, 2002), PtO_2 on Si with native SiO_2 (Knoops *et al.,* 2009), and W on SiO_2 (Elam *et al.*, 2001). In all cases, the initial radius value, r_0, was set to zero. The Δr value was set to the GPC at the linear regime, and the nucleation density value, N_d, was fitted. The results are presented in Figure 6.1.
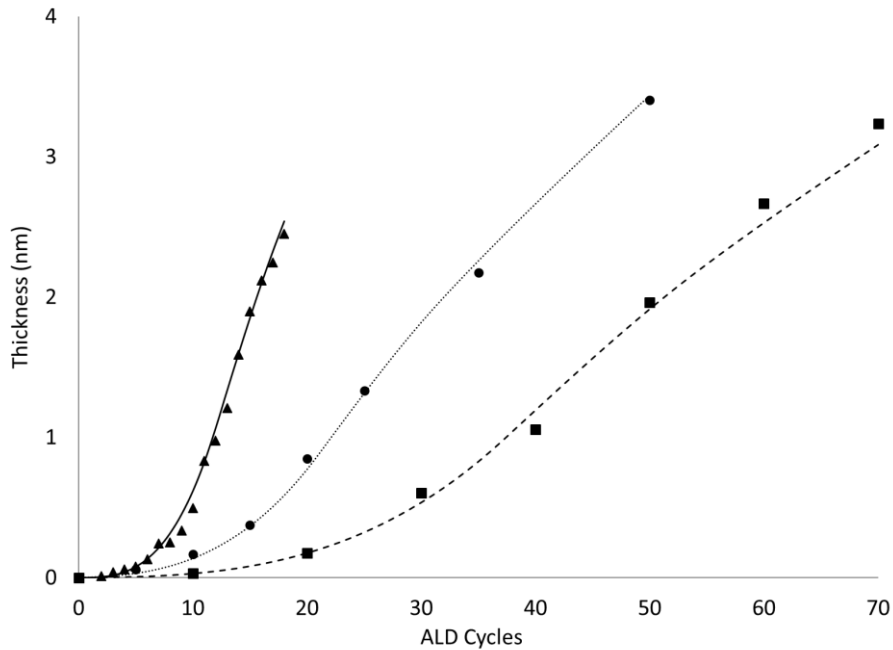
Figure 6.1. Comparison of island growth model predictions with literature data, using $r_0=0$: Data from literature: Triangles: W on SiO_2 (Elam *et al.*, 2001). Circles: Al_2O_3 on Si (Besling *et al.*, 2002). Squares: PtO_2 on SiO_2, (Knoops *et al.*, 2009). Model predictions: Continuous line: $N_d=0.06$ groups/nm^2, $\Delta r=0.17$ nm. Dotted line: $N_d=0.09$ groups/nm^2, $\Delta r=0.07$ nm. Dashed line: $N_d=0.07$ groups/nm^2, $\Delta r=0.047$ nm.

A good agreement is observed between model predictions and literature data, proving that the model can be used to analyze the deposition during the first cycles, and extract an estimation of the nucleation density. The growth mode can be predicted and characterized, without considering any chemical reactions, but only geometrical principles, using two fitting parameters. Hence, the initial growth evolution can be explained by geometrical aspects of the film growth, without assuming an increasing surface reactivity with the number of ALD cycles. The growth regimes during the first steps of deposition can be separated and studied, as well as the transition between them. The nucleation density fitted for the data in Figure 6.1 varies between 0.06 and 0.09 groups/nm^2. Nucleation densities derived from the fitting of such models to

experimental measurements have previously been assigned to surface defect sites (Puurunen *et al.,* 2004)(Nilsen *et al.,* 2007).

6.2. Initial growth of Al$_2$O$_3$ on HF-cleaned Si

The ALD films, deposited using various numbers of cycles at 300°C, with the same conditions as experiment 11 in Table 2.1, (TMA pulse: 0.025 s, H$_2$O pulse: 0.1 s, purge for reactants: 5 s) were characterized by XRR to obtain their thickness. The XRR measurements and fit are shown in Figure 6.2a. The island growth model was fitted to the obtained XRR thickness, as shown in Figure 6.2b. For the island growth model, the GPC at the linear regime calculated from the reactor and wafer scale chemistry model was implemented as a value for Δr (0.1 nm/cycle). The initial island radius was set to zero, and the nucleation density, N$_d$, was fitted to the thickness derived from the XRR measurements. The predicted evolution of the GPC and the different growth regimes are shown in Figure 6.2c.

Results of Figure 6.2b show that an induction period occurs during the initial stages of Al$_2$O$_3$ ALD on H-terminated Si. This behavior has been previously reported by Puurunen et al. (Puurunen and Vandervorst, 2004)(Puurunen *et al.*, 2004) for the ALD of alumina on Si-H. This is due to the low reactivity of the Si-H surface towards ALD reactants (Frank *et al.*, 2003)(Halls and Raghavachari, 2003). This low reactivity prevents TMA and H$_2$O to deposit on the surface.

Nucleation is reported to start on surface defect sites (Puurunen and Vandervorst, 2004)(Puurunen *et al.*, 2004)(Frank *et al.*, 2003), such as surface OH groups or oxygen bridges that have not been totally removed during the substrate

cleaning process. Then, subsequent exposure leads to preferential deposition of the reactants on the already deposited material and its adjacent surface sites (Puurunen and Vandervorst, 2004)(Frank *et al.*, 2003), thus leading to the formation of islands, as assumed by the island growth model. The good agreement between the island growth model and the XRR measurements shows that indeed island growth can explain the apparent initial growth evolution of the film.

(a)

(b)

(c)
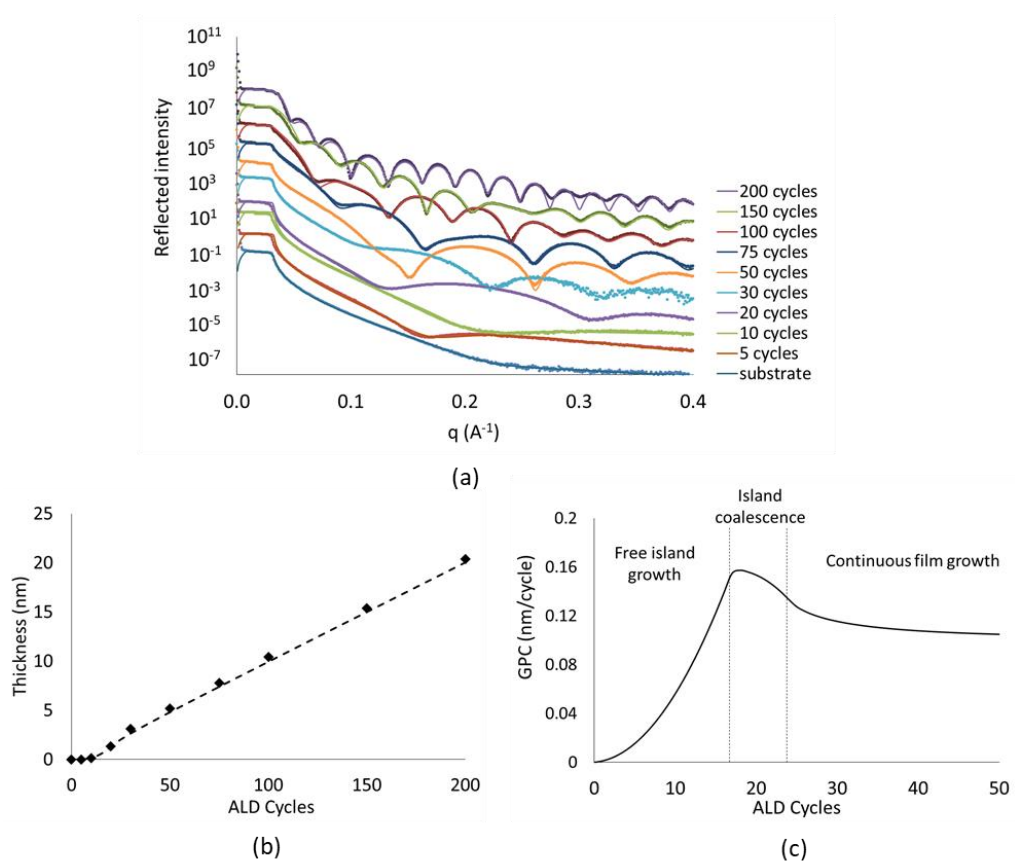
Figure 6.2. a) XRR measurements and fit. b) Layer thicknesses derived from XRR fitting (rhombus) and island growth model predictions (dashed line) for the ALD of Al_2O_3 on a H-terminated Si substrate. c) Evolution of the GPC as a function of the number of cycles: model predictions, using $\Delta r = 0.1$ nm. Model fitting parameters: $N_d=0.08$ groups per nm^2, $r_0=0$ nm.

211

The fitting of the model yields to an estimation of the surface concentration of the initial nucleation sites, i.e. the surface defect sites. The GPC at the steady ALD regime is 0.1 nm/cycle, taken from the ellipsometry measurements and the wafer scale surface chemistry surface kinetic model presented in Chapter 5. Thus, by setting Δr=0.1nm, the resulting N_d value needed to fit the model to the XRR measurements is N_d=0.08 groups/nm^2. If this value is assigned to OH groups, it is 1.27% of the surface concentration of OH groups on silica at 300°C, as reported by Haukka and Root (Haukka and Root, 1994). This means that the HF cleaning is efficient to remove the native oxide layer.

As the number of cycles increases, island growth and coalescence occurs. The different regimes are dictated by the state of the growing islands and are shown by the characteristic evolution of the GPC in Figure 6.2c. Islands growing freely on the surface increase the available surface for deposition and hence the GPC is enhanced. This occurs until $r = r_{c\,1-2} = \frac{b}{2}$, as described in Chapter 3. In the present case, this happens after 18 ALD cycles. From the moment the islands start to coalesce, the surface available for deposition starts to decrease, until the formation of a continuous film. This happens when $r = r_{c\,2-3} = \frac{\sqrt{2}\cdot b}{2}$, which in the present case is after 25 ALD cycles. This prediction is in agreement with the experimental observations of Puurunen et al. (Puurunen *et al.*, 2004). From then onwards, the coalescence continues, decreasing the surface available for deposition, and thus the GPC, until layer by layer growth is reached, where the GPC becomes constant. The above analysis shows that at least 25 ALD cycles must be performed, in order to obtain a continuous Al$_2$O$_3$ film. This approach also shows that the evolution of the film growth can be explained by the

geometric aspects of nucleation and growth, without assuming an increasing surface reactivity with the number of ALD cycles.

In order to validate this effect, the island growth model is compared to results of the stochastic kMC model, using the coarse graining scheme A. For the kMC model, the surface is initially assumed to be covered by Si-H species. The activation energies for desorption and surface reactions of the adsorbed reactants on the Si-H species are taken from Halls and Raghavachari (Halls and Raghavachari, 2003). A concentration of surface defects, corresponding to OH species is assumed *a priori*. These surface defects are then randomly distributed on the surface. Once an Al_2O_3 group has been deposited on the surface, its neighboring Si-H sites are assumed to be hydroxylated and become OH sites, hence making deposition on those sites more favorable.

The computed thickness evolution for the island growth model (N_d=0.08 groups/nm^2, r_0=0 nm, Δr=0.1 nm/cycle) and the kMC model assuming 1%, 3%, 5% and 8% of the initial surface being covered by OH defects, is plotted in Figure 6.3a, and compared to the thickness derived from the XRR measurements. The computed GPC from the different models is shown in Figure 6.3b. Finally, in order to compare to the GPC derived from XRR measurements, the averaged GPC for the models after the respective number of cycles of the deposited samples (5, 10, 20, 30, 50, 75, 100, 150, 200 cycles), is shown in Figure 6.3c.
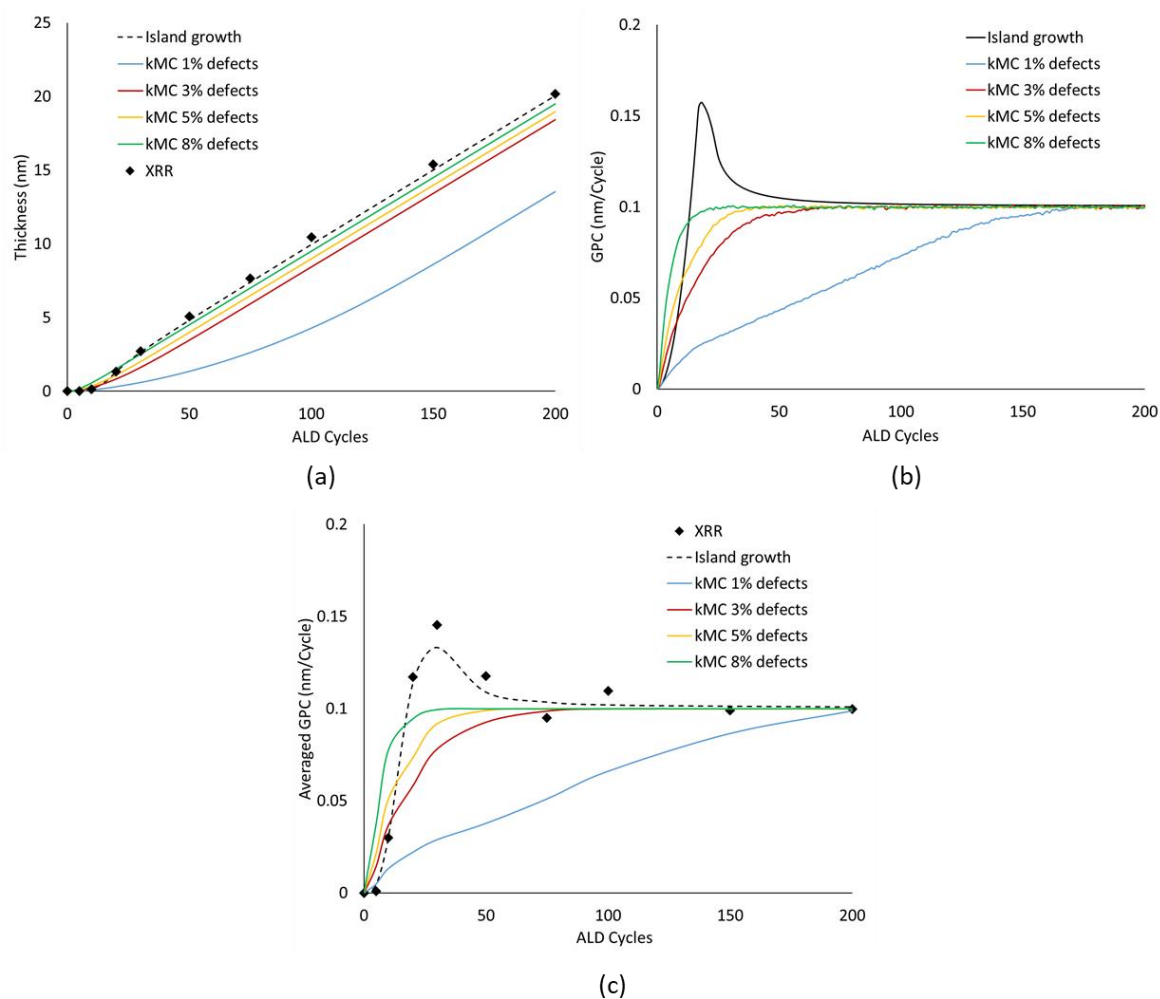
Figure 6.3. a) Thickness evolution as a function of the number of cycles: kMC model, island growth model and thickness from XRR. b) GPC evolution as a function of the number of cycles: kMC model, island growth model. c) Average GPC evolution as a function of the number of cycles: kMC model, island growth model and GPC from XRR.

Figure 6.3a shows the different behavior of the models. The kMC is unable to fit the XRR thickness for 1%, 3% and 5% of initial OH defect concentration of the surface. Although the kMC model with an 8% of initial OH defect concentration provides a better agreement, it nonetheless cannot fit the measurements as well as the island growth model. This is due to the different behavior of the thickness evolution, due to the three-dimensional geometrical aspects of the growth, such as the increase of

214

the available surface for deposition and island coalescence, as previously discussed. The kMC model does not take these aspects into account, and hence cannot predict the thickness evolution behavior. This is evident in the GPC results of Figure 6.3b.

For the kMC model predictions, the GPC starts from zero and increases until reaching the value of the linear ALD regime (0.1 nm/cycle). By altering the initial OH concentration, the model reaches this value in a lower number of cycles, as the surface is more quickly covered by ALD material. However, the kMC model does not take into account the three dimensional islands, and only computes deposition on already determined surface sites. On the other hand, the island growth model takes into account the three dimensional aspects of the growth and the island coalescence, as previously described, and predicts the evolution of the surface available for deposition.

Figure 6.3c shows the averaged GPC over the number of cycles used for each deposited sample, in order to be able to compute with the average GPC derived from the XRR measurements. Figure 6.3c indeed shows that the behavior of the GPC is better predicted by the island growth model, hence validating the island growth regime during the first cycles, and the effect of the island coalescence on the ALD growth evolution.

Having validated the above approach with experimental measurements, the computational analysis can be extended to study the effect of the process conditions, such as the process temperature and the TMA pulse duration, on the initial steps of deposition. This is done by setting the Δr value equal to the predicted GPC from the reactor and wafer scale chemistry model (Figure 5.1), for each set of process parameters. The nucleation density is assumed to be independent of the temperature and is set to the value derived by the fitting of the island growth model to the XRR

measurements: N_d=0.08 groups/nm^2. The effect of temperature and TMA pulse duration on the thickness evolution is presented in Figure 6.4.
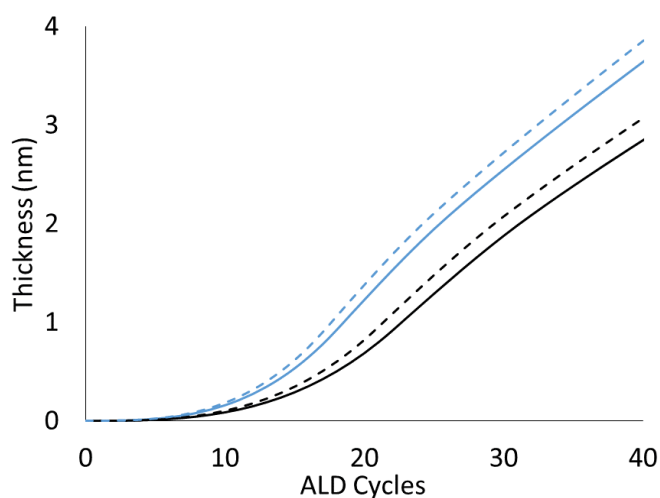
Figure 6.4. Thickness evolution predicted by the island growth model as a function of the number of cycles. Black lines: 125°C, Blue lines: 200°C. Continuous lines: 0.025 s TMA pulse, Dashed lines: 0.060 s TMA pulse.

Figure 6.4 shows that the temperature increase between 125°C and 200°C leads to a slight decrease of the nucleation period. The TMA pulse duration increase between 0.025 and 0.060 s has the same effect. As the GPC is smaller during these first steps, more cycles are needed to obtain a continuous film. Specifically, 32 cycles are needed to obtain a continuous film at 125°C, using a 0.025 s TMA pulse. Increasing the TMA pulse to 0.060 s, reduces the number of cycles needed to 30. For the ALD at 200°C, 26 cycles are needed to obtain continuity with a 0.025 s TMA pulse, while this value is incrementally reduced to 25 cycles, with the 0.060 s TMA pulse.

6.3. Morphological characterizations of Al$_2$O$_3$ films on HF-cleaned Si

For the morphological characterizations of the films, a series of samples was deposited at 300°C, with the same conditions as experiment 11 of Table 2.1 (0.025 s TMA pulse, 0.100 s H$_2$O pulse, 5 s purge for both reactants), using different number of cycles. The obtained Al$_2$O$_3$ films after different numbers of ALD cycles were characterized by TEM. The bulk of the Al$_2$O$_3$ is distinguished from the Si substrate and the C capping layer. The films are all amorphous, confirmed by Fast Fourier Transform (FFT) analysis of the TEM images, in contrast to the crystalline Si substrate. The TEM images of the film deposited after 200 and 550 ALD cycles are shown in Figure 6.5.
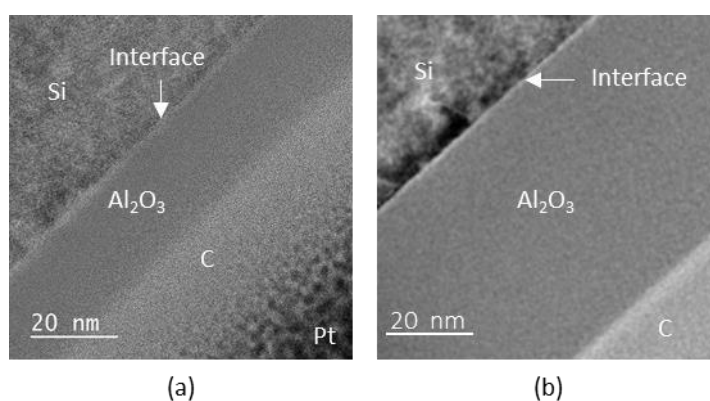
Figure 6.5. TEM images of ALD Al$_2$O$_3$ layers after a) 200 cycles, b) 550 cycles

It is seen that the Al$_2$O$_3$ film is uniform and conformal. It is distinguished by a darker contrast than both the Si substrate and the C capping layer. The ALD layer after 200 ALD cycles (Figure 6.5.a) has a thickness of ~20.3 nm. The GPC computed from the wafer scale surface kinetics model, as well as the GPC derived from the XRR and ellipsometry measurements are consistent with this measurement. A similar GPC was also measured for the sample deposited using 550 ALD cycles (Figure 6.5b).

An interfacial layer between the ALD film and the Si substrate is also observed in Figure 6.5 as a bright-contrast layer. Literature reports have previously shown the presence of this interfacial layer, between the Al_2O_3 film and the Si substrate (Kaur *et al.*, 2017)(Chang *et al.,* 2004)(Werner *et al.*, 2011), as presented in Figure 1.12 and discussed in Section 1.2.3.2 of Chapter 1. This interface is reported to mainly consist of Si oxides (Renault *et al.*, 2002)(Naumann *et al.*, 2012)(Gosset *et al.*, 2002), formed by interdiffusion of Si and O species. To further investigate the interfacial layer morphology and film evolution, TEM images of the Al_2O_3 films formed after 5, 20 and 200 ALD cycles, deposited with the process conditions of experiment 11 in Table 2.1, are shown in Figure 6.6. The films deposited using 5 and 20 ALD cycles were characterized by STEM in bright-field, for a more clear distinction of the interface.
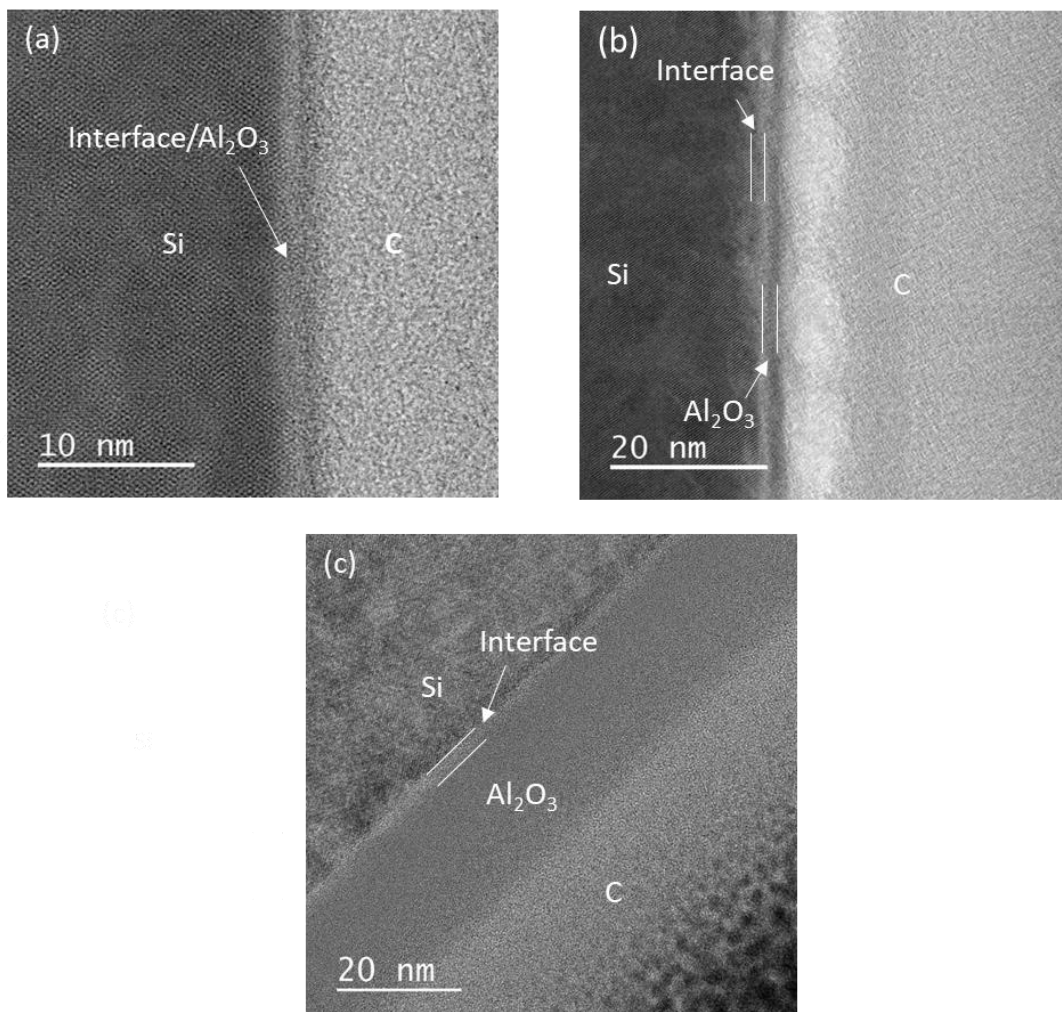
Figure 6.6. TEM and STEM images of ALD Al_2O_3 layers using: a) 5 b) 20 c) 200 cycles

For the sample deposited using 5 cycles (Figure 6.6a), the STEM micrograph shows no clear distinction between an Al_2O_3 layer and the interface. According to the island growth model and the results of Puurunen et al. [16], the deposition is still in the nucleation period, where island growth takes place. A layer with a varying darker contrast could be argued to be present between the C layer and the brighter contrast oxide layer. It could be attributed to islands closely behind each other in the cross-sectional sample, giving the appearance of a continuous layer (Puurunen *et al.*, 2004). The layer's varying contrast consolidates this explanation. For this sample, a combined layer of ~1.6 nm is measured between the crystalline structure of the Si substrate and the brighter contrast of the C layer.

For films deposited using 20 and 200 cycles (Figures 6.6b and 6.6c, respectively) the interfacial layer is clearly visible and can be distinguished from both the Si substrate and the Al_2O_3 layer. The measured Al_2O_3 and interface layer thicknesses by the TEM and STEM analysis are summarized in Table 6.1 for all samples.

An interface of ~1.8nm was measured for the 20 cycles sample (Figure 6.6b), while the 200 cycles sample showed an interface of ~2 nm (Figure 6.6c). The interfacial layer thickness is close for both samples, which shows that between 20 and 200 cycles, little or no Si oxidation took place. So, after a certain thickness, the Al_2O_3 layer serves as a diffusion barrier for Si and O species. This has been previously reported for the Al_2O_3 deposition on Cr surfaces, where a thin thermal ALD Al_2O_3 layer was found to serve as an efficient diffusion barrier to prevent Cr oxidation during subsequent plasma enhanced ALD (Foroughi-Abari and Cadien, 2012).

The 20 cycles sample (Figure 6.6b) also exhibited a slightly higher roughness on its interface with the C capping layer. This is attributed to the end of the island growth mode. According to the island growth model, the island coalescence has started at that point and a continuous layer is obtained only after 25 cycles. The varying contrast along the layer in Figure 6.6b could be assigned to this phenomenon. In their work, Puurunen et al. (Puurunen *et al.*, 2004) revealed the Al_2O_3 islands on Si, by *in situ* depositing an amorphous Si layer on top of their samples. When the Al_2O_3 layer was not continuous, the deposited Si aligned epitaxially on the Si substrate, thus making the Al_2O_3 islands visible. They estimated that the film becomes continuous between 20 and 30 cycles, in agreement with the predictions of the island growth model presented here.

No. of ALD cycles	Al_2O_3 thickness (nm)	Interface thickness (nm)
5	1.6 (impossible to distinguish between film and interface)	
20	~1.3	~1.8
200	~20.3	~2
550	~55.4	~2

Table 6.1. Experimental thickness of the Al_2O_3 film and of the interfacial layer measured by TEM and STEM, for all samples

6.4. Chemical composition of Al₂O₃ films and their interface with HF cleaned Si

The deposited films were characterized by XPS, in order to study the chemical nature of the deposited films and their interface with Si. The Al 2p, O 1s and Si 2p spectra are presented in Figure 6.7, for ALD films deposited using 10 and 50 cycles. The intensity scales have been adjusted to highlight the different features of the spectra.
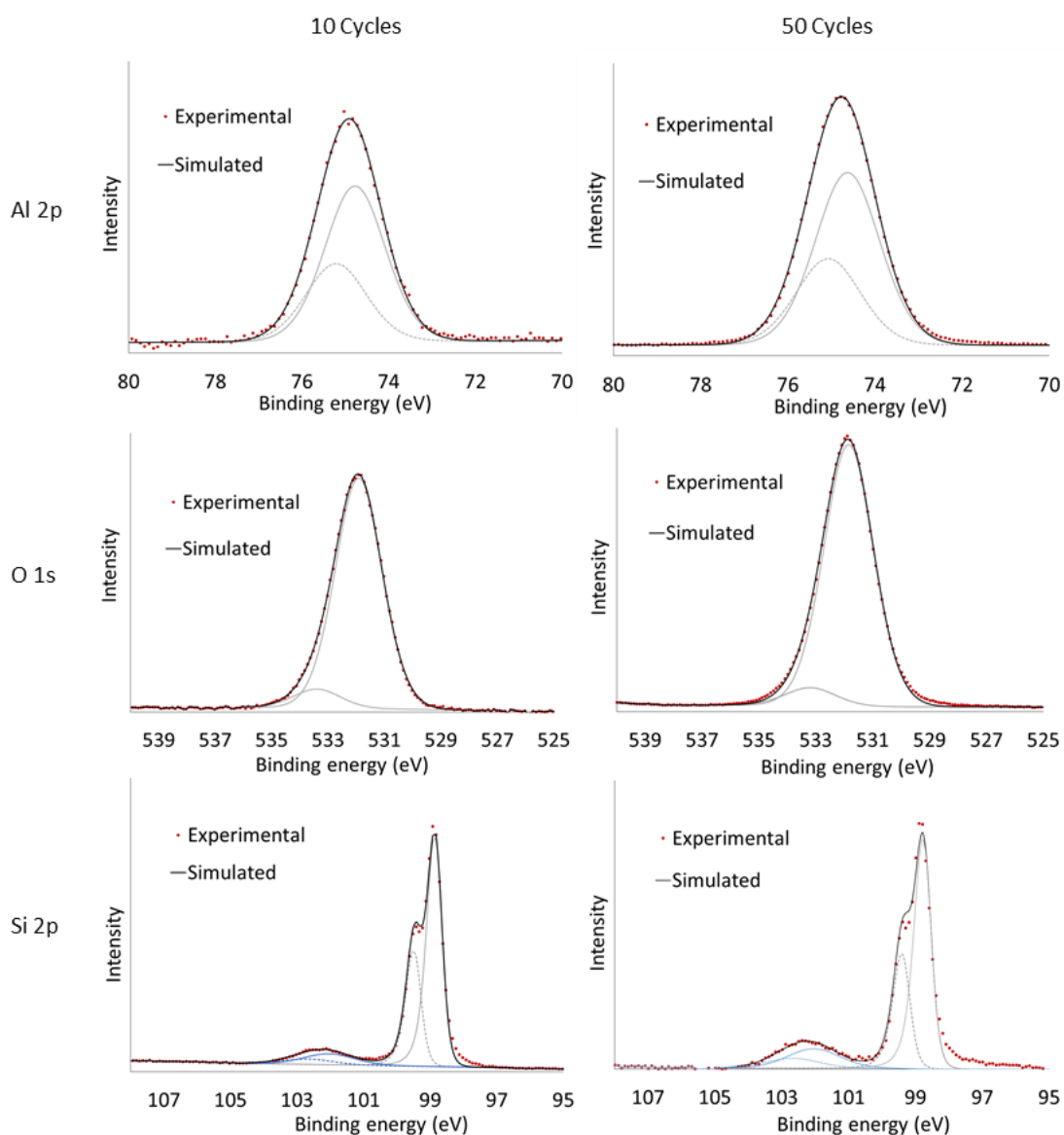
Figure 6.7. Al 2p (top), O 1s (middle) and Si 2p (bottom) XPS spectra for Al_2O_3 films deposited using 10 (left) and 50 (right) cycles

Figure 6.7 shows that Al is detected on the surface even for the 10 cycles sample. Although the intensity is lower than for the 50 cycles one, the peak position is the same. The main peak is located at 74.77 eV and can be simulated by a doublet peak, showing the presence of O-Al-O bonds. The Al 2p peak for both samples could also be fitted by a single symmetrical peak at 74.77 eV. From the TEM analysis performed on films deposited with just a few cycles (<20), the deposited layer could not be distinguished, probably due to the fact that the film growth is still in the island regime (as shown by the island growth model, Figure 6.2) and no continuous ALD layer has been deposited on the surface. However, Figure 6.7 shows a clear Al 2p peak, meaning that Al has already been deposited on the surface.

The O 1s spectra were fitted using a main peak at 531.8 eV, assigned to Al-O bonds. A small contribution from a second peak at 533.3 eV was also used for the fitting. Renault et al. (Renault *et al.*, 2002) attributed such a peak situated at $\Delta E = 1.3$-1.4 eV higher in energy than the main O 1s peak to Al-OH species. The presence of these species are consistent with the chemistry of TMA and H_2O (Puurunen, 2005). As presented in Chapters 3 and 5, TMA deposits on the surface in the form of $Al(CH_3)_x$ species. During the subsequent reactant exposure, H_2O reacts with the surface species, leading to the formation of Al-OH species, and CH_4 as a byproduct. Non-complete coverage of the Al-OH species during the next TMA exposure can lead to the incorporation of those Al-OH species in the film bulk.

The Si 2p spectra presented in Figure 6.7 show the chemical nature of the interface. For both samples, a clear doublet peak is situated at 98.9 eV, which is attributed to elemental Si^0. This shows that the depth of the analysis reaches the Si substrate, for the 10 and 50 cycles samples. A second peak is situated at 102.3 eV, for both samples, to a $\Delta E=3.4$ eV from the Si^0 peak. This ΔE value assigns this peak to Si into higher oxidation states, such as Si^{3+} and Si^{4+}. In Figure 6.7, this peak has been fitted by a doublet peak. However, different deconvolution schemes have been presented in the literature. By using the data treatment of Renault et al. (Renault *et al.,* 2002), a peak at $\Delta E=3.01$ eV is found in our results, between the Si^{4+} and Si^{2+} peaks. This peak has a ΔE that is too high to be assigned to Si^{3+}, and has previously been attributed to Al-silicate bonds (Renault *et al.*, 2002). This analysis concludes in the existence of multiple oxidation states of Si at the interface, including the presence of Al-silicates.

In order to study the elemental composition along the film depth, probing of Al, Si, and O species was performed by EDX on TEM cross sections. Measurements were performed along a straight-line perpendicular to the sample surface, starting from the Si substrate and the obtained elemental profiles, excluding carbon, are shown in Figure 6.8 for samples after 5, 20 and 200 cycles. In order to study the passivation efficiency of the Si substrate pre-treatment, the EDX measurements along the film depth are also shown for the HF-cleaned Si substrate without Al_2O_3 deposition in Figure 6.8. Although this analysis is qualitative, it provides valuable insight for the evolution of the film and of the interface
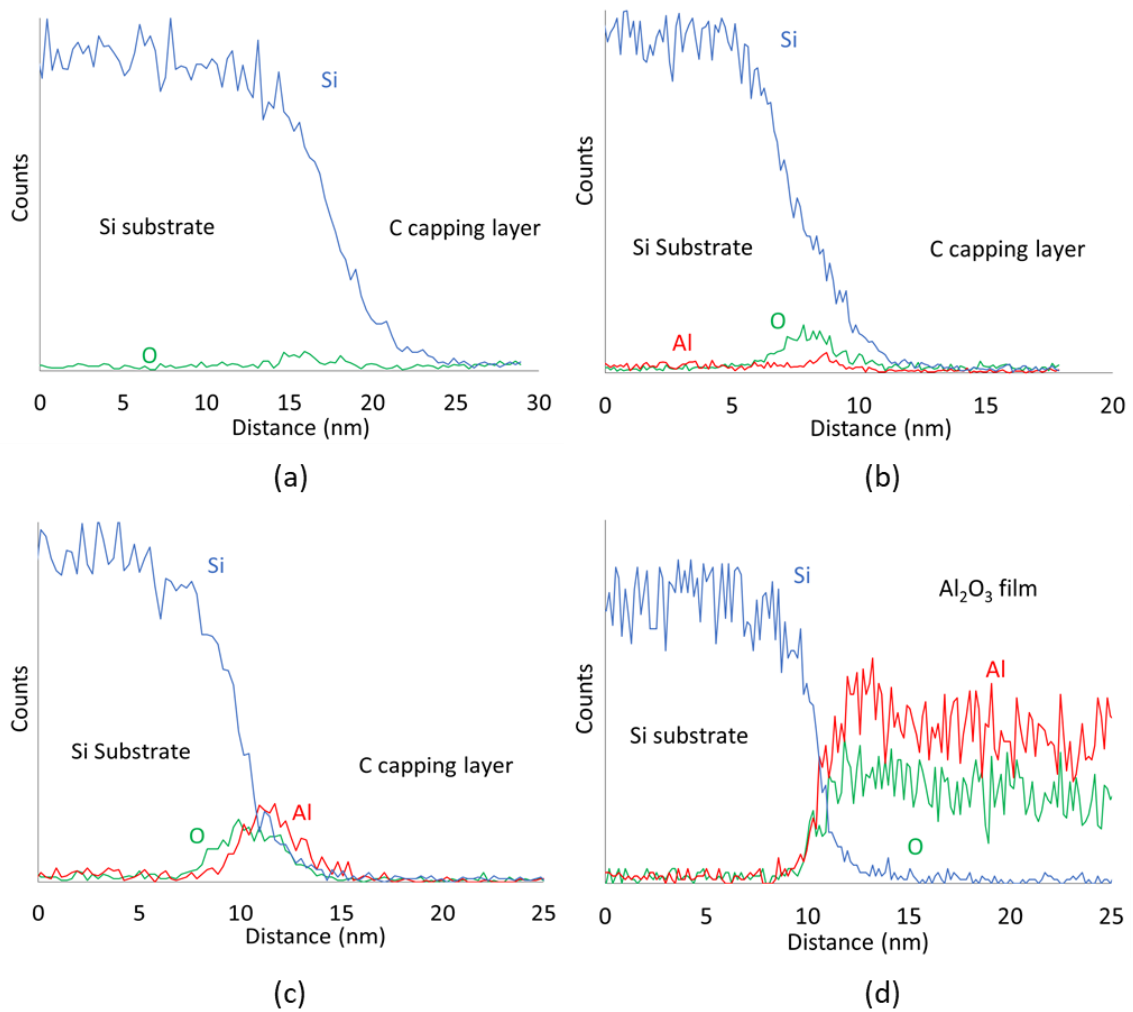
Figure 6.8. EDX measurements along the film depth for a) Si substrate without ALD
b) 5 cycles Al_2O_3 c) 20 cycles Al_2O_3 d) 200 cycles Al_2O_3.

A very small rise on the O counts is detected on the Si surface (interface between Si substrate and C capping layer), for the substrate sample without deposition (Figure 6.8a). This shows that the HF cleaning of the substrate removes the majority of surface oxides, leaving the surface H-terminated. The Si-H surface is passivated towards oxidation. Frank et al. showed that the Si-H surface does not react with deuterated water, D_2O, even after repeated D_2O exposures (Frank *et al.*, 2003). They report a weak O presence on H-terminated Si(100) substrates, attributed to defect sites (Si-OH) remaining on the surface after the substrate cleaning due to the higher atomic roughness

of the Si(100) surface (Frank *et al.*, 2003). Halls et al. performed theoretical studies using DFT calculations on the H- terminated Si surface reactions with TMA and H_2O (Halls and Raghavachari, 2003). Their results confirm the low reactivity of the surface towards both reactants.

The small amount of detected O on the surface is therefore assigned to such surface defect sites, like O bridges or Si-OH groups that have not been appropriately removed, or to SiO_x formed after the sample exposure to air. The ALD nucleation during the first ALD cycles is reported to take place on such defects (Puurunen *et al.*, 2004)(Puurunen and Vandervorst, 2004)(Frank *et al.*, 2003). The island growth model, fitted to the XRR measurements, estimated the surface concentration of those defects, at 0.08 groups/nm². This corresponds to 1.26% of the surface concentration of OH sites on the SiO_2 surface, at 300°C (Haukka and Root, 1994). The ALD film starts forming on those defects. Then, subsequent deposition of Al on the surface catalyzes further Al_2O_3 deposition on nearby sites, as well as substrate oxidation (Frank *et al.*, 2003)(Lim *et al.*, 2000).

This effect is seen on the Al, O, Si profiles on a 5 cycles Al_2O_3 sample on Figure 6.8b. In this case, between the Si substrate and the C layer, a clear peak on the O counts is observed, together with a small peak of Al. The presence of Al was also detected by XPS on a 10 cycles Al_2O_3 sample (Figure 6.7). These results show that after 5 cycles, only a very small amount of Al has been deposited. This is consistent with the island growth model results and XRR measurements. After 5 cycles, the film deposition is still in its nucleation period and only small Al_2O_3 islands are deposited. However, even on the 5 cycles sample (Figure 6.8b), the O peak is more significant than on the substrate sample (Figure 6.8a). Starting from the Si substrate and moving to the C layer, the O counts increase before the appearance of Al. This is attributed to the oxidation of the Si

substrate, with an oxidation of the Si substrate under the Al_2O_3 deposition. This result shows that the Al deposition enhances Si oxidation, even at low Al surface concentration (Frank *et al.*, 2003)(Lim *et al.*, 2000). Frank et al. also showed that after the first TMA pulse, subsequent D_2O exposures lead to subsurface oxidation of Si (Frank *et al.*, 2003). By using the full width at half maximum (FWHM) of the element count peaks, the total thickness of the oxidized layer can be estimated at ~1.93 nm, of which ~1.63 nm consist of SiO_x with no traces of Al, while the thickness where Al was traced is ~0.3 nm. These values show a slightly higher thickness of the oxidized layer than in Table 6.1.

Figure 6.8c shows an Al_2O_3 sample deposited with 20 cycles. The clear Al and O peaks in the profile are due to the deposition of Al_2O_3. Our island growth analysis shows that after 20 cycles, the growth regime is near the end of the island growth regime, however non continuity of the film was still predicted. By using the FWHM of the element count peaks, a region of ~1.5 nm is deduced, where only Si and O species are present, thus confirming the formation of a SiO_x layer. A ~0.7 nm region, where Si, O and Al species are all present, then is detected before the Al_2O_3 layer. This region can consist of Al-silicates or a mix of SiO_x and AlO_x. The presence of Al-silicates has also been reported before (Renault *et al.*, 2002), and is one possible conclusion from this XPS analysis (Figure 6.7). The total thickness of the interface containing Si is 2.2 nm, slightly higher than the one measured by TEM (Table 6.1).

The proposed mechanism for the Si oxide formation is the diffusion of O species from the deposited Al_2O_3 film (Foroughi-Abari and Cadien, 2012), leading to Si oxidation. However, the reaction of H_2O with surface Si groups during the island growth where the surface is not fully covered by the ALD film, catalyzed by the presence of Al, has also been suggested as a mechanism for the interfacial oxide

formation (Frank *et al.*, 2003)(Naumann *et al.*, 2012). Naumann et al. reported that the OH groups formed during the initial island growth lead to the formation of SiOH species (Naumann *et al.*, 2012). These species lead to further substrate oxidation after further increase of the ALD cycles. Xu et al. showed that by using a long exposure to TMA prior to ALD deposition, the interfacial Si oxide thickness is strongly restricted due to the covering of a larger fraction of the surface by Al species (Xu *et al.*, 2006) (Xu *et al.*, 2006). Thus, oxidation by H_2O and surface OH groups of the non-covered Si surface is restricted. The diffusion of O through the ALD layer is also a possible source of oxidation, which is however limited as the ALD film continues to grow due to the presence of Al_2O_3 as a diffusion barrier.

The EDX elemental profiles for the sample deposited using 200 ALD cycles shown in Figure 6.8d, reveal the several nm thick Al_2O_3 film. Within the bulk of the Al_2O_3 film, a uniform Al and O concentration is measured by quantitative analysis (not shown), with a Al/O ratio close to the Al_2O_3 stoichiometry. Using the FWHM of the count peaks, a 1.2 nm interface is deduced, containing Si, O and Al. This value is smaller than the one measured by TEM (Table 6.1).

ToF-SIMS allows detailed investigation of the chemical composition of the film along its depth. Figure 6.9 shows the elemental profile of the 200 cycles sample from the surface to the substrate.
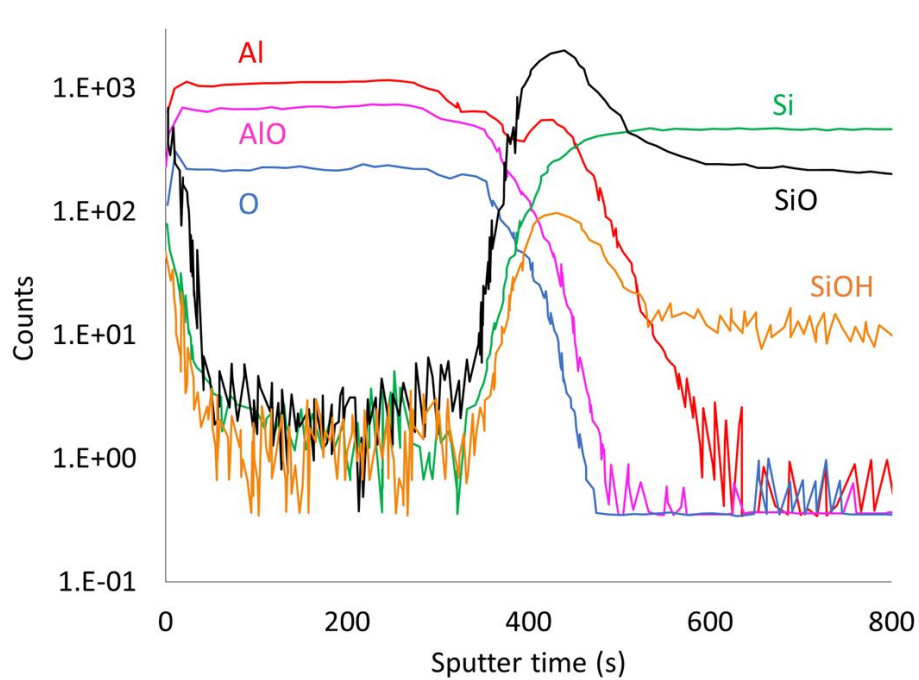
Figure 6.9. SIMS depth profiles for the 200 ALD cycles sample

The SIMS analysis shows a uniform concentration profile for Al and O species in the core of the film, where no Si is detected. This confirms that during the ALD regime, the Al_2O_3 film is deposited with constant composition during each cycle. The surface is regenerated after the end of each ALD cycle, and the deposition process is repeated.

When the sputtering reaches the interface, the AlO and O counts decrease, until the Si substrate is reached, where AlO and O are no longer detected. The Si signal has the opposite behavior: Si counts start to increase at the same sputtering time where the AlO and O counts decrease, until the Si substrate is reached where the Si counts remain constant. The behavior of Al counts is different. First, they start to decrease when sputtering reaches the interface. Then, the Al counts increase exhibiting a small peak in the interface, before decreasing to zero in the Si substrate region. This leads to the distinction of two regions in the interface: an Al depleted region at the top of the interface, close to the core of the ALD film, and an Al enriched region, in the interface.

The different behavior of the Al and AlO depth profiles within the interface witness a possible different chemical environment of Al within the interface. Al could be present in the interface in different from Al_2O_3 states, such as Al-silicates. Gosset et al. also performed SIMS characterizations on ALD deposited AlO_3 on H-terminated Si (Gosset *et al.*, 2002). They observed a similar behavior for the Al and OH species at the interface. After annealing in N_2 at 800ºC and 1000ºC, they observed Al and H diffusion from the interface towards the film bulk. Al diffusion from the interface towards the surface during thermal annealing has also been shown by Krug et al. (Krug *et al.*, 2000).

The SiO and SiOH depth profiles also show a similar behavior: in the interface, SiO and SiOH counts increase, exhibiting a peak of their concentrations, before decreasing as the Si substrate is reached by the sputtering. These peaks appear at the same position as the Al peak, thus confirming that within the interface a different chemical environment of Al is present. These results show that Al, O, Si species are all present within the film interface, as indicated by EDX results in Figure 6.8. The interface, formed by interdiffusion and reaction of species during the first ALD cycles, is hence a mixture of SiO_x, AlO_x and SiOH. The presence of Al silicates is also possible, as discussed in the XPS analysis (Figure 6.7).

Al-OH groups have been suggested to enhance O diffusion and Si oxidation, as bulk defect sites (Gosset *et al.*, 2002). The analysis of O 1s spectra from XPS (Figure 6.7) yields a small contribution that has previously been assigned to Al-OH bonds (Renault *et al.*, 2002). The SIMS results of Figure 6.9 reveal the presence of the SiOH groups in the interface. This presence could be the source of the substrate oxidation during the island growth regime (Naumann *et al.*, 2012). The SiOH groups are formed during the island growth regime that takes place during the first cycles of deposition. The mechanism for their formation could be the reaction of Al-OH species created from

the ALD surface chemistry (Puurunen, 2005)(Vandalon and Kessels, 2016)(Vandalon and Kessels, 2017)(Seo *et al.*, 2018) with Si surface species, which are non-fully covered by Al species during the island growth.

6.5. Effect of Si surface pretreatment

In this section, the effect of an *in situ* N_2-NH_3 plasma pre-treatment of the HF-cleaned Si surface on the ALD of Al_2O_3 from TMA and H_2O is presented. The ALD films deposited on the HF cleaned Si surfaces are onwards called non-pre-treated or NPT samples, while the ALD films on the HF-cleaned and *in situ* N_2-NH_3 plasma pre-treated Si are called pre-treated or PT samples. In order to directly compare NPT and PT samples, some results from the previous sections are presented again.

6.5.1. Si surface pretreatment

Figure 6.10a presents a STEM-HAADF image taken from the N_2-NH_3 plasma pre-treated Si (100) samples, with no Al_2O_3 deposition. It appears that an amorphous layer has been formed (PT layer) due to the pre-treatment on the Si surface (Figure 6.10a), whose thickness is ~1.8 nm.

Brewer et al. reported the formation of a Si_xN_y layer after the exposure of Si to N_2-NH_3 plasma, at temperatures above 380°C (Brewer *et al.*, 2004). In the present case, even at 300°C, it is evident that an amorphous layer has been formed on the Si surface. This is due to the use of N_2-NH_3 plasma, instead of thermal nitridation with N_2-NH_3. Furthermore, in the work of Brewer et al., the plasma N_2- NH_3 gas mixture for the

pretreatment had a lower NH_3 molar composition (4%) compared to the present study (16.67%) (Brewer *et al.*,2004).
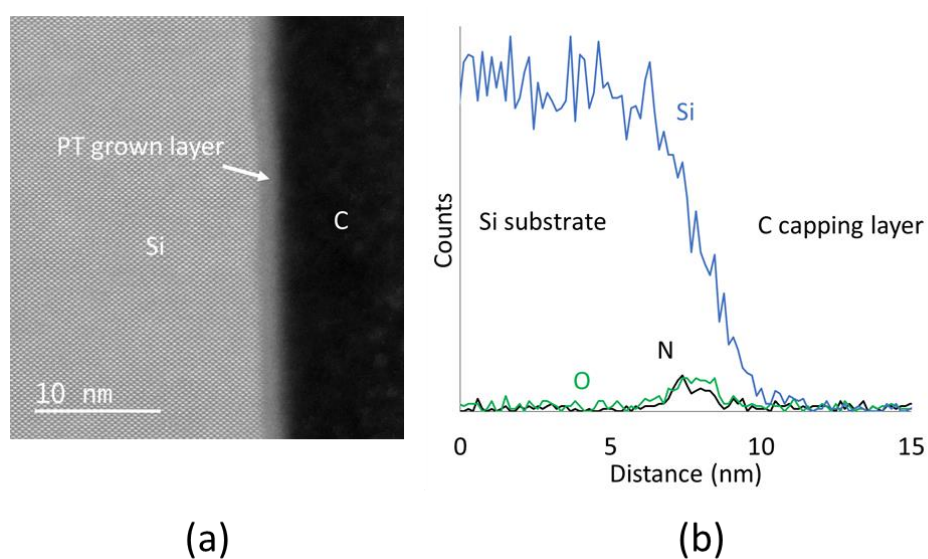
Figure 6.10. a) STEM image of the NH_3 plasma pretreated substrate b) EDX analysis along the film depth: N (black), O (green) and Si (blue) depth profiles

To investigate the layer composition, EDX analysis along the layer depth was performed. The EDX profiles (raw count data) for N, Si and O species along the length of the layer are shown in Figure 6.10b. It appears that a layer consisting of Si and N is present after the N_2-NH_3 plasma pretreatment on the Si substrate surface. The layer also consists of a significant amount of O, along its whole thickness. This O content could come from subsequent oxidation of the layer, due to its exposure to air after the sample was taken out from the chamber. It could also be assigned to native SiO_x which was not removed during the HF cleaning. The layer could also contain amounts of H (not detectable by EDX) coming from NH_3 decomposition within the plasma, hence, it is assumed that a Si_xN_yH layer has been formed by the pre-treatment.

Although Si nitride is known to be an oxygen diffusion barrier (Takeuchi and King, 2003), in the present case the layer is nonetheless oxidized. This behavior is

(a)

(b)
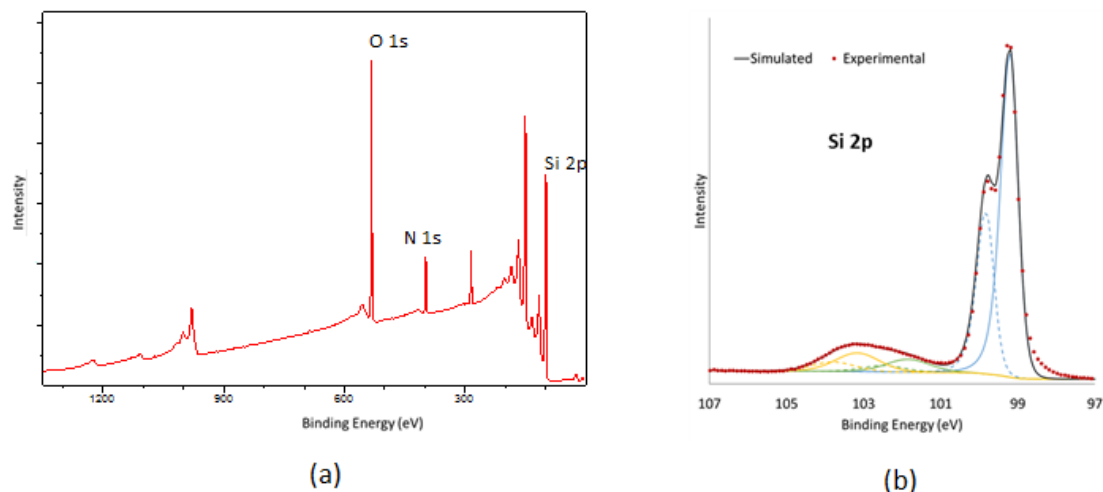
attributed to the poor stoichiometry and low density of the layer, due to its potential high H content. These features make the layer porous, which facilitates O diffusion. Such oxidation of the Si_xN_y layer was also reported by Brewer et al. (Brewer *et al.*,2004). However, by analyzing several EDX profiles similar to the one shown in Figure 6.10b, it is found that, when moving from the Si substrate towards the C capping layer, the increase in the O and N profiles is such that their half-maximum position occurs at the same depth. This suggests that although the Si_xN_yH layer is oxidized, the oxidation of the substrate itself and the formation of an interfacial SiO_x layer can be neglected, i.e. the Si surface is protected from oxidation by the formed layer.

Further characterization of this layer composition was made by XPS (Figure 6.11). The XPS spectrum exhibits a O 1s peak at 532.8 eV, attributed to Oxygen in a SiO_x environment, a N 1s peak at 398.0 eV, attributed to Nitrogen in a Si_3N_4 environment (Chourasia and Chopra, 1993) and a Si 2p doublet peak (blue continuous and dashed lines on Figure 6.11b) at ~99.2 eV, corresponding to Si^0.

Figure 6.11. a) XPS experimental spectrum of the pretreated Si substrate b) Zoom on Si 2p peak : experimental and simulated

A second peak is revealed by the Si 2p spectra, situated at higher binding energies ~103.3 eV. The peak deconvolution was done using two double peaks, one at ~103.2 eV (orange continuous and dashed lines), and one at ~101.9 eV (green continuous and dashed lines). The first peak corresponds to an energy shift of ~4.1 eV from Si^0, is assigned to oxidized Si in higher oxidation states (Renault *et al.*, 2002), such as Si^{4+}. The second peak (energy shift of ~ 2.7 eV) can be assigned to Si-N bonds (Chourasia and Chopra, 1993), with some contributions from Si in lower oxidation sates, such as SiO_x species or Si-O-N bonds.

In order to investigate the source of the layer oxidation, an *in situ* ALD capping by an AlN layer of a plasma N_2-NH_3 pre-treated Si substrate was performed. As this *in situ* process does not involve any oxygen, it is adequate to reveal the source of the Si_xN_yH layer oxidation shown in Figure 6.10. The resulting STEM-HAADF image and EDX analysis are shown in Figure 6.12.

(a)   (b)
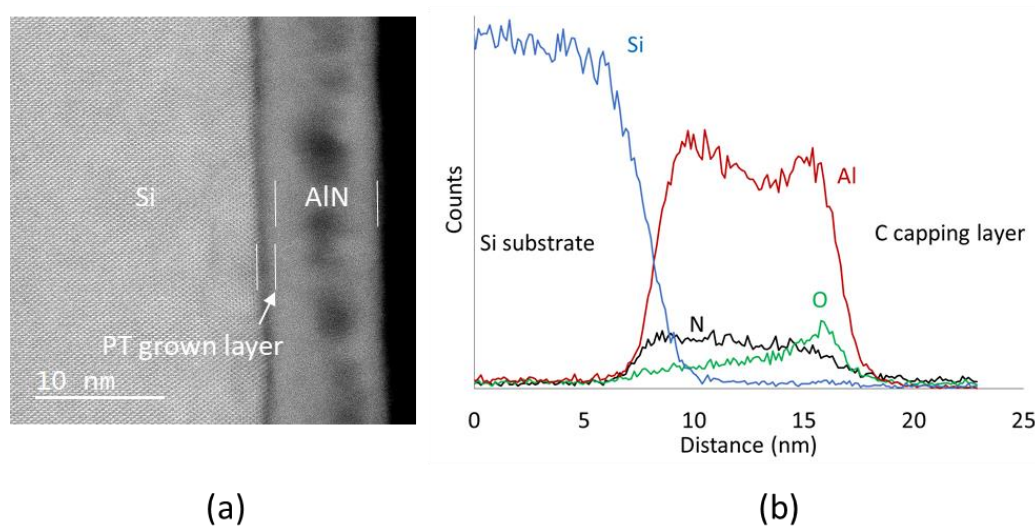
Figure 6.12. a) STEM image b) EDX analysis along the film depth of the pretreated Si substrate after AlN capping

A Si$_x$N$_y$H PT layer is still observed between the Si substrate and the AlN capping layer, as indicated by the thin dark contrast layer located at the Si surface in Figure 6.12a, whose thickness is ~1.1 nm. The elemental EDX profiles in Figure 6.12b show that O atoms are contained in the AlN layer, with a maximum oxygen concentration located at the surface. Since the deposition does not involve any oxygen source, it is concluded that oxidation of the AlN layer occurs during the subsequent exposure to ambient air. In addition, the O content is much lower in the Si$_x$N$_y$H layer suggesting that no oxidation of the PT layer occurs in the presence of a capping layer. It is thus concluded that the oxidation of the PT layer previously observed in the uncapped sample (Figure 6.10b) is mainly due to the exposure to ambient air (after deposition), and not to unremoved SiO$_x$ by the HF cleaning.

The oxidized Si$_x$N$_y$H layer thickness measured in Figure 6.10 was of ~1.8 nm, which means that a slight increase of the thickness could occur due to oxidation. However, this is expected to be the case during ALD, as H$_2$O can also oxidize the layer (Brewer *et al.*,2004). Hence, for subsequent discussion, the PT layer thickness formed by the pre-treatment will be taken at ~1.8 nm.

6.5.2. Effect on initial growth

To study the effect of the N$_2$-NH$_3$ plasma pretreatment on the ALD nucleation and growth, the Al$_2$O$_3$ films deposited using 5, 20 and 75 ALD cycles, with and without PT were analyzed by STEM-HAADF, as presented in Figure 6.13. The Al$_2$O$_3$ thickness on the NPT and the PT Si measured by STEM is also plotted in Figure 6.13. For the Al$_2$O$_3$ films deposited on PT Si, the thickness is deduced by subtracting that of the PT layer (~1.8 nm, Figure 6.10). The TEM results for the 5 and 20 cycles samples on NPT

surfaces have already been shown in Figure 6.6. They are again shown in Figure 6.13, for direct comparison with the PT samples.
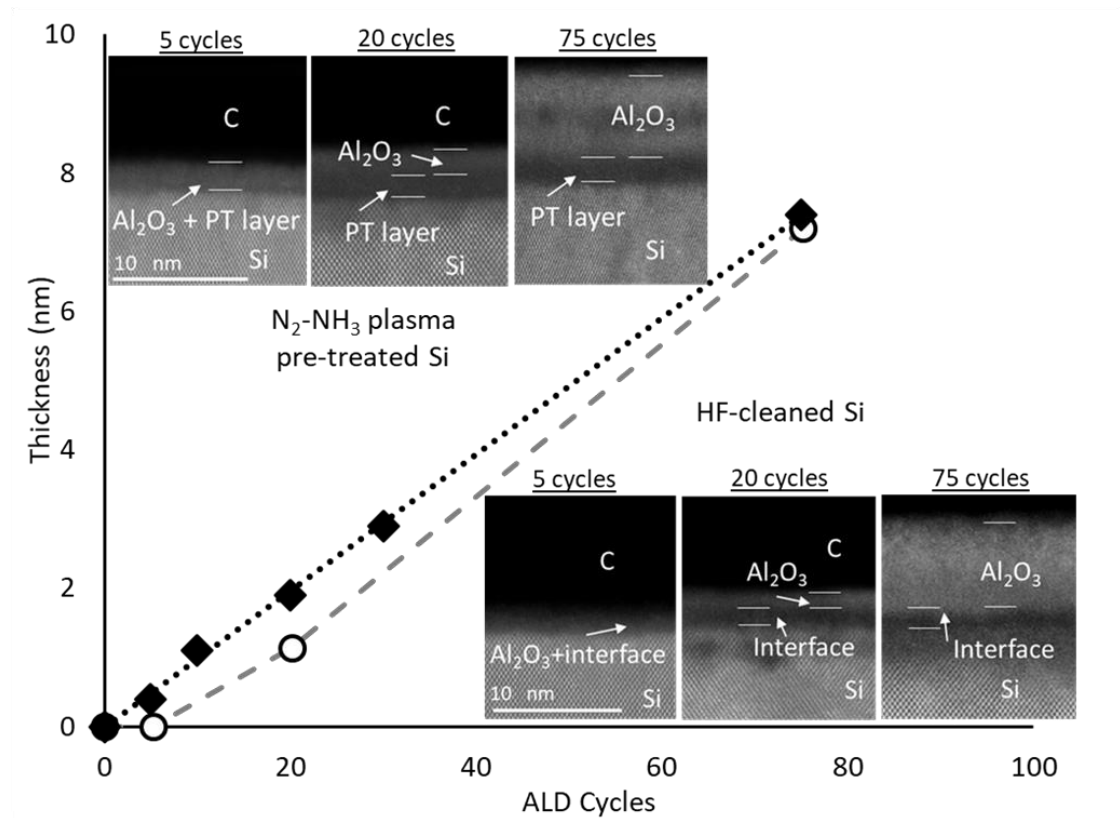
Figure 6.13. Dark field STEM images of the ALD samples, and the derived Al_2O_3 thickness as a function of ALD cycles, on NPT (open circles) and PT (black rhombus) Si surfaces.

Figure 6.13 shows that after 5 ALD cycles, no clear continuous deposition of Al_2O_3 is observable on the NPT samples. This confirms the low reactivity of the H-terminated surface resulting from the HF cleaning towards the ALD reactants (Halls and Raghavachari, 2003)(Frank *et al.*, 2003)(Frank *et al.*, 2003), as discussed in section 6.3. In order to deposit a continuous layer, more ALD cycles are needed.

After 20 cycles (Figure 6.13), a denser deposited layer with a brighter contrast attributed to Al_2O_3, can be seen. This layer has a thickness of ~1.3 nm, and an interfacial layer of ~1.6 nm, measured from the STEM image, as well as from the combined island growth model results and XRR measurements (Figure 6.2b) and the TEM analysis in Figure 6.6 and Table 6.1.

After 75 cycles, a ~7.2 nm layer of Al_2O_3 is deposited. An increase of the Si substrate oxidation is also observed, as the interfacial oxide layer reaches ~2.2 nm. The Si surface on the 75 cycles sample is also rougher than on the other two samples. This could lead to a higher apparent thickness of the interfacial oxide.

When the N_2-NH_3 plasma pretreatment is performed prior to deposition, the STEM images show that even after 5 ALD cycles, a ~2.2 nm thick layer has been deposited. The contrast difference between the PT layer and the ALD Al_2O_3 film is not clear. The Al_2O_3 thickness can be obtained by subtracting the ~1.8 nm layer measured for the sample without deposition (Figure 6.10a), from the total layer thickness. This leads to a value of ~0.4 nm. The deposited layer also has a brighter contrast than the PT layer (Figure 6.10a), which is assigned to a higher density. This can be due to diffusion and reaction of TMA and H_2O within the lower density Si_xN_yH layer, thus leading to a layer densification.

After 20 and 75 cycles, the total deposited film thickness increases to ~3.7 nm and ~9.1 nm respectively, which correspond to an Al_2O_3 thickness increment of ~1.9 nm and ~7.3 nm respectively, compared to the PT layer. As the denser Al_2O_3 film is deposited, the contrast difference between the PT layer and Al_2O_3 becomes clearer and the two layers can be identified, as shown in Figure 6.13.

The above results show an enhanced deposition during the first ALD cycles, in comparison with the NPT samples. For the NPT substrates, no clear deposited film is observable after 5 cycles, while the averaged GPC is only of ~0.07 nm/cycle after 20 cycles and reaches ~0.1 nm/cycle after 30 cycles, as shown by the XRR measurements and the island growth model results (Figure 6.2). On the PT substrates, the mean GPC is ~0.1 nm/cycle between 5 and 75 cycles, which is the GPC obtained at 300°C during the linear ALD regime in our process setup (Chapter 5) and derived from the island growth model and XRR measurements (Figure 6.2). Hence, the nucleation period, reported to occur during the first ALD cycles (Puurunen, 2005)(Puurunen and Vandervorst, 2004)(Puurunen $et\ al.,$2004)(Frank $et\ al.,$ 2003), has successfully been restricted by using the N_2-NH_3 plasma pre-treatment of the Si surface.

Xu et al. also reported a higher deposition during the first ALD cycles when using a NH_3 plasma PT (Xu $et\ al.$, 2006). However, in their study, the total thickness of the film observed by TEM is assumed to consist of Al_2O_3, leading to a 6.7 nm film thickness after 35 ALD cycles. This value would imply a mean GPC of ~0.19 nm/cycle, which is almost two times the GPC of Al_2O_3 from TMA and H_2O, as reported by the results of the island growth model and the XRR measurements (Figure 6.2), the surface chemistry model (Chapter 5) and works in literature (Vandalon and Kessels, 2017)(Puurunen and Vandervorst, 2004). Once the Al_2O_3 film is continuous, the initial surface does not affect anymore the deposition and the process enters in its steady ALD regime. Hence, no surface pretreatment should affect the deposition once the system attains the linear ALD regime. In this Chapter, it was shown (Figure 6.10a) that the N_2-NH_3 plasma PT results in an amorphous Si_xN_yH layer. The film thicknesses obtained in our present study reveals that after 5 cycles, the deposition indeed reaches the linear ALD regime, with a constant GPC of 0.1 nm/cycle. This is in agreement with reported

values from literature (Vandalon and Kessels, 2017)(Puurunen and Vandervorst, 2004), as well as experimental and computational predictions performed for our ALD system (Figure 6.2 and Chapter 5).

A literature review is now used to explain the effect of the N_2-NH_3 plasma PT on the initial deposition increase. Widjaja and Musgrave studied the nitridation of the Si surface under the exposure of NH_3, using DFT calculations (Widjaja and Musgrave, 2001). NH_3 adsorption is dissociative on the Si surface, leading to the formation of Si-NH_2 surface species. They showed that around 600K, further dissociation is possible, with the insertion of N in the Si-Si bonds (Widjaja and Musgrave, 2001). A combined experimental and theoretical study from Rodríguez-Reyes and Teplyakov, using DFT calculations and IR spectroscopy (Rodríguez-Reyes and Teplyakov, 2007) validates the above results, showing that the Si-NH_2 surface species start to dissociate between 500-600K to form $(Si)_2NH$, in two different structures, bridged and backbonded, where neither of the two could be ruled out. In our case, as the exposure to N_2-NH_3 plasma is performed at 300ºC, i.e. 573 K, it is assumed that all three structures could be formed: Si-NH_2 which has not completely dissociated, and $(Si)_2NH$ in both bridged and backbonded structures (Rodríguez-Reyes and Teplyakov, 2007).

Lin and Teplyakov studied the mechanisms occurring during different TMA exposures of the Si surface using DFT calculations and computed energy barriers for TMA adsorption and reaction on Si-H bonds (Lin and Teplyakov, 2013). The authors performed the same study for Si-NH_2 and $(Si)_2NH$ bonds in both bridged and backbonded structures (Lin and Teplyakov, 2013). The mechanisms taken into account are the following:

TMA on Si-H:

Al(CH$_3$)$_3$ reversibly adsorbs on Si-H forming a weak Al-Si bond. The predominant reaction yields a surface Si-Al(CH$_3$)$_2$, with the desorption of CH$_4$. This reaction is considered as irreversible. The mechanism is shown hereafter:

$$Al(CH_3)_{3(g)} + SiH_{(s)} \leftrightarrow SiH(Al(CH_3)_3)_{ads} \rightarrow SiAl(CH_3)_{2(s)} + CH_{4(g)} \qquad (R\ 6.1)$$
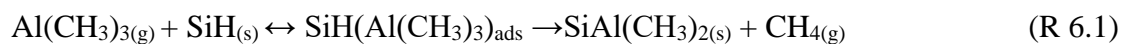
TMA on NH$_x$- terminated Si

Al(CH$_3$)$_3$ reversibly adsorbs on surface NH forming an Al-N bond. The reaction yields a surface N-Al(CH$_3$)$_2$, with the desorption of CH$_4$. This reaction is considered as irreversible. The above mechanism is shown below, for SiNH$_2$ and both of the two different (Si)$_2$NH structures:

$$Al(CH_3)_{3(g)} + SiNH_{2(s)} \leftrightarrow SiNH_2(Al(CH_3)_3)_{ads} \rightarrow SiN(Al(CH_3)_2)H_{(s)} + CH_{4(g)} \qquad (R\ 6.2)$$

$$Al(CH_3)_{3(g)} + (Si)_2NH_{(s)} \leftrightarrow (Si)_2NH(Al(CH_3)_3)_{ads} \rightarrow (Si)_2NAl(CH_3)_{2(s)} + CH_{4(g)} \quad (R\ 6.3)$$
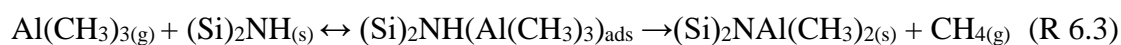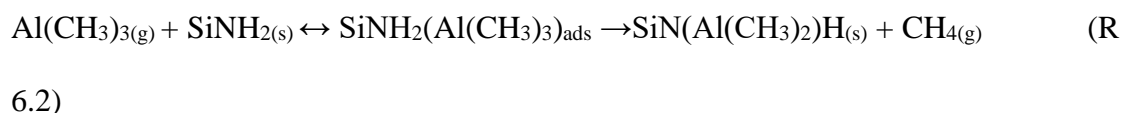
Their results are presented in Figure 6.14.

239
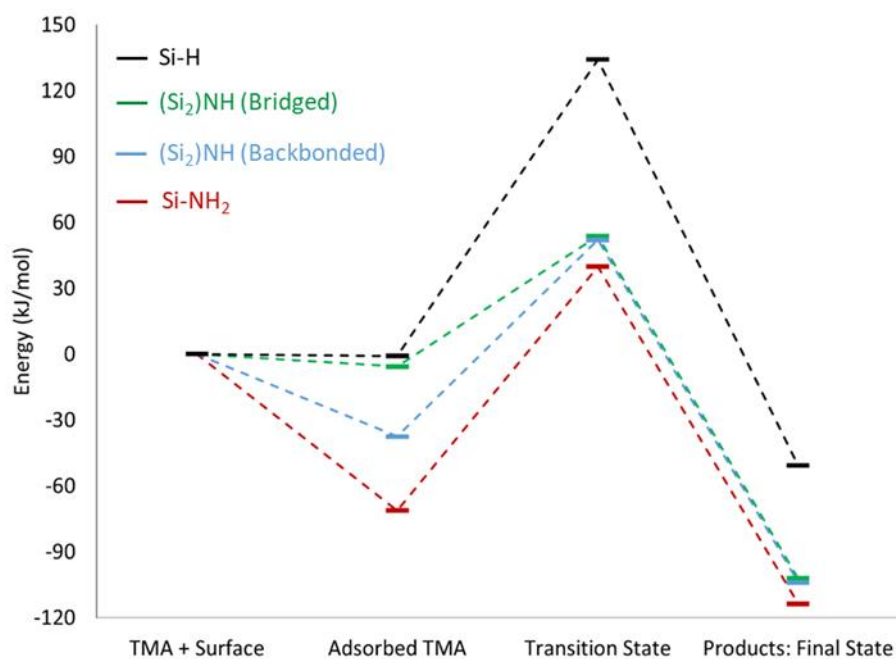
Figure 6.14. Literature data for the deposition of TMA on Si with different surface

terminations (Lin and Teplyakov, 2013).

Figure 6.14 shows that the deposition is favored for the three different NH bonds, compared to the Si-H bonds. TMA is found to adsorb more exothermically on the Si-NH$_x$ bonds, than on the SiH ones. The overall energy barrier to reach the transition state is significantly smaller for the NH-terminated bonds and the final products are in a much lower energy state. In particular, the NH$_2$ is the most favorable surface termination for the deposition of TMA, presenting the lower overall energy barrier, of 39.9 kJ/mol, while the reaction products are 113.7 kJ/mol lower in energy than the reactants (Lin and Teplyakov, 2013).

A reaction probability study of an already adsorbed TMA molecule on the surface is now realized, in order to analyze the N$_2$-NH$_3$ plasma pretreatment effect on the TMA deposition kinetics. The same principles as in Chapter 5 are used. The reaction probability ($p_{reaction}$) of an adsorbed TMA molecule on the surface is calculated by dividing its forward reaction rate ($R_{reaction}$) with the total rate of all possible events, which for the adsorbed TMA are forward reaction and desorption ($R_{desorption}$):

$$p_{reaction} = \frac{R_{reaction}}{R_{reaction} + R_{desorption}} \tag{6.1}$$

Both mechanisms are assumed to follow first order Arrhenius kinetics. The activation energy for desorption ($E_{desorption}$) is assumed to be equal to the energy released during the adsorption step, while the forward reaction energy barrier ($E_{reaction}$) is the difference between the energies of the transition state and the adsorbed TMA state. By assuming that the pre-exponential factors for both reaction and desorption are equal, the reaction probability can be expressed as:

$$p_{reaction} = \frac{e^{\frac{-E_{reaction}}{RT}}}{e^{\frac{-E_{reaction}}{RT}} + e^{\frac{-E_{desorption}}{RT}}}$$

(6.2)

Where R is the ideal gas constant and T the temperature in K.

The results for the reaction probabilities calculated at 300°C are shown in Table 6.2, using the activation energies computed by Lin and Teplyakov (Lin and Teplyakov, 2013).

Surface termination	Reaction probability at 300°C
Si-H	$5.96 \cdot 10^{-13}$
Si-NH$_2$	$2.3 \cdot 10^{-4}$
(Si)$_2$NH (bridged)	$1.27 \cdot 10^{-5}$
(Si)$_2$NH (backbonded)	$1.81 \cdot 10^{-5}$

Table 6.2: Reaction probabilities for the different surface bonds calculated at 300°C, using the energies calculated by Lin and Teplyakov (Lin and Teplyakov, 2013).

Results of Table 6.2 show a clear increase of the reactivity with the N$_2$-NH$_3$ plasma PT. An adsorbed TMA molecule has a reaction probability increased by more than seven orders of magnitude on NH-terminated surfaces, than on the Si-H surface. Specifically, the highest reaction probability is computed on Si-NH$_2$.

It must also be noted that besides the TMA reactions with the N$_2$-NH$_3$ plasma PT Si surface, the H$_2$O reactions are also favored. The low reactivity of the H-terminated Si surface towards H$_2$O has been previously studied theoretically (Halls and Raghavachari, 2003), and experimentally (Frank *et al.,* 2003). Brewer et al. showed that on the NH$_3$ pre-treated Si, deuterated water D$_2$O reacts and oxidizes the PT layer, even at temperatures as low as 190°C (Brewer *et al.*, 2004). These reactions could lead to the

formation of oxygen containing species, such as Si-O-N or OH bonds on which TMA can chemisorb more favorably during the subsequent reactant pulse.

6.5.2. Effect on Si oxidation

In order to study the efficiency of the N_2-NH_3 plasma pre-treatment on the restriction of the substrate oxidation, profiles of the EDX counts of Si, O, Al and N species along the film depth for films deposited on both NPT and N_2-NH_3 plasma PT Si surfaces are presented in Figure 6.15. The EDX results for the samples deposited using 5 and 20 cycles on NPT surfaces, although previously presented in Figure 6.8, are shown again for a direct comparison with the respective samples on PT surfaces.
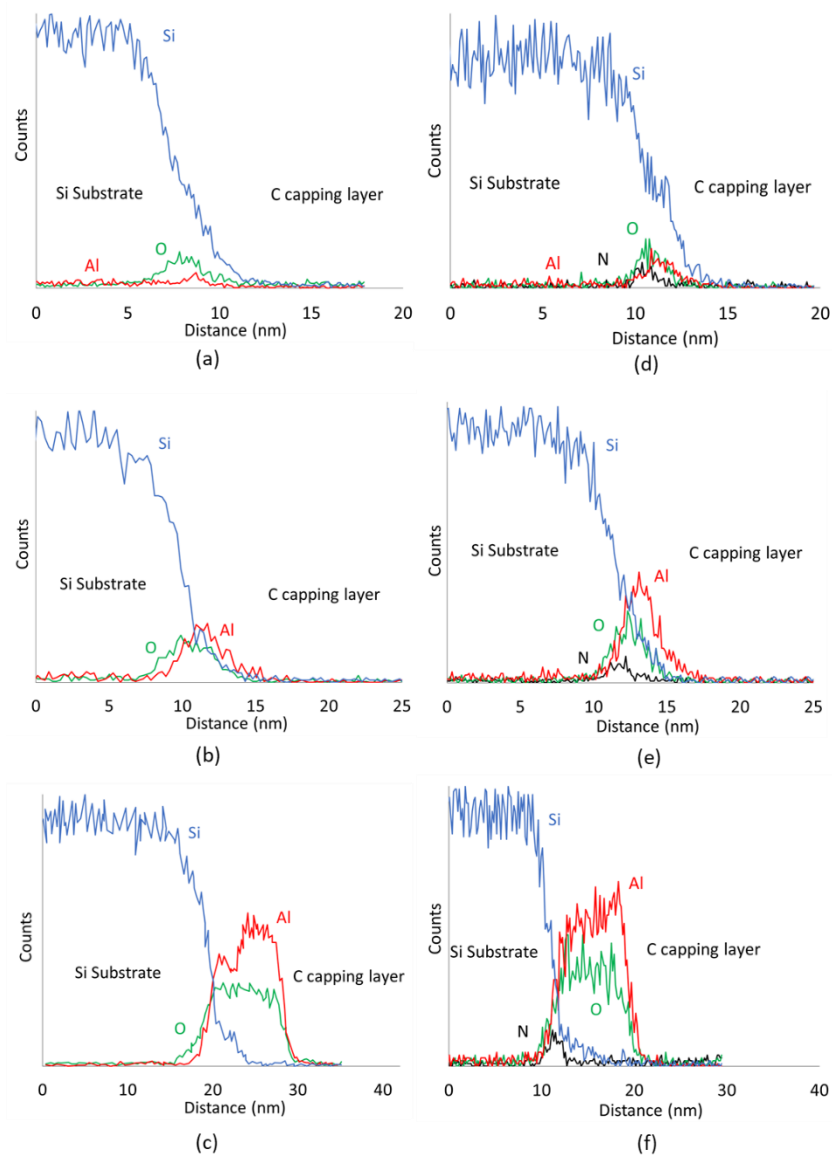
Figure 6.15. EDX count profiles for Al, Si, O, N species of the ALD films: Left column: NPT Si surfaces: a) 5 cycles, b) 20 cycles, c) 75 cycles. Right column: PT Si surfaces: d) 5 cycles, e) 20 cycles, f) 75 cycles.

After 5 ALD cycles on the NPT Si surface (Figure 6.15a), only a very small amount of Al can be traced on the Si surface. This confirms that the Si surface is highly passivated towards TMA by the HF cleaning, which leaves the surface H-terminated. This low reactivity has been discussed in the previous sections of the present Chapter.

After 20 cycles (Figure 6.15b), a clear rise of the Al counts can be seen on the EDX profile, showing that Al was indeed deposited on the surface, confirming the island growth model predictions and the previous TEM, STEM, XRR, EDX analysis presented in the present Chapter.

In both the 20 and 75 cycles samples on NPT Si, moving from the Si substrate to the C capping layer, the O counts rise before the respective Al counts. This shows that there is an interface between the deposited film and the Si substrate, which consists of oxidized silicon. The thickness of the oxidized Si layer is ~2.2 nm for the 20 cycles sample, as estimated from the FWHM of the element counts. This layer consists of ~1.5 nm of SiO_x, and ~0.7 nm of a region where Si, O, Al species are simultaneously present, as presented in section 6.4 of the present Chapter. For the sample deposited using 75 cycles, the Si oxidized layer has a thickness of ~2.4 nm, consisting of ~1 nm SiO_x and ~1.4 nm of the Si, O, Al region. These values are consistent with the STEM measurements, and are close to values reported by previous works (Xu *et al.*, 2006)(Kaur *et al.*, 2017).

When the PT is introduced prior to deposition, unambiguous Al deposition is evidenced already after 5 ALD cycles (Figure 6.15d). A clear Al count peak can be seen moving from the Si substrate to the C capping layer. The PT is efficient in enhancing the reactivity of the surface, thanks to the formation of a Si_xN_yH layer, as discussed in the previous section. Figure 6.15d also shows a significant reduction of the Si oxidation. No region is detected, where only Si and O species are present. A layer of Si, O and N appears, with a thickness of ~0.9 nm. Then a region of ~0.8 nm is measured where Si, O, Al, N are all present. Al diffusion and deposition in the less dense Si_xN_yH layer could explain this result, as the fact that although the less dense amorphous PT layer could not be easily observable by STEM, the layer with 5 ALD cycles could be seen with a

darker contrast. The total thickness of the N-containing layer is ~1.7 nm and the Al_2O_3 layer thickness is ~0.4 nm. These values are consistent with the STEM measurements.

After 20 and 75 cycles, more intense peaks of the Al counts are observed on the EDX profiles (Figures 6.15e and 6.15f respectively). The Si substrate oxidation is reduced compared to the respective NPT samples (Figures 6.15b and 6.15c). For the 20 cycles sample, the SiONH region thickness is ~1 nm. Between the Si-O-N-H layer and the deposited Al_2O_3 film, a region of Si, N, Al and O exists, with a thickness of 0.8 nm, leading to a total N-containing layer of ~1.8 nm. The respective SiONH for the 75 cycles sample is ~0.5 nm thick, while the region of Si, N, Al and O has a thickness of ~1 nm, leading to a total N-containing layer of ~1.5 nm.

In order to confirm this low substrate oxidation on PT samples, XPS characterizations were also performed on a PT Si sample with 20 ALD cycles of TMA/H_2O. The Si 2p XPS spectra and their deconvolution are shown in Figure 6.16.

It shows that the Si 2p XPS spectra exhibit a doublet peak (blue continuous and dashed lines) at ~99.1 eV, corresponding to Si^0. It can be seen (Figure 6) that the second peak in the Si 2p spectra is now situated at 101.7 eV. For this peak deconvolution, only a doublet peak at 101.6 eV was used (green continuous and dashed lines, energy shift of ~2.5 eV).
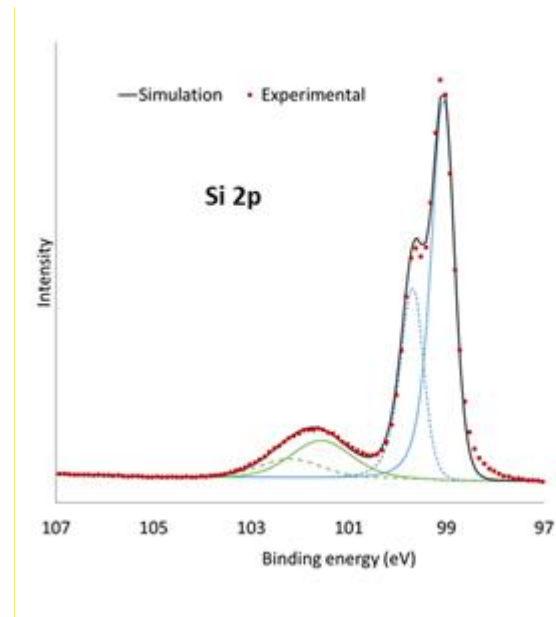
Figure 6.16. Si 2p XPS spectra for PT Si sample with 20 cycles ALD. Experimental and simulated

Si in higher oxidation states was hence not detected on the 20 cycle PT sample, while the peak is assigned mainly to Si-N bonds (Chourasia and Chopra, 1993), with some contributions from Si in lower oxidation sates, such as SiO_x species, Si-O-Al or Si-O-N bonds. It is evident from Figures 6.15 and 6.16, that the Si oxidation was reduced when 20 cycles of ALD were performed. This shows the barrier properties of the Al_2O_3 film, in reducing the substrate oxidation.

XPS characterizations of ALD deposited Al_2O_3 films on NPT Si (Figure 6.7) revealed main peaks situated ~ 3.4 eV higher in energy than the Si^0 main peak, with the main contribution being from higher Si oxidation states (Renault *et al.*, 2002). In Figure 6.16, it is seen that this energy shift is lower (~2.5 eV), and the main contribution of the secondary peak at 101.6 eV is assigned to Si-N bonds (Chourasia and Chopra, 1993).

The above results show that besides increasing the initial deposition steps, the PT is also effective in suppressing the Si surface oxidation (Figures 6.15, 6.16). For the

NPT Si surfaces, the interfacial oxide thickness remains close to 2 nm for all samples. As previously discussed, the interfacial layer has been reported to be formed by species interdiffusion and reaction through Al-OH defects in the film bulk (Renault *et al.*, 2002)(Gosset *et al.*, 2002). Si-OH bonds created during the island growth mode of the first cycles are also a source of Si oxidation (Naumann *et al.*, 2012).

In the case of PT Si surfaces, our results indicate that for all samples, the substrate oxidation is significantly reduced. This shows that the PT layer along with the ALD deposited film serve as an effective barrier towards the oxidation of the Si substrate. This substrate oxidation suppression has been previously reported by Brewer et al. (Brewer *et al.*, 2004) , as well as by Xu et al. (Xu *et al.*, 2006), who reported low interface oxidation. In their work, Brewer et al. exposed the NH_3 pretreated Si surfaces to D_2O (Brewer *et al.*, 2004). They reported that although D_2O oxidizes the formed Si_xN_yH layer even at modest temperatures, the substrate surface beneath it is not oxidized. This shows that the pre-treatment formed layer protects the Si surface from oxidation. Results of Figures 6.10b and 6.15 validate these observations. To determine whether the oxidized Si_xN_yH interface of the PT samples presents better interfacial properties than the SiO_x interface of the NPT samples, electrical characterizations should be performed, which are not the topic of the present study. Xu et al. have shown that Al_2O_3 films deposited on N_2-NH_3 plasma pre-treated Si present better better thermal stability, lower leakage current and smaller CV hysteresis (Xu *et al.,* 2006).

Summary – Conclusions

In this Chapter, the ALD of Al_2O_3 films from TMA and H_2O was studied on HF-cleaned and HF-cleaned and *in situ* N_2-NH_3 plasma pre-treated Si (100) substrates.

The aim of the study was to thoroughly investigate the initial film deposition evolution and interface formation and the pre-treatment effect on those drawbacks of ALD. A series of samples using a different number of ALD cycles were deposited at 300°C. The films and their interface with the substrate were characterized by XRR, TEM, XPS, EDX and ToF-SIMS. The geometrical island growth model, described in Chapter 3 was used to reproduce the nucleation and growth steps during the first cycles.

The model succeeded in representing the Al_2O_3 thickness evolution during the first ALD cycles, without involving the modelling of surface reactions. This approach showed that the evolution of the film deposition can be explained by the geometric aspects of nucleation and growth, without assuming an increasing surface reactivity during the first ALD cycles. It allowed to estimate the surface concentration of defect sites, such as Si-OH and O bridges on the initial Si surface as close to 0.08 groups/nm^2 and revealed that 25 ALD cycles are needed to achieve film continuity on HF-cleaned Si.

Results by TEM, XPS, SIMS and EDX also showed that an interfacial layer was formed between the Al_2O_3 film and the Si substrate. This layer consists of oxidized Si in various oxidation states, while Al is also present, suggesting the presence of AlO_x and Al-silicates. In agreement with the reported results, the interfacial layer formation starts with the Al_2O_3 film during the first cycles. The mechanisms involve Si oxidation during the first cycles, when island growth takes place, and the surface is not fully covered by the Al_2O_3 film. Although this oxidation was highly restricted for the H-terminated Si surface, the presence of Al on the surface catalyzes Si oxidation, and thus the interfacial layer formation. This oxidation could occur through the formation of SiOH groups during the island growth. These SiOH groups could be formed from the reaction of OH species on the deposited islands with non-covered Si on the surface.

SIMS results validated the presence of SiOH groups in the interface, thus further consolidating this assumption. Once the whole surface is covered by the ALD film, the interfacial oxide layer may continue to grow due to interdiffusion of O species through the layer up to a certain point, where the Al_2O_3 film serves as a diffusion barrier. This interdiffusion has been assigned to bulk defect species, present in the form of AlOH, facilitating the oxygen diffusion.

The effect of an *in situ* plasma N_2-NH_3 pre-treatment of the Si(100) substrate prior to Al_2O_3 ALD from TMA and H_2O was also studied both experimentally and theoretically, considering literature results. This pre-treatment leads to significant deposition increase during the first ALD cycles, as observed by STEM and EDX measurements. This is explained by the fact that the pre-treated surface consists of Si-NH_2 and $(Si)_2NH$ groups, which are considerably more reactive towards TMA than the H-terminated Si surface formed during the standard HF cleaning of the Si substrate. The substrate inhibition leading to island growth is then suppressed, and a constant GPC is reached only after 5 cycles, instead of more than 30 cycles without such pretreatment.

This pretreatment is also effective in suppressing the substrate oxidation. The interfacial oxide layer is ~2nm for the non-pretreated samples, while no SiO_x layer is detected for the samples with pretreatment. The amorphous Si_xN_yH layer formed by the pretreatment serves as an effective protective layer for the Si surface. Although this layer is itself oxidized, the Si surface oxidation is blocked. Previous works (Xu *et al.*, 2006) reported that Al_2O_3 films deposited on NH_3 pre-treated Si presenting a similar Si_xN_yH interface, result in improved dielectric properties.

This study shows that two of the main disadvantages of Al_2O_3 ALD from TMA and H_2O on Si, i.e. initial deposition inhibition and the formation of the interfacial SiO_x layer, can be suppressed by using an appropriate Si surface pre-treatment.

General summary, conclusions and perspectives

The research work presented in this thesis deals with the thorough study of the phenomena and mechanisms involved during the ALD of Al_2O_3 on Si. The analysis is performed using a combined computational and experimental framework. This framework consists of physical and chemical based models in various scales, making the computational approach multiscale, while the experimental investigation used a commercial ALD setup and a complete set of characterization techniques. With this framework, the individual mechanisms and their effect on several aspects of deposition and film properties are illuminated, thus leading to an in depth understanding and control of the ALD process.

The constant shrinking of the microelectronic devices has pushed towards the need for the production of nanometric thin films with a high compositional purity and control over the film thickness, uniformity and conformality. In this context, ALD has emerged as the favorable technique to produce such films. Drawing its advantages from the self-terminating nature of the surface reactions involved during the process, it can theoretically produce films with a film thickness control down to the monolayer. Its excellent compositional purity, step coverage and uniformity have made it an essential tool for the production of metal oxide layers on Si used as high-k gate oxides in today's MOSFETs.

Although the advantages of ALD are incomparable among other deposition techniques, it nonetheless exhibits some drawbacks for the deposition of films of some nanometers. The initial deposition can be affected by the substrate nature, leading to complex initial deposition phenomena such as island growth, that require a minimum

number of ALD cycles to obtain a continuous layer. A non-abrupt interface is also formed between the deposited film and the Si substrate, which affects the compositional purity and thus the potential applications of the deposited structure.

The scale up of ALD processes also presents drawbacks for the industrial applications of ALD. In order to achieve uniform and conformal deposition on large area substrates, the reactant fluxes must be homogeneous along the substrate. These aspects affect the required exposure and purge times in ALD, making the process slow and costly, thus requiring reactor and process design optimization. The above requires a thorough understanding of the mechanisms and phenomena involved inside the ALD reactor. As these phenomena take place in various space and time scales, some of them being very short, the experimental study of the ALD process in detail is challenging and needs to be completed by a multi-scale computational modelling work.

The ALD of Al_2O_3 on Si from TMA and H_2O is selected as the process of choice, as it represents a case of metal oxide ALD on Si. Although it is one of the most studied ALD processes and is considered a "model process", it nonetheless exhibits the above drawbacks, and the mechanisms involved have not yet been thoroughly studied and understood. This work aims to find ways to overcome the difficulties arising from the initial substrate surface, the interfacial Si oxidation and the interplay of transport phenomena and surface mechanisms for deposition on large area wafers.

ALD deposition took place in a commercial Veeco® Fiji F200 ALD reactor, on Si(100) substrates with a diameter up to 200 mm. The experiments were performed using a variety of process conditions, to investigate the effect of process parameters on the Al_2O_3 deposition. The deposited films were characterized using a complete set of characterization techniques, including ellipsometry, XRR, TEM, STEM, EDX, XPS

and SIMS. These characterizations yielded information regarding the deposited film thickness, morphology, structure, chemical nature and composition.

The computational investigation was performed using four different computational models dealing with different space scales, making the approach multiscale. Two CFD models were developed for the ALD reactor and the reactant feeding system, coupled between them through a computational strategy. The ALD system simulation, along with the vacuum pump simulation is a novel approach towards the modelling of ALD processes, allowing the investigation of the process dynamics in detail. The CFD model of the reactor was coupled to a wafer-scale surface reaction model, which takes into account adsorption, desorption and surface reaction of species on the surface. This allows the investigation of the interplay between surface mechanisms and transport phenomena, and in turn the study of the effects of process parameters and phenomena in the reactor on film properties, such as film uniformity.

The CFD model was also coupled to a stochastic kMC surface chemistry model, which allows the thorough study of the different events taking place on the substrate surface at the nanoscale. Microscopic aspects of the film deposition, such as the evolution of roughness, the deposited mass, and the film stoichiometry during the ALD regime can be calculated using this model. Finally, an island growth model, based on geometric principles, was used to study the nucleation and the initial growth regime during the initial steps of deposition. This model is fed by the GPC of the steady ALD regime, derived from the coupled CFD and wafer scale surface chemistry model.

The investigation of the process dynamics revealed that although ALD is conceived as a process dependent only on surface reactions, complex phenomena occur during deposition at the reactor scale. In particular, the configuration of the purging

flows through the reactor three inlets can lead to a non-ideal flow field inside the reactor main volume. The temperature distribution is non-uniform inside the reactor, with the presence of a cold zone in the reactor loading door region leading to a non-uniform temperature profile on the substrate surface. This temperature field can lead to an increased minimum purge time duration to effectively purge the reactor chamber in order to achieve film uniformity. Furthermore, gas phase recirculation during the reactant exposures was found to take place in the reactor volume, leading to non-uniform reactant species distribution on the substrate surface.

The combined experimental and computational approach revealed a complex behavior of the GPC within the ALD temperature window. The competition between surface reactions and desorption of H_2O on MMAOH species was found to be the limiting factor for ALD deposition at lower temperatures. The effect of this competition revealed by an original reaction probability study and the stochastic kMC model, has not been discussed in detail before. The H_2O reactions are activated by increasing the temperature. After a certain point, further increase of temperature leads to decrease of the GPC, due to the decrease of the number of OH species that are stable on the surface.

The effect of the interplay between the surface mechanisms and transport phenomena was found to have a substantial effect on the film uniformity. The gas flow recirculation occurring during the TMA exposure was found to lead to a non-uniform film deposition on the substrate surface for a process temperature of 300°C. By increasing the TMA pulse duration, uniform films were obtained, as the surface was saturated during the increased TMA exposure. For lower temperatures, the film uniformity was found to be dependent on the temperature distribution inside the reactor. H_2O adsorbed on the cold walls of the loading door was not desorbed and removed

during the purge time, leading to CVD deposition on the side of the substrate exposed to the loading door. Non-uniformity increased as the purging time was decreased.

A combined computational and experimental investigation was used to study the initial steps of deposition. XRR and TEM measurements, along with the geometrical island growth model revealed that a substrate-inhibited island growth regime takes place during the first ALD cycles. The low reactivity of the initial Si-H species prevents the deposition during the first cycles, and the nucleation occurs on surface defects. Preferential deposition on already deposited material during the next cycles leads to island growth. 25 cycles are needed to deposit a continuous film over the surface, consistent with observations in the literature. Once the islands coalesce, the deposition attains the layer by layer steady ALD regime.

The interfacial layer formed between Al_2O_3 and Si was studied using TEM, EDX, XPS and SIMS. Results showed that the HF pre-treatment of the Si substrate is efficient to remove the native oxide from the Si surface, yielding protection from further oxidation. Traces of O species were found, assigned to surface defects. However, even after 5 ALD cycles, the Si substrate was indeed oxidized, showing that the Si oxidation is catalyzed by the presence of Al.

A ~2 nm interfacial oxide layer was formed between the Si substrate and the Al_2O_3 layer, when a continuous ALD layer was deposited. The interfacial layer was found to consist of oxidized Si, in various oxidation states. Al silicates were also present at the interface. The interfacial layer grows with the ALD film, until a certain thickness of Al_2O_3 is deposited, which serves as an oxygen diffusion barrier. The presence of SiOH species in the interfacial layer was validated by SIMS, assigning their formation

as the potential mechanism for the Si substrate oxidation during the island growth regime.

In order to combat the initial deposition inhibition responsible for island growth and the interfacial Si oxidation, leading to the formation of an interfacial oxide layer, an *in situ* N_2-NH_3 plasma pre-treatment of the Si substrate was used, after the HF cleaning procedure and prior to ALD. An amorphous Si_xN_yH layer was formed on the substrate surface from this *in situ* pre-treatment.

This pre-treatment led to significant deposition increase during the first ALD cycles, as observed by STEM images and EDX measurements. This was explained by the fact that the pre-treated surface consists of Si-NH_2 and $(Si)_2NH$ groups, which are considerably more reactive towards TMA than the H-terminated Si surface formed during the standard HF cleaning of the Si substrate. The substrate inhibition leading to island growth is then reduced, and a constant GPC is reached after 5 ALD cycles, instead of tens of cycles without such pretreatment.

The N_2-NH_3 plasma pre-treatment was also effective in reducing the substrate oxidation: no SiO_x layer is detected for the samples with pretreatment. The amorphous Si_xN_yH layer formed by the pretreatment serves as an effective protective layer for the Si surface. Although this layer is itself oxidized, the Si surface oxidation is reduced, resulting in improved dielectric behavior according to literature results, reported for similar Si_xN_yH interfaces.

The research work presented in this thesis provides a framework for the detailed analysis of the mechanisms involved in thermal ALD processes. The combined computational and experimental approach can be used to illuminate certain aspects of ALD, which are challenging to investigate only experimentally. This multiscale

approach allows the integrated study of thermal ALD processes, from the surface mechanisms to the transport phenomena inside the ALD reactor and the process dynamics.

This framework can be used for a variety of ALD systems, once the energy barriers for the chemical mechanisms are determined, using DFT calculations and/or experimental measurements. From this point onwards, the computational framework along with complementary experimental measurements, can be used to illuminate the competition between surface mechanisms, as well as determine the individual mechanisms or phenomena that are either limiting or enhancing the growth. In this way, it is possible to explore the mechanisms involved using different ALD precursors, over the ALD window. This could be an invaluable tool for the research on novel precursors that are able to extend the ALD window to higher or lower temperatures, for the deposition of films with new crystalline phases, or films that are sensitive to higher temperatures, such as polymers.

Furthermore, the present framework can be used to study the scale-up of ALD processes. Deposition uniformity on large area wafers, or in multi-wafer ALD reactors can be investigated using the combined computational and experimental approach developed in this thesis. In this way, by studying the interplay between surface mechanisms and transport phenomena, the optimal reactor design and process setup can be determined for the uniform deposition on the surfaces to be coated. The whole process can be optimized by such investigations, thus minimizing reactant consumption as well as the purging steps duration, thus limiting the process time and cost. This framework can also be used for the detailed study and optimization of spatial ALD, which is emerging as high throughput industrial ALD process.

The present approach regarding the initial growth on HF-cleaned Si can be used for the ALD of other *high k* oxides, such as HfO_2 and ZrO_2. The understanding of the initial growth inhibition mechanisms and the interfacial layer formation can be used to develop appropriate pre-treatment techniques, in order to control the reactivity of the initial substrate surface and protect the Si substrate from interfacial oxidation. Furthermore, these pretreatment techniques could be used for the production of substrates with different surface termination along the surface, used for area selective deposition on complex three dimensional nanostructures. This research could pave the way for ALD to become the adequate technique to deposit conformal and uniform nanometric thin film with abrupt interfaces and high purity, used for the micro-nano-electronic applications of the future.

Communications and published work produced from this thesis

Journal publications:

- G.P. Gakis, H. Vergnes, F. Cristiano, Y. Tison, C. Vahlas, B. Caussat, A.G. Boudouvis, E. Scheid, "In situ N2-NH3 plasma pre-treatment of silicon substrate enhances the initial growth and restricts the substrate oxidation during alumina ALD." *Journal of Applied Physics* 126(12), 125305 (2019).

- G. P. Gakis, C. Vahlas, H. Vergnes, S. Dourdain, Y. Tison, H. Martinez, J. Bour, D. Ruch, A. G. Boudouvis, B. Caussat and E. Scheid "Investigation of the initial deposition steps and the interfacial layer of Atomic Layer Deposited (ALD) Al2O3 on Si." *Applied Surface Science* 492, 245 (2019)

- G. P. Gakis, H. Vergnes, E. Scheid, C. Vahlas, A. G. Boudouvis and B. Caussat "Detailed investigation of the surface mechanisms and their interplay with transport phenomena in alumina atomic layer deposition from TMA and water." *Chemical Engineering Science* 195, 399 (2019)

- G. P. Gakis, H. Vergnes, E. Scheid, C. Vahlas, B. Caussat and A. G. Boudouvis "Computational Fluid Dynamics simulation of the ALD of alumina from TMA and H2O in a commercial reactor." *Chemical Engineering Research and Design* 132, 795 (2018)

Conference communications:

- G.P. Gakis, H. Vergnes, E. Scheid, A.G. Boudouvis, C. Vahlas and B. Caussat "Combined experimental investigation and reactive transport modelling of ALD of alumina from TMA and water". 5th Réseau des Acteurs Français de l' Atomic Layer Deposition (RAFALD), Toulouse, France, 5-7 November 2019.

- G.P. Gakis, H. Vergnes, F. Cristiano, C. Vahlas, B. Caussat, A. G. Boudouvis and E. Scheid "Reduction of the growth inhibition and substrate oxidation during the

first steps of alumina ALD on Si by an in situ N2-NH3 plasma surface pre-treatment." 5th Réseau des Acteurs Français de l' Atomic Layer Deposition (RAFALD), Toulouse, France, 5-7 November 2019

- G.P. Gakis, H. Vergnes, E. Scheid, C. Vahlas, A. G. Boudouvis and B. Caussat "Initial growth of Alumina ALD: Effect of substrate pretreatment on nucleation period reduction. A computational mechanistic investigation." 4th Réseau des Acteurs Français de l' Atomic Layer Deposition (RAFALD), Lyon, France, 6-8 November 2018.

- G.P. Gakis, H. Vergnes, E. Scheid, C. Vahlas, A. G. Boudouvis and B. Caussat "Alumina ALD from TMA and Water: Unravelling the surface mechanisms and linking transport phenomena with growth uniformity." 2018 Fall Meeting of the European Materials Research Society (EMRS), Warsaw, Poland, 17-20 September 2018.

- G.P. Gakis, H. Vergnes, E. Scheid, C. Vahlas, B. Caussat and A. G. Boudouvis "Experimental investigation and CFD-based analysis of an ALD reactor depositing alumina from TMA and water." 3rd Réseau des Acteurs Français de l' Atomic Layer Deposition (RAFALD), Montpellier, France, 7-9 November 2017.

- G.P. Gakis, H. Vergnes, E. Scheid, A. G. Boudouvis, C. Vahlas and B. Caussat "Experimental investigation and CFD-based analysis of an ALD reactor depositing alumina from TMA and water." Joint 21st European Chemical Vapor Deposition & 15th Baltic Atomic Layer Deposition Conference (EuroCVD 21 – Baltic ALD 15), Linköping, Sweden, 11 – 14 June 2017.

- G.P. Gakis, H. Vergnes, E. Scheid, A. G. Boudouvis, C. Vahlas and B. Caussat "CFD analysis of an ALD reactor: gaseous species distribution and cycle time." 2nd Réseau des Acteurs Français de l' Atomic Layer Deposition (RAFALD), Chatou/Paris, France, 14-16 November 2016.

References

Adhikari, S., Selvaraj, S., Kim, D.-H. Progress in Powder Coating Technology Using Atomic Layer Deposition. *Advanced Materials Interfaces*, **2018**, 5(16),1800581

Adomaitis, R.A. A ballistic transport and surface reaction model for simulating atomic layer deposition processes in high-aspect-ratio nanopores. *Chemical Vapor Deposition*, **2011**, 17(10-12), 353-365

Adomaitis, R.A. Development of a multiscale model for an atomic layer deposition process. *Journal of Crystal Growth*, **2010**, 312(8), 1449-1452

Adomaitis, R.A. Time-scale analysis of atomic layer deposition processes: Predicting the transition from mass-transfer to kinetically limited regimes. *Physica Status Solidi (C) Current Topics in Solid State Physics*, **2015**, 12(7), 934-943

Aleskovskii, V.B., Koltsov, S. I., Some characteristics of molecular layering reactions. *Abstract of Scientific and Technical Conference*, Goskhimizdat, Leningrad,1965, 67

Arwin, H., Aspnes, D.E. Unambiguous determination of thickness and dielectric function of thin films by spectroscopic ellipsometry. *Thin Solid Films*, **1984**, 113(2), 101-113

Aviziotis, I.G., Cheimarios, N., Duguet, T., Vahlas, C., Boudouvis, A.G. Multiscale modeling and experimental analysis of chemical vapor deposited aluminum films: Linking reactor operating conditions with roughness evolution. *Chemical Engineering Science*, **2016**, 155, 449-458

Aviziotis, I.G., *Chemical vapor deposition of Al, Fe and of the Al13Fe4 approximant intermetallic phase: experiments and multiscale simulations*, Institut National Polytechnique de Toulouse. PhD thesis, **2016**

Bae, D., Kwon, S., Oh, J., Kim, W.K., Park, H. Investigation of Al_2O_3 diffusion barrier layer fabricated by atomic layer deposition for flexible $Cu(In,Ga)Se_2$ solar cells, *Renewable Energy*, **2013**, 55, 62-68

Battaile, C.C., Srolovitz, D.J. Kinetic Monte Carlo simulation of chemical vapor deposition. *Annual Review of Materials Science*, **2002**, 32, 297-319

Besling, W.F.A., Young, E., Conard, T., Zhao, C., Carter, R., Vandervorst, W., Caymax, M., De Gendt, S., Heyns, M., Maes, J., Tuominen, M., Haukka, S., Characterisation of ALCVD Al_2O_3-ZrO_2 nanolaminates, link between electrical and structural properties, *Journal of Non-Crystalline Solids*, **2002**, 303123-133

Brewer, R.T., Ho, M.-T., Zhang, K.Z., Goncharova, L.V., Starodub, D.G., Gustafsson, T., Chabal, Y.J., Moumen, N. Ammonia pretreatment for high-k dielectric growth on silicon. *Applied Physics Letters*, **2004**, 85(17), 3830-3832

Cavallotti, C., Di Stanislao, M., Moscatelli, D., Veneroni, A. Materials computation towards technological impact: The multiscale approach to thin films deposition, *Electrochimica Acta*, **2005**, 50(23 SPEC. ISS.), 4566-4575

Chang, Y., Ducroquet, F., Gautier, E., Renault, O., Legrand, J., Damlencourt, J.F., Martin, F. Surface preparation and post thermal treatment effects on interface properties of thin Al_2O_3 films deposited by ALD. *Microelectronic Engineering*, **2004**, 72(1-4), 326-331

Cheimarios, N., Garnelis, S., Kokkoris, G., Boudouvis, A.G. Multiscale modeling of chemical vapor deposition of silicon. *Computer Aided Chemical Engineering*, **2011**, 29, 131-135

CHEMKIN-PRO 15131, Reaction Design: San Diego, 2013

Chen, J.R., Huang, J.R., Hsiung, G.Y. Outgassing Behavior on Aluminum Surfaces: Water in Vacuum Systems. *Journal of Vacuum Science and Technology A: Vacuum, Surfaces and Films*. **1994**, 12(4), 1750-1754.

Chourasia, A.R., Chopra, D.R. A Study of Si3N4 by XPS. *Surface Science Spectra.* **1993**, 2(2), 117-122

COMSOL Multiphysics Reference Manual, version 5.2, COMSOL, Inc

Crose, M., Sang-Il Kwon, J., Nayhouse, M., Ni, D., Christofides, P.D. Multiscale modeling and operation of PECVD of thin film solar cells. *Chemical Engineering Science*, **2015**, 136, 50-61

Damlencourt, J.-F., Renault, O., Chabli, A., Martin, F., Séméria, M.-N., Bedu, F. Surface treatment for high-quality Al_2O_3 and HfO_2 layers deposited on HF-dipped surface by atomic layer deposition. *Journal of Materials Science: Materials in Electronics*. **2003**, 14(5-7), 379-382

Delabie, A., Puurunen, R.L., Brijs, B., Caymax, M., Conard, T., Onsia, B., Richard, O., Vandervorst, W., Zhao, C., Heyns, M.M., Meuris, M., Viitanen, M.M., Brongersma, H.H., De Ridder, M., Goncharova, L.V., Garfunkel, E., Gustafsson, T., Tsai, W. Atomic layer deposition of hafnium oxide on germanium substrates. Journal of Applied Physics, **2005**, 97(6), 064104

Delabie, A., Sioncke, S., Rip, J., Van Elshocht, S., Pourtois, G., Mueller, M., Beckhoff, B., Pierloot, K. Reaction mechanisms for atomic layer deposition of aluminum oxide on semiconductor substrates. *Journal of Vacuum Science and Technology A: Vacuum, Surfaces and Films*, **2012**, 30(1),01A127

Deng, Z., He, W., Duan, C., Shan, B., Chen, R. Atomic layer deposition process optimization by computational fluid dynamics. *Vacuum*, **2016**, 123, 103-110

Dillon, A.C., Ott, A.W., Way, J.D., George, S.M. Surface chemistry of Al2 O3 deposition using Al(CH3)3 and H2 O in a binary reaction sequence. *Surface Science*, **1995**, 322(1-3), 230-242

Dkhissi, A., Mazaleyrat, G., Estève, A., Rouhani, M.D. Nucleation and growth of atomic layer deposition of HfO2 gate dielectric layers on silicon oxide: A multiscale modelling investigation. *Physical Chemistry Chemical Physics*, **2009**, 11(19), 3701-3709

Elam, J.W., Groner, M.D., George, S.M. Viscous flow reactor with quartz crystal microbalance for thin film growth by atomic layer deposition, *Review of Scientific Instruments*, **2002** 73(8), 2981

Elam, J.W., Nelson, C.E., Grubbs, R.K., George, S.M. Nucleation and growth during tungsten atomic layer deposition on SiO_2 surfaces, *Thin Solid Films,* **2001**, 386 41-52

Elliott, S.D., Greer, J.C. Simulating the atomic layer deposition of alumina from first principles. *Journal of Materials Chemistry*, **2004**, 14(21), 3246-3250

Fan, J-F, Toyoda, K., Dependence of the growth of Al2 O3 films on the growth conditions in the ALE-like process, *Materials Research Society Symposium Proceedings*, **1993**, 284, 517-522

Fiji F200 Atomic Layer Deposition System Installation and Use Manual V2. Cambridge NanoTech Inc. Cambridge, MA, USA, July 25, 2009

Foroughi-Abari, A., Cadien, K.C. In situ spectroscopic ellipsometry study of plasma-enhanced ALD of Al 2O 3 on chromium substrates. *Journal of the Electrochemical Society,* **2012**, 159(2), D59-D64

Först, C.J., Ashman, C.R., Schwarz, K., Blöchl, P.E. The interface between silicon and a high-k oxide. *Nature*, **2004**, 427(6969), 53-56

Frank, M.M. Chabal, Y.J., Wilk, G.D. Nucleation and interface formation mechanisms in atomic layer deposition of gate oxides. *Applied Physics Letters*, **2003**, 82(26), 4758-4760

Frank, M.M., Chabal, Y.J., Green, M.L., Delabie, A., Brijs, B., Wilk, G.D., Ho, M.-Y., Da Rosa, E.B.O., Baumvol, I.J.R., Stedlle, F.C. Enhanced initial growth of atomic-layer-deposited metal oxides on hydrogen-terminated silicon. *Applied Physics Letters*, **2003,** 83(4), 740-742

Fryauf, D.M., Phillips, A.C., Bolte, M.J., Feldman, A., Tompa, G.S., Kobayashi, N.P. Scaling Atomic Layer Deposition to Astronomical Optic Sizes: Low-Temperature Aluminum Oxide in a Meter-Sized Chamber. *ACS Applied Materials and Interfaces*, **2018**, 10(48), 41678-41689.

Gakis, G.P., Koronaki, E.D., Boudouvis, A.G. Numerical investigation of multiple stationary and time-periodic flow regimes in vertical rotating disc CVD reactors. *Journal of Crystal Growth*, **2015**, 432, 152-159.

Gakis, G.P., Vahlas, C., Vergnes, H., Dourdain, S., Tison, Y., Martinez, H., Bour, J., Ruch, D., Boudouvis, A.G., Caussat, B., Scheid, E. Investigation of the initial

deposition steps and the interfacial layer of Atomic Layer Deposited (ALD) Al_2O_3 on Si. *Applied Surface Science*, **2019**, 492, 245-254.

Gakis, G.P., Vergnes, H., Cristiano, F., Tison, Y., Vahlas, C., Caussat, B., Boudouvis, A.G., Scheid, E. In situ N_2-NH_3 plasma pre-treatment of silicon substrate enhances the initial growth and restricts the substrate oxidation during alumina ALD. *Journal of Applied Physics*, **2019**, 126(12), 125305.

Gakis, G.P., Vergnes, H., Scheid, E., Vahlas, C., Boudouvis, A.G., Caussat, B. Detailed investigation of the surface mechanisms and their interplay with transport phenomena in alumina atomic layer deposition from TMA and water. *Chemical Engineering Science*, **2019**, 195, 399-412.

Gakis, G.P., Vergnes, H., Scheid, E., Vahlas, C., Caussat, B., Boudouvis, A.G. Computational Fluid Dynamics Simulation of the ALD of Alumina from TMA and H_2O in a Commercial Reactor. *Chemical Engineering Research and Design*, **2018**, 132, 795-811.

George, S.M. Atomic Layer Deposition: An Overview. *Chemical Reviews.* **2010**, 110(1), 111-131.

George, S.M., Ott, A.W., Klaus, J.W. Surface chemistry for atomic layer growth. *Journal of Physical Chemistry*, **1996**, 100(31), 13121-13131.

Gkinis, P.A., Aviziotis, I.G., Koronaki, E.D., Gakis, G.P., Boudouvis, A.G. The effects of flow multiplicity on GaN deposition in a rotating disk CVD reactor. *Journal of Crystal Growth*, **2017**, 458, 140-148.

Gobbert, M.K., Prasad, V., Cale, T.S. Predictive modeling of atomic layer deposition on the feature scale. *Thin Solid Films*, **2002**, 410(1-2), 129-141

Gong, Y.-P., Li, A.-D., Liu, X.-J., Zhang, W.-Q., Li, H., Wu, D. Effect of surface treatments on interfacial characteristics and band alignments of atomic-layer-deposited Al2 O3 films on GaAs substrates. *Surface and Interface Analysis*, **2011**, 43(3), 734-737

Gosset, L.G., Damlencourt, J.-F., Renault, O., Rouchon, D., Holliger, P, Ermolieff, A., Trimaille, I., Ganem, J.-J., Martin, F., Séméria, M.-N., Interface and material characterization of thin Al_2O_3 layers deposited by ALD using TMA/H_2O. *Journal of Non-Crystalline Solids*, **2002**, 303(1), 17-23

Green, M.L., Ho, M.-Y., Busch, B., Wilk, G.D., Sorsch, T., Conard, T., Brijs, B., Vandervorst, W., Räisänen, P.I., Muller, D., Bude, M., Grazul, J. Nucleation and growth of atomic layer deposited HfO2 gate dielectric layers on chemical oxide (Si-O-H) and thermal oxide (SiO2 or Si-O-N) underlayers. *Journal of Applied Physics,* **2002**, 92(12), 7168-7174

Groner, M.D., Elam, J.W., Fabreguette, F.H., George, S.M. Electrical characterization of thin Al_2O_3 films grown by atomic layer deposition on silicon and various metal substrates. *Thin Solid Films*, **2002**, 413(1-2), 186-197

Groner, M.D., Fabreguette, F.H., Elam, J.W., George, S.M. Low-Temperature Al2O3 Atomic Layer Deposition. *Chemistry of Materials*, **2004**, 16(4), 639-645

Ha, S. C., Choi, E. Kim, S.H. Roh J.S., Influence of oxidant source on the property of atomic layer deposited Al2 O3 on hydrogen-terminated Si substrate. *Thin Solid Films*, **2005**, 476 252-257

Hakuli, A., Kytökivi, A., Krause, A.O.I. Dehydrogenation of i-butane on CrOx /Al2 O3 catalysts prepared by ALE and impregnation techniques. *Applied Catalysis A: General*, **2000**, 190(1-2), 219-232

Halls, M.D., Raghavachari, K. Atomic Layer Deposition Growth Reactions of Al 2O 3 on Si(100)-2×1. *Journal of Physical Chemistry B*, **2004**, 108(13), 4058-4062

Halls, M.D., Raghavachari, K. Atomic layer deposition of Al2 O3 on H-passivated Si. I. Initial surface reaction pathways with H/Si(100)-2×1. *Journal of Chemical Physics*, **2003**, 118(22), 10221-10226

Halls, M.D., Raghavachari, K., Frank, M.M., Chabal, Y.J. Atomic layer deposition of Al$_2$O$_3$ on H-passivated Si: Al(CH$_3$)$_2$OH surface reactions with H/Si(100)−2×1. *Physical Review B - Condensed Matter and Materials Physics,* **2003**, 68(16)

Haukka, S., Root, A. The reaction of hexamethyldisilazane and subsequent oxidation of trimethylsilyl groups on silica studied by solid-state NMR and FTIR. *Journal of Physical Chemistry*, **1994**, 98(6), 1695-1703

Henn-Lecordier, L., Anderle, M., Robertson, E., Rubloff, G.W. Impact of parasitic reactions on wafer-scale uniformity in water-based and ozone-based atomic layer deposition. *Journal of Vacuum Science and Technology A: Vacuum, Surfaces and Films,* 2011; 29(5),051509

Houska, J., Blazek, J., Rezek, J., Proksova, S. Overview of optical properties of Al2O3 films prepared by various techniques, *Thin Solid Films*, **2012**, 520(16), 5405–5408

Johnson, R.W.; Hultqvist, A.; Bent, S.F. A Brief Review of Atomic Layer Deposition: From Fundamentals to Applications. *Materials Today*. **2014**, 17 (5), 236-246.

Juppo, M., Rahtu, A., Ritala, M., Leskelä, M. In situ mass spectrometry study on surface reactions in atomic layer deposition of Al2 O3 thin films from trimethylaluminum and water. *Langmuir*, **2000**, 16(8), 4034-4039

Katamreddy, R., Inman, R., Jursich, G., Soulet, A., Takoudis, C. ALD and characterization of aluminum oxide deposited on Si(100) using tris(diethylamino) aluminum and water vapor. *Journal of the Electrochemical Society*, **2006**, 153(10), C701-C706

Kaur, G., Dwivedi, N., Zheng, X., Liao, B., Peng, L.Z., Danner, A., Stangl, R., Bhatia, C.S. Understanding Surface Treatment and ALD AlOx Thickness Induced Surface Passivation Quality of c-Si Cz Wafers. *IEEE Journal of Photovoltaics*, **2017**, 7(5),7976302, 1224-1235

Kazmerski, L.L. Analysis and characterization of thin films: A tutorial. *Solar Cells*, **1988**, 24(3-4), 387-418

Kim, H., Rossnagel, S.M. Growth kinetics and initial stage growth during plasma-enhanced Ti atomic layer deposition. *Journal of Vacuum Science and Technology, Part A: Vacuum, Surfaces and Films*, **2002**, 20(3), 802-808

Kim, J.-Y., Ahn, J.-H., Kang, S.-W., Kim, J.-H. Step coverage modeling of thin films in atomic layer deposition. *Journal of Applied Physics*, **2007**, 101(7),073502

Kingon, A.I., Maria, J.-P., Streiffer, S.K. Alternative dielectrics to silicon dioxide for memory and logic devices. *Nature*, **2000**, 406(6799), 1032-1038

Knoops, H.C.M., MacKus, A.J.M., Donders, M.E., Van De Sanden, M.C.M., Notten, P.H.L., Kessels, W.M.M., Remote plasma ALD of platinum and platinum oxide films. *Electrochemical and Solid-State Letters*, **2009**; 12(7), G34-G36

Koronaki, E.D., Gakis, G.P., Cheimarios, N., Boudouvis, A.G. Efficient tracing and stability analysis of multiple stationary and periodic states with exploitation of commercial CFD software. *Chemical Engineering Science*, 2016, 150, 26-34.

Krug, C., Da Rosa, E.B.O., De Almeida, R.M.C., Morais, J., Baumvol, I.J.R., Salgado, T.D.M., Stedile, F.C., Atomic transport and chemical stability during annealing of ultrathin Al2O3 films on Si, *Physical Review Letters*, **2000**, 85, 4120-4123

Kuse, R., Kundu, M., Yasuda, T., Miyata, N., Toriumi, A. Effect of precursor concentration in atomic layer deposition of Al2 O3. *Journal of Applied Physics*, **2003**, 94(10), 6411-6416

Kytökivi, A., Jacobs, J.-P., Hakuli, A., Meriläinen, J., Brongersma, H.H. Surface characteristics and activity of chromia/alumina catalysts prepared by atomic layer epitaxy. *Journal of Catalysis*, **1996**, 162(2),0276, 190-197

Lee, B., Choi, K.J., Hande, A., Kim, M.J., Wallace, R.M., Kim, J., Senzaki, Y., Shenai, D., Li, H., Rousseau, M., Suydam, J. A novel thermally-stable zirconium amidinate ALD precursor for ZrO2 thin films, *Microelectronic Engineering*, **2009**, 86(3), 272-276

Lee, S.S., Baik, J.Y., An, K.-S., Suh, Y.D., Oh, J.-H., Kim, Y. Reduction of incubation period by employing OH-terminated Si(001) substrates in the atomic layer deposition of Al2 O3. *Journal of Physical Chemistry B*, **2004**,108(39), 15128-15132

Li, M.-Y., Chang, Y.-Y., Wu, H.-C., Huang, C.-S., Chen, J.-C., Lue, J.-L., Chang, S.-M. Effect of process pressure on atomic layer deposition of Al2O3, *Journal of the Electrochemical Society*, **2007**, 154(11), H967-H972

Lim, S.W., Machuca, F., Liao, H., Chiarello, R.P., Helms, R.C. Effect of initial Al contamination on ultrathin gate oxides. *Journal of the Electrochemical Society*, **2000**, 147(3), 1136-1140

Lin, J.-M., Teplyakov, A.V. Computational investigation of surface reactivity of functionalized silicon surfaces in deposition processes. *Theoretical Chemistry Accounts*, **2013**, 132(12), 1-14

Lu, H.-L., Xu, M., Ding, S.-J., Chen, W., Zhang, D.W., Wang, L.-K. X-ray reflectometry and spectroscopic ellipsometry characterization of Al2 O3 atomic layer deposition on HF-last and NH3 plasma pretreatment Si substrates. *Journal of Materials Research*, **2007**, 22(5), 1214-1218

Lu, J., Aarik, J., Sundqvist, J., Kukli, K., Hårsta, A., Carlsson, J.-O. Analytical TEM characterization of the interfacial layer between ALD HfO2 film and silicon substrate. *Journal of Crystal Growth*, **2005**, 273(3-4), 510-514

Mack, P., White, R.G., Wolstenholme, J., Conard, T. The use of angle resolved XPS to measure the fractional coverage of high-k dielectric materials on silicon and silicon dioxide surfaces. *Applied Surface Science*, **2006**, 252(23), 8270-8276

Marturano, M., Aglietti, E.F., Ferretti, O. α-Al2 O3 catalyst supports for synthesis gas production: Influence of different alumina bonding agents on support and catalyst properties, *Materials Chemistry and Physics*, **1997**, 47(2-3), 252-256

Mazaleyrat, G., Estève, A., Jeloaica, L., Djafari-Rouhani, M. A methodology for the kinetic Monte Carlo simulation of alumina atomic layer deposition onto silicon. *Computational Materials Science*, **2005**, 33(1-3), 74-82

McBride, B.J., Gordon, S., Reno, M.A. Coefficients for Calculating Thermodynamic and Transport Properties of Individual Species. *NASA Technical Memorandum 4513*, **1993**. Washington, D.C.:National Aeronautics and Space Administration.

Muñoz-Rojas, D., Maindron, T., Esteve, A., Piallat, F., Kools, J.C.S., Decams, J.-M. Speeding up the unique assets of atomic layer deposition, *Materials Today Chemistry*, **2019,** 12, 96-120

Naumann, V., Otto, M., Wehrspohn, R.B., Hagendorf, C. Chemical and structural study of electrically passivating Al_2O_3 /Si interfaces prepared by atomic layer deposition. *Journal of Vacuum Science and Technology A: Vacuum, Surfaces and Films*, **2012**, 30(4),04D106

Neizvestny, I.G., Shwartz, N.L., Yanovitskaja, Z.Sh., Zverev, A.V. Simulation of surface relief effect on ALD process. *Computational Materials Science*, **2006**, 36(1-2), 36-41

Nilsen, O., Mohn, C.E., Kjekshus, A., Fjellvåg, H. Analytical model for island growth in atomic layer deposition using geometrical principles. *Journal of Applied Physics,* **2007**, 102(2),024906

NIST Chemistry WebBook, NIST Standard Reference Database Number 69; National Institute of Standards and Technology: Gaithersburg, MD, USA, 2005. Available online: http://webbook.nist.gov

Ott, A.W., Klaus, J.W., Johnson, J.M., George, S.M. Al_2O_3 thin film growth on Si(100) using binary reaction sequence chemistry. *Thin Solid Films*, **1997**, 292(1-2), 135-144

Pan, D., Ma, L., Xie, Y., Wang, F., Jen, T.-C., Yuan, C. Experimental and numerical investigations into the transient multi-wafer batch atomic layer deposition process with vertical and horizontal wafer arrangements. *International Journal of Heat and Mass Transfer*, **2015**; 91, 416-427

Pan, D., Guan, D., Jen, T.-C., Yuan, C. Atomic Layer Deposition Process Modeling and Experimental Investigation for Sustainable Manufacturing of Nano Thin Films. *Journal of Manufacturing Science and Engineering, Transactions of the ASME*, **2016**, 138(10),101010

Pan, D.; Ma, L.; Xie, Y.; Jen, T.C.; Yuan, C. On the Physical and Chemical Details of Alumina Atomic Layer Deposition: A Combined Experimental and Numerical Approach. *Journal of Vacuum Science and Technology A: Vacuum, Surfaces and Films.* **2015**, 33(2), 021511.

Park, D.-G., Cho, H.-J., Lim, K.-Y., Lim, C., Yeo, I.-S., Roh, J.-S., Park, J.W. Characteristics of n+ polycrystalline-Si/Al2O3/Si metal-oxide-semiconductor structures prepared by atomic layer chemical vapor deposition using Al(CH3)3 and H2O vapor. *Journal of Applied Physics*, **2001,** 89(11 I), 6275-6280

Peltonen, P., Vuorinen, V., Marin, G., Karttunen, A.J., Karppinen, M. Numerical study on the fluid dynamical aspects of atomic layer deposition process. *Journal of Vacuum Science and Technology A: Vacuum, Surfaces and Films.* **2018**, 36(2),021516

Petford-Long, A.K., Chiaramonti, A.N. Transmission electron microscopy of multilayer thin films. *Annual Review of Materials Research*, **2008**, 38, 559-584

Ponraj, J.S., Attolini, G., Bosi, M. Review on atomic layer deposition and applications of oxide thin films. *Critical Reviews in Solid State and Materials Sciences*, **2013**, 38(3), 203-233

Puurunen, R.L. Correlation Between the Growth-Per-Cycle and the Surface Hydroxyl Group Concentration in the Atomic Layer Deposition of Aluminum Oxide from Trimethylaluminum and Water. *Applied Surface Science.* **2005**, 245(1-4), 6-10.

Puurunen, R.L. Random deposition as a growth mode in atomic layer deposition. *Chemical Vapor Deposition*, **2004**, 10(3), 159-170

Puurunen, R.L. Surface Chemistry of Atomic Layer Deposition: A Case Study for the Trimethylaluminum/Water Process. *Journal of Applied Physics.* **2005**, 97 (12), 121301.

Puurunen, R.L., Vandervorst, W. Island growth as a growth mode in atomic layer deposition: A phenomenological model. *Journal of Applied Physics*, **2004**, 96(12),10, 7686-7695

Puurunen, R.L.; Vandervorst, W.; Besling, W.F.A.; Richard, O.; Bender, H.; Conard, T.; Zhao, C.; Delabie, A.; Caymax, M.; De Gendt, S.; Heyns, M.; Viitanen, M.M.; De Ridder, M.; Brongersma, H.H.; Tamminga, Y.; Dao, T.; De Win, T.e, Verheijen, M.; Kaiser, M.; Tuominen, M. Island growth in the atomic layer deposition of zirconium oxide and aluminum oxide on hydrogen-terminated silicon: Growth mode modeling and transmission electron microscopy. *Journal of Applied Physics*. **2004**. 96(9), 4878-4889

Remmers, E.M., Travis, C.D., Adomaitis, R.A. Reaction factorization for the dynamic analysis of atomic layer deposition kinetics. *Chemical Engineering Science*, **2015**, 127, 374-391

Renault, O., Gosset, L.G., Rouchon, D., Ermolieff, A. Angle-resolved x-ray photoelectron spectroscopy of ultrathin Al_2O_3 films grown by atomic layer deposition. *Journal of Vacuum Science and Technology A: Vacuum, Surfaces and Films.* **2002**, 20(6), 1867-1876

Ritala, M., Leskelä, M., Dekker, J.-P., Mutsaers, C., Soininen, P.J., Skarp, J. Perfectly conformal TiN and Al2 O3 films deposited by atomic layer deposition. *Chemical Vapor Deposition*, **1999**, 5(1), 7-9

Ritala, M., Saloniemi, H., Leskelä, M., Prohaska, T., Friedbacher, G., Grasserbauer, M. Studies on the morphology of Al2 O3 thin films grown by atomic layer epitaxy, *Thin Solid Films*, 286(1-2), **1996**, 54-58

Rodríguez-Reyes, J.C.F., Teplyakov, A.V. Cooperative nitrogen insertion processes: Thermal transformation of N H3 on a Si(100) surface. *Physical Review B - Condensed Matter and Materials Physics*, **2007**, 76(7),075348

Rodríguez-Reyes, J.C.F., Teplyakov, A.V. Surface transamination reaction for tetrakis(dimethylamido)titanium with NH X -terminated Si(100) surfaces. *Journal of Physical Chemistry C*, **2007**,111(44), 16498-16505

Salami, H., Poissant, A., Adomaitis, R.A. Anomalously high alumina atomic layer deposition growth per cycle during trimethylaluminum under-dosing conditions. *Journal of Vacuum Science and Technology A: Vacuum, Surfaces and Films*, **2017**; 35(1),01B101

Salaün, A., Newcomb, S.B., Povey, I.M., Salaün, M., Keeney, L., O'Mahony, A., Pemble, M.E. Nucleation and chemical transformation of RuO2 films grown on (100) Si substrates by atomic layer deposition. *Chemical Vapor Deposition*, **2011**, 17(4-6), 114-122

Schilirò, E., Greco, G., Fiorenza, P., Tudisco, C., Condorelli, G.G., Di Franco, S., Roccaforte, F., Lo Nigro, R. Effects of surface nature of different semiconductor substrates on the plasma enhanced atomic layer deposition growth of Al2 O3 gate dielectric thin films. **2015**, *Physica Status Solidi (C) Current Topics in Solid State Physics* 12(7), 980-984.

Seo, S., Nam, T., Lee, H.B.R., Kim, H., Shong, B. Molecular oxidation of surface – CH_3 during atomic layer deposition of Al_2O_3 with H_2O, H_2O_2, and O_3: A theoretical study, *Applied Surface Science*, **2018**, 457 376-380

Shaeri, M.R., Jen, T.-C., Yuan, C.Y., Behnia, M. Investigating atomic layer deposition characteristics in multi-outlet viscous flow reactors through reactor scale simulations. *International Journal of Heat and Mass Transfer*, **2015**, 89, 480-481

Shi, S., Qian, S., Hou, X., Mu, J., He, J., Chou, X. Structural and optical properties of amorphous Al 2 O 3 thin film deposited by atomic layer deposition, Advances in Condensed Matter Physics, **2018**, 2018,7598978

Shirazi, M., Elliott, S.D. Atomistic kinetic Monte Carlo study of atomic layer deposition derived from density functional theory. *Journal of Computational Chemistry*, **2014**, 35(3), 244-259

Suntola, T., Antson, J., International patent, FIN 52359, US 4 058 430,priority Nov 29,1974, publication Nov 15,1977.

Tai, T.B., Cao, L., Mattelaer, F., Rampelberg, G., Hashemi, F.S.M., Dendooven, J., Van Ommen, J.R., Detavernier, C., Reyniers, M.-F. Atomic Layer Deposition of Al2 O3 Using Aluminum Triisopropoxide (ATIP): A Combined Experimental and Theoretical Study. *Journal of Physical Chemistry C*, **2019**, 123(1), 485-494

Takeuchi, H., King, T.-J. Scaling limits of hafnium –silicate films for gate-dielectric applications. *Applied Physics Letters,* **2003**, 83(4), 788-790

Travis, C.D. Adomaitis, R.A. Modeling ALD Surface Reaction and Process Dynamics Using Absolute Reaction Rate Theory. *Chemical Vapor Deposition*. **2013**, 19(1-3), 4-14.

Travis, C.D. Adomaitis, R.A. Modeling Alumina Atomic Layer Deposition Reaction Kinetics During the Trimethylaluminum Exposure. *Theoretical Chemistry Accounts*. **2014**, 133(1), 3-11.

Tutas, D.J., Stromberg, R., Passagila, E. Studies of the thicknesses of adsorbed glass finishes by ellipsometry. *Polymer Engineering & Science*, **1964**, 4(4), 256-262

Van Bui, H., Wiggers, F.B., Gupta, A., Nguyen, M.D., Aarnink, A.A.I., De Jong, M.P., Kovalgin, A.Y. Initial growth, refractive index, and crystallinity of thermal and plasma-enhanced atomic layer deposition AlN films. *Journal of Vacuum Science and Technology A: Vacuum, Surfaces and Films*, **2015**, 33(1),01A111

Van Bui, H., Grillo, F., Van Ommen, J.R. Atomic and molecular layer deposition: off the beaten track. *Chemical Communications.* **2017**. 53(1), 45-71

Vandalon, V., Kessels, W.M.M. Revisiting the Growth Mechanism of Atomic Layer Deposition of Al_2O_3: A Vibrational Sum-Frequency Generation Study. *Journal of Vacuum Science and Technology A: Vacuum, Surfaces and Films.* **2017**, 35 (5), 4993597.

Vandalon, V., Kessels, W.M.M. What is Limiting Low-Temperature Atomic Layer Deposition of Al_2O_3? A Vibrational Sum-Frequency Generation Study. *Applied Physics Letters*. **2016**, 108 (1), 011607.

Vignaud, G., Gibaud, A. REFLEX: A program for the analysis of specular X-ray and neutron reflectivity data. *Journal of Applied Crystallography,* **2019**, 52, 201-213

Wang, P., He, Y.-D., Deng, S.-J., Zhang, J. Porous α-Al2 O3 thermal barrier coatings with dispersed Pt particles prepared by cathode plasma electrolytic deposition, *International Journal of Minerals, Metallurgy and Materials*, **2016**, 23(1), 92-101

Wen, Y., Liu, Y., Guo, Y., Yu, G., Hu, W. Experimental techniques for the fabrication and characterization of organic thin films for field-effect transistors. *Chemical Reviews*, **2011**, 111(5), 3358-3406

Werner, F., Veith, B., Zielke, D., Kühnemund, L., Tegenkamp, C., Seibt, M., Brendel, R. Schmidt, J. Electronic and chemical properties of the c-Si/Al2 O3 interface. *Journal of Applied Physics*, **2011**, 109(11),113701

Whiteside, P.J.D., Chininis, J.A., Hunt, H.K. Techniques and challenges for characterizing metal thin films with applications in photonics. *Coatings*, **2016**, 6(3),35

Widjaja, Y., Musgrave, C.B. Ab initio study of the initial growth mechanism of silicon nitride on Si(100)-(2 × 1) using NH3. *Physical Review B - Condensed Matter and Materials Physics,* **2001**, 64(20),205303, 2053031-2053039

Widjaja, Y., Musgrave, C.B. Quantum Chemical Study of the Mechanism of Aluminum Oxide Atomic Layer Deposition. *Applied Physics Letters*. **2002**, 80(18), 3304-3306.

Wind, R.A., George, S.M. Quartz crystal microbalance studies of Al2 O3 atomic layer deposition using trimethylaluminum and water at 125 °C. *Journal of Physical Chemistry A*, **2010**, 114(3), 1281-1289

Xie, Y., Pan, D., Ma, L., Yuan, C. Optimizing the process efficiency of atomic layer deposition of alumina for its sustainability improvement: a combined experimental and modeling study. *Journal of Cleaner Production*, **2016**, 133, 338-347

Xie, Y.; Ma, L.; Pan, D.; Yuan, C. Mechanistic Modeling of Atomic Layer Deposition of Alumina Process with Detailed Surface Chemical Kinetics. *Chemical Engineering Journal.* **2015**, 259, 213-220.

Xu, M., Xu, C.-H., Ding, S.-J., Lu, H.-L., Zhang, D.W., Wang, L.-K. Spectroscopic and electrical properties of atomic layer deposition Al_2O_3 gate dielectric on surface pretreated Si substrate. *Journal of Applied Physics,* **2006**, 99(7),074109

Xu, M., Zhang, C., Ding, S.-J., Lu, H.-L., Chen, W., Sun, Q.-Q., Zhang, D.W., Wang, L.-K. Mechanism of interfacial layer suppression after performing surface $Al(CH_3)_3$ pretreatment during atomic layer deposition of Al_2O_3. *Journal of Applied Physics,* **2006,** 100(10),106101

Zhuravlev, L.T. The Surface Chemistry of Amorphous Silica. Zhuravlev Model. *Colloids and Surfaces A: Physicochemical and Engineering Aspects.* **2000**, 173(1-3), 1-38.